Random porous media and magnetic separation of magnetic colloids

ISBN: 978-90-393-6470-3

Random porous media and magnetic separation of magnetic colloids

Ongeordende poreuze media en magnetische scheiding van magnetische colloïden

(met een samenvatting in het Nederlands)

Proefschrift

ter verkrijging van de graad van doctor aan de Universiteit Utrecht op gezag van de rector magnificus, prof. dr. G. J. van der Zwaan, ingevolge het besluit van het college voor promoties in het openbaar te verdedigen op woensdag 13 januari 2016 des ochtends te 10.30 uur

door

Roel Johannes Baars

geboren op 17 januari 1988 te Tiel

Promotor: Prof. dr. A. P. Philipse

This research is supported by the Dutch Technology Foundation STW, which is part of the Netherlands Organisation for Scientific Research (NWO) and partly funded by the Ministry of Economic Affairs (project number 11398, "SMART Separations for complex systems" program).

Contents

1 Introduction

This thesis deals with various topics that all relate to the investigation of a high-gradient magnetic separation process for the capture of magnetic nanoparticles. This chapter provides some essential background information and introduces some reoccurring elements and terminology. It also outlines the structure of this thesis.

1.1 Nanoparticles and colloids

While many subtly different definitions are in use, a nanoparticle can be defined roughly as any object with a size ranging from 1–100 nm. Once dispersed in a medium, it may also be referred to as a colloidal particle, or colloid. However, the definition of a colloid (strictly speaking a colloidal dispersion), does not necessarily refer to solid particles, but applies to any finely dispersed phase (gas, liquid, solid) in a different continuous phase. Here the dispersed phase has at least one dimension in the approximate range 1 nm – 1 µm [1], which is often referred to as the colloidal size range. Common examples of colloidal dispersions are blood, paint and smoke, but colloids are also found in foams, cosmetics and emulsified food products such as milk and mayonnaise.

Colloidal model systems Nanoparticles (and colloids) are distinguished from macroscopic objects by the display of continuous motion due to their inherent kinetic energy. For colloids in a liquid dispersion, colliding continuously with much smaller solvent molecules, this results in the uncorrelated, random displacement of the particle, i.e. Brownian motion. This behaviour is similar to that of atoms, but occurs on much longer time-scales, allowing these dynamics to be observed by various microscopy techniques. This makes colloids ideal model particles for the study of the behaviour of atomic and molecular systems. A plethora of colloidal model systems exist, usually with specifically designed interactions and, more recently, with an additional chemical, physical or geometrical anisotropy. A few recent highlights include strongly anisometric colloids [2–4], particles with a tunable interaction potential [5, 6], or surface modifications designed for highly specific interactions [7–9].

Magnetic particles Magnetically susceptible nanoparticles and colloids are also of great interest, as they can be manipulated at a distance using an external magnetic field. Such particles have been used, for example, in the search for a colloidal equivalent of a dipolar fluid and evidence for dipolar chain formation [10, 11], and for the formation of novel self-assembly structures [12, 13]. Concentrated stable dispersions of magnetic nanoparticles, so-called ferrofluids, were first synthesised in the 1960's at NASA [14]. They have found their use as mechanical sealants, dampening liquids and magnetic inks [15, 16], but also in diverse biomedical applications [17], such as cancer treatment [18] or as contrast agent in magnetic resonance imaging (MRI) [19]. Further applications of magnetic nanoparticles are found in (bio-)catalysis [20–22], waste-water purification [23, 24] and biological analyses and purification techniques [25–27].

In these last few scenarios, the magnetic particles usually act as carrier particles and have a specific surface functionalisation that binds to other moieties. For these situations, the major advantage of using nanoparticles over larger particles becomes apparent: nanoparticles have a much larger specific surface area, and therefore have a much higher capacity of performing reactions, capturing molecules, etc. The particles are typically collected after use for recycling by some means of magnetic separation.

1.2 Magnetic separation

The process of magnetically separating magnetically susceptible materials of macroscopic dimensions is widespread in industry, for example in the extraction of iron ores in mining [28] or ferrous materials from waste-processing streams [29]. Permanent magnets or electromagnets are used to attract and direct any magnetic materials away from non-magnetic materials. This capture process is driven by magnetic forces acting on the material, where the force is proportional to the magnetic properties of the material (specifically, its overall magnetic moment) and the gradient of the applied magnetic field.

As magnetic materials become smaller and enter the colloidal size range, increasingly stronger field gradients are required for successful capture, as the magnetic moment decreases proportionally to the volume of the material (or particle). Separation is often still possible by using high-gradient magnetic separation (HGMS) devices [27, 30], where a fine mesh or matrix of a ferrous material (e.g. steel wool) is magnetised externally, producing strong local field gradients. In a typical scenario, a liquid containing magnetic nanoparticles is passed through such a magnetised matrix, which will then retain the particles.

Applying the HGMS technique to capture particles smaller than (roughly) 100 nm is still challenging [31], as Brownian forces start to dominate over the magnetic forces. Despite this, experiments and theoretical models have shown that capture of ~ 10 nm particles is possible [32–34]. These findings are explained by a careful choice of the particle chemistry and a collaborative effect, e.g. reversible aggregation, where actually clusters of particles are being separated, and not individual ones. One can argue that there is still an open challenge to find (the best approximation to) the 'holy grail' in HGMS: a device that can fully, reversibly and selectively, capture magnetic particles of any given size. The investigation in this thesis contributes to this search.

1.3 Particle packings

Ordered and disordered packings of particles are found throughout nature and technology [35, 36]. As such, scientists from many disciplines have been involved in discerning their mathematical and physical properties. Insight into the packing characteristics helps understanding the properties of e.g. simple liquids, crystalline and glassy solids, foams, packed reactor beds, various biological systems, and granular materials in general. Of particular note is the fact that ordered and random packings occur experimentally at very different length-scales with strikingly similar characteristics, suggesting that the local and global packing properties are strongly determined by the particle's geometry.

Ordered packings A classical example of a densest packing problem is proposed by Johannes Kepler in his 1611 paper "*Strena Seu de Nive Sexangula*" ("On the six-cornered snowflake") [37]. He conjectured that for non-overlapping spheres the highest packing density achievable equals $\pi/(3\sqrt{2}) \approx 0.74$, corresponding to the structure of a face-centred cubic lattice. A computer-aided proof of his conjecture was given only in 1998 by Thomas Hales, published later [38]. A formal proof was given recently [39], illustrating that rigorous treatment of packing problems is extremely challenging.

In spite of this difficulty, there has been an on-going search for the densest structures of non-spherical particles. Experimental and simulation studies have investigated, among others, ellipsoids [40, 41], various polyhedra [42–45], superballs [46, 47], and other shapes [48–50]. Connections to experimental systems that exhibit ordered and crystalline structures are readily available, for example in colloid and nanomaterials science [3, 51–58].

Disordered packings In 1960, Bernal was one of the first to publish experimental results on *random* sphere packings, finding a reproducible 'random close packing' (RCP) density of $\phi \approx 0.64$ [59]. Others have found very similar values from very different experiments (cf. Scott and Kilgour [60], Philipse and Pathmamanoharan [61], and Nowak *et al.* [62]), suggesting a certain uniqueness of the RCP-state.

Despite very comparable experimental results, the notion of the RCP-state is mathematically ill-defined [63, 64]. Torquato *et al.* [63] argue that the terms 'random' and 'close packing' cannot be unified, as a random packing can always be made more dense by sacrificing some of its disorder. Alternatively, one may consider 'maximally random jammed' (MRJ) packings, in which all particles are jammed (i.e. cannot be translated without creating overlap), while simultaneously having a minimal value of certain order parameters. These criteria can be rigorously enforced in computer simulations, as shown for example in [65]. For spheres the MRJ-state and RCP-state have matching densities [66].

The investigation of random dense packings has seen widespread attention, in particular in relation to theories and experiments on (granular) jammed systems and the glass transition [67–70]. See [71] for an in-depth review on jammed particle packings. Also of note is the recent work by Baule *et al.* who develop a mean-field theory for random dense packing [72], accurately predicting the RCP-densities of many axisymmetric particles.

Random rod packing A specific case of random particle packings, relevant in the context of this thesis, is the random packing of rod-like particles. As discussed extensively by Philipse [73], these packings are widespread in nature and technology, but had seen very little attention compared to spheres. Philipse provides a theoretical argument, based on excluded volume effects, that for sufficiently thin, long rods the packing fraction ϕ is related to the average number of contacts per particle $\langle C \rangle$ through the particle aspect ratio,

$$\phi \frac{L}{D} \sim \frac{\langle C \rangle}{2} \qquad \text{for} \qquad \frac{L}{D} \gg 1 \tag{1.1}$$

where L and D are the length and diameter of a rod, respectively. Such an explicit relation is not known for spheres. Equation 1.1 is known as the *random contact equation* for rods and gives a very good approximation for the experimental random close packing density of rods with an aspect ratio of $L/D > 15$ (cf. [74–76] and later [77–79]). The relation breaks down for smaller aspect ratios, as particle contacts become increasingly correlated. Several computer simulation studies have shed light on the relation between the particle aspect ratio and packing fraction in this small aspect-ratio limit [80–82].

Computer simulations Computer simulations have been an essential tool for investigating particle packings. They allow a virtually unlimited variation in experimental conditions, including particle shape, size distribution and interactions (e.g. friction). They also make it possible to observe the inner structure of a packing and perform more extensive analysis than possible in laboratory experiments, although recent advances in X-ray tomography proved highly useful for that purpose as well [83, 84].

In the past decades, many different techniques have been developed to generate both densest ordered and disordered packings. A few examples include: random sequential addition algorithms [85–87], Monte Carlo based methods [88, 89], (event-driven) molecular dynamics [46, 90–92], discrete-element methods [93–95] and linear programming techniques [96]. For a more thorough discussion on the various approaches, see elsewhere [97].

Another class of packing algorithms are the overlap removal algorithms (or overlap relaxation algorithms), where particles are allowed to enter an unphysical overlapping situation with another particle, that is subsequently removed. Among the first to use this approach for sphere packings was Finney [98], but many variants were devised afterwards [82, 99–101]. The step towards non-spherical particles was made by Nolan and Kavanagh [102], followed by a related overlap removal algorithm specifically for spherocylinder particles by Williams [80]. The latter is known as the *mechanical contraction method* and is used as the method of choice in this thesis.

1.4 Scope of this thesis

The work described in this thesis covers several different topics, with the central theme being the high-gradient magnetic separation of magnetic nanoparticles. Our approach makes specific use of a model separation matrix of randomly packed magnetisable rods. Our primary goal is to provide insight into theoretical and experimental aspects of the

separation process, and simultaneously lay a foundation for further investigation. We focus on three different topics: random particle packings (Part 1), magnetic separation (Part 2) and particle synthesis (Part 3).

In Chapter 2 random dense packings of spherocylinder particles are simulated, as a model for the experimental separation matrix, using the mechanical contraction method. A method is developed to enforce hard boundaries, and the effect of a confining cylindrical boundary on the bulk packing density is investigated. The general approach of the hard boundary method is also demonstrated for a wedge-shaped boundary. In order to broaden the applicability of the mechanical contraction method, outside the scope of modelling the magnetic separation matrix, we revisit the simulation method in Chapter 3. We re-derive the underlying equations and simultaneously formulate them such that it allows the simulation of particles of any convex shape. As proof-of-principle, this revised method is applied to simulate random dense packings of superquadric particles in Chapter 4.

At this point our attention turns towards understanding the magnetic separation process in more detail. In Chapter 5 we derive exact equations for the magnetic field produced by a magnetic cylinder of a finite length, and with an arbitrarily oriented magnetization vector. This allows us to calculate the magnetic force acting on a particle directly and to high accuracy. These equations are used in Chapter 6 where Brownian dynamics simulations are performed to calculate the motion of magnetic nanoparticles in the presence of a single magnetised cylinder. We obtain quantitative information on how quickly, and under which circumstances particles can be captured. An estimation is made of the efficiency of a separation matrix comprising many cylinders. Furthermore, the effect of concentration is studied by inclusion of hydrodynamic interactions. Chapter 7 describes the experimental realisation of the magnetic separation device using a fibrous porous separation matrix. Preliminary experiments on the separation of magnetic nanoparticles are performed and the separation efficiency is discussed.

Finally, in Chapter 8 a versatile and simple chemical synthesis method is presented to prepare functional colloidal particles, for example magnetically loaded particles, based on the protein zein. Additionally, the particles are modified with a layer of silica that enables further surface modification. Such particles may eventually be used for magnetic separation purposes.

References

1. J. Lyklema, *Fundamentals of Interface and Colloid Science*, *Vol. 4*, Academic Press, **2005**.
2. M. Marechal, R. J. Kortschot, A. F. Demirörs, A. Imhof, M. Dijkstra, 'Phase Behavior and Structure of a New Colloidal Model System of Bowl-Shaped Particles', *Nano Letters* **2010**, *10*, 1907–1911, DOI 10.1021/nl100783g.
3. L. Rossi, S. Sacanna, W. T. M. Irvine, P. M. Chaikin, D. J. Pine, A. P. Philipse, 'Cubic crystals from cubic colloids', *Soft Matter* **2011**, *7*, 4139–4142, DOI 10.1039/C0SM01246G.
4. J. R. Wolters, PhD thesis, Universiteit Utrecht, The Netherlands, **2015**.
5. A. Yethiraj, A. van Blaaderen, 'A colloidal model system with an interaction tunable from hard sphere to soft and dipolar', *Nature* **2003**, *421*, 513–517, DOI 10.1038/nature01328.
6. M. E. Leunissen, C. G. Christova, A.-P. Hynninen, C. P. Royall, A. I. Campbell, A. Imhof, M. Dijkstra, R. van Roij, A. van Blaaderen, 'Ionic colloidal crystals of oppositely charged particles', *Nature* **2005**, *437*, 235–240, DOI 10.1038/nature03946.

7. Y. Wang, Y. Wang, D. R. Breed, V. N. Manoharan, L. Feng, A. D. Hollingsworth, M. Weck, D. J. Pine, 'Colloids with valence and specific directional bonding', *Nature* **2012**, *491*, 51–55, DOI 10.1038/nature11564.
8. *Janus Particle Synthesis, Self-Assembly and Applications*, (Eds.: S. Jiang, S. Granick), Royal Society of Chemistry, **2012**, DOI 10.1039/9781849735100.
9. B. G. P. van Ravensteijn, M. Kamp, A. van Blaaderen, W. K. Kegel, 'General Route toward Chemically Anisotropic Colloids', *Chemistry of Materials* **2013**, *25*, 4348–4353, DOI 10.1021/cm4025606.
10. A. P. Philipse, M. P. B. van Bruggen, C. Pathmamanoharan, 'Magnetic silica dispersions: preparation and stability of surface-modified silica particles with a magnetic core', *Langmuir* **1994**, *10*, 92–99, DOI 10.1021/la00013a014.
11. K. Butter, P. H. H. Bomans, P. M. Frederik, G. J. Vroege, A. P. Philipse, 'Direct observation of dipolar chains in iron ferrofluids by cryogenic electron microscopy', *Nature Materials* **2003**, *2*, 88–91, DOI 10.1038/nmat811.
12. S. Sacanna, L. Rossi, D. J. Pine, 'Magnetic Click Colloidal Assembly', *Journal of the American Chemical Society* **2012**, *134*, 6112–6115, DOI 10.1021/ja301344n.
13. A. I. Abrikosov, S. Sacanna, A. P. Philipse, P. Linse, 'Self-assembly of spherical colloidal particles with off-centered magnetic dipoles', *Soft Matter* **2013**, *9*, 8904–8913, DOI 10.1039/C3SM27128E.
14. S. S. Papell, Low viscosity magnetic fluid obtained by the colloidal suspension of magnetic particles, US Patent no. 3,215,572, **1965**.
15. K. Raj, B. Moskowitz, R. Casciari, 'Advances in ferrofluid technology', *Journal of Magnetism and Magnetic Materials* **1995**, *149*, 174–180, DOI 10.1016/0304-8853(95)00365-7.
16. P. Berger, N. B. Adelman, K. J. Beckman, D. J. Campbell, A. B. Ellis, G. C. Lisensky, 'Preparation and properties of an aqueous ferrofluid', *Journal of Chemical Education* **1999**, *76*, 943, DOI 10.1021/ed076p943.
17. Q. A. Pankhurst, J. Connolly, S. K. Jones, J. Dobson, 'Applications of magnetic nanoparticles in biomedicine', *Journal of Physics D: Applied Physics* **2003**, *36*, R167, DOI 10.1088/0022-3727/36/13/201.
18. A. Jordan, R. Scholz, K. Maier-Hauff, M. Johannsen, P. Wust, J. Nadobny, H. Schirra, H. Schmidt, S. Deger, S. Loening, W. Lanksch, R. Felix, 'Presentation of a new magnetic field therapy system for the treatment of human solid tumors with magnetic fluid hyperthermia', *Journal of Magnetism and Magnetic Materials* **2001**, *225*, 118–126, DOI 10.1016/S0304-8853(00)01239-7.
19. C. Sun, J. S. H. Lee, M. Zhang, 'Magnetic nanoparticles in MR imaging and drug delivery', *Advanced drug delivery reviews* **2008**, *60*, 1252–1265, DOI 10.1016/j.addr.2008.03.018.
20. T.-J. Yoon, W. Lee, Y.-S. Oh, J.-K. Lee, 'Magnetic nanoparticles as a catalyst vehicle for simple and easy recycling', *New Journal of Chemistry* **2003**, *27*, 227–229, DOI 10.1039/B209391J.
21. L. Gao, J. Zhuang, L. Nie, J. Zhang, Y. Zhang, N. Gu, T. Wang, J. Feng, D. Yang, S. Perrett, X. Yan, 'Intrinsic peroxidase-like activity of ferromagnetic nanoparticles', *Nature Nanotechnology* **2007**, *2*, 577–583, DOI 10.1038/nnano.2007.260.
22. E. M. Claesson, N. C. Mehendale, R. J. M. Klein Gebbink, G. van Koten, A. P. Philipse, 'Magnetic silica colloids for catalysis', *Journal of Magnetism and Magnetic Materials* **2007**, *311*, 41–45, DOI 10.1016/j.jmmm.2006.11.166.
23. Y. Shen, J. Tang, Z. Nie, Y. Wang, Y. Ren, L. Zuo, 'Preparation and application of magnetic Fe_3O_4 nanoparticles for wastewater purification', *Separation and Purification Technology* **2009**, *68*, 312–319, DOI 10.1016/j.seppur.2009.05.020.
24. P. Xu, G. M. Zeng, D. L. Huang, C. L. Feng, S. Hu, M. H. Zhao, C. Lai, Z. Wei, C. Huang, G. X. Xie, Z. F. Liu, 'Use of iron oxide nanomaterials in wastewater treatment: a review', *Science of the Total Environment* **2012**, *424*, 1–10, DOI 10.1016/j.scitotenv.2012.02.023.
25. J. Ugelstad, T. Ellingsen, A. Berge, O. Helgee, Magnetic polymer particles and process for the preparation thereof, US Patent no. 4,654,267, **1987**.
26. R. S. Molday, D. Mackenzie, 'Immunospecific ferromagnetic iron-dextran reagents for the labeling and magnetic separation of cells', *Journal of Immunological Methods* **1982**, *52*, 353–367, DOI 10.1016/0022-1759(82)90007-2.
27. S. Miltenyi, W. Müller, W. Weichel, A. Radbruch, 'High gradient magnetic cell separation with MACS', *Cytometry* **1990**, *11*, 231–238, DOI 10.1002/cyto.990110203.
28. P. Darling, *SME Mining Engineering Handbook*, 3rd ed., Society for Mining, Metallurgy, and Exploration, Inc., **2011**.

29. W. D. Robinson, *The Solid Waste Handbook: A Practical Guide*, John Wiley & Sons, Inc., **1986**.
30. J. A. Oberteuffer, 'Magnetic separation: A review of principles, devices, and applications', *IEEE Transactions on Magnetics* **1974**, *10*, 223–238, DOI 10.1109/TMAG.1974.1058315.
31. K. Mandel, F. Hutter, 'The magnetic nanoparticle separation problem', *Nano Today* **2012**, *7*, 485–487, DOI 10.1016/j.nantod.2012.05.001.
32. G. D. Moeser, K. A. Roach, W. H. Green, T. A. Hatton, P. E. Laibinis, 'High-gradient magnetic separation of coated magnetic nanoparticles', *AIChE Journal* **2004**, *50*, 2835–2848, DOI 10.1002/aic.10270.
33. C. T. Yavuz, J. T. Mayo, W. Y. William, A. Prakash, J. C. Falkner, S. Yean, L. Cong, H. J. Shipley, A. Kan, M. Tomson, D. Natelson, V. L. Colvin, 'Low-field Magnetic Separation of Monodisperse Fe_3O_4 Nanocrystals', *Science* **2006**, *314*, 964–967, DOI 10.1126/science.1131475.
34. J. S. Beveridge, J. R. Stephens, A. H. Latham, M. E. Williams, 'Differential Magnetic Catch and Release: Analysis and Separation of Magnetic Nanoparticles', *Analytical Chemistry* **2009**, *81*, 9618–9624, DOI 10.1021/ac9016456.
35. T. Aste, D. Weaire, *The Pursuit of Perfect Packing*, 2nd ed., CRC Press/Taylor & Francis Group, **2008**, p. 216.
36. D. Bideau, A. Hansen, 'Disorder and Granular Media' in *Random Materials and Processes*, Elsevier, Amsterdam, **1993**.
37. J. Kepler, *Strena seu de Nive Sexangula*, **1611**, English translation: C. Hardie, *The six-cornered snowflake*, Clarendon Press, Oxford, UK, **1966**.
38. T. C. Hales, 'A proof of the Kepler conjecture', *Annals of Mathematics* **2005**, 1065–1185, DOI 10.4007/annals.2005.162.1065.
39. T. Hales, M. Adams, G. Bauer, D. T. Dang, J. Harrison, T. L. Hoang, C. Kaliszyk, V. Magron, S. McLaughlin, T. T. Nguyen, T. Q. Nguyen, T. Nipkow, S. Obua, J. Pleso, J. Rute, A. Solovyev, A. H. T. Ta, T. N. Tran, D. T. Trieu, J. Urban, K. K. Vu, R. Zumkeller, 'A formal proof of the Kepler conjecture', *arXiv preprint arXiv:1501.02155* **2015**.
40. A. Donev, F. H. Stillinger, P. M. Chaikin, S. Torquato, 'Unusually Dense Crystal Packings of Ellipsoids', *Physical Review Letters* **2004**, *92*, 255506, DOI 10.1103/PhysRevLett.92.255506.
41. W. Man, A. Donev, F. H. Stillinger, M. T. Sullivan, W. B. Russel, D. Heeger, S. Inati, S. Torquato, P. M. Chaikin, 'Experiments on Random Packings of Ellipsoids', *Physical Review Letters* **2005**, *94*, 198001, DOI 10.1103/PhysRevLett.94.198001.
42. J. H. Conway, S. Torquato, 'Packing, tiling, and covering with tetrahedra', *Proceedings of the National Academy of Sciences* **2006**, *103*, 10612–10617, DOI 10.1073/pnas.0601389103.
43. S. Torquato, Y. Jiao, 'Dense packings of the Platonic and Archimedean solids', *Nature* **2009**, *460*, 876–879, DOI 10.1038/nature08239, (erratum) **2009**, *461*, 828 (corrigendum), **2010**, *463*, 1106.
44. A. Haji-Akbari, M. Engel, A. S. Keys, X. Zheng, R. G. Petschek, P. Palffy-Muhoray, S. C. Glotzer, 'Disordered, quasicrystalline and crystalline phases of densely packed tetrahedra', *Nature* **2009**, *462*, 773–777, DOI 10.1038/nature08641.
45. P. F. Damasceno, M. Engel, S. C. Glotzer, 'Predictive Self-Assembly of Polyhedra into Complex Structures', *Science* **2012**, *337*, 453–457, DOI 10.1126/science.1220869.
46. Y. Jiao, F. H. Stillinger, S. Torquato, 'Optimal packings of superballs', *Physical Review E* **2009**, *79*, 041309, DOI 10.1103/PhysRevE.79.041309, (erratum) **2011**, *84*, 069902.
47. R. Ni, A. P. Gantapara, J. de Graaf, R. van Roij, M. Dijkstra, 'Phase diagram of colloidal hard superballs: from cubes *via* spheres to octahedra', *Soft Matter* **2012**, *8*, 8826–8834, DOI 0.1039/C2SM25813G.
48. A. Bezdek, W. Kuperberg, 'Dense Packing of Space with Various Convex Solids', *arXiv preprint arXiv:1008.2398* **2010**.
49. J. de Graaf, R. van Roij, M. Dijkstra, 'Dense Regular Packings of Irregular Nonconvex Particles', *Physical Review Letters* **2011**, *107*, 155501, DOI 10.1103/PhysRevLett.107.155501.
50. S. Torquato, Y. Jiao, 'Organizing principles for dense packings of nonspherical hard particles: Not all shapes are created equal', *Physical Review E* **2012**, *86*, 011102, DOI 10.1103/PhysRevE.86.011102.
51. P. N. Pusey, W. van Megen, P. Bartlett, B. J. Ackerson, J. G. Rarity, S. M. Underwood, 'Structure of crystals of hard colloidal spheres', *Physical Review Letters* **1989**, *63*, 2753.
52. C. B. Murray, C. R. Kagan, M. G. Bawendi, 'Self-Organization of CdSe Nanocrystallites into Three-Dimensional Quantum Dot Superlattices', *Science* **1995**, *270*, 1335–1338, DOI 10.1126/science.270.5240.1335.

53. Y. A. Vlasov, X.-Z. Bo, J. C. Sturm, D. J. Norris, 'On-chip natural assembly of silicon photonic bandgap crystals', *Nature* **2001**, *414*, 289–293, DOI 10.1038/35104529.
54. S. Yang, L. Gao, 'Controlled synthesis and self-assembly of CeO_2 nanocubes', *Journal of the American Chemical Society* **2006**, *128*, 9330–9331, DOI 10.1021/ja063359h.
55. T. Ding, K. Song, K. Clays, C.-H. Tung, 'Fabrication of 3D Photonic Crystals of Ellipsoids: Convective Self-Assembly in Magnetic Field', *Advanced Materials* **2009**, *21*, 1936–1940, DOI 10.1002/adma.200803564.
56. J.-M. Meijer, F. Hagemans, L. Rossi, D. V. Byelov, S. I. R. Castillo, A. Snigirev, I. Snigireva, A. P. Philipse, A. V. Petukhov, 'Self-Assembly of Colloidal Cubes via Vertical Deposition', *Langmuir* **2012**, *28*, 7631–7638, DOI 10.1021/la3007052.
57. W. van der Stam, A. P. Gantapara, Q. A. Akkerman, G. Soligno, J. D. Meeldijk, R. van Roij, M. Dijkstra, C. de Mello Donega, 'Self-assembly of colloidal hexagonal bipyramid-and bifrustum-shaped ZnS nanocrystals into two-dimensional superstructures', *Nano Letters* **2014**, *14*, 1032–1037, DOI 10.1021/nl4046069.
58. L. Rossi, V. Soni, D. J. Ashton, D. J. Pine, A. P. Philipse, P. M. Chaikin, M. Dijkstra, S. Sacanna, W. T. M. Irvine, 'Shape-sensitive crystallization in colloidal superball fluids', *Proceedings of the National Academy of Sciences* **2015**, *112*, 5286–5290, DOI 10.1073/pnas.1415467112.
59. J. D. Bernal, J. Mason, 'Packing of Spheres: Coordination of Randomly Packed Spheres', *Nature* **1960**, *188*, 910–911, DOI 10.1038/188910a0.
60. G. D. Scott, D. M. Kilgour, 'The density of random close packing of spheres', *Journal of Physics D: Applied Physics* **1969**, *2*, 863, DOI 10.1088/0022-3727/2/6/311.
61. A. P. Philipse, C. Pathmamanoharan, 'Liquid permeation (and sedimentation) of dense colloidal hard-sphere packings', *Journal of Colloid and Interface Science* **1993**, *159*, 96–107, DOI 10.1006/jcis.1993.1301.
62. E. R. Nowak, J. B. Knight, E. Ben-Naim, H. M. Jaeger, S. R. Nagel, 'Density fluctuations in vibrated granular materials', *Physical Review E* **1998**, *57*, 1971, DOI 10.1103/PhysRevE.57.1971.
63. S. Torquato, T. M. Truskett, P. G. Debenedetti, 'Is Random Close Packing of Spheres Well Defined?', *Physical Review Letters* **2000**, *84*, 2064, DOI 10.1103/PhysRevLett.84.2064.
64. R. D. Kamien, A. J. Liu, 'Why is Random Close Packing Reproducible?', *Physical Review Letters* **2007**, *99*, 155501, DOI 10.1103/PhysRevLett.99.155501.
65. A. Donev, I. Cisse, D. Sachs, E. A. Variano, F. H. Stillinger, R. Connelly, S. Torquato, P. M. Chaikin, 'Improving the Density of Jammed Disordered Packings Using Ellipsoids', *Science* **2004**, *303*, 990–993, DOI 10.1126/science.1093010.
66. A. R. Kansal, S. Torquato, F. H. Stillinger, 'Diversity of order and densities in jammed hard-particle packings', *Physical Review E* **2002**, *66*, 041109, DOI 10.1103/PhysRevE.66.041109.
67. C. S. O'Hern, L. E. Silbert, A. J. Liu, S. R. Nagel, 'Jamming at zero temperature and zero applied stress: The epitome of disorder', *Physical Review E* **2003**, *68*, 011306, DOI 10.1103/PhysRevE.68.011306.
68. T. S. Majmudar, M. Sperl, S. Luding, R. P. Behringer, 'Jamming Transition in Granular Systems', *Physical Review Letters* **2007**, *98*, 058001, DOI 10.1103/PhysRevLett.98.058001.
69. C. Song, P. Wang, H. A. Makse, 'A phase diagram for jammed matter', *Nature* **2008**, *453*, 629–632, DOI 10.1038/nature06981.
70. G. Parisi, F. Zamponi, 'Mean-field theory of hard sphere glasses and jamming', *Reviews of Modern Physics* **2010**, *82*, 789, DOI 10.1103/RevModPhys.82.789.
71. S. Torquato, F. H. Stillinger, 'Jammed hard-particle packings: From Kepler to Bernal and beyond', *Reviews of Modern Physics* **2010**, *82*, 2633, DOI 10.1103/RevModPhys.82.2633.
72. A. Baule, R. Mari, L. Bo, L. Portal, H. A. Makse, 'Mean-field theory of random close packings of axisymmetric particles', *Nature Communications* **2013**, *4*, 2194, DOI 10.1038/ncomms3194.
73. A. P. Philipse, 'The Random Contact Equation and Its Implications for (Colloidal) Rods in Packings, Suspensions, and Anisotropic Powders', *Langmuir* **1996**, *12*, 1127–1133, DOI 10.1021/la950671o, (correction) **1996**, *12*, 5971–5971.
74. J. V. Milewski, 'The Combined Packing of Rods and Spheres in Reinforcing Plastics', *Industrial & Engineering Chemistry Product Research and Development* **1978**, *17*, 363–366, DOI 10.1021/i360068a016.
75. M. Nardin, E. Papirer, J. Schultz, 'Contribution à l'Etude des Empilements au Hasard de Fibres et/ou de Particules Sphériques', *Powder Technology* **1985**, *44*, 131–140, DOI 10.1016/0032-5910(85)87019-4.

76. K. E. Evans, A. G. Gibson, 'Prediction of the maximum packing fraction achievable in randomly oriented short-fibre composites', *Composites Science and Technology* **1986**, *25*, 149–162, DOI 10.1016/0266-3538(86)90040-0.
77. J. Blouwolff, S. Fraden, 'The coordination number of granular cylinders', *EPL (Europhysics Letters)* **2006**, *76*, 1095, DOI 10.1209/epl/i2006-10376-1.
78. K. Desmond, S. V. Franklin, 'Jamming of three-dimensional prolate granular materials', *Physical Review E* **2006**, *73*, 031306, DOI 10.1103/PhysRevE.73.031306.
79. G. Lumay, N. Vandewalle, 'Experimental study of the compaction dynamics for two-dimensional anisotropic granular materials', *Physical Review E* **2006**, *74*, 021301, DOI 10.1103/PhysRevE.74.021301.
80. S. R. Williams, A. P. Philipse, 'Random packings of spheres and spherocylinders simulated by mechanical contraction', *Physical Review E* **2003**, *67*, 051301, DOI 10.1103/PhysRevE.67.051301.
81. M. Bargieł, 'Geometrical Properties of Simulated Packings of Spherocylinders' in *Computational Science–ICCS 2008*, (Eds.: M. Bubak, G. D. van Albada, J. Dongarra, P. M. A. Sloot), Springer-Verlag Berlin Heidelberg, **2008**, pp. 126–135.
82. J. Zhao, S. Li, R. Zou, A. Yu, 'Dense random packings of spherocylinders', *Soft Matter* **2012**, *8*, 1003–1009, DOI 10.1039/C1SM06487H.
83. D. M. Mueth, G. F. Debregeas, G. S. Karczmar, P. J. Eng, S. R. Nagel, H. M. Jaeger, 'Signatures of granular microstructure in dense shear flows', *Nature* **2000**, *406*, 385–389, DOI 10.1038/35019032.
84. L. B. Wang, J. D. Frost, J. S. Lai, 'Three-Dimensional Digital Representation of Granular Material Microstructure from X-Ray Tomography Imaging', *Journal of Computing in Civil Engineering* **2004**, *18*, 28–35, DOI 10.1061/(ASCE)0887-3801(2004)18:1(28).
85. E. L. Hinrichsen, J. Feder, T. Jøssang, 'Geometry of random sequential adsorption', *Journal of Statistical Physics* **1986**, *44*, 793–827, DOI 10.1007/BF01011908.
86. J. Talbot, P. Schaaf, G. Tarjus, 'Random sequential addition of hard spheres', *Molecular Physics* **1991**, *72*, 1397–1406, DOI 10.1080/00268979100100981.
87. J. D. Sherwood, 'Packing of spheroids in three-dimensional space by random sequential addition', *Journal of Physics A: Mathematical and General* **1997**, *30*, L839, DOI 10.1088/0305-4470/30/24/004.
88. B. J. Buchalter, R. M. Bradley, 'Orientational order in random packings of ellipses', *Physical Review A* **1992**, *46*, 3046, DOI 10.1103/PhysRevA.46.3046.
89. D. He, N. N. Ekere, L. Cai, 'Computer simulation of random packing of unequal particles', *Physical Review E* **1999**, *60*, 7098, DOI 10.1103/PhysRevE.60.7098.
90. B. D. Lubachevsky, F. H. Stillinger, 'Geometric Properties of Random Disk Packings', *Journal of Statistical Physics* **1990**, *60*, 561–583, DOI 10.1007/BF01025983.
91. M. D. Rintoul, S. Torquato, 'Computer simulations of dense hard-sphere systems', *The Journal of Chemical Physics* **1996**, *105*, 9258–9265, DOI 10.1063/1.473004.
92. A. Donev, S. Torquato, F. H. Stillinger, 'Neighbor list collision-driven molecular dynamics simulation for nonspherical hard particles. I. Algorithmic details', *Journal of Computational Physics* **2005**, *202*, 737–764, DOI 10.1016/j.jcp.2004.08.014.
93. P. A. Cundall, O. D. L. Strack, 'A discrete numerical model for granular assemblies', *Géotechnique* **1979**, *29*, 47–65, DOI 10.1680/geot.1979.29.1.47.
94. X. Jia, R. A. Williams, 'A packing algorithm for particles of arbitrary shapes', *Powder Technology* **2001**, *120*, 175–186, DOI 10.1016/S0032-5910(01)00268-6.
95. F. Radjaï, F. Dubois, *Discrete-element modeling of granular materials*, Wiley-ISTE, **2011**.
96. S. Torquato, Y. Jiao, 'Robust algorithm to generate a diverse class of dense disordered and ordered sphere packings via linear programming', *Physical Review E* **2010**, *82*, 061302, DOI 10.1103/PhysRevE.82.061302.
97. A. Wouterse, PhD thesis, Universiteit Utrecht, The Netherlands, **2007**, Chapter 2.
98. J. L. Finney, 'Fine structure in randomly packed, dense clusters of hard spheres', *Materials Science and Engineering* **1976**, *23*, 199–205, DOI 10.1016/0025-5416(76)90194-4.
99. W. S. Jodrey, E. M. Tory, 'Computer simulation of isotropic, homogeneous, dense random packing of equal spheres', *Powder Technology* **1981**, *30*, 111–118, DOI 10.1016/0032-5910(81)80003-4.
100. A. S. Clarke, J. D. Wiley, 'Numerical simulation of the dense random packing of a binary mixture of hard spheres: Amorphous metals', *Physical Review B* **1987**, *35*, 7350, DOI 10.1103/PhysRevB.35.7350.

101. G. T. Nolan, P. E. Kavanagh, 'Computer simulation of random packing of hard spheres', *Powder Technology* **1992**, *72*, 149–155, DOI 10.1016/0032-5910(92)88021-9.
102. G. T. Nolan, P. E. Kavanagh, 'Random packing of nonspherical particles', *Powder Technology* **1995**, *84*, 199–205, DOI 10.1016/0032-5910(95)98237-S.

Part I

Particle packing

2

Spherocylinders in confinement

Abstract

The influence of a confining boundary on the random dense packing structure of spherocylinders is investigated and compared with results for periodic systems. A virtual particle method is used to emulate bounding surfaces, and a hard cylindrical and wedge-shaped boundary are investigated. Simulations of (random) dense packings are performed with the mechanical contraction method. A strong increase in particle alignment in a cylinder is found only when the cylinder diameter is of similar size as the particle length. The packing fraction and mean contact numbers follow very similar trends, nearly independent of the particle aspect ratio. A similar aspect ratio independent behaviour is found for the bounding wedge, but particle alignment with the wedge walls is found in all cases. Already a small distance away from the boundary ordering is virtually absent. Various ordered structures are found depending on the specific particle and boundary geometry, requiring further investigation.

2.1 Introduction

The optimal packing of particles has been studied extensively, as early as the days of Kepler [1] who investigated how spheres could be packed together as efficiently as possible. Ever since, scientists from different backgrounds have been involved in the search for optimal packing structures for many differently shaped particles [2].

In contrast with ordered packings are the disordered or *random* packings. In such systems, long-range positional and orientational order is absent, and local ordering is minimal. The investigation of this class of packings was initiated by Bernal's experiments with spheres [3], for which he found a reproducible 'random close packing' (RCP) density of $\phi \approx 0.64$. A theoretical definition of the RCP packing remains elusive however (see e.g. [4–6]), but much effort is still being put into developing suitable theories [7–10].

Simulations of random particle packings are usually performed using periodic boundary conditions. However, hard boundaries present are always in experiments. While their influence may be negligible when considering a large number of particles, in general some (local) boundary-induced ordering of particles will occur. Sometimes confinement of particles is even used explicitly to induce order, as can be seen for example in colloidal deposition techniques [11], patterned growth [12] and self-assembly in confinement [13]. Our interest in confined packings comes from the design of a magnetic separation filter consisting of many randomly packed fibres in a cylinder, as further discussed in Chapter 6 and Chapter 7.

In this chapter we aim to investigate the influence of particle ordering and alignment due to a hard boundary, on the random dense packing properties of spherocylinders. To this end, we perform simulations using the mechanical contraction method (MCM), originally developed for periodic spherocylinder systems by Williams and Philipse [14]. Besides the investigation of spherocylinder packings [15], the MCM has also been applied successfully to packings of bidisperse spheres [16], ellipsoids and cut-spheres [17, 18] and rod-sphere mixtures [19–22]. Recently the method was revisited by Ferreiro-Córdova and Van Duijneveldt [23], who simulated spherocylinder packings and simplified the equations for overlap removal in order to obtain reproducible results more easily. Their final results are similar to those we present in this chapter.

We expand the applicability of the MCM by developing a simple method to deal with hard boundaries, using virtual particles. Specifically, a bounding cylinder and a bounding wedge are discussed. Since any form of boundary in a packing of finite size is likely to induce order in the system, the results can no longer be considered as *random* dense packings. Our aim is to quantify the extent of the influence of the boundary. Additionally, by extrapolating to infinitely large boundaries, bulk properties can be deduced.

In this chapter, first, the mechanical contraction method for spherocylinders is explained and discussed. Second, the virtual particle method for hard boundaries is introduced for a cylinder and wedge shape. Some simulation details are given next, followed by obtained results for periodic and confined systems. The results are discussed in light of the order induced by the boundaries.

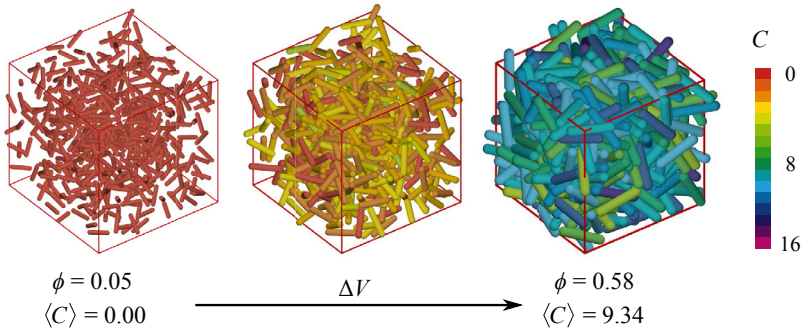

Figure 2.1. Three snapshots of a typical MCM simulation of spherocylinders with an aspect ratio of $\Lambda = 5.00$. From left to right, the packing fraction ϕ and the mean contact number $\langle C \rangle$ increase until further compression is no longer possible. The particles are coloured based on their number of contacting neighours.

2.2 Method

In this section the principle of the mechanical contraction method is restated based on previous work in [14] and [17], and some clarifying comments are added. The method is then expanded by introducing the ability to impose a hard cylindrical or wedge-shaped boundary on the packings. While we will only consider packings of monodisperse particles, it is worth to note that the presented method can also be applied directly to bidisperse and polydisperse particles.

2.2.1 Mechanical Contraction Method

The MCM is a simulation technique to generate random dense packings of particles, and can be summarized as follows. A dilute (non-overlapping) starting configuration of randomly positioned and oriented particles in a periodic cubic simulation box is compressed in steps of ΔV. The particle coordinates are scaled at every step, which may cause particles to overlap. An iterative procedure tries to remove overlaps by translating and rotating the affected particles (including any new overlaps due to these operations). If all overlaps are removed within a reasonable amount of computational effort, the simulation proceeds with the next compression step. If some overlaps cannot be removed, the simulation reverts to the last non-overlapping configuration and the run ends. See Figure 2.1 for a graphical representation of a typical MCM run.

From a physical perspective, the MCM can be envisioned as operating in the theoretical limit of infinite pressure, and in complete absence of thermal motion. Particles are only repositioned and reoriented based on geometrical considerations.

2.2.2 Spherocylinder

A spherocylinder is defined as a cylinder of length L and radius R, capped with two hemispheres of radius R (see Figure 2.2). Equivalently, a spherocylinder is the surface at

a constant distance R from a line segment. We define the aspect ratio of a spherocylinder, Λ, as the ratio between the total particle length and its diameter, $D = 2R$,

$$\Lambda = \frac{L + D}{D} = \frac{L}{D} + 1 \tag{2.1}$$

The particle volume is given by,

$$V = \pi R^2 \left(\frac{4}{3} R + L \right) \tag{2.2}$$

where for $L = 0$ a sphere is obtained. Because a spherocylinder is axisymmetric, its orientation can be represented by a single unit vector $\hat{\mathbf{e}}_z$ defining the direction of its long axis. Two additional, mutually perpendicular axes can be chosen arbitrarily to form an orthogonal local coordinate system. The corresponding rotation matrix $\mathbf{R} = (\hat{\mathbf{e}}_x, \hat{\mathbf{e}}_y, \hat{\mathbf{e}}_z)$ can be used to rotate vectors between the global and the local frame of reference. For a spherocylinder with its centre of mass located at $\mathbf{x}$, its end points are given by $\mathbf{p}^{\pm} = \mathbf{x} + \frac{1}{2} L \hat{\mathbf{e}}_z$ (Figure 2.2). The principle moments of inertia for a z-aligned spherocylinder, about its axes can be written as [24],

$$\begin{aligned} I_x = I_y &= m \frac{1}{20} \left(5L^3 + 20L^2 R + 45LR^2 + 32R^3 \right) / (3L + 4R) \\ I_z &= m \frac{1}{10} \left(15LR^2 + 16R^3 \right) / (3L + 4R) \end{aligned} \tag{2.3}$$

where m is the mass of the particle.

2.2.3 Overlap removal

The central part of the MCM is the overlap removal procedure, consisting of two parts. First, overlapping pairs of particles have to be found, and second, overlapping particles have to be translated and rotated such that the overlap is reduced and eventually removed.

The minimal distance between two spherocylinders can be determined exactly from the minimal distance between two line-segments. The algorithm by Vega and Lago [25], later improved by Abreu *et al.* [26], provides an efficient routine to calculate the minimal connecting vector $\mathbf{k}_{ij}$ between two spherocylinders i and j (see Figure 2.2). The amount of overlap is given by the overlap distance $\delta_{ij} = \|\mathbf{k}_{ij}\| - R_i - R_j$. Positive values indicate particle overlap, while negative values indicate that particles are separated. During the overlap removal procedure, only particles within a certain cut-off distance from a central particle are tested for overlap to speed up calculations. A modified Verlet list [27] is maintained containing a list of neighbouring particles. The list is updated whenever the end points of a particle have moved a predefined distance. Suitable values for this distance and the cut-off distance are determined empirically.

To remove overlap, the concerning particles are translated and rotated with a constant linear and angular velocity. There are five degrees of freedom concerned with this movement: three components along the Cartesian axes, $n = 1, 2, 3$, determining the

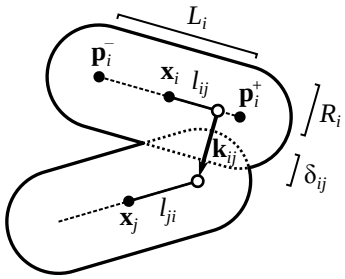

Figure 2.2. A two dimensional representation of two overlapping spherocylinders i and j located at $\mathbf{x}_i$ and $\mathbf{x}_j$. For spherocylinder i the radius R and length L are marked, as well as the endpoints $\mathbf{p}^{\pm}$. The vector $\mathbf{k}_{ij}$ connects the two points on the spherocylinder's axes (marked with open circles) that are closest to each other. The distances along the axes of the spherocylinders from their respective centres of mass to these points are l_{ij} and l_{ji}. The overlap distance is given by δ_{ij}.

linear velocity, and two components along two axes perpendicular to the long axis of the particle, $n = 4, 5$, determining the angular velocity. We can now quantify the rate of change of the overlap between particles i and j due to this movement as,

$$\frac{\partial \delta_{ij}}{\partial t} = k_{ij}^{(1)} a_1 + k_{ij}^{(2)} a_2 + k_{ij}^{(3)} a_3 + l_{ij} k_{ij}^{(4)} a_4 + l_{ij} k_{ij}^{(5)} a_5 \tag{2.4}$$

where a_n are the velocity components along the described axes, $k_{ij}^{(n)}$ are the scalar projections of $\mathbf{k}_{ij}$ on the different axes and $l_{ij} \in [-\frac{1}{2}L, \frac{1}{2}L]$ is the location of the endpoint of the contact vector along the axis of the particle (see Figure 2.2)[1]. A sixth velocity component a_6 is absent here, since it would result only in a rotation of the particle about its long axis, which does not contribute to overlap removal.

When multiple particles overlap with a central particle i, the total rate of change in overlap distance is given by a summation over all C contacts[2],

$$s_i = \sum_{j=1}^{C} \delta_{ij} \frac{\partial \delta_{ij}}{\partial t} \tag{2.5}$$

The factor δ_{ij} is added here as a bias towards particle pairs with the largest overlap [14]. However, omission of this factor did not result in quantitative changes of the simulation results.

In order to find optimal values for the velocity components a_n, Equation 2.5 is maximized using the method of Lagrange multipliers. A kinetic energy-type constraint is introduced,

$$a_1^2 + a_2^2 + a_3^2 + \xi a_4^2 + \xi a_5^2 = 1 \tag{2.6}$$

[1]Note that the right-hand side of Equation 2.4 is a *scalar*. In the original work [14] it is defined incorrectly as the partial derivative of the *vector* $\mathbf{k}_{ij}$. Later work corrected this, cf. [17].

[2]The summation index should correctly start at $j = 1$ and not $j = 0$. This minor oversight was also corrected by others [17].

where ξ is a parameter related to the particle's moment of inertia [14]. The importance of this factor will be investigated in Section 2.3. The results from the Lagrange treatment as given in [14] are,

$$a_n = \begin{cases} \sum_{j=1}^{C} \delta_{ij} k_{ij}^{(n)} & \text{if} n = 1, 2, 3 \\ \frac{1}{\xi} \sum_{j=1}^{C} \delta_{ij} l_{ij} k_{ij}^{(n)} & \text{if} n = 4, 5 \end{cases} \tag{2.7}$$

At this point it has to be remarked, that strictly following the Lagrange optimization using Equation 2.5 with the constraint of Equation 2.6, will not lead exactly to Equation 2.7. The strict derivation is presented in Section 2.A, and is the basis for further discussion in Chapter 3. Here we continue using Equation 2.7 to be able to compare with the results of previous simulations in a more straightforward way.

According to Williams [14], the direction in which each particle will move is determined by the calculated values of a_n and "each particle should move a small distance, further than half the distance necessary to break the first contact". The implementation of these instructions is not mentioned. Analysis of the available computer code shows that the following procedure is used, which we use as well in the context of this chapter.

Consider linear and angular velocity vectors $\mathbf{v} = (a_1, a_2, a_3)$ and $\boldsymbol{\omega} = \mathbf{R}_i \cdot (a_4, a_5, 0)$, respectively, with the angular velocity expressed in the local coordinate system. It is straightforward to consider the following manner of updating a particle's position and orientation,

$$\mathbf{x}_i^{n+1} = \mathbf{x}_i^n + \Delta t_i \mathbf{v}_i \tag{2.8}$$

$$\hat{\mathbf{e}}_{z,i}^{n+1} = \hat{\mathbf{e}}_{z,i}^n + \Delta t_i \boldsymbol{\omega}_i \tag{2.9}$$

where $\hat{\mathbf{e}}_z$ is normalized afterwards[3], and periodic boundary conditions are checked. Note that $\mathbf{v}$ and $\boldsymbol{\omega}$ are not normalized, and therefore not only determine the *direction* of movement (as may be inferred from [14] as their intended use), but to some extent also the *magnitude* of movement. The time step Δt is determined by calculating,

$$\Delta t_i = \beta \min_{1 \le j \le C} \left[\frac{\delta_{ij}}{\left(\mathbf{v}_i + l_{ij}\boldsymbol{\omega}_i\right) \cdot \hat{\mathbf{k}}_{ij}} \right] \quad \text{where} \quad \left(\mathbf{v}_i + l_{ij}\boldsymbol{\omega}_i\right) \cdot \hat{\mathbf{k}}_{ij} > 0 \tag{2.10}$$

where β is an arbitrary parameter, typically close to 0.5, to alleviate numerical problems and ensure optimal densification of the packing. Note that the overlap distance in the numerator has the unit of length, and the expression in the denominator has the unit of speed, so that Δt correctly represents a time-step. The expression in the denominator

[3] Updating the particle's orientation in this manner requires re-orthogonalizing the entire rotation matrix $\mathbf{R}$, which is relatively costly. A better approach is to use Rodrigues' rotation formula [28], which is explained in more detail in Chapter 3.

resembles the overlap removal rate in Equation 2.4 and is required to be positive to ensure overlap removal instead of formation. By minimizing the inverse of the overlap removal rate, multiplied by the overlap distance, preference is given to the particle pair with the largest overlap removal rate and smallest overlap distance. The latter is in slight contrast to Equation 2.5 where δ_{ij} was included to bias movement towards larger overlap distances.

From Equation 2.10 it is unclear how a situation where each particle is moved such that at least one contact is broken, is accomplished. Even if only a single pair of overlapping particles is considered, this criterion is not easily satisfied by Equation 2.10. In Chapter 3 we revise the way how particles are translated and rotated based on the outcome of the Lagrange multipliers method, to circumvent this issue. There we simultaneously address other minor issues that have been mentioned in this section. Notwithstanding these issues, the present implementation of the MCM has generated reproducible results, that are comparable to other simulations and experimental evidence. This suggests that the incomplete treatment of the Lagrange method (Equation 2.7) and the method of calculating Δt (Equation 2.10) have a relatively minor influence on the overall behaviour of the MCM.

Finally, as mentioned before, the overlap removal procedure described in this section is repeated until all particle overlaps have been removed, or until they can no longer be removed within reasonable computational effort, i.e. a maximum number of tries.

2.2.4 Hard boundaries

The presence of a hard boundary will prohibit particles from entering a certain region of the simulation space. If the initial configuration is generated such that particles are always within the defined boundary, then the only way for a particle to cross the boundary is during its displacement while removing overlaps. Different methods to deal with such particle-boundary overlaps can be envisaged.

A simple approach is to push back protruding particles in the opposite direction of the boundary surface normal to the protrusion point. This is not a physically intuitive approach, and it will likely induce a lot of particle-particle overlaps that have to be removed subsequently.

A more elegant method is by using *virtual particles* that are placed temporarily at the outside of the boundary at the protrusion point. These particles effectively act as an *ad hoc* explicit boundary. The overlap of the protruding particle with the boundary can now be removed in the same way as any other particle-particle overlap: the summation of the velocity components in Equation 2.7 is simply extended by the additional, virtual particle. The following paragraphs will illustrate the use of virtual particles for a cylindrical and wedge-shaped boundary.

Cylinder A cylindrical boundary of diameter D_{cyl} and length L_{cyl} is centred at the origin (Figure 2.3, left). The outer ends are periodic so that only the influence of the lateral surface of the cylinder is investigated. The starting configuration is generated uniformly in the volume of the cylinder, where care is taken that particles do not

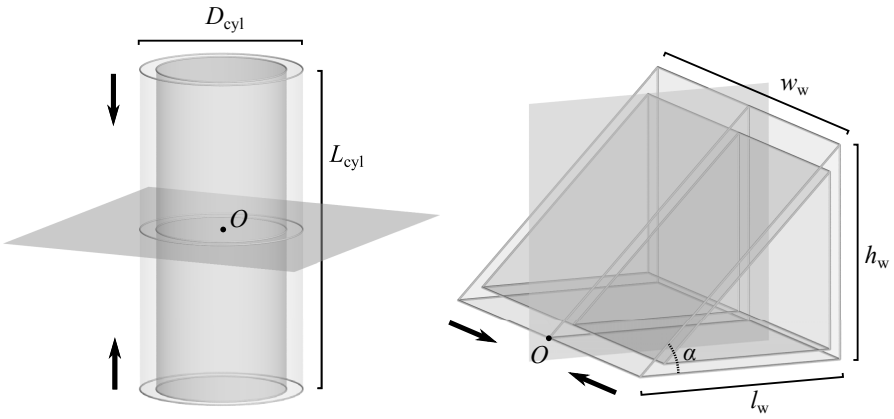

Figure 2.3. Confining geometries of a cylinder (*left*) en wedge (*right*). The relevant dimensions are indicated. The lighter shaded volume indicates the region in which the particles' centre of mass cannot enter. The cylinder is periodic along its long axes and is compressed while keeping D_{cyl} constant. The wedge is periodic in the direction of w_{w} and is compressed while keeping l_{w} and h_{w} constant.

penetrate the boundary. During the compression of the simulation box, D_{cyl} is kept constant and only L_{cyl} is adjusted. The movement of a particle during the overlap removal procedure may cause one of the particle's end points $\mathbf{p}^{\pm}$ to penetrate the boundary. This is the case whenever $p_x^2 + p_y^2 > (R_{\text{cyl}} - R)^2$, for either of the end points. The penetration check is performed for all particles prior to the calculation of the velocity vectors a_n in Equation 2.7. If penetration is found, a temporary (virtual) particle identical to the penetrating particle is placed aligned with the boundary, according to a simple geometric construction (Figure 2.4). The contact detection between these two particles is carried out normally, and the resulting overlap vector contributes to the summation in Equation 2.7, just like any other particle-particle overlap does.

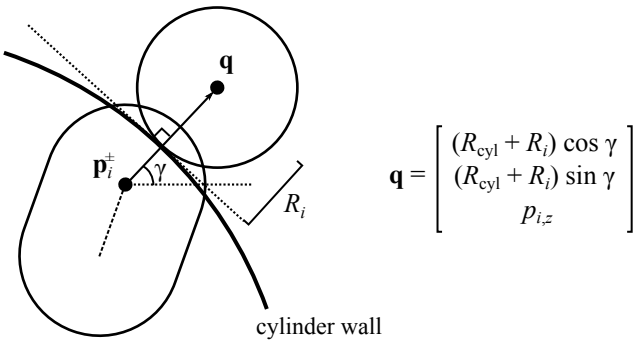

Figure 2.4. A top-down view of the placement of a virtual rod at the boundary of a cylinder. The virtual rod is aligned in the z-direction (here in-plane).

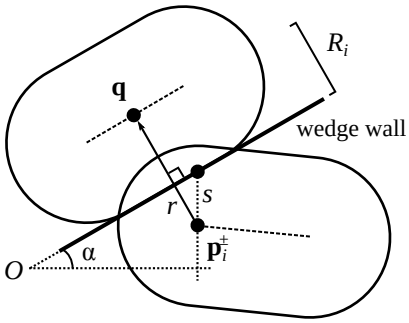

Where,

$$s = p_x \tan \alpha - p_y$$
$$r = s \cos \alpha$$

and,

$$\mathbf{q} = \begin{bmatrix} p_x - (R_i + r) \sin \alpha \\ p_y + (R_i + r) \cos \alpha \\ p_{i,z} \end{bmatrix}$$

Figure 2.5. A side-view representation of the placement of a virtual rod on the slope of the wedge, and the resulting movement of an overlapping particle.

Wedge A wedge boundary is defined by a right triangular prism of dimensions $(l_\mathrm{w}, h_\mathrm{w}, w_\mathrm{w})$ for the length, height and width, respectively (see Figure 2.3, where also the origin is marked). These dimensions correspond with the Cartesian x, y and z coordinates. The acuteness (angle) of the wedge α is given by $h_\mathrm{w}/l_\mathrm{w} = \tan \alpha$. The wedge is periodic in the direction of its width. Similar to the cylinder, the starting configuration is generated uniformly within the volume of the wedge such that particles do not penetrate the boundary. The dimensions l_w and h_w are kept constant during the compression. The boundary penetration detection and placement of the virtual particles is slightly more complicated than for the cylinder, as three different boundary planes have to be considered. For the 'back' plane, penetration is found if $p_x > l_\mathrm{w} - R$ for either end point. The virtual particle will be placed at $(l_\mathrm{w} + R, p_y, p_z)$, oriented along the y-axis. Penetration with the 'bottom' plane is found if $p_y < R$ and the virtual particle is placed at $(p_x, -R, p_z)$, aligned with the x-axis. The treatment of the 'slope' plane requires some basic trigonometry. The penetration criterion is given by $p_y > p_x \tan \alpha - R/\cos \alpha$, and the position of the virtual rod is described in Figure 2.5.

As before, after the placement of the virtual particle, the contact detection is performed and the velocity components are calculated.

2.2.5 Characterization

Packings are characterized by their packing fraction $\phi = V_\mathrm{particles}/V_\mathrm{system}$ and mean contact number $\langle C \rangle$ (the average number of contacting particles per particle). A simple way to obtain the value of $\langle C \rangle$ is by counting the number of particle pairs for which the inter-particle distance d is smaller than a certain cut-off δ, divided by the total number of particles. The parameter δ is chosen small with respect to the length scale of the particle. This approach does not always lead to an accurate estimation of $\langle C \rangle$, due to the influence of the finite numerical precision inherent to computer simulations on the MCM method. A more accurate estimation for the mean contact number can be found by evaluating $\langle C \rangle$ for a range of different δ (typically 10^{-8}–10^{-5}) and making a linear extrapolation of $\langle C \rangle$ towards $\delta = 0$, see also [17].

Preferential orientational ordering of particles can be quantified by the uniaxial

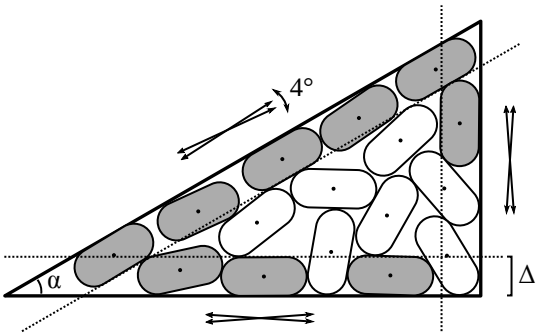

Figure 2.6. The fraction of aligned particles is calculated by counting the number of particles that have their centre of mass inside a volume close to the bounding walls, and are approximately oriented tangential to the wall (dark grey particles). A deviation of 4° in orientational angle is allowed for a particle to still be considered aligned. The distance Δ is chosen equal to the particle's diameter.

order parameter S [29, 30], also called nematic order parameter. First, a tensor $\mathbf{Q}$ is calculated as,

$$\mathbf{Q} = \frac{1}{N}\sum_{i}^{N}\left(\tfrac{3}{2}\hat{\mathbf{e}}_{z,ij}\otimes\hat{\mathbf{e}}_{z,ij} - \tfrac{1}{2}\mathbf{I}\right) \tag{2.11}$$

where N is the number of particles, $\mathbf{e}_{z,ij}$ is the orientation of the particle's long axis, $\otimes$ is the tensor product and $\mathbf{I}$ is the identity tensor. The order parameter is given by the largest positive eigenvalue of $\mathbf{Q}$, resulting in $S = 1$ for full nematic ordering and $S = 0$ for the absence of nematic ordering.

The uniaxial order parameter can not describe local orientational ordering or multiple ordered domains effectively. While multiple domains are not expected in the case of a periodic system or with a cylindrical boundary, particles may align with all three bounding faces of the wedge. Therefore, in order to quantify the amount of alignment in the wedge system, we construct two dimensional density histograms of the polar and azimuthal angles of the particle's orientations. Furthermore, the fraction of particles near the walls that show alignment with the wall is calculated, see Figure 2.6.

2.2.6 Simulation details

All simulations in this chapter consider $N = 500$ identical particles with $R = 1/2$ and varying Λ. The number of particles has been increased in some cases for the confined simulations, if the simulation would otherwise result in a final cylinder height or wedge width smaller than the particle length. For aspect ratios below $\Lambda = 50$, the initial configurations have a packing fraction of $\phi_0 = 0.05$. For higher aspect ratios $\phi_0 = 0.005$. The box volume is reduced in steps of $\Delta V = 0.1$ every iteration. This volume step is scaled down several times (typically 4 times) by a factor of 0.5 after a configuration is found where overlaps could no longer be removed. The iterative overlap removal attempts many times to remove any existing overlap, with a maximum number of tries

of typically 10^5. A larger number of tries usually leads to a slightly denser packing, at the cost of a much increased simulation duration. In the contact detection algorithm a small deviation in overlap distance is allowed to alleviate numerical rounding off errors. While in principle this value should be as small as possible, a value of 10^{-4} resulted in the fastest calculations, without significantly influencing the final results.

2.2.7 Implementation

The MCM algorithm with the extension for hard boundaries is implemented in C++ and analysis of particle packings is done using Wolfram Mathematica v10.2 [31]. Graphical renderings of packing structures are made by ray-tracing with POV-Ray v3.7 [32]. Codes are available from the author upon request.

2.3 Preliminary investigation

In Equation 2.6 the parameter ξ is introduced, claimed to be related to the moment of inertia [14]. In a modified version of the MCM, Wouterse *et al.* mention that modifying the value of the moment of inertia "often leads to slightly denser packings" [17]. However, in both cases the exact choice of ξ is not specified. Scrutiny of the simulation data from [15] shows that different values for ξ have been used for different aspect ratios, but no clear pattern or relation between ξ and Λ could be deduced. Our own simulations suggest that the value of ξ can actually have a significant influence on the packing density and contact numbers; an improper choice of ξ can lead to hardly any compaction of the initial configuration. In this section therefore, we aim to find the optimal value for ξ for each aspect ratio, which will then be used in all further simulations.

We hypothesize that the densest random packings are actually obtained when ξ equals the moment of inertia, $\xi \equiv I_{x,y}$, eliminating ξ as a free parameter in the MCM. This is plausible when considering the modified MCM for non-spherical particles [17], where the exact moment of inertia appears in place of ξ in the kinetic-energy type constraint. To investigate this hypothesis, simulations are performed in a periodic cubic simulation box for spheres ($\Lambda = 1.0$) and short spherocylinders ($\Lambda < 5.0$) and values of $\xi = 10^{-2}$–10^{2}. Identical starting configurations are used for the different values of ξ. The maximum number of overlap removal tries is set to 10^4 and ΔV is scaled down twice. The results plotted against $1/\xi$ are shown in Figure 2.7.

From Figure 2.7 it can be seen that, while the maximum packing fractions and contact numbers are found *close* to the point where $\xi = I_{x,y}$, the maxima are always found for higher values of $1/\xi$. The reason for this discrepancy is yet unclear and may simply be due to the nature of the overlap removal algorithm, or the choice of e.g. the maximum number of tries in the overlap removal step. However, the differences in obtained packing fractions and contact numbers are relatively small over a wide range of values for ξ. This is illustrated by the horizontal bars in Figure 2.7a and b, that indicate for the different aspect ratios the ranges in which the deviation from the maximum packing fraction or mean contact number is less than 2.5 % or 5 %, respectively. For most aspect ratios, the results fall within these margins for two full orders of magnitude

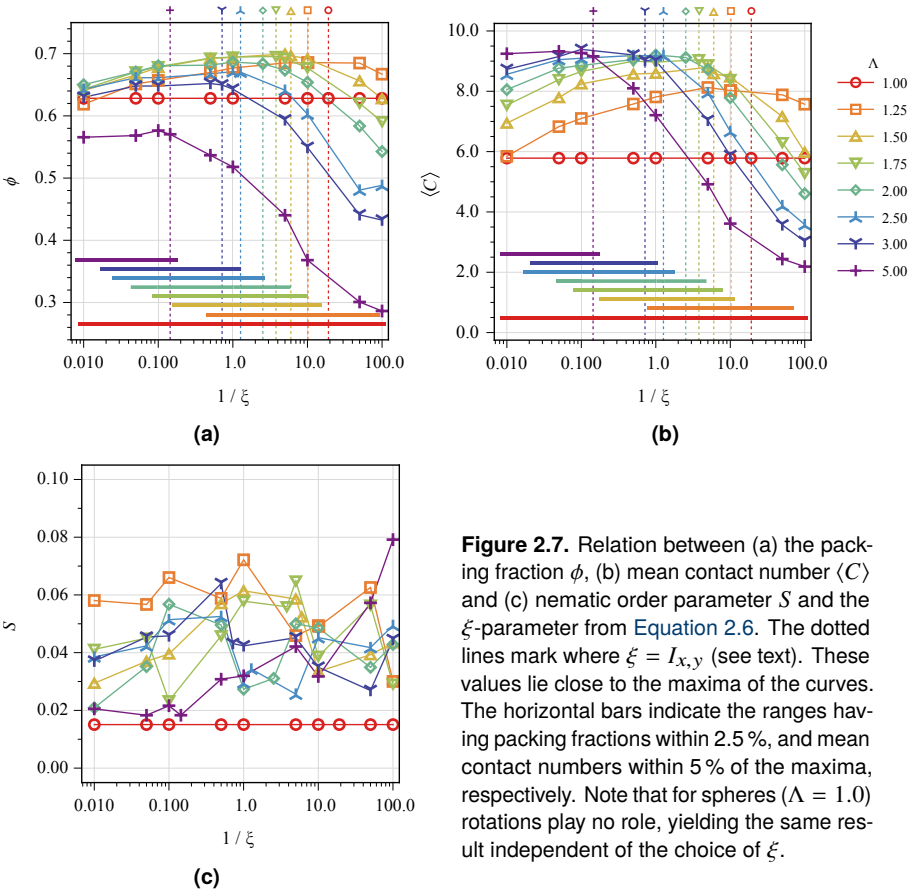

Figure 2.7. Relation between (a) the packing fraction ϕ, (b) mean contact number $\langle C \rangle$ and (c) nematic order parameter S and the ξ-parameter from Equation 2.6. The dotted lines mark where $\xi = I_{x,y}$ (see text). These values lie close to the maxima of the curves. The horizontal bars indicate the ranges having packing fractions within 2.5 %, and mean contact numbers within 5 % of the maxima, respectively. Note that for spheres ($\Lambda = 1.0$) rotations play no role, yielding the same result independent of the choice of ξ.

difference in ξ. The nematic order parameter never exceeds $S = 0.08$, indicating that no significant amount of orientational ordering is present.

This relative insensitivity to the choice of ξ explains why earlier simulations with *ad hoc* chosen values for ξ were successful in obtaining results close to those of others and comparable with experiments. The same insensitivity argument justifies our choice to adhere to the theoretical argument that ξ is given by the moment of inertia. Therefore, $\xi = I_{x,y}$ will be used in all further simulations.

To determine baseline values for the packing fractions and mean contact numbers for a fully periodic system, we repeat the simulations for the appropriate values of ξ three times, and for a wider range of aspect ratios. Average values and confidence intervals for the packing fraction and mean contact number are reported in Figure 2.8. The intervals are calculated assuming a Student's t-distribution ($\bar{x} \pm ts/\sqrt{n}$, with $\alpha = 0.95$ and $t_{\nu=2} = 4.303$). The nematic order parameter (not shown) never exceeded $S = 0.08$, as before. The dotted line in Figure 2.8a represents the theoretical limit for thin rods $\phi L/D = \langle C \rangle/2 = 5$ according to Philipse [33]. The limiting equation matches our simulation results perfectly from $\Lambda \approx 25.0$ onwards, as was also the case in the original

MCM [14]. Despite the agreement in packing fraction, the mean contact numbers are unrealistically low for high aspect ratio's. The exact cause of this decrease is difficult to assess, but may be inherent to the MCM algorithm and the overlap removal method. A possible explanation is that longer particles are displaced over relatively large distances in comparison with smaller particles during overlap removal. This causes gaps to appear between particles that cannot be removed by subsequent compression steps, and prevent these particles from being detected as in contact.

Previous simulations (cf. [14]) included Monte Carlo-like compression steps following the MCM, successfully increasing the packing fractions and mean contact numbers.

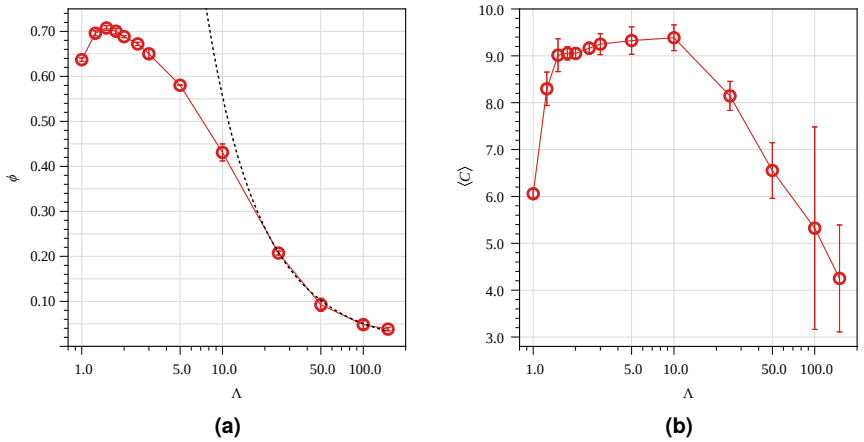

Figure 2.8. Relation between (a) the volume fraction ϕ and (b) mean contact number $\langle C \rangle$ of spherocylinders of different aspect ratios in a periodic simulation box, by setting the free parameter ξ equal to the particle's moment of inertia (see text). The dotted line in (a) represents the theoretical limit for thin rods $\phi L/D = \langle C \rangle/2 = 5$ [33].

2.4 Investigation of boundaries

To investigate the effect of the cylindrical boundary, we perform simulations where we vary the aspect ratio (Λ = 1.0–5.0) and generate configurations with increasing bounding cylinder diameters, starting from $D_{\text{cyl}} \approx D_{\text{particle}}$. In this lower limiting situation, it is obvious that disordered packings are impossible, and particles can only align head-to-tail upon densification. In the (theoretical) upper limit of an infinite cylinder diameter, the results from the fully periodic system will be retrieved.

Five runs with different starting configurations were averaged for each combination of Λ and D_{cyl}. Confidence intervals were calculated as before, assuming a Student's t-distribution ($\alpha = 0.95$ and $t_{\nu=4} = 2.776$). The acquired packing fractions are normalized by their periodic values, $\phi^* = \phi/\phi_{\text{periodic}}$. The mean contact numbers are rescaled such that they range between the minimum value of 2 (set to 0) and the corresponding periodic value (set to 1). In shorthand this is written as, $\langle C \rangle^* = [2, \langle C \rangle_{\text{periodic}}] \rightarrow [0, 1]$.

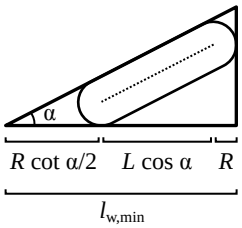

Figure 2.9. The minimum length of the wedge is defined as the length where a single row of particles is aligned with the wedge slope.

Note that if a value of $\langle C \rangle$ is found larger than the periodic value, $\langle C \rangle^*$ will be larger than one.

The effect of the wedge is investigated by simulating packings of different aspect ratios (as before) for increasing wedge acuteness α =9°–45° and wedge length l_w, scaled by the minimal wedge length $l_{w,min}$. The minimal wedge length is defined as the length necessary to contain exactly one single row of particles aligned with the wedge slope (see Figure 2.9),

$$l_{w,min} = \frac{R}{\tan \alpha/2} + R + L \cos \alpha \tag{2.12}$$

Using Equation 2.12, an exact value for the packing fraction for the lower limiting case can be calculated as,

$$\phi_{l_{w,min}} = \frac{\pi R^2 \left(\frac{4}{3}R + L\right)}{\frac{1}{2} 2 R l_{w,min}^2 \tan \alpha} \tag{2.13}$$

For all angles, upon increasing l_w towards infinity, the system will tend to the periodic results. Three runs with different starting configurations are averaged, and confidence intervals are calculated (α = 0.95 and $t_{\nu=2}$ = 4.303). Different from the results for the cylindrical boundary, here the packing fractions are rescaled to the range $\phi^* = [\phi_{l_{w,min}}, \phi_{periodic}] \rightarrow [0, 1]$. The mean contact numbers are scaled between 2 and the periodic value, as before.

2.5 Results and discussion

The effect of the cylindrical boundary on the values of the packing fraction, mean contact number and nematic order parameter is shown in Figure 2.10. It is immediately clear that for increasing cylinder diameter, the values for ϕ^* and $\langle C \rangle^*$ tend to unity for all aspect ratios, i.e. towards the periodic values. This is also clear from a linear extrapolation of the values for the packing fraction towards a cylinder with 'infinite' diameter ($1/D_{cyl} \rightarrow 0$), following the approach in [34].

Interestingly, by our rescaling of the packing fraction and mean contact number, the curves for the different aspect ratios collapse to a large extent. There are some deviations visible, for example in the case of $\Lambda = 5.0$ where the values for ϕ^* are somewhat erratic,

or for $\Lambda = 1.0$ where there is a distinct increase in $\langle C \rangle^*$ near $D_{\text{cyl}} = 2.5$. However, the trend is comparable for all cases: the packing fraction gradually decreases from the widest cylinder diameter until $D_{\text{cyl}} \approx 2.0$, when the decrease is sharpest and arrives at a minimum. The packing fraction then increases again for even lower cylinder diameters due to the forced alignment of the particles. For the mean contact number there is a gradual decrease until $D_{\text{cyl}} \approx 2.0$, after which particle alignment prevents the particles from having more than two contacts.

The data collapse suggests that the influence of the cylindrical boundary on the overall packing properties is similar for all particle aspect ratios. This seems rather counter intuitive for the longer aspect ratios, where particle alignment *must* start at larger cylinder diameters than for smaller aspect ratios: as soon as the cylinder diameter becomes smaller than the length of the particle ($2R + L$), some particle orientations will be excluded. Apparently, also for these longer particles, the strong decrease in packing fraction occurs only when the cylinder diameter approaches twice the particle diameter. At that point two particles can no longer fit side by side in the cylinder and head-to-tail configurations are required, which greatly increase the void volume in the packing. Prior to this point, ϕ decreases at most 20 % and the particles apparently have enough positional and rotational freedom to still allow for a dense packing with mixed ordered and disordered regions.

The onset of alignment is more clearly seen from the values of the nematic order parameter in Figure 2.10c, which has been plotted against D_{cyl}/Λ. The sharp transition from no orientational ordering, $S \lessapprox 0.2$, to complete ordering, $S \gtrapprox 0.8$, starts when the cylinder diameter is slightly larger than the particle aspect ratio. This coincides with the point described before, when certain particle orientations are no longer possible in the cylinder.

Only analysing the packing fraction and mean contact numbers, is insufficient to determine the actual packing structure present in narrow cylinders. Particles will start to display a variety of (semi-)crystalline phases upon increased confinement, which may strongly depend on the particular choice of cylinder diameter or particle aspect ratio. Figure 2.11 shows a few snapshots of the final configuration of confined spheres and spherocylinders to illustrate this. An experimental example of confinement dependent ordering can be seen in [13]. Further analysis of the exact nature of these ordered packings is left for future work.

The results for the packing simulations in the wedge are shown in Figure 2.12, Figure 2.13 and Figure 2.14. Similar to the situation for the cylindrical boundary, the packing fractions and contact numbers tend to unity upon increasing relative wedge length, i.e. towards the periodic values. For the packing fraction, this tendency is stronger for increasing particle aspect ratio. The mean contact numbers never rise above $\langle C \rangle^* \approx 0.8$, indicating that even for the largest wedge angle and wedge length, the fraction of particles missing contacts due to being located near a boundary is significant. Increasing the wedge length further or simulating a larger number of particles, will likely diminish this effect.

The rescaling of the packing fraction and mean contact numbers, causes a striking collapse of most curves unto each other, with deviations visible only for the smallest

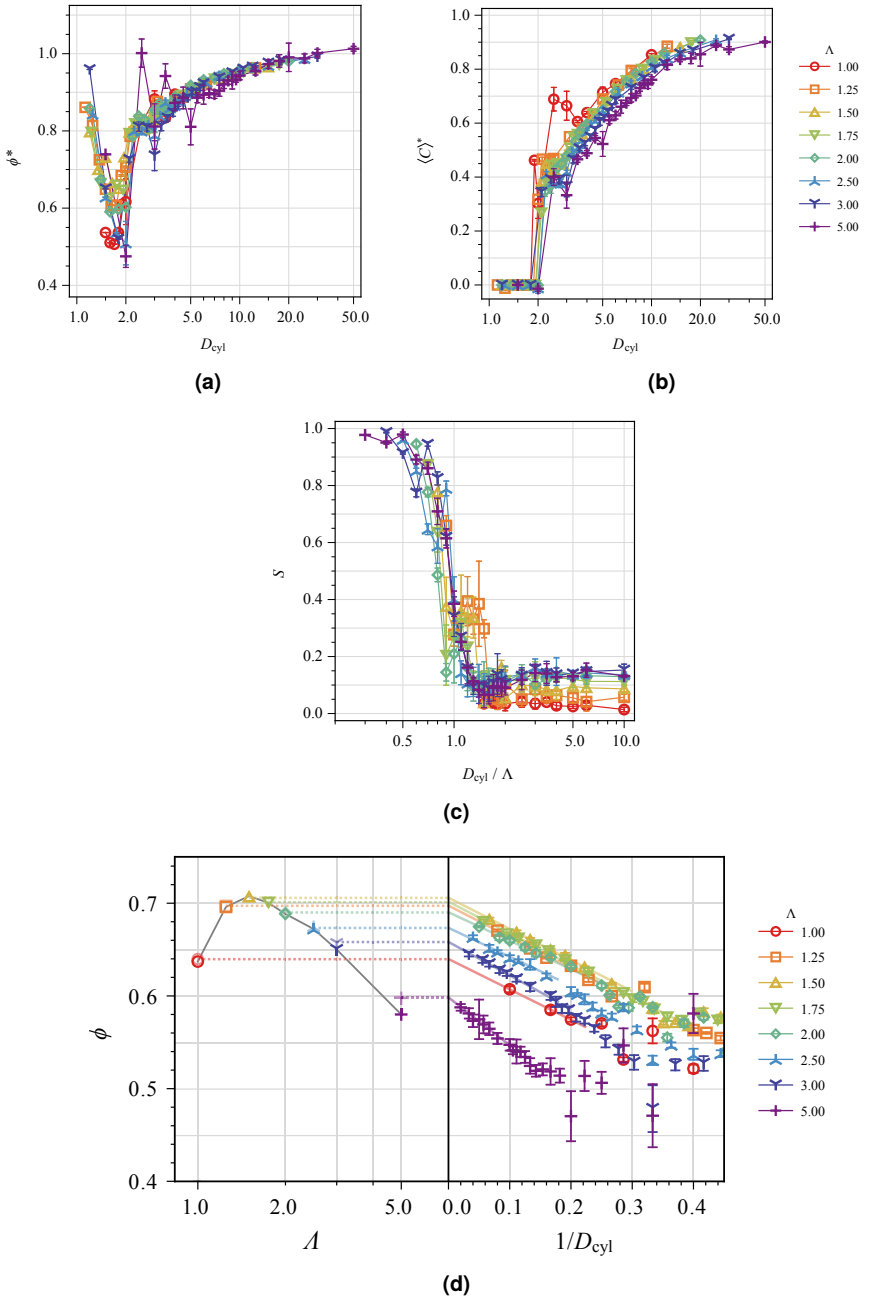

Figure 2.10. The (a) normalized volume fraction ϕ^*, (b) normalized mean contact number $\langle C \rangle^*$ and nematic order parameter S obtained from MCM simulations of spherocylinders of different aspect ratio in a hard cylinder. In (d) the values for the packing fraction are extrapolated towards an infinite cylinder ($1/D_{cyl} \to 0$, *right*). The bulk packing fractions are plotted (*left*) for comparison.

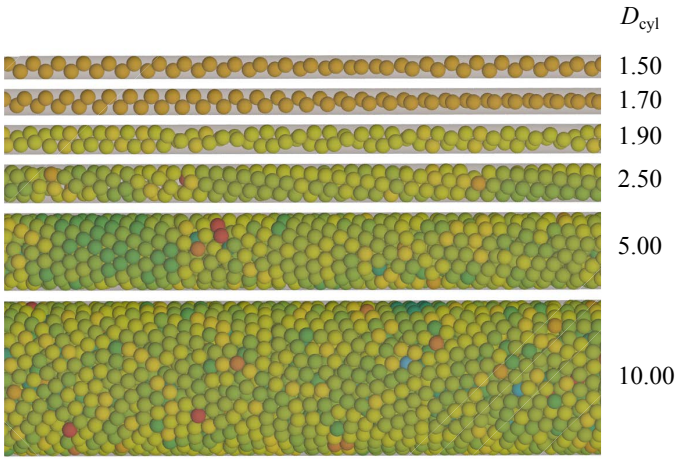

(a) Spheres ($\Lambda = 1.0$)

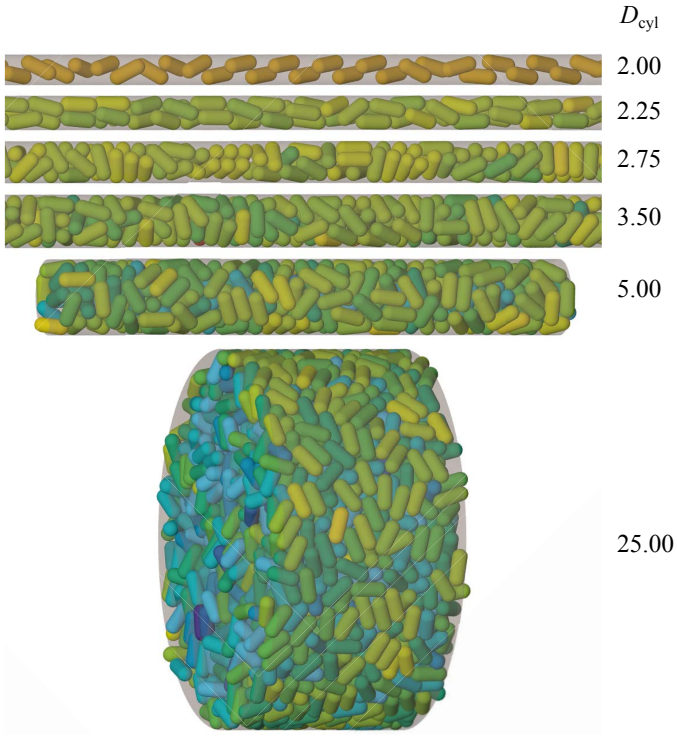

(b) Short spherocylinders ($\Lambda = 2.5$)

Figure 2.11. Snapshots of (a segment from) the final configurations of confined spheres and short spherocylinders in a series of cylinders with increasing diameter. For the smaller cylinder diameters, ordered structured can be observed. The particles are coloured based on their number of contacts, see Figure 2.1.

and highest aspect ratios studied. This indicates that comparable to the cylinder, the wedge boundaries influence the final packing properties independent of the particle aspect ratio.

The fraction of aligned particles near the wedge walls (see Figure 2.6) increases only very slightly upon increasing the relative wedge length. This indicates that the influence of the larger wedge surface area on the relative amount of aligned particles near the walls is small, as can be expected. Contrary to what could be expected due to the extreme confinement, there is a decrease in f_{align} for the smallest wedge angle and wedge lengths. This anomaly can be explained by the fact that for the determination of f_{align} a region with a fixed distance $\Delta = 2R$ is chosen (see Figure 2.6), and that f_{align} has separate contributions from the 'back', 'bottom' and 'slope' planes of the wedge. In the aforementioned cases, Δ is of the same order of size as the wedge dimensions, causing particles to be counted multiple times, but only being aligned with a single plane. The amount of aligned particles in these cases is therefore underestimated. Here, splitting f_{align} into the separate contributions from the three wedge planes, or reducing Δ may clarify the actual fraction of aligned particles.

For the lower aspect ratios $\Lambda \leq 2.00$ approximately half of the particles near the walls are aligned. Higher aspect ratios increase the fraction of alignment to more than 80 %. This increase can be explained by the fact that for longer particles, the probability of finding a particle's centre of mass in that region *without* the particle being aligned is much smaller than for shorter particles.

The alignment of the particles can also be visualized with a two dimensional density histogram of the polar and azimuthal angles of the particles' orientations. In Figure 2.15 a series of typical histograms is given for a single particle aspect ratio $\Lambda = 3.00$ and wedge angle $\alpha = 9°$, for increasing wedge length. Particle orientations have been calculated accounting for symmetry, so that the angles are limited to $0 \leq \cos\theta < 1$ and $0 \leq \phi < 90°$. It can be seen that for the smallest wedge length, certain orientations are excluded. This excluded area shrinks when the wedge length increases and the particles obtain more rotational freedom. Most particles are aligned with the wedge bottom or slope, $\phi = 0°$ or $\phi = 9°$ respectively, or with the back of the wedge, $\cos\theta = 1$. Particles not aligned with either of the bounding planes are shown to be almost uniform in orientation for the larger wedge lengths. This suggests that for sufficiently large wedges, the inner volume contains a normal random dense packing of rods.

In Figure 2.16 a few snapshots of final packings are shown, graphically illustrating the effects of increased wedge length and angle. For the smaller angle, the presence of ordered domains is apparent, with near-hexagonal packing in the case of $\Lambda = 1.25$, and multiple particles aligning in the same orientation for $\Lambda = 3.00$. The larger angle reduces the fraction of aligned particles as compared to the total amount of particles, but alignment is still visible near the edges. From the side views in the case of $\alpha = 45°$, it can be seen that the particles near the centre of the wedge have a higher number of contacts (more blue in colour), than the outer particles (more yellow in colour). This supports the idea that the particle packing inside the wedge is still random in nature.

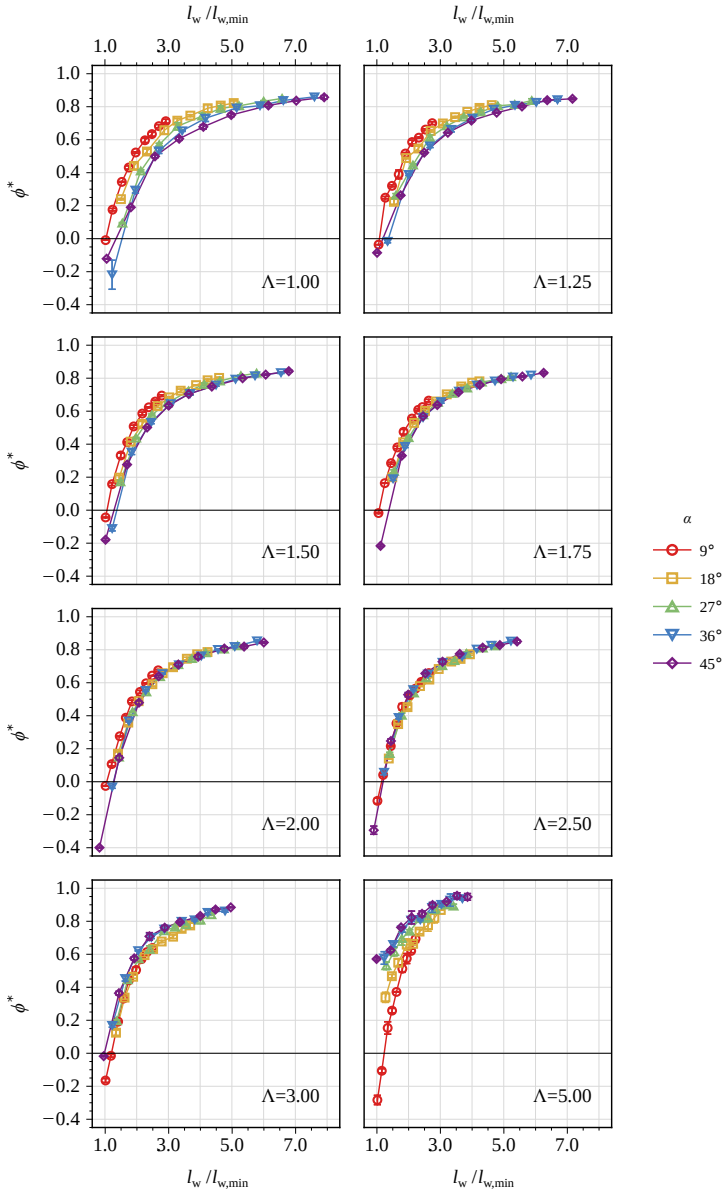

Figure 2.12. The volume fraction ϕ obtained from MCM simulations of spherocylinders of different aspect ratio in a hard wedge, scaled by $\phi^* = [\phi_{l_{w,min}}, \phi_{periodic}] \rightarrow [0, 1]$.

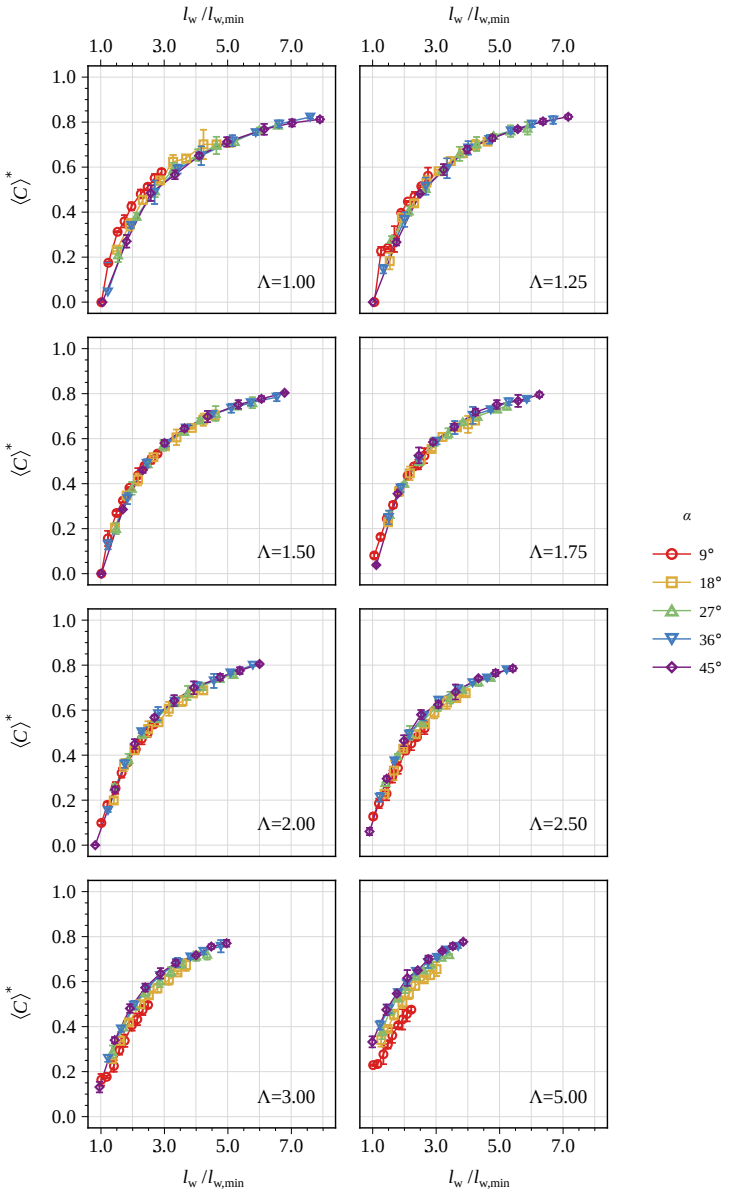

Figure 2.13. The mean contact number $\langle C \rangle$ obtained from MCM simulations of spherocylinders of different aspect ratio in a hard wedge, scaled by $\langle C \rangle^* = [2, \langle C \rangle_{\text{periodic}}] \rightarrow [0, 1]$.

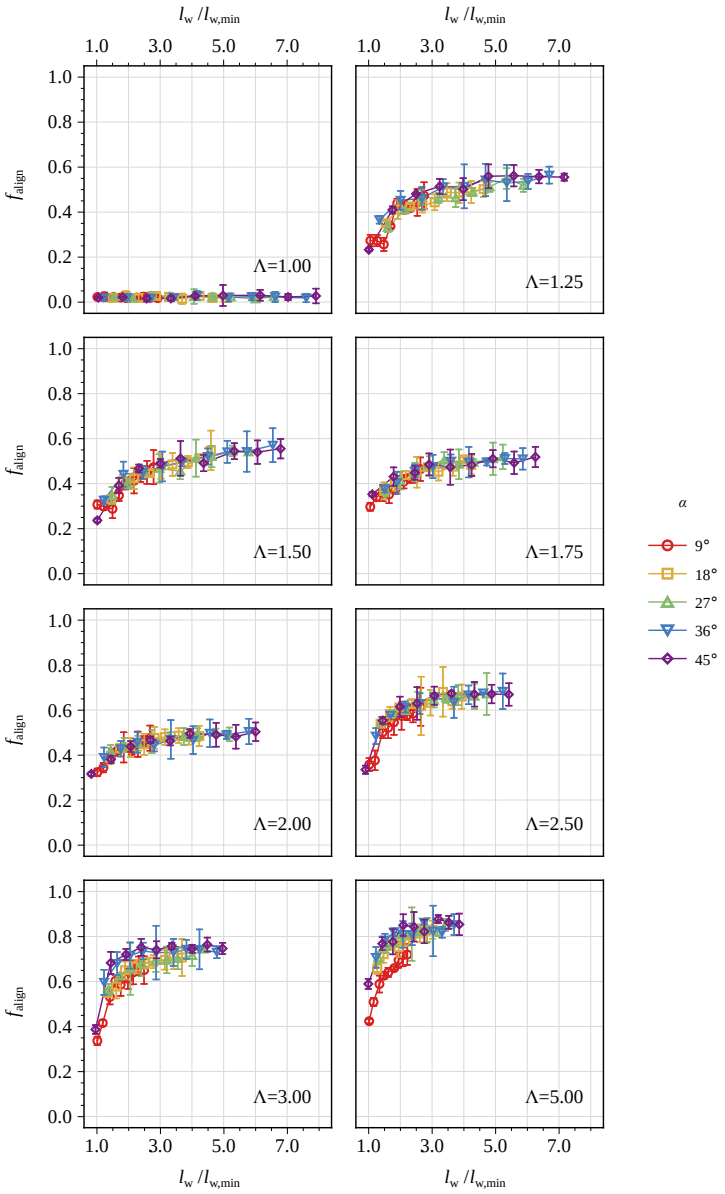

Figure 2.14. The fractions of aligned particles obtained from MCM simulations of spherocylinders of different aspect ratio in a hard wedge. See Figure 2.6 for a description how the fraction is determined.

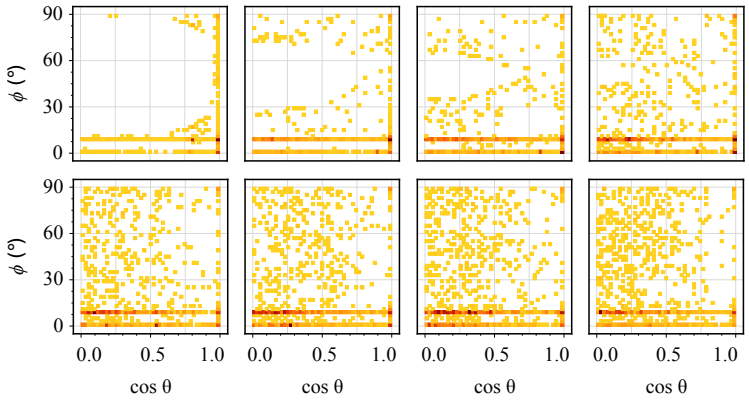

Figure 2.15. Two dimensional density histogram of the orientations of the spherocylinder particles ($\Lambda = 3.00$) confined in a wedge of $\alpha = 9°$ with increasing wedge length l_w from top left to bottom right. A fully randomly oriented system would show a uniform density distribution in the histogram.

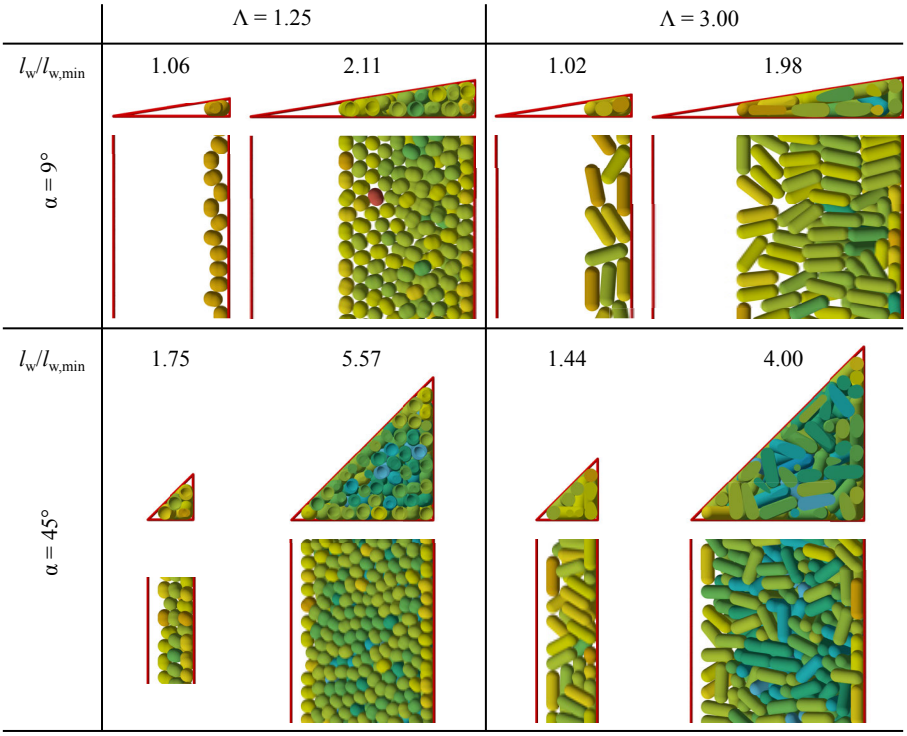

Figure 2.16. Partial snapshots of the final configurations in wedges with angles of 9° and 45° for two different wedge lengths and aspect ratios. The particles are coloured based on their number of contacts, see Figure 2.1.

2.6 Conclusion and outlook

In this chapter we have investigated the influence of a confining boundary on the packing properties of spherocylinder particles using a modified version of the mechanical contraction method. The existing simulation method has been discussed and various peculiarities have been highlighted, which prompted us to carefully re-examine the MCM in Chapter 3. The particular choice of the free parameter ξ in the original MCM has been shown to influence the packing fraction and mean contact numbers greatly. We show that this free parameter can be represented correctly by the exact moment of inertia of the concerned spherocylinder particles.

A virtual particle method has been introduced, which expands the MCM to include hard boundaries. We have considered only a cylindrical and wedge-shaped boundary, but other simple bounding geometries are possible to implement. The virtual particle method can be applied as long as a particle can be placed tangent to the boundary, and at a position such that it overlaps with the protruding particle. Difficulties with the virtual particle method may arise when sharp cusps or features with sizes of the order of the dimensions of the particle are present in the boundary.

The influence of a cylindrical boundary on spherocylinder packings has been shown to be at most weakly dependent on the particle aspect ratio. The relative packing fractions follow the same trend of decrease upon narrowing of the cylinder until approximately twice the particle diameter, followed by an increase due to forced particle alignment. Extrapolating values to cylinders of infinite diameter correctly reproduces the bulk packing fractions. The mean contact numbers decrease gradually from the periodic values to the minimum value of two contacts per particle. The transition between no preferential orientational alignment and full alignment of the particles, was found to be between cylinder diameters of 1.5 and 0.75 times the particle aspect ratio. In these strongly confining situations, particles assume various ordered structures depending on the particle aspect ratio and exact cylinder diameter. Closer inspection of these structures is left for future investigation, including comparison with simulations of others [24, 26].

Similar to the cylinder, confinement by a wedge shows an influence on the packing parameters almost independent of the particle aspect ratio. The relative packing fractions and mean contact numbers increase gradually from small wedge dimensions towards their periodic values. The fraction of aligned particles near the wall remains nearly constant, as expected. Also here, the packings in strong confinement show various ordered structures which may be analysed more in depth. The inner region of a wedge has been shown to have the characteristics of a regular random dense packing, thereby limiting the confinement effects to a relatively small region close to the boundaries.

Acknowledgements

Álvaro González García is thanked for many useful discussions and his simulation work, which were invaluable in the realization of this chapter. Alan Wouterse is thanked for initial discussions on the interpretation of the MCM.

References

1. J. Kepler, *Strena seu de Nive Sexangula*, **1611**, English translation: C. Hardie, *The six-cornered snowflake*, Clarendon Press, Oxford, UK, **1966**.
2. T. Aste, D. Weaire, *The Pursuit of Perfect Packing*, 2nd ed., CRC Press/Taylor & Francis Group, **2008**, p. 216.
3. J. D. Bernal, J. Mason, 'Packing of Spheres: Coordination of Randomly Packed Spheres', *Nature* **1960**, *188*, 910–911, DOI 10.1038/188910a0.
4. S. Torquato, T. M. Truskett, P. G. Debenedetti, 'Is Random Close Packing of Spheres Well Defined?', *Physical Review Letters* **2000**, *84*, 2064, DOI 10.1103/PhysRevLett.84.2064.
5. R. D. Kamien, A. J. Liu, 'Why is Random Close Packing Reproducible?', *Physical Review Letters* **2007**, *99*, 155501, DOI 10.1103/PhysRevLett.99.155501.
6. S. Torquato, F. H. Stillinger, 'Jammed hard-particle packings: From Kepler to Bernal and beyond', *Reviews of Modern Physics* **2010**, *82*, 2633, DOI 10.1103/RevModPhys.82.2633.
7. G. Parisi, F. Zamponi, 'Mean-field theory of hard sphere glasses and jamming', *Reviews of Modern Physics* **2010**, *82*, 789, DOI 10.1103/RevModPhys.82.789.
8. S. Torquato, Y. Jiao, 'Organizing principles for dense packings of nonspherical hard particles: Not all shapes are created equal', *Physical Review E* **2012**, *86*, 011102, DOI 10.1103/PhysRevE.86.011102.
9. A. Baule, R. Mari, L. Bo, L. Portal, H. A. Makse, 'Mean-field theory of random close packings of axisymmetric particles', *Nature Communications* **2013**, *4*, 2194, DOI 10.1038/ncomms3194.
10. A. Baule, H. A. Makse, 'Fundamental challenges in packing problems: from spherical to non-spherical particles', *Soft Matter* **2014**, *10*, 4423–4429, DOI 10.1039/C3SM52783B.
11. J.-M. Meijer, F. Hagemans, L. Rossi, D. V. Byelov, S. I. R. Castillo, A. Snigirev, I. Snigireva, A. P. Philipse, A. V. Petukhov, 'Self-Assembly of Colloidal Cubes via Vertical Deposition', *Langmuir* **2012**, *28*, 7631–7638, DOI 10.1021/la3007052.
12. P. Yang, T. Deng, D. Zhao, P. Feng, D. Pine, B. F. Chmelka, G. M. Whitesides, G. D. Stucky, 'Hierarchically ordered oxides', *Science* **1998**, *282*, 2244–2246, DOI 10.1126/science.282.5397.2244.
13. L. Jiang, J. W. J. de Folter, J. Huang, A. P. Philipse, W. K. Kegel, A. V. Petukhov, 'Helical Colloidal Sphere Structures through Thermo-Reversible Co-Assembly with Molecular Microtubes', *Angewandte Chemie International Edition* **2013**, *52*, 3364–3368, DOI 10.1002/anie.201209767.
14. S. R. Williams, A. P. Philipse, 'Random packings of spheres and spherocylinders simulated by mechanical contraction', *Physical Review E* **2003**, *67*, 051301, DOI 10.1103/PhysRevE.67.051301.
15. A. Wouterse, S. Luding, A. P. Philipse, 'On contact numbers in random rod packings', *Granular Matter* **2009**, *11*, 169–177, DOI 10.1007/s10035-009-0126-6.
16. K. de Lange Kristiansen, A. Wouterse, A. Philipse, 'Simulation of random packing of binary sphere mixtures by mechanical contraction', *Physica A: Statistical Mechanics and its Applications* **2005**, *358*, 249–262, DOI 10.1016/j.physa.2005.03.057.
17. A. Wouterse, S. R. Williams, A. P. Philipse, 'Effect of particle shape on the density and microstructure of random packings', *Journal of Physics: Condensed Matter* **2007**, *19*, 406215, DOI 10.1088/0953-8984/19/40/406215.
18. S. Sacanna, L. Rossi, A. Wouterse, A. P. Philipse, 'Observation of a shape-dependent density maximum in random packings and glasses of colloidal silica ellipsoids', *Journal of Physics: Condensed Matter* **2007**, *19*, 376108, DOI 10.1088/0953-8984/19/37/376108.
19. A. V. Kyrylyuk, A. Wouterse, A. P. Philipse, 'Random Packings of Rod-Sphere Mixtures Simulated by Mechanical Contraction', **2009**, *1145*, 211–214, DOI 10.1063/1.3179895.
20. A. V. Kyrylyuk, A. Wouterse, A. P. Philipse, 'Percolation and Jamming in Random Heterogeneous Materials with Competing Length Scales' in *Trends in Colloid and Interface Science XXIII*, (Ed.: S. Bucak), Springer-Verlag Berlin Heidelberg, **2010**, pp. 29–33, DOI 10.1007/978-3-642-13461-6.
21. A. V. Kyrylyuk, A. P. Philipse, 'Effect of particle shape on the random packing density of amorphous solids', *physica status solidi (a)* **2011**, *208*, 2299–2302, DOI 10.1002/pssa.201000361.
22. A. V. Kyrylyuk, M. A. van der Haar, L. Rossi, A. Wouterse, A. P. Philipse, 'Isochoric ideality in jammed random packings of non-spherical granular matter', *Soft Matter* **2011**, *7*, 1671–1674, DOI 10.1039/C0SM00754D.
23. C. Ferreiro-Córdova, J. S. van Duijneveldt, 'Random Packing of Hard Spherocylinders', *Journal of Chemical & Engineering Data* **2014**, *59*, 3055–3060, DOI 10.1021/je500119r.

24. L. Pournin, M. Weber, M. Tsukahara, J.-A. Ferrez, M. Ramaioli, Th. M. Liebling, 'Three-dimensional distinct element simulation of spherocylinder crystallization', *Granular Matter* **2005**, *7*, 119–126, DOI 10.1007/s10035-004-0188-4.
25. C. Vega, S. Lago, 'A fast algorithm to evaluate the shortest distance between rods', *Computers & Chemistry* **1994**, *18*, 55–59, DOI 10.1016/0097-8485(94)80023-5.
26. C. R. A. Abreu, F. W. Tavares, M. Castier, 'Influence of particle shape on the packing and on the segregation of spherocylinders via Monte Carlo simulations', *Powder Technology* **2003**, *134*, 167–180, DOI 10.1016/S0032-5910(03)00151-7.
27. L. Verlet, 'Computer "Experiments" on Classical Fluids. I. Thermodynamical Properties of Lennard-Jones Molecules', *Physical Review* **1967**, *159*, 98–103, DOI 10.1103/PhysRev.159.98.
28. O. Rodrigues, 'Des lois géométriques qui régissent les déplacements d'un système solide dans l'espace, et de la variation des coordonnées provenant de ces déplacements considérés indépendamment des causes qui peuvent les produire', *Journal de mathématiques pures et appliquées* **1840**, *5*, 380–440.
29. C. Zannoni, 'Distribution Functions and Order Parameters' in *The Molecular Physics of Liquid Crystals*, (Eds.: G. Luckhurst, G. Gray), Academic Press, **1979**, Chapter 3, pp. 51–83.
30. R. Eppenga, D. Frenkel, 'Monte Carlo study of the sotropic and nematic phases of infinitely thin hard platelets', *Molecular Physics* **1984**, *52*, 1303–1334, DOI 10.1080/00268978400101951.
31. Wolfram Research, Inc., Mathematica v10.1, **2015**.
32. Persistence of Vision Pty. Ltd., POV-Ray v.3.7, **2004**.
33. A. P. Philipse, 'The Random Contact Equation and Its Implications for (Colloidal) Rods in Packings, Suspensions, and Anisotropic Powders', *Langmuir* **1996**, *12*, 1127–1133, DOI 10.1021/la950671o, (correction) **1996**, *12*, 5971–5971.
34. G. D. Scott, D. M. Kilgour, 'The density of random close packing of spheres', *Journal of Physics D: Applied Physics* **1969**, *2*, 863, DOI 10.1088/0022-3727/2/6/311.

Appendix 2.A Lagrange multiplier

In this section the method of Langrange multipliers is applied strictly to Equation 2.5 with the constraint of Equation 2.6.

For convenience we repeat these equations here,

$$s_i = \sum_{j=1}^{C} \delta_{ij} \left(k_{ij}^{(1)} a_1 + k_{ij}^{(2)} a_2 + k_{ij}^{(3)} a_3 + l_{ij} k_{ij}^{(4)} a_4 + l_{ij} k_{ij}^{(5)} a_5 \right) \\ a_1^2 + a_2^2 + a_3^2 + \xi a_4^2 + \xi a_5^2 = 1 \tag{2.14}$$

In order to find the maximum total overlap removal rate, an additional function Λ is constructed,

$$\Lambda = \sum_{j=1}^{C} \delta_{ij} \left(k_{ij}^{(1)} a_1 + k_{ij}^{(2)} a_2 + k_{ij}^{(3)} a_3 + l_{ij} k_{ij}^{(4)} a_4 + l_{ij} k_{ij}^{(5)} a_5 \right) - \\ \lambda \left(a_1^2 + a_2^2 + a_3^2 + \xi a_4^2 + \xi a_5^2 - 1 \right) \tag{2.15}$$

where λ is the so-called Lagrange multiplier. Now the partial derivatives of Λ with respect to a_n are taken, yielding,

$$\frac{\partial \Lambda}{\partial a_n} = \begin{cases} 2\lambda a_n - \sum_{j=1}^{C} \delta_{ij} k_{ij}^{(n)} & \text{if} n = 1, 2, 3 \\ 2\xi\lambda a_n - \sum_{j=1}^{C} l_{ij} \delta_{ij} k_{ij}^{(n)} & \text{if} n = 4, 5 \end{cases} \tag{2.16}$$

To find stationary points, the partial derivatives are equated to zero. They can be rewritten to find,

$$a_n = \begin{cases} \frac{1}{2\lambda} \sum_{j=1}^{C} \delta_{ij} k_{ij}^{(n)} & \text{if} n = 1, 2, 3 \\ \frac{1}{2\xi\lambda} \sum_{j=1}^{C} l_{ij} \delta_{ij} k_{ij}^{(n)} & \text{if} n = 4, 5 \end{cases} \tag{2.17}$$

These expressions closely resemble those in Equation 2.7, but are only identical when $\lambda = \frac{1}{2}$. An exact expression for λ can be found by substituting the expressions for a_n back into the original constraint. We drop the summation indices for clarity.

$$\left(\frac{1}{2\lambda} \sum \delta_{ij} k_{ij}^{(1)} \right)^2 + \left(\frac{1}{2\lambda} \sum \delta_{ij} k_{ij}^{(2)} \right)^2 + \left(\frac{1}{2\lambda} \sum \delta_{ij} k_{ij}^{(3)} \right)^2 + \\ \xi \left(\frac{1}{2\xi\lambda} \sum l_{ij} \delta_{ij} k_{ij}^{(4)} \right)^2 + \xi \left(\frac{1}{2\xi\lambda} \sum l_{ij} \delta_{ij} k_{ij}^{(5)} \right)^2 = 1 \tag{2.18}$$

from which λ can be deduced,

$$\lambda = \pm\frac{1}{2}\left[\left(\sum \delta_{ij} k_{ij}^{(1)}\right)^2 + \left(\sum \delta_{ij} k_{ij}^{(2)}\right)^2 + \left(\sum \delta_{ij} k_{ij}^{(3)}\right)^2 + \frac{1}{\xi}\left(\sum l_{ij}\delta_{ij} k_{ij}^{(4)}\right)^2 + \frac{1}{\xi}\left(\sum l_{ij}\delta_{ij} k_{ij}^{(5)}\right)^2\right]^{\frac{1}{2}} \quad (2.19)$$

It is clear that following the method of Lagrange multipliers strictly, does not result in a situation where $\lambda = \frac{1}{2}$ as is used in Equation 2.7. This implies that the total overlap removal rate in Equation 2.5 in the original MCM is not (fully) maximized, possibly leading to a sub-optimal overlap removal scheme.

However, as results previously obtained with the MCM were found to be in good agreement with other simulations and experimental data, it is likely that the overall efficiency of the overlap removal is relatively insensitive to the particular choice of λ.

3

The mechanical contraction method: revision and generalization

Abstract

The mechanical contraction method (MCM) is one of several techniques to simulate random dense packings of various particle shapes, in order to study their structure and properties. It was originally developed for spheres and spherocylinders, but has also been successfully applied to ellipsoids and cut-spheres. In Chapter 2, some difficulties with the theoretical foundation of the method were reported, prompting a revision of the governing MCM equations in this chapter. Simultaneously, the method is generalized and extended to allow the simulation of packings of particles of arbitrary convex shape. Combined with the virtual-particle method introduced in Chapter 2, the revised mechanical contraction presented here method opens up possibilities for an extensive investigation of a variety of random packings, both in bulk and confinement.

3.1 Introduction

Disordered, or random dense packings of particles occur frequently in both nature and technology, for example in the storage of granular matter in silos [1], in the reinforcement of plastics [2] and in the formation of glassy structures of colloidal particles [3]. Common features of these packings are their mechanical stability and lack of long-range positional and orientational ordering. Despite many attempts to formulate a comprehensive and general theory describing the structural features of such packings, this remains an open problem [4–12]. The experimental work of Bernal and Mason [13] on the random packing of spheres initiated many experimental and simulation studies, attempting to shed light on the random packing behaviour of (non-)spherical particles, see for example [14–22].

Of particular interest for this chapter is the development of the mechanical contraction method (MCM) by Williams [18]. This method was developed based on the hypothesis that the random packing density of (frictionless) particles is only dependent on the particle shape [5]. As such, the MCM is developed as a geometry-based technique. Specifically, it sets itself apart from other methods, such as the well-known Lubachevsky-Stillinger algorithm [23, 24], by not using force calculation, or rather complex movement calculations that are needed in event-driven molecular dynamics [25, 26]. The MCM has been successfully applied to spheres and spherocylinders [18, 27–32], ellipsoids [33] and cut-spheres [21].

Despite the excellent results obtained with the MCM, some difficulties with the method were brought to light upon closer inspection. For example, in Chapter 2 we argue that a physical interpretation of the MCM would justify the explicit inclusion of the moment of inertia in the equations, instead of having a free parameter. In this chapter we set out to re-derive the MCM, emphasizing a physical interpretation of the equations where necessary, and following a more mathematically precise derivation. We simultaneously follow the ideas from Wouterse *et al.* [21] and generalize the MCM to any convex particle shape. First, we will briefly recapitulate the premises of the MCM. Then, the central algorithms for overlap detection and removal are re-derived. Some key differences with the original MCM are highlighted, and finally a comparison between the results from the original and revised method is made.

3.2 Preliminaries

The aim of the mechanical contraction method is to generate a dense packing of particles by—in essence—maximizing the packing fraction ϕ, without inducing significant (long-range) positional and orientational ordering. Without assuming any particular particle shape, or distribution in shape or size, the packing fraction is given by the total volume of the particles, divided by the total volume of the simulation box V_{box},

$$\phi = \frac{\sum_{i=1}^{N} V_{\text{p},i}}{V_{\text{box}}} \tag{3.1}$$

where N is the number of particles, and $V_{\text{p},i}$ is the volume of the i-th particle. Each particle is further characterized by a position vector $\mathbf{x}_i$, orientation matrix $\mathbf{R}_i$ and some

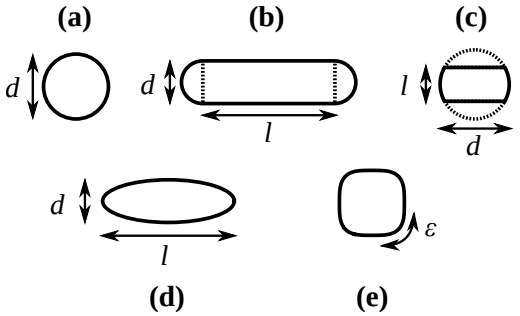

Figure 3.1. Two dimensional representations of several particle shapes that can be simulated with the MCM: (a) spheres [18, 27], (b) spherocylinders [18, 28], (c) cut-spheres [21], (d) ellipsoids [21] and (e) superquadrics (see Chapter 4).

shape dependent parameters (e.g. radius, length, etc.). For computational purposes, unit quaternions $\mathbf{q}_i$ are a better choice to describe particle orientations [34].

The methodology of the MCM places only a few restrictions on the type of particles that can be simulated. In addition to a known particle volume for the calculation of the packing fraction, the only strict requirements are the ability to calculate inter-particle distances, overlap distances and moments of inertia. For convenience, we restrict ourselves to convex particles in three dimensions. Specifically, the MCM is not restricted to the simulation of identical particles, see for example [27, 30] where mixtures of differently sized spheres and mixtures of spheres and spherocylinders have been simulated. Some of the particle shapes that have been investigated so far are shown in Figure 3.1. A detailed description of the simulation of spheres and spherocylinders is presented in Chapter 2, but the modifications presented in this chapter can be applied to these shapes as well. In Chapter 4 the additional superquadric shape is discussed.

An MCM simulation starts from a configuration of randomly positioned and oriented particles at a low packing fraction, typically $\phi = 0.05$. Care is taken to ensure no initial particle-particle overlaps exist. Typically, a cubic simulation box with periodic boundary conditions is used, but confining boundaries can be implemented via a virtual particle method (see Chapter 2). In the latter case, the particles are placed such that no initial particle-boundary overlaps exist. The simulation box is then gradually compressed in steps of ΔV, its value typically an order of magnitude smaller than a single particle volume. All particle positions are scaled according to the reduction in volume, but orientations are unaffected. The scaling may cause particles to overlap, and any overlap is subsequently removed by translation and rotation of the affected particles. This two-step process of compressing and removing overlaps is repeated until particle overlaps cannot be removed within a set limit of attempts (typically on the order of $200 \times N$ attempts per compression step). The last configuration without overlaps is taken as the final result. Optionally, using this final configuration, ΔV can be scaled down several times to attempt further compression in smaller steps.

3.3 Characterization

In addition to the packing fraction, other measures characterizing the packing can be calculated. A commonly used parameter is the mean contact number $\langle C \rangle$, or average coordination number, which is the average number of contacting particles per particle. A particle pair is assumed to be in contact when their minimal surface-to-surface distance is lower than a small value, typically $\delta = 10^{-4}$. A more accurate approach in finding $\langle C \rangle$ is by extrapolating its value at different δ towards $\delta = 0$. The mean contact number plays an important role in the discussion of mechanical stability of a packing, the 'isostatic conjecture' and the jamming transition [12, 16, 28, 35, 36]. Note however, that the MCM considers frictionless particles and has no inherent means of determining if a packing is mechanically stable, or jammed.

The positional and orientational ordering in the packing can currently be quantified through the calculation of the radial distribution function $g(r)$, nematic and cubatic order parameters [37, 38], and for spheres only, the orientational bond order parameters [39]. Additional order metrics have been proposed in literature, including those based on Voronoi-cells [40], or Minkowski tensors [41].

3.4 Implementation

The MCM has been implemented in the C++ language and codes are available from the author upon request. In order to speed up calculation, a neighbourhood list is constructed, similar to a Verlet list [42]. The list maintains an index of the particles within a certain cut-off radius of each particle, and only these particles are checked for overlap. The list is updated after the particle has moved more than a predefined distance. This method may not be the most efficient for very anisometric particles, and may be improved by considering different near-neighbour lists [25].

3.5 Overlap detection and removal

In this section we will discuss the two central steps of the MCM, concerning the particle overlap detection and subsequent removal. The derivation here is based on the modified MCM for spheroids and cut-spheres [21], which in turn was a generalization of the original method for spheres and spherocylinders [18], also described in Chapter 2. In the remained of this chapter we refer to both methods as the 'original MCM'. Key differences between our derivation and the original method will be highlighted.

3.5.1 Detection

During the MCM, particle overlap is induced due to the scaling of the simulation box. In general, an overlap can be described by a vector $\mathbf{k}_{ij}$, connecting two contact points $\mathbf{r}_{c,i}$ and $\mathbf{r}_{c,j}$ on the particle surfaces (see Figure 3.2). $\mathbf{k}_{ij}$ is chosen collinear with the surface normals $\hat{\mathbf{n}}_{i,j}$ at the contact points. This is referred to as the common-normal principle [43], and is derived from the notion that in a physical contact, particles exhibit a force along a common normal. The overlap distance is given by $\delta_{ij} = \|\mathbf{k}_{ij}\|$. Our definition of $\mathbf{r}_c$ connects the particle's centre of mass with a point on the surface. This differs slightly from the definition in [21], but is more general.

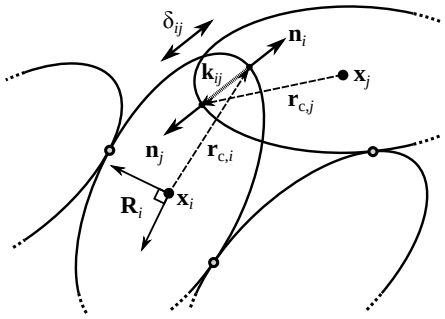

Figure 3.2. An overview of the relevant vectors quantities in the contact detection process. As a typical example, here a two dimensional representation of a packing of ellipsoids is used with one particle overlap.

The method of finding $\mathbf{k}_{ij}$ needs to be specifically tailored for each particle shape. For example, for spheres, $\mathbf{k}_{ij}$ is collinear with $\mathbf{x}_j - \mathbf{x}_i$ and the overlap distance is simply $\delta_{ij} = r_i + r_j - \|\mathbf{x}_j - \mathbf{x}_i\|$, where $r_{i,j}$ are the radii of the spheres. For spherocylinders, finding $\mathbf{k}_{ij}$ involves finding the closest distance between two line segments. An efficient algorithm for this procedure was developed by Vega and Lago [44] and later improved by Abreu *et al.* [45]. For ellipsoids, one has to resort to one of many available numerical methods [46–48]. Contact detection algorithms are widely studied in discrete element modelling (see for example [49]). Note that testing whether two particles overlap, without calculating the exact overlap distance, is sometimes easier than performing a full minimal distance calculation [46, 50]. Such methods are useful in Monte Carlo simulations where overlapping situations can be rejected, but they provide ultimately insufficient contact information for use in the MCM.

3.5.2 Removal

Once the overlap vector $\mathbf{k}_{ij}$ is known, particles will be translated and rotated to remove their overlap. To quantify this change in overlap, an overlap removal speed can be defined. Approximated to first order, this is the speed with which the contact point on the particle's surface moves with a constant linear and angular velocity along the contact normal,

$$\frac{\partial\, \delta_{ij}}{\partial t} = \left(\mathbf{v}_i + \boldsymbol{\omega}_i \times \mathbf{r}_{c,ij}\right) \cdot \hat{\mathbf{n}}_{ij} \tag{3.2}$$

where $\mathbf{v}_i$ is the linear velocity, $\boldsymbol{\omega}_i$ the angular velocity of the particle, and $\mathbf{r}_{c,ij}$ and $\hat{\mathbf{n}}_{ij}$ are defined as before. When multiple overlaps are present, a total overlap removal speed for the i-th particle is defined by summing individual contributions,

$$s_i = \sum_{j=1}^{C} \frac{\partial \delta_{ij}}{\partial t} \tag{3.3}$$

where C is the number of contacting particles.

In the original MCM, an additional factor δ_{ij} was included in the summation, to bias the speed towards the largest particle overlap (see Equation 2.5 in Chapter 2). We do not include it here, as we find no compelling physical or computational argument why the largest particle overlap should have preference. Additionally, results obtained with the original MCM, but with omission of this factor, did not significantly change the final results.

The velocity vectors in Equation 3.2 that maximize the overlap removal speed are found by maximizing Equation 3.3 using the method of Lagrange multipliers. The assumption of the conservation of kinetic energy per particle is introduced as a constraint. Using expressions from classical mechanics we have,

$$c = \tfrac{1}{2} m_i \mathbf{v}_i \cdot \mathbf{v}_i + \tfrac{1}{2} \boldsymbol{\omega}_i \mathbf{I}_i \boldsymbol{\omega}_i \tag{3.4}$$

where c is an arbitrary constant, m_i the mass of the particle and $\mathbf{I}_i$ the inertia tensor. Note that this tensor also contains the mass of the particle. The inertia tensor is calculated from the principal moments of inertia in the body frame of reference via $\mathbf{I}_i = \mathbf{R}_i \mathbf{I}_{i,\text{body}} \mathbf{R}_i^{\mathsf{T}}$. The constraint from the original MCM is retrieved when we take Equation 3.4 and set $c = 2$ and $m_i = 1$, treating all particles as having identical masses. Other constraints may be considered, for example a constraint on the preservation of randomness in the packing, but this would quickly and severely complicate calculations.

A Lagrange function $\Lambda(\mathbf{v}, \boldsymbol{\omega}, \lambda)$ is now constructed by combining Equation 3.3 and Equation 3.4 into,

$$\Lambda = \sum_{j=1}^{C} \left(\mathbf{v}_i + \boldsymbol{\omega}_i \times \mathbf{r}_{\text{c},ij} \right) \cdot \hat{\mathbf{n}}_{ij} + \lambda \left(\tfrac{1}{2} m_i \mathbf{v}_i \cdot \mathbf{v}_i + \tfrac{1}{2} \boldsymbol{\omega}_i \mathbf{I}_i \boldsymbol{\omega}_i - c \right) \tag{3.5}$$

where λ is the Lagrange multiplier. The velocity vectors maximizing the overlap removal rate are found by taking the derivatives of Equation 3.5 with respect to the components of $\mathbf{v}_i$ and $\boldsymbol{\omega}_i$, and setting them to zero. For the linear velocity this results in,

$$\frac{\partial \Lambda}{\partial \mathbf{v}_i} = \lambda m_i \mathbf{v}_i + \sum_{j=1}^{C} \hat{\mathbf{n}}_{ij} = 0 \qquad \rightarrow \qquad \mathbf{v}_i = -\lambda^{-1} m_i^{-1} \sum_{j=1}^{C} \hat{\mathbf{n}}_{ij} \tag{3.6}$$

and for the angular velocity we find,

$$\frac{\partial \Lambda}{\partial \boldsymbol{\omega}_i} = \lambda \mathbf{I}_i \boldsymbol{\omega}_i - \sum_{j=1}^{C} \hat{\mathbf{n}}_{ij} \times \mathbf{r}_{\text{c},ij} = 0 \qquad \rightarrow \qquad \boldsymbol{\omega}_i = \lambda^{-1} \mathbf{I}_i^{-1} \sum_{j=1}^{C} \hat{\mathbf{n}}_{ij} \times \mathbf{r}_{\text{c},ij} \tag{3.7}$$

The value of the Lagrange multiplier λ can be found by substitution of Equation 3.6 and Equation 3.7 back into the original constraint in Equation 3.4, leading to,

$$\lambda = \sqrt{\frac{1}{2c} \left(m_i^{-1} \left(\sum \hat{\mathbf{n}}_{ij} \right) \cdot \left(\sum \hat{\mathbf{n}}_{ij} \right) + \left(\sum \hat{\mathbf{n}}_{ij} \times \mathbf{r}_{\text{c},ij} \right) \mathbf{I}_i^{-1} \left(\sum \hat{\mathbf{n}}_{ij} \times \mathbf{r}_{\text{c},ij} \right) \right)} \tag{3.8}$$

where the summations run over all contacting particles. The negative solution of the

square root of λ^2 is discarded, as it would lead to a change of sign in Equation 3.6 causing overlap *formation*. The original MCM appears to ignore the multiplier λ completely, although its value during a simulation run was found to range from approximately 1.0 to 10.0, clearly showing it cannot be omitted.

The obtained vectors $\mathbf{v}_i$ and $\boldsymbol{\omega}_i$ provide the velocities for particle i to maximize its overlap removal. The new particle position is now calculated as a finite difference,

$$\mathbf{x}_{t+1} = \mathbf{x}_t + \delta_{ij,\min}\, \Delta t\, \mathbf{v}_i \tag{3.9}$$

where Δt is a constant time-step that modulates the change in overlap removal. Small values $\Delta t = 0.1$ generally work well. The additional factor $\delta_{ij,\min}$ is the minimal overlap distance found for the i-th particle. The inclusion of this factor assures that the moment when two particles become separated is approached very gradually. In other words, it prevents a particle to change its position more than the distance of its smallest overlap. This allows the system to attain higher packing fractions and mean contact numbers, at the cost of an increased number of steps before overlap is removed.

To update the particle orientation, Rodrigues' rotation formula is used [51]. The rotation matrix for a rotation by a small angle $\delta\theta$ about an axis, here represented by the angular velocity vector $\boldsymbol{\omega}$, is given by,

$$\mathbf{r} = \mathbf{I} + \sin(\delta\theta)\boldsymbol{\Omega} + (1 - \cos(\delta\theta))\boldsymbol{\Omega}^2 \tag{3.10}$$

where $\boldsymbol{\Omega}$ is a skew-symmetric matrix associated with a normalized $\boldsymbol{\omega}$,

$$\boldsymbol{\Omega} = \begin{pmatrix} 0 & -\omega_z & \omega_y \\ \omega_z & 0 & -\omega_x \\ -\omega_y & \omega_x & 0 \end{pmatrix} / \|\boldsymbol{\omega}\| \tag{3.11}$$

The small change in angle θ is calculated as,

$$\delta\theta = \|\boldsymbol{\omega}\|\, \delta_{ij,\min}\, \Delta t \tag{3.12}$$

where the multiplication with the minimal overlap distance and the time-step ensures the particle rotation is gradual. The new orientation is now given by,

$$\mathbf{R}_{t+1} = \mathbf{R}_t \mathbf{r} \tag{3.13}$$

Due to the properties of $\mathbf{r}$ by construction via Rodrigues' formula (Equation 3.10), $\mathbf{R}_{t+1}$ will automatically be an orthogonal matrix. The original MCM requires a re-orthogonalisation of the rotation matrix (Equation 2.9 in Chapter 2).

3.6 Results and discussion

First we assess how the improved MCM in this chapter compares to earlier results. The particle of choice for this comparison is the spherocylinder (see Chapter 2 for more details). We perform a series of simulations of spherocylinder particles for increasing aspect ratio, $\Lambda = 1.0$–150.0, and plot these together with results from [28]

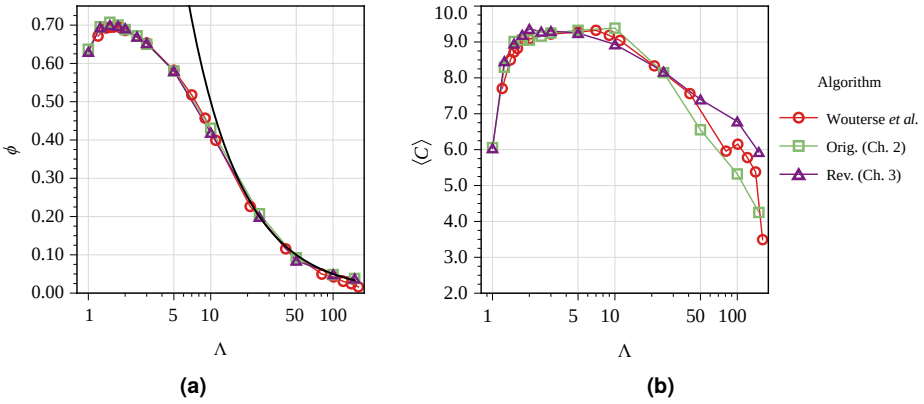

Figure 3.3. Comparison of the packing fraction (a) and mean contact numbers (b), between the revised MCM (this chapter), our own results using the original MCM (Chapter 2) and earlier results by Wouterse *et al.* [28]. The thick black line indicates the theoretical prediction by the random contact equation from [5], namely $\phi L/D = \langle C \rangle / 2 = 5$.

and Chapter 2 in Figure 3.3. The constant c in Equation 3.8 was set to unity, and a value of $\Delta t = 0.1$ was used. The mass of the particle is calculated from its volume, by setting the particle density to unity.

From Figure 3.3 it is clear that the revised MCM obtains results very similar to previous work, showing that our revisions also result in the formation of random dense packings. The obtained packing fractions match, and a slight increase is seen in the mean contact number for high aspect ratios. This latter observation may be regarded as a relevant improvement over previous results, but values are nevertheless still too low compared to experimental values of $\langle C \rangle \approx 9.8$ [35]. Further discussion of this result falls outside the scope of this chapter, including a more extensive comparion to different simulation methods (e.g. [45, 52, 53]).

We recapitulate here the changes we made to the MCM, with respect to the original method in [18, 21] and as discussed in Chapter 2.

1. A slightly different definition of $\mathbf{r}_c$ is used;
2. The factor δ_{ij} in Equation 3.3 is omitted;
3. The particle mass is explicitly used in Equation 3.4;
4. The Lagrange multiplier λ in Equation 3.6 is explicitly used;
5. A modified way to update particle positions and rotations is employed.

While these changes in the MCM may seem minor, together they contribute to a method that is now general in terms of particle shape, that can be used for polydisperse packings, that employs expressions closely related to classical mechanics, and is derived in a mathematically more precise way.

Finally, we compare the behaviour of the previous and current version of the MCM, with respect to how quickly and how gradually particle overlap is removed and make an additional comparison with the case where random particle movement is used to remove overlap. We generate $n = 1000$ configurations of three spherocylinder particles

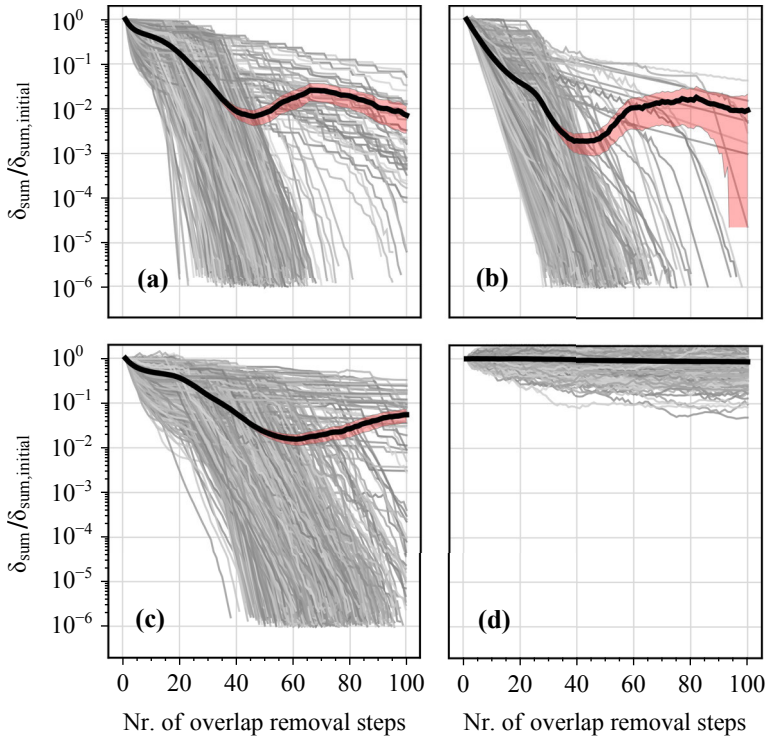

Figure 3.4. The relative total overlap distance for three spherocylinder particles while performing (a) the revised MCM (this chapter), (b) the original MCM (Chapter 2, and [18, 21]), (c) the revised MCM but with a random direction for ω, and (d) the revised MCM but with a random direction for $\mathbf{v}$ and ω. Each grey line corresponds to a single run, where the lines vary slightly in intensity for clarity. The thick black line indicates the average value, and the red area gives the 95 % confidence interval for the average value.

($\Lambda = 5.0$) that each have a small overlap with each other. For each starting configuration the method from Chapter 2 and the revised method from this chapter are applied, and the sum of the overlap distances δ_{ij} is monitored. Additionally, the method from this chapter is used but a *random direction* of ω or both $\mathbf{v}$ and ω from Equation 3.6 and Equation 3.7 is chosen instead, while keeping the magnitude unchanged. The results are given in Figure 3.4.

The comparison shows that the relative total overlap decreases in a very comparable way for the original and revised MCM (Figure 3.4a and b). On average the original MCM shows a slightly faster decrease in total overlap distance, and fewer cases where overlap removal occurs slowly (the grey lines that do not reach an overlap total of $\sim 10^{-6}$). Interestingly, the overlap distance for the original MCM shows oscillations in several cases, whereas in the revised MCM the total overlap distance almost always decreases. When the direction of ω is randomized (Figure 3.4c), it is clear that on average more steps are requires to remove all overlaps. For the randomization of both

ω and $\mathbf{v}$ (Figure 3.4d), this change is even more apparent. These latter two cases clearly show the benefit of using the Lagrange multiplier method to determine how particles should (optimally) move.

3.7 Conclusion and outlook

In this chapter a revised and generalized version of the mechanical contraction method has been presented, used to simulate random dense packings of convex particles. We have presented a mathematically more precise and physically straightforward implementation. In our formulation, the translation and rotation of the particles is determined fully by the outcome of a Lagrange optimization and the choice of a time-step. Using the revised MCM, results are obtained for spherocylinder particles that match the behaviour of earlier simulations very well, and even show a slight improvement in the attainable mean contact numbers for higher aspect ratios. Close examation and comparison with results from other simulations are still required.

We have shown previously (Chapter 2) that by using a virtual particle method, the implementation of a hard boundary is possible which enables us to investigate the influence of a wall on random particle structure. Together with the generalization that allows many more different convex particles to be simulated, and that places no restriction on the polydispersity of the particles, the versatility of the MCM is greatly enhanced. For example, the MCM could be used to verify theoretical predictions for random packings of bi-, tri- and polydisperse spheres [54–56]. In Chapter 4, the superquadric shape is introduced as a versatile new particle shape for simulation with the revised MCM.

Acknowledgements

Álvaro González García is thanked for many fruitful discussions.

References

1. D. Hirshfeld, D. C. Rapaport, 'Granular flow from a silo: Discrete-particle simulations in three dimensions', *The European Physical Journal E* **2001**, *4*, 193–199, DOI 10.1007/s101890170128.
2. J. V. Milewski, 'The Combined Packing of Rods and Spheres in Reinforcing Plastics', *Industrial & Engineering Chemistry Product Research and Development* **1978**, *17*, 363–366, DOI 10.1021/i360068a016.
3. A. van Blaaderen, P. Wiltzius, 'Real-Space Structure of Colloidal Hard-Sphere Glasses', *Science* **1995**, *270*, 1177–1179, DOI 10.1126/science.270.5239.1177.
4. S. F. Edwards, R. B. S. Oakeshott, 'The transmission of stress in an aggregate', *Physica D: Nonlinear Phenomena* **1989**, *38*, 88–92, DOI 10.1016/0167-2789(89)90176-0.
5. A. P. Philipse, 'The Random Contact Equation and Its Implications for (Colloidal) Rods in Packings, Suspensions, and Anisotropic Powders', *Langmuir* **1996**, *12*, 1127–1133, DOI 10.1021/la950671o, (correction) **1996**, *12*, 5971–5971.
6. S. Torquato, T. M. Truskett, P. G. Debenedetti, 'Is Random Close Packing of Spheres Well Defined?', *Physical Review Letters* **2000**, *84*, 2064, DOI 10.1103/PhysRevLett.84.2064.
7. R. D. Kamien, A. J. Liu, 'Why is Random Close Packing Reproducible?', *Physical Review Letters* **2007**, *99*, 155501, DOI 10.1103/PhysRevLett.99.155501.
8. C. Song, P. Wang, H. A. Makse, 'A phase diagram for jammed matter', *Nature* **2008**, *453*, 629–632, DOI 10.1038/nature06981.

9. M. Clusel, E. I. Corwin, A. O. N. Siemens, J. Brujić, 'A 'granocentric' model for random packing of jammed emulsions', *Nature* **2009**, *460*, 611–615, DOI 10.1038/nature08158.
10. S. Torquato, F. H. Stillinger, 'Jammed hard-particle packings: From Kepler to Bernal and beyond', *Reviews of Modern Physics* **2010**, *82*, 2633, DOI 10.1103/RevModPhys.82.2633.
11. G. Parisi, F. Zamponi, 'Mean-field theory of hard sphere glasses and jamming', *Reviews of Modern Physics* **2010**, *82*, 789, DOI 10.1103/RevModPhys.82.789.
12. A. Baule, R. Mari, L. Bo, L. Portal, H. A. Makse, 'Mean-field theory of random close packings of axisymmetric particles', *Nature Communications* **2013**, *4*, 2194, DOI 10.1038/ncomms3194.
13. J. D. Bernal, J. Mason, 'Packing of Spheres: Coordination of Randomly Packed Spheres', *Nature* **1960**, *188*, 910–911, DOI 10.1038/188910a0.
14. G. T. Nolan, P. E. Kavanagh, 'Computer simulation of random packing of hard spheres', *Powder Technology* **1992**, *72*, 149–155, DOI 10.1016/0032-5910(92)88021-9.
15. X. Jia, R. A. Williams, 'A packing algorithm for particles of arbitrary shapes', *Powder Technology* **2001**, *120*, 175–186, DOI 10.1016/S0032-5910(01)00268-6.
16. C. S. O'Hern, S. A. Langer, A. J. Liu, S. R. Nagel, 'Random Packings of Frictionless Particles', *Physical Review Letters* **2002**, *88*, 075507, DOI 10.1103/PhysRevLett.88.075507.
17. C. S. O'Hern, L. E. Silbert, A. J. Liu, S. R. Nagel, 'Jamming at zero temperature and zero applied stress: The epitome of disorder', *Physical Review E* **2003**, *68*, 011306, DOI 10.1103/PhysRevE.68.011306.
18. S. R. Williams, A. P. Philipse, 'Random packings of spheres and spherocylinders simulated by mechanical contraction', *Physical Review E* **2003**, *67*, 051301, DOI 10.1103/PhysRevE.67.051301.
19. A. Donev, I. Cisse, D. Sachs, E. A. Variano, F. H. Stillinger, R. Connelly, S. Torquato, P. M. Chaikin, 'Improving the Density of Jammed Disordered Packings Using Ellipsoids', *Science* **2004**, *303*, 990–993, DOI 10.1126/science.1093010.
20. T. Aste, M. Saadatfar, T. J. Senden, 'Geometrical structure of disordered sphere packings', *Physical Review E* **2005**, *71*, 061302, DOI 10.1103/PhysRevE.71.061302.
21. A. Wouterse, S. R. Williams, A. P. Philipse, 'Effect of particle shape on the density and microstructure of random packings', *Journal of Physics: Condensed Matter* **2007**, *19*, 406215, DOI 10.1088/0953-8984/19/40/406215.
22. M. van Hecke, 'Jamming of soft particles: geometry, mechanics, scaling and isostaticity', *Journal of Physics: Condensed Matter* **2010**, *22*, 033101, DOI 10.1088/0953-8984/22/3/033101.
23. B. D. Lubachevsky, F. H. Stillinger, 'Geometric Properties of Random Disk Packings', *Journal of Statistical Physics* **1990**, *60*, 561–583, DOI 10.1007/BF01025983.
24. A. Donev, F. H. Stillinger, P. M. Chaikin, S. Torquato, 'Unusually Dense Crystal Packings of Ellipsoids', *Physical Review Letters* **2004**, *92*, 255506, DOI 10.1103/PhysRevLett.92.255506.
25. A. Donev, S. Torquato, F. H. Stillinger, 'Neighbor list collision-driven molecular dynamics simulation for nonspherical hard particles. I. Algorithmic details', *Journal of Computational Physics* **2005**, *202*, 737–764, DOI 10.1016/j.jcp.2004.08.014.
26. Y. Jiao, F. H. Stillinger, S. Torquato, 'Distinctive features arising in maximally random jammed packings of superballs', *Physical Review E* **2010**, *81*, 041304, DOI 10.1103/PhysRevE.81.041304.
27. K. de Lange Kristiansen, A. Wouterse, A. Philipse, 'Simulation of random packing of binary sphere mixtures by mechanical contraction', *Physica A: Statistical Mechanics and its Applications* **2005**, *358*, 249–262, DOI 10.1016/j.physa.2005.03.057.
28. A. Wouterse, S. Luding, A. P. Philipse, 'On contact numbers in random rod packings', *Granular Matter* **2009**, *11*, 169–177, DOI 10.1007/s10035-009-0126-6.
29. A. V. Kyrylyuk, A. Wouterse, A. P. Philipse, 'Random Packings of Rod-Sphere Mixtures Simulated by Mechanical Contraction', **2009**, *1145*, 211–214, DOI 10.1063/1.3179895.
30. A. V. Kyrylyuk, A. Wouterse, A. P. Philipse, 'Percolation and Jamming in Random Heterogeneous Materials with Competing Length Scales' in *Trends in Colloid and Interface Science XXIII*, (Ed.: S. Bucak), Springer-Verlag Berlin Heidelberg, **2010**, pp. 29–33, DOI 10.1007/978-3-642-13461-6.
31. A. V. Kyrylyuk, A. P. Philipse, 'Effect of particle shape on the random packing density of amorphous solids', *physica status solidi (a)* **2011**, *208*, 2299–2302, DOI 10.1002/pssa.201000361.
32. A. V. Kyrylyuk, M. A. van der Haar, L. Rossi, A. Wouterse, A. P. Philipse, 'Isochoric ideality in jammed random packings of non-spherical granular matter', *Soft Matter* **2011**, *7*, 1671–1674, DOI 10.1039/C0SM00754D.

33. S. Sacanna, L. Rossi, A. Wouterse, A. P. Philipse, 'Observation of a shape-dependent density maximum in random packings and glasses of colloidal silica ellipsoids', *Journal of Physics: Condensed Matter* **2007**, *19*, 376108, DOI 10.1088/0953-8984/19/37/376108.
34. D. J. Evans, 'On the representatation of orientation space', *Molecular Physics* **1977**, *34*, 317–325, DOI 10.1080/00268977700101751.
35. J. Blouwolff, S. Fraden, 'The coordination number of granular cylinders', *EPL (Europhysics Letters)* **2006**, *76*, 1095, DOI 10.1209/epl/i2006-10376-1.
36. P. M. Chaikin, A. Donev, W. Man, F. H. Stillinger, S. Torquato, 'Some Observations on the Random Packing of Hard Ellipsoids', *Industrial & Engineering Chemistry Research* **2006**, *45*, 6960–6965, DOI 10.1021/ie060032g.
37. R. Eppenga, D. Frenkel, 'Monte Carlo study of the sotropic and nematic phases of infinitely thin hard platelets', *Molecular Physics* **1984**, *52*, 1303–1334, DOI 10.1080/00268978400101951.
38. B. S. John, C. Juhlin, F. A. Escobedo, 'Phase behavior of colloidal hard perfect tetragonal parallelepipeds', *The Journal of Chemical Physics* **2008**, *128*, 044909, DOI 10.1063/1.2819091.
39. P. J. Steinhardt, D. R. Nelson, M. Ronchetti, 'Bond-orientational order in liquids and glasses', *Physical Review B* **1983**, *28*, 784–805, DOI 10.1103/PhysRevB.28.784.
40. F. M. Schaller, S. C. Kapfer, M. E. Evans, M. J. F. Hoffmann, T. Aste, M. Saadatfar, K. Mecke, G. W. Delaney, G. E. Schröder-Turk, 'Set Voronoi diagrams of 3D assemblies of aspherical particles', *Philosophical Magazine* **2013**, *93*, 1–25, DOI 10.1080/14786435.2013.834389.
41. G. E. Schröder-Turk, W. Mickel, S. C. Kapfer, F. M. Schaller, B. Breidenbach, D. Hug, K. Mecke, 'Minkowski tensors of anisotropic spatial structure', *New Journal of Physics* **2013**, *15*, 083028, DOI 10.1088/1367-2630/15/8/083028.
42. L. Verlet, 'Computer "Experiments" on Classical Fluids. I. Thermodynamical Properties of Lennard-Jones Molecules', *Physical Review* **1967**, *159*, 98–103, DOI 10.1103/PhysRev.159.98.
43. C. Wellmann, C. Lillie, P. Wriggers, 'A contact detection algorithm for superellipsoids based on the common-normal concept', *Engineering Computations* **2008**, *25*, 432–442, DOI 10.1108/02644400810881374.
44. C. Vega, S. Lago, 'A fast algorithm to evaluate the shortest distance between rods', *Computers & Chemistry* **1994**, *18*, 55–59, DOI 10.1016/0097-8485(94)80023-5.
45. C. R. A. Abreu, F. W. Tavares, M. Castier, 'Influence of particle shape on the packing and on the segregation of spherocylinders via Monte Carlo simulations', *Powder Technology* **2003**, *134*, 167–180, DOI 10.1016/S0032-5910(03)00151-7.
46. J. W. Perram, M. S. Wertheim, 'Statistical mechanics of hard ellipsoids. I. Overlap algorithm and the contact function', *Journal of Computational Physics* **1985**, *58*, 409–416, DOI 10.1016/0021-9991(85)90171-8.
47. X. Lin, T.-T. Ng, 'Contact detection algorithms for three-dimensional ellipsoids in discrete element modelling', *International Journal for Numerical and Analytical Methods in Geomechanics* **1995**, *19*, 653–659, DOI 10.1002/nag.1610190905.
48. W. X. Xu, H. S. Chen, Z. Lv, 'An overlapping detection algorithm for random sequential packing of elliptical particles', *Physica A: Statistical Mechanics and its Applications* **2011**, *390*, 2452–2467, DOI 10.1016/j.physa.2011.02.048.
49. J. R. Williams, R. O'Connor, 'Discrete element simulation and the contact problem', *Archives of Computational Methods in Engineering* **1999**, *6*, 279–304, DOI 10.1007/BF02818917.
50. J. Vieillard-Baron, 'Phase Transitions of the Classical Hard-Ellipse System', *The Journal of Chemical Physics* **1972**, *56*, 4729–4744, DOI 10.1063/1.1676946.
51. O. Rodrigues, 'Des lois géométriques qui régissent les déplacements d'un système solide dans l'espace, et de la variation des coordonnées provenant de ces déplacements considérés indépendamment des causes qui peuvent les produire', *Journal de mathématiques pures et appliquées* **1840**, *5*, 380–440.
52. M. Bargieł, 'Geometrical Properties of Simulated Packings of Spherocylinders' in *Computational Science–ICCS 2008*, (Eds.: M. Bubak, G. D. van Albada, J. Dongarra, P. M. A. Sloot), Springer-Verlag Berlin Heidelberg, **2008**, pp. 126–135.
53. J. Zhao, S. Li, R. Zou, A. Yu, 'Dense random packings of spherocylinders', *Soft Matter* **2012**, *8*, 1003–1009, DOI 10.1039/C1SM06487H.
54. H. J. H. Brouwers, 'Random packing fraction of bimodal spheres: An analytical expression', *Physical Review E* **2013**, *87*, 032202, DOI 10.1103/PhysRevE.87.032202.

55. H. J. H. Brouwers, 'Packing fraction of trimodal spheres with small size ratio: An analytical expression', *Physical Review E* **2013**, *88*, 032204, DOI 10.1103/PhysRevE.88.032204.
56. H. J. H. Brouwers, 'Packing fraction of particles with lognormal size distribution', *Physical Review E* **2014**, *89*, 052211, DOI 10.1103/PhysRevE.89.052211.

4

Packing of superquadric particles

Abstract

A method is developed to study the random packing properties of superquadric (SQ) particles. The SQ-shape is introduced, and a contact detection algorithm is described. Spheres, ellipsoids, superballs, and close analogues of disks, spherocylinders and cubes are some of the many shapes that can be described by SQs, making it a very versatile shape for packing simulations. The SQ-shape is implemented in a revised version of the mechanical contraction method (MCM) and preliminary results are obtained for the random packing properties of superballs of varying sharpness. The contact detection algorithm used can be applied to many other shapes, making the combination with the MCM a valuable tool to study the random packing behaviour of so-far unexplored particle shapes.

4.1 Introduction

The packing behaviour of spherical and non-spherical particles has attracted much attention in recent years. Numerous theoretical [1–3], simulation [4–6] and experimental [7–10] papers have been dedicated to describe and explain both the random and crystalline packing behaviour of various particle shapes. Of particular note for our purposes is the mechanical contraction method (MCM), originally developed to generate random dense packings of spheres and spherocylinders [4]. In Chapter 2 and Chapter 3 we expand the applicability of the MCM by generalizing the method to particles of arbitrary convex shape and by including hard simulation boundaries.

From a simulation perspective, it is relatively easy to prepare packings of particles with quite exotic shapes, see for example De Graaf *et al.* [11]. It is, however, not difficult to appreciate the benefit of having a single mathematical description that allows for the simulation of a great variety of particle shapes. One of such descriptions is the *superquadric* shape, first introduced by Barr [12], that allows a smooth transition from spheres to ellipsoids and cuboids, and several other shapes. Due to their versatility, super-shapes have been applied in shape recovery in medical imaging [13–15], and robotics and computer vision [16–19]. Lately there also has been attention for super-shapes from a chemical and physical perspective. The structure of ordered and disordered packings of superellipsoids have been studied [20], and densest packings of superballs have been found [21–24]. Superballs have been studied in greater detail because they have an experimental analogue in the form of silica cubes with rounded edges [25–27].

In this chapter we provide a method to simulate superquadric particles (which are more general than previously studied superellipsoids and superballs) and use it in combination with the MCM to provide some preliminary results for the random dense packings of superballs. We describe an iterative numerical procedure to calculate the minimal distance between superquadrics, or their overlap distance [28], and provide an additional fast method to approximate this distance. These calculations are required for the MCM, but are also of great importance when precise distance information is required, e.g. in robotics.

The following sections will first introduce the superquadric shape and some of its properties, and continue with a description of the numerical algorithm. The algorithm is integrated into the mechanical contraction method and results from a first exploration of the random packing density and structure of superballs are presented and discussed.

4.2 Definitions

Quadric surfaces in Euclidean space describe shapes such as ellipsoids, paraboloids, hyperboloids, cones and cylinders. They are characterized by equations containing quadratic exponents, for example for a general ellipsoid,

$$F(\mathbf{x}) = \left(\frac{x}{a_1}\right)^2 + \left(\frac{y}{a_2}\right)^2 + \left(\frac{z}{a_3}\right)^2 - 1 = 0 \tag{4.1}$$

where $\mathbf{x} = (x, y, z)$ is a coordinate vector and $a_i > 0$ are scaling factors that determine the lengths of the principal axes. The term *superquadric* (SQ) was coined by Barr

[12] to describe super-equivalents of ellipsoids, hyperboloids and toroids, by allowing arbitrary exponents. As an example, the implicit expression for a *superellipsoid* (or superquadric ellipsoid, SE, using Barr's terminology) is given by,

$$F(\mathbf{x}) = \left(\left| \frac{x}{a_1} \right|^{\gamma_1} + \left| \frac{y}{a_2} \right|^{\gamma_1} \right)^{\gamma_2/\gamma_1} + \left| \frac{z}{a_3} \right|^{\gamma_2} - 1 = 0 \tag{4.2}$$

where γ_i determines the squareness of the surface. Strictly convex surfaces are obtained for $\gamma_i \in [2, \infty)$, which deform the shape from a sphere (ellipsoid) to a cube (cuboid). An unfortunate, but persisting complication in terminology arose when Equation 4.2 started to be simply referred to as the equation for a 'superquadric' (notably in the well-cited paper of Solina and Bajcsy [29]). To avoid further confusion, we will strictly refer to Equation 4.2 as the equation for a *superellipsoid*. While not present in Barr's original paper, we adhere to the following, general definition of a *superquadric* surface [30, 31][1],

$$F(\mathbf{x}) = \left| \frac{x}{a_1} \right|^{\gamma_1} + \left| \frac{y}{a_2} \right|^{\gamma_2} + \left| \frac{z}{a_3} \right|^{\gamma_3} - 1 = 0 \tag{4.3}$$

or equivalently, and computationally more convenient,

$$F(\mathbf{x}) = a_1^{-\gamma_1} \left(x^2 \right)^{\frac{\gamma_1}{2}} + a_2^{-\gamma_2} \left(y^2 \right)^{\frac{\gamma_2}{2}} + a_3^{-\gamma_3} \left(z^2 \right)^{\frac{\gamma_3}{2}} - 1 = 0 \tag{4.4}$$

The parametric representation of Equation 4.3 is,

$$\mathbf{x}(u, v) = \begin{bmatrix} a_1 \operatorname{sgn}(\cos v) \, |\cos v|^{\epsilon_1} \operatorname{sgn}(\cos u) \, |\cos u|^{\epsilon_1} \\ a_2 \operatorname{sgn}(\cos v) \, |\cos v|^{\epsilon_2} \operatorname{sgn}(\sin u) \, |\sin u|^{\epsilon_2} \\ a_3 \operatorname{sgn}(\sin v) \, |\sin v|^{\epsilon_3} \end{bmatrix}, \quad \begin{matrix} -\pi \le u < \pi \\ -\pi/2 \le v < \pi/2 \end{matrix} \tag{4.5}$$

where $\epsilon_i = 2/\gamma_i$, and $\operatorname{sgn}(x)$ gives the sign of its argument. The normals to the surface are found by taking the derivatives of Equation 4.3 with respect to x, y and z,

$$\mathbf{n}(\mathbf{x}) = \begin{bmatrix} a_1^{-\gamma_1} \gamma_1 x \left(x^2 \right)^{\frac{\gamma_1}{2} - 1} \\ a_2^{-\gamma_2} \gamma_2 y \left(y^2 \right)^{\frac{\gamma_2}{2} - 1} \\ a_3^{-\gamma_3} \gamma_3 z \left(z^2 \right)^{\frac{\gamma_3}{2} - 1} \end{bmatrix} \tag{4.6}$$

In addition to superquadrics and superellipsoids, we also define *superballs* ($a_1 = a_2 = a_3, \gamma_1 = \gamma_2 = \gamma_3$) and *supercuboids* ($a_1 \neq a_2 \neq a_3, \gamma_1 = \gamma_2 = \gamma_3$). Figure 4.1 gives an overview of some shapes obtainable with Equation 4.3. As superquadrics have not been intensively studied in the context of particle simulations, we derive some useful properties in Section 4.A, such as its volume and moments of inertia.

[1] Note that the set of superellipsoid shapes from Equation 4.2 and the set of superquadric shapes from Equation 4.3 do not contain each other, i.e. many superellipsoid shapes can not be represented by the superquadric expression and *vice versa*. The sets only intersect when $\gamma_1 = \gamma_2 = \gamma_3$.

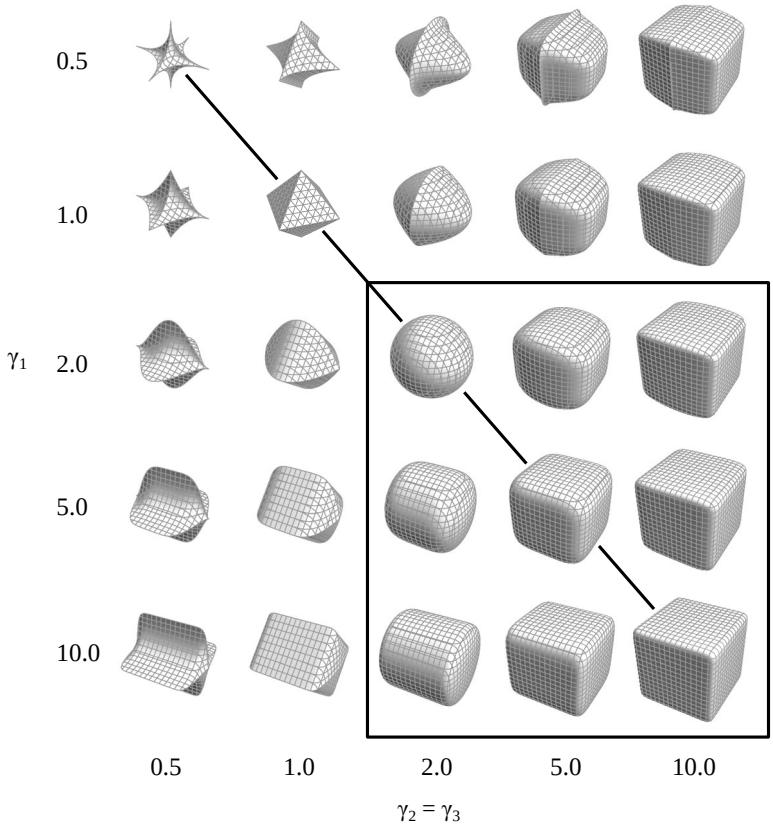

Figure 4.1. An overview of some of the shapes that can be obtained with the superquadric shape (Equation 4.3) using $a_1 = a_2 = a_3 = 1$. The shapes in the marked rectangle are strictly convex, and are the type of shape under consideration in this chapter. The shapes along the diagonal line are part of the superball shape family ($\gamma_1 = \gamma_2 = \gamma_3$). For $\gamma_{1,2,3} \to \infty$ a cube is obtained.

4.3 Mechanical Contraction Method

The MCM is a method to generate dense random packings of particles with various shapes, originally developed for spheres and spherocylinders [4]. In short, the algorithm gradually compresses a dilute and random starting configuration of particles, until compression is no longer possible. Any particle overlap that occurs after a compression of the box and rescaling of the particle positions, is removed according to a specific overlap removal procedure. For a detailed description of the MCM algorithm and its revision and generalization, see Chapter 2 and Chapter 3. Using the revised MCM, it is relatively easy to incorporate superquadrics as an additional particle shape. The main requirement is the calculation of the vector $\mathbf{k}_{ij}$, quantifying the amount of overlap between two particles, as this requires specific treatment for each particle shape. The next section describes an approach suitable for superquadrics.

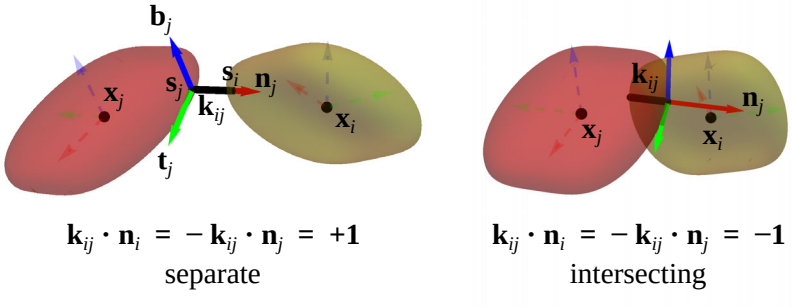

Figure 4.2. The final result for the contact detection algorithm for two arbitrary superquadrics, for (*left*) a situation where the particles are separated, and (*right*) a situation with particle overlap. The particle's centres of mass $\mathbf{x}_{i,j}$ are indicated together with their local coordinate system. The dashed red, green and blue arrows correspond to the local x, y and z axes, respectively. The normal $\mathbf{n}$ (red), tangent $\mathbf{t}$ (green), and binormal $\mathbf{b}$ (blue) vectors for particle j are indicated by the solid arrows (see text).

4.4 Contact detection for superquadrics

Contact detection for superquadric shapes has been investigated by several authors [28, 32, 33], all using numerical (un)constrained optimization to solve their respective minimization problems. Different algorithms are used, such as the interior point method [32], sequential quadratic programming [32] or a Levenberg-Marquardt scheme [33]. Lopes *et al.* [28] employ a direct calculation using analytic Jacobians in conjunction with a simple Newton-Raphson iteration procedure, leading to a rapid convergence. Furthermore, their method is general, in the sense that it can be easily extended to other strictly convex shapes that have an implicit definition and are at least twice continuously differentiable. Similar to e.g. Wellman *et al.* [33], the common-normal principle is used, which constrains the connecting vector between two particles to be collinear with the surface normals. We choose to implement the method from Lopes *et al.* [28], and proceed by giving an overview of the algorithm.

4.4.1 Algorithmic details

Consider a pair of (not necessarily identical) superquadric particles i and j, described by Equation 4.3. Each particle has a position $\mathbf{x}_i$ and an associated orientation matrix $\mathbf{R}_i$. The distance vector between any two points $\mathbf{s}_i$ and $\mathbf{s}_j$ on the respective particle's surfaces, is given by (see also Figure 4.2),

$$\mathbf{k}_{ij} = (\mathbf{x}_j + \mathbf{R}_j\mathbf{s}_j) - (\mathbf{x}_i + \mathbf{R}_i\mathbf{s}_i) \tag{4.7}$$

where the surface points $\mathbf{s}_{i,j}$ are given in local coordinates. The minimal distance between the two particles is found by minimizing $\|\mathbf{k}\|$. The common-normal principle constrains the distance minimization by requiring the surface normals $\mathbf{n}_{i,j}$ at the surface

points to be collinear with $\mathbf{k}$. This can be formulated in terms of two cross products,

$$\begin{aligned} \mathbf{k}_{ij} \times \mathbf{n}_j &= \mathbf{0} \\ \mathbf{n}_i \times \mathbf{n}_j &= \mathbf{0} \end{aligned} \tag{4.8}$$

It is computationally more convenient to express these constraints in terms of four dot products, making use of two additional vectors orthogonal to $\mathbf{n}$: the tangent vector $\mathbf{t}$ and the binormal vector $\mathbf{b}$ (see Figure 4.2). Equivalently, the constraints now become,

$$\begin{aligned} \mathbf{k}_{ij} \cdot \mathbf{t}_j &= 0 & \mathbf{n}_i \cdot \mathbf{t}_j &= 0 \\ \mathbf{k}_{ij} \cdot \mathbf{b}_j &= 0 & \mathbf{n}_i \cdot \mathbf{b}_j &= 0 \end{aligned} \tag{4.9}$$

Other combinations of vectors may be chosen equivalently, as long as they form a linearly independent set. The final two constraints restrict the contact points to lie on the surface,

$$\begin{aligned} F_i(\mathbf{s}_i) &= 0 \\ F_j(\mathbf{s}_j) &= 0 \end{aligned} \tag{4.10}$$

The constraints form a system of six non-linear equations that must be solved to find the minimal distance,

$$\mathbf{\Phi}(\mathbf{q}) = \mathbf{0} \qquad \Rightarrow \qquad \begin{bmatrix} \mathbf{n}_i \cdot \mathbf{t}_j \\ \mathbf{n}_i \cdot \mathbf{b}_j \\ \mathbf{k}_{ij} \cdot \mathbf{t}_j \\ \mathbf{k}_{ij} \cdot \mathbf{b}_j \\ F_i \\ F_j \end{bmatrix} = \begin{bmatrix} 0 \\ 0 \\ 0 \\ 0 \\ 0 \\ 0 \end{bmatrix} \tag{4.11}$$

here $\mathbf{\Phi}$ contains the six constraints and $\mathbf{q}$ is a 6×1 vector that contains the local coordinates $\mathbf{s}_i$ and $\mathbf{s}_j$. This system can be solved iteratively by means of a Newton-Raphson approach [34]. Since all equations are continuously differentiable, an analytical Jacobian (6×6 matrix) can be constructed and the optimization procedure can be written as,

$$\mathbf{q}_{n+1} = \mathbf{q}_n - \left(\frac{\partial \mathbf{\Phi}(\mathbf{q}_n)}{\partial \mathbf{q}_n} \right)^{-1} \mathbf{\Phi}(\mathbf{q}_n) \tag{4.12}$$

where n is an iteration index. The iterations continue until $\|\mathbf{q}_{n+1} - \mathbf{q}_n\| < \delta_{\text{tol}}$, where δ_{tol} is a small tolerance value, typically 10^{-6}. If a maximum number of iterations has been reached ($n_{\max} \approx 50$), a non-convergence is assumed. This occurs occasionally, and is usually due to an improper choice of the starting values of $\mathbf{s}_{i,j}$, which will be discussed in the next section. Whenever a non-convergence of the algorithm is found, the MCM will assume particles are not in contact.

Calculating the inverse of the Jacobian matrix in Equation 4.12 can be done computationally efficient using a QR-decomposition [35]. The Jacobian is explicitly

given by,

$$\frac{\partial \mathbf{\Phi}(\mathbf{q})}{\partial \mathbf{q}} = \begin{bmatrix} \mathbf{t}_j \frac{\partial}{\partial \mathbf{q}} \mathbf{n}_i + \mathbf{n}_i \frac{\partial}{\partial \mathbf{q}} \mathbf{t}_j \\ \mathbf{b}_j \frac{\partial}{\partial \mathbf{q}} \mathbf{n}_i + \mathbf{n}_i \frac{\partial}{\partial \mathbf{q}} \mathbf{b}_j \\ \mathbf{t}_j \frac{\partial}{\partial \mathbf{q}} \mathbf{k}_{ij} + \mathbf{k}_{ij} \frac{\partial}{\partial \mathbf{q}} \mathbf{t}_j \\ \mathbf{b}_j \frac{\partial}{\partial \mathbf{q}} \mathbf{k}_{ij} + \mathbf{k}_{ij} \frac{\partial}{\partial \mathbf{q}} \mathbf{b}_j \\ \frac{\partial}{\partial \mathbf{q}} F_i(\mathbf{s}_i) \\ \frac{\partial}{\partial \mathbf{q}} F_j(\mathbf{s}_j) \end{bmatrix} \tag{4.13}$$

where each partial derivative is a 3×6 matrix. Expressions for $\mathbf{t}$ and $\mathbf{b}$ can be obtained by applying a Householder transformation [36] to the vector along an axis $\mathbf{h}$, collinear to the normal vector $\mathbf{n}$. The symmetric and orthogonal transformation matrix $\mathbf{H}$ is given by,

$$\mathbf{H} = \mathbf{I} - 2\frac{\mathbf{h} \otimes \mathbf{h}}{\mathbf{h} \cdot \mathbf{h}} = \begin{bmatrix} 1 - 2\frac{h_x^2}{h^2} & -2\frac{h_x h_y}{h^2} & -2\frac{h_x h_z}{h^2} \\ -2\frac{h_y h_x}{h^2} & 1 - 2\frac{h_y^2}{h^2} & -2\frac{h_y h_z}{h^2} \\ -2\frac{h_z h_x}{h^2} & -2\frac{h_z h_y}{h^2} & 1 - 2\frac{h_z^2}{h^2} \end{bmatrix} \tag{4.14}$$

where $\mathbf{I}$ is the identity matrix, $\otimes$ is the tensor product and where we define,

$$\mathbf{h} \equiv \mathbf{h}(\mathbf{n}) = (h_x, h_y, h_z) = (n_x + \|\mathbf{n}\|, n_y, n_z) \tag{4.15}$$

The second and third column in Equation 4.14 are assigned to $\mathbf{t}$ and $\mathbf{b}$, respectively. Explicit expressions for the parameters in the previous formulas are provided in Section 4.B for convenience.

To evaluate Equation 4.12 and quickly converge to a solution, an appropriate choice of starting points $\mathbf{s}_{i,j}$ has to be made. A simple method may be to choose points along the line connecting the particle's centres of mass. This method works reasonably well for nearly spherical particles, but fails for more elongated or very sharp particles, as these starting points become increasingly unlikely to be close to the actual points of minimal distance. The next section provides a method to find starting points that already lie close to the final solution.

To check if a proper solution has been found, $\mathbf{k}_{ij} \times \mathbf{n}_i \approx \mathbf{0}$ must hold at the end of the simulation for $\mathbf{s}_{i,j,\text{optimal}}$. If not, the solution is discarded and particles are assumed not to be in contact. The sign of $\mathbf{k}_{ij} \cdot \mathbf{n}_i$ determines if the particles overlap (≤ 0) or not (> 0). Figure 4.2 shows two final situations for the algorithm: an overlapping case and a non-overlapping case.

4.4.2 Approximate contact detection

The algorithm for contact detection described in the previous section, is computationally much more expensive than contact detection for e.g. spheres or spherocylinders. During an MCM compression step, all neighbouring particles of a central particle are checked for overlap, which can become a very time-consuming operation if the full Newton-

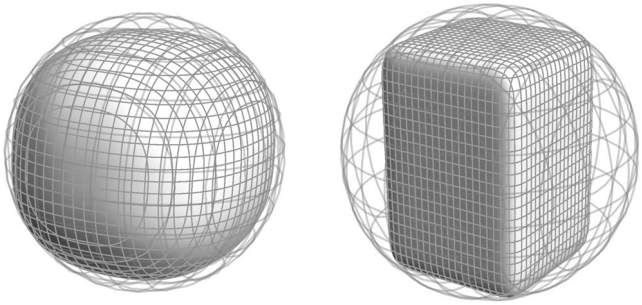

$a_1 = a_3 = 1.1, a_2 = 1.0$
$\gamma_1 = \gamma_2 = \gamma_3 = 0.8$

$a_1 = a_3 = 1.0, a_2 = 1.5$
$\gamma_1 = \gamma_2 = \gamma_3 = 0.2$

Figure 4.3. Two different supercuboids with their analytically calculated bounding spheres. For the elongated and sharper supercuboid (*right*), more void space is available, so that non-overlapping situations get detected less often.

Raphson method has to be invoked each time. This issue is even more prominent when the Verlet-like neighbour list has to be rebuilt. Two methods are implemented in the SQ contact detection algorithm to quickly estimate whether or not particles are strictly separated: a bounding sphere approximation and a point-sampling of the superquadric surface. When the separation criterion is not fulfilled, the full iterative minimization is used. The method of point-sampling of the superquadric additionally provides a good initial estimate for the Newton-Raphson solver.

Bounding sphere By constructing of bounding spheres around two superquadrics, a simple sphere-sphere contact check can be used to determine whether or not the particles are strictly separated. The radius of the minimal bounding sphere has to be determined only once during the entire simulation, and can be determined analytically for supercuboids and superballs. For a general superquadric no analytical expression is possible, and a numerical optimization scheme has to be employed; see Section 4.C for more detail.

Point-sampled surface The bounding sphere approach works well for nearly spherical particles, but for elongated or acute particles the separation criterion increasingly underestimates the actual probability of an overlapping pair (see Figure 4.3). This results in too many situations where the (slow) Newton-Raphson solver is used, when there is clearly no overlap present. Therefore, another approximation is needed, that is still comparatively fast. To this end, we 'discretize' a superquadric by sampling a number of points on its surface in a near-uniform fashion, based on the method in [37]. The sampled coordinates ($\mathbf{r}_n, n = 1, 2, \ldots N$) are stored in a binary search structure, known as a k-d tree [38]. The purpose of this tree is to allow the fast finding of the coordinate nearest to a given other coordinate, e.g. finding the approximate nearest point on the discretized superquadric to another point in space. This procedure has strong analogies to the tessellation of a geometric object into edges and vertices.

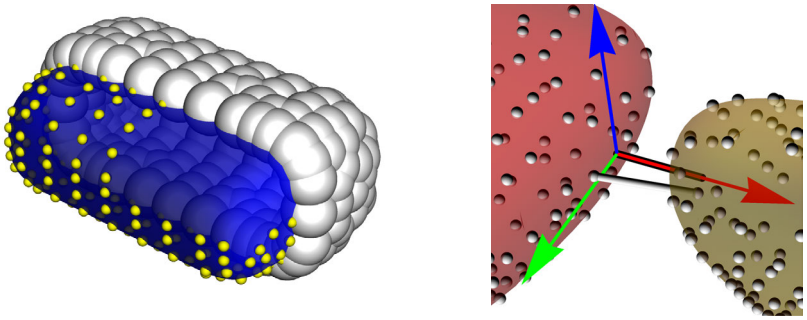

Figure 4.4. (*left*) A discretized superquadric. The blue shape is a contour plot of the full superquadric. The yellow dots are the sampled points on the surface. The white spheres are centred on the yellow dots and are shown here to indicate that the surface coverage is complete, within the accuracy of the sampling distance. A portion of the white spheres and yellow dots is removed to give a cut-out view. (*right*) A close-up view of the minimal distance vector (black) and initial estimate (white). The initial estimate connects two of the sampled surface points, and lies close to the final solution.

The discretization of the superquadric shape has advantages in several steps of the contact detection procedure,

1. To find an approximate closest distance between two superquadrics, a loop is made over all N sampled points of particle j, expressed in the local coordinate system of particle i. For each point of particle j the nearest coordinate is looked up in the tree and the indices of the coordinates with a minimal distance are stored. If this distance is larger than the sampling distance, the particles are assumed not to be in contact. This procedure is useful, for example, in the fast construction of a Verlet-type neighbour list.

2. To test if particles overlap, again, the sampled points of particle j (or i) are expressed in the local coordinate system of particle i (or j). If any $F(\mathbf{r}) < 0.0$ (Equation 4.3) the two particles definitely overlap. The pair of coordinates for which this holds, and for which the product $(\mathbf{n}_{\mathbf{r}_i} \cdot \mathbf{n}_{\mathbf{r}_j})(\mathbf{n}_{\mathbf{r}_i} \cdot \Delta\mathbf{r})(\mathbf{n}_{\mathbf{r}_j} \cdot \Delta\mathbf{r})$ is largest, is used as the starting point for the Newton-Raphson procedure. This product is an approximate (and arbitrary) criterion to choose the point-pair that corresponds most to the common-normal principle.

3. If no overlaps are found by the above procedure, an overlapping situation is not ruled out completely, because the overlap distance may be smaller than the sampling distance. In that case, the first method is applied and the corresponding surface points are used as starting point for the Newton-Raphson procedure to accurately find if there is overlap or not.

By combining the bounding sphere approximation with the point-sampling of the surface, the computational time to perform contact detection is greatly reduced, and non-converging solutions become very rare.

4.5 Results and discussion

The contact detection algorithm for superquadrics is implemented in the MCM and is tested for the superball shape (superquadrics with equal γ_i and equal a_i). Dense random packings of $N = 750$ superballs are generated, and the shape parameter γ is varied from 2.0 (spheres) to 4.0 (rounded cubes). Other simulation parameters are taken similar to those mentioned in Chapter 3.

To characterize the packing, the packing fraction ϕ and mean contact number $\langle C \rangle$ are calculated. See Section 3.3 in Chapter 3 for more details. To quantify the orientational ordering of the packings along a certain direction j, the nematic order parameter is calculated as described by Batten *et al.* [23],

$$S_{2,j} = \max_{\mathbf{n}_j} \frac{1}{N} \sum_i \left(\tfrac{3}{2} \left| \mathbf{u}_{ij} \cdot \mathbf{n}_j \right|^2 - \tfrac{1}{2} \right) \tag{4.16}$$

where N is the number of particles, $\mathbf{u}_{ij}$ are the particle axes and $\mathbf{n}_j$ is the director for a direction j. This equation can be solved as an eigenvalue problem. Full nematic ordering has $S_2 = 1$ and the absence nematic ordering has $S_2 = 0$. Additionally, a cubatic order parameter is calculated to quantify the ordering in three orthogonal directions. Again following Batten *et al.* [23],

$$S_4 = \max_{\mathbf{n}} \frac{1}{14N} \sum_{i,j} \left(35 \left| \mathbf{u}_{ij} \cdot \mathbf{n} \right|^4 - 30 \left| \mathbf{u}_{ij} \cdot \mathbf{n} \right|^2 + 3 \right) \tag{4.17}$$

where $\mathbf{n}$ is the unit director for which the order parameter is maximized. This maximum is found by trying a large number of random trail vectors for $\mathbf{n}$. Perfect cubatic ordering gives $S_4 = 1$ and the absence of any long-range cubatic ordering gives $S_4 = 0$.

The main results from the simulations are shown in Figure 4.5, and graphical representations of the final packings and contact number distributions are given in Figure 4.6 for a selection of data points.

It can be seen that in the case of spheres ($\gamma = 2$) the packing fractions obtained here are slightly too low in comparison with well-established earlier findings (see Chapter 2). We find values of $\phi \approx 0.61$, compared to the expected value of $\phi \approx 0.64$. The packing fraction for increasing values of γ first increases and then decays to lower values, which is the same trend as observed for spherocylinders, spheroids and cut-spheres [4, 9, 39]. Others have also observed a similar trend for superellipsoid packings [20]. The order parameters S_2 and S_4 are low and show no clear trend upon changing γ, indicating the absence of long-range orientational ordering, as expected for random dense packings. The mean contact numbers show a continuous linear decrease, starting from a value of $\langle C \rangle = 5.84$ for spheres, going down to $\langle C \rangle = 2.1$ for $\gamma = 5.0$. The former value is close to the theoretical 'isostatic' value of 6 for spheres, and values found experimentally and in earlier simulations [4, 7, 40]. For higher γ, the decrease in contact number renders our packings highly hypostatic, indicating that it is unlikely that our packings are mechanically stable.

The behaviour of the packing fraction and mean contact numbers can be explained through an excluded volume argument. A small deviation from the spherical shape,

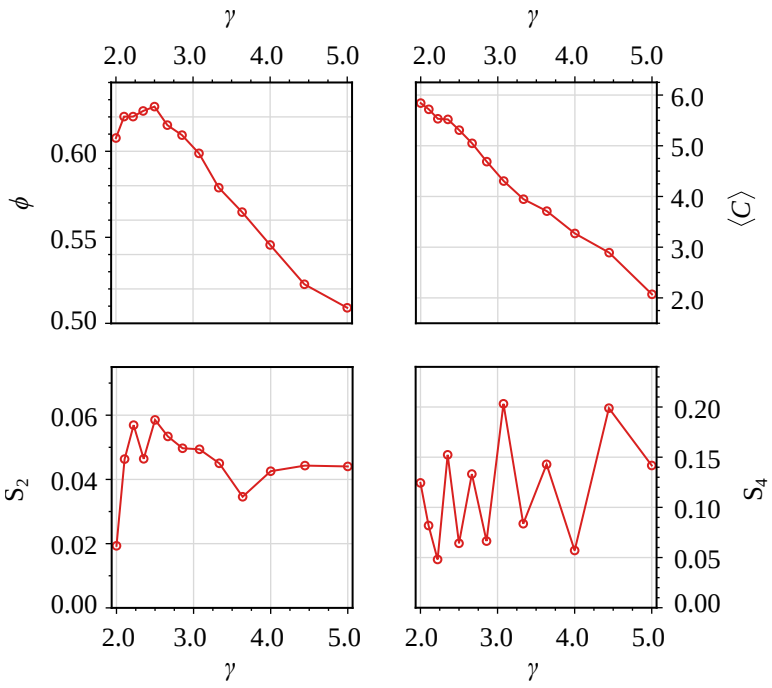

Figure 4.5. The relation between the shape parameter of a superball, γ, and the packing fraction ϕ, mean contact number $\langle C \rangle$, nematic order parameter S_2, and cubatic order parameter S_4 for values ranging from $\gamma = 2.0$ (spheres) to $\gamma = 5.0$ (rounded cuboids). See Figure 4.6 for a graphical representation of the packings.

allows particles to re-orient slightly and fill up more void space, similar to spherocylinders and ellipsoids, increasing the packing fraction. At greater deviations from the spherical shape, and the more cubical the particle gets, the greater its excluded volume becomes. If no face-to-face ordering is induced, this can only result in a packing that becomes less dense. The absence of ordering simultaneously makes the low mean contact numbers plausible: for relatively sharp particles that are randomly oriented, the contacts will primarily be formed with the relatively small 'edges' and 'corners' of the particle, leaving a relatively large volume unoccupied by and inaccessible for other particles.

Our results are in marked contrast with the maximally random jammed (MRJ) packings of superball particles by Jiao *et al.* [22], who find an continuous increase in the packing fraction for increasing γ, up to values of $\phi > 0.75$, and mean contact numbers increasing up to $\langle C \rangle \approx 8.0$. The authors find an parallel increase of the cubatic order parameter, indicating that for more cubic particles, ordering is required to attain final jammed packings. Contasting the packing algorithm used in [22], the MCM does not incorporate a notion of inherent jamming or mechanical stability. This makes our final packings likely to be structurally very different from the MRJ packings, and not necessarily mechanically stable, making further comparisons difficult. Furthermore,

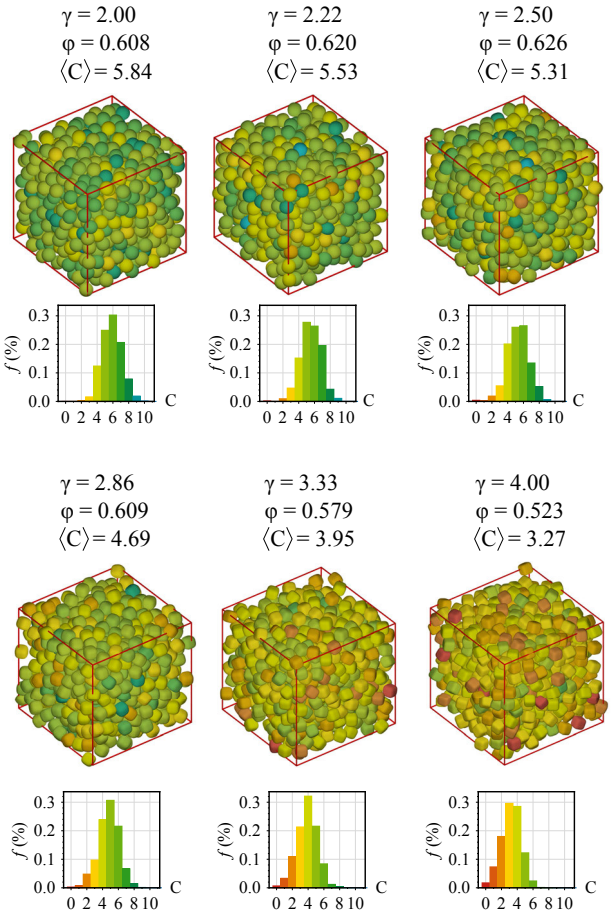

Figure 4.6. A graphical overview of six superball packings for increasing shape parameter γ from spheres to rounded cuboids (see also Figure 4.5). The corresponding packing fraction and mean contact numbers are also indicated, together with a histogram of the contact number distribution. The colours of the particles and in the histograms indicate the number of contacting neighbours.

because of their inherent stability, the packings by Jiao *et al.* are likely to exhibit more similarities to experimental packings than ours.

Finally, note that due to the increased computational cost of the MCM for superquadric particles, some simulation parameters have not been set to their maximal or optimal values. Therefore, an increase in packing fractions and contact numbers is expected for more accurate simulations.

4.6 Conclusion and outlook

In this chapter, superquadrics are introduced as a new family of particle shapes for the study of random dense packings, allowing a smooth transition from spheres to ellipsoids and cuboids. A Newton-Raphson based numerical method was described to determine the minimal distance between two superquadrics, or the maximal overlap distance. Contact detection was facilitated by using an analytical bounding-sphere method. The near-uniform sampling of the superquadric surface allows for an additional fast contact check, and simultaneously provides excellent starting points for the Newton-Raphson method, improving the rate of convergence.

We showed initial results of the random dense packing of superballs, by implementing the superquadric shape in the mechanical contraction method. For an increase in shape parameter, going from spheres to more cubic particles, first an increase in packing fraction is seen followed by a steady decrease. While similar behaviour is seen for, for example, spherocylinders, our results are also markedly different from maximally random jammed packings of superballs. The implications of this difference are yet unclear and require further investigation.

The description and contact detection method for the superquadric shape set out in this chapter, can be easily extended to other simulation techniques, such as Monte Carlo simulations. One immediate possibility would be to investigate crystalline packings of superquadrics, as an extension of work done on superballs [21, 24].

Acknowledgements

Álvaro González García is thanked for his work on the superquadric particles and implementation in the MCM. Furthermore, Julian Gonggrijp, Bert Massop and Michiel Bouwhuis are acknowledged for useful discussion regarding the contact detection.

References

1. S. F. Edwards, R. B. S. Oakeshott, 'The transmission of stress in an aggregate', *Physica D: Nonlinear Phenomena* **1989**, *38*, 88–92, DOI 10.1016/0167-2789(89)90176-0.
2. A. P. Philipse, 'The Random Contact Equation and Its Implications for (Colloidal) Rods in Packings, Suspensions, and Anisotropic Powders', *Langmuir* **1996**, *12*, 1127–1133, DOI 10.1021/la950671o, (correction) **1996**, *12*, 5971–5971.
3. A. Baule, R. Mari, L. Bo, L. Portal, H. A. Makse, 'Mean-field theory of random close packings of axisymmetric particles', *Nature Communications* **2013**, *4*, 2194, DOI 10.1038/ncomms3194.
4. S. R. Williams, A. P. Philipse, 'Random packings of spheres and spherocylinders simulated by mechanical contraction', *Physical Review E* **2003**, *67*, 051301, DOI 10.1103/PhysRevE.67.051301.
5. A. Donev, F. H. Stillinger, P. M. Chaikin, S. Torquato, 'Unusually Dense Crystal Packings of Ellipsoids', *Physical Review Letters* **2004**, *92*, 255506, DOI 10.1103/PhysRevLett.92.255506.

6. P. F. Damasceno, M. Engel, S. C. Glotzer, 'Predictive Self-Assembly of Polyhedra into Complex Structures', *Science* **2012**, *337*, 453–457, DOI 10.1126/science.1220869.
7. J. D. Bernal, J. Mason, 'Packing of Spheres: Coordination of Randomly Packed Spheres', *Nature* **1960**, *188*, 910–911, DOI 10.1038/188910a0.
8. P. Richard, P. Philippe, F. Barbe, S. Bourlès, X. Thibault, D. Bideau, 'Analysis by x-ray microtomography of a granular packing undergoing compaction', *Physical Review E* **2003**, *68*, 020301, DOI 10.1103/PhysRevE.68.020301.
9. A. Donev, I. Cisse, D. Sachs, E. A. Variano, F. H. Stillinger, R. Connelly, S. Torquato, P. M. Chaikin, 'Improving the Density of Jammed Disordered Packings Using Ellipsoids', *Science* **2004**, *303*, 990–993, DOI 10.1126/science.1093010.
10. J. Blouwolff, S. Fraden, 'The coordination number of granular cylinders', *EPL (Europhysics Letters)* **2006**, *76*, 1095, DOI 10.1209/epl/i2006-10376-1.
11. J. de Graaf, R. van Roij, M. Dijkstra, 'Dense Regular Packings of Irregular Nonconvex Particles', *Physical Review Letters* **2011**, *107*, 155501, DOI 10.1103/PhysRevLett.107.155501.
12. A. H. Barr, 'Superquadrics and angle-preserving transformations', *IEEE Computer graphics and Applications* **1981**, *1*, 11–23, DOI 10.1109/MCG.1981.1673799.
13. E. Bardinet, L. D. Cohen, N. Ayache, 'Tracking and motion analysis of the left ventricle with deformable superquadrics', *Medical Image Analysis* **1996**, *1*, 129–149, DOI 10.1016/S1361-8415(96)80009-0.
14. E. Bardinet, L. D. Cohen, N. Ayache, 'A Parametric Deformable Model to Fit Unstructured 3D Data', *Computer Vision and Image Understanding* **1998**, *71*, 39–54, DOI 10.1006/cviu.1997.0595.
15. T. McInerney, D. Terzopoulos, 'Deformable models in medical image analysis: a survey', **1996**, 91–108, DOI 10.1016/S1361-8415(96)80007-7.
16. P. Khosla, R. Volpe in Proceedings of the IEEE International Conference on Robotics and Automation, **1988**, pp. 1778–1784, DOI 10.1109/ROBOT.1988.12323.
17. W. Kropatsch, R. Klette, F. Solina, R. Albrecht, 'Theoretical foundations of computer vision' in *Computing Supplementa*, 11, Springer Science & Business Media, **2002**.
18. G. Biegelbauer, M. Vincze in Proceedings of the IEEE International Conference on Robotics and Automation, **2007**, pp. 1086–1091, DOI 10.1109/ROBOT.2007.363129.
19. D. Katsoulas, C. C. Bastidas, D. Kosmopoulos, 'Superquadric segmentation in Range Images via Fusion of Region and Boundary Information', *IEEE Transactions on Pattern Analysis and Machine Intelligence* **2008**, *30*, 781–795, DOI 10.1109/TPAMI.2007.70736.
20. G. W. Delaney, P. W. Cleary, 'The packing properties of superellipsoids', *EPL (Europhysics Letters)* **2010**, *89*, 34002, DOI 10.1209/0295-5075/89/34002.
21. Y. Jiao, F. H. Stillinger, S. Torquato, 'Optimal packings of superballs', *Physical Review E* **2009**, *79*, 041309, DOI 10.1103/PhysRevE.79.041309, (erratum) **2011**, *84*, 069902.
22. Y. Jiao, F. H. Stillinger, S. Torquato, 'Distinctive features arising in maximally random jammed packings of superballs', *Physical Review E* **2010**, *81*, 041304, DOI 10.1103/PhysRevE.81.041304.
23. R. D. Batten, F. H. Stillinger, S. Torquato, 'Phase behavior of colloidal superballs: Shape interpolation from spheres to cubes', *Physical Review E* **2010**, *81*, 061105, DOI 10.1103/PhysRevE.81.061105.
24. R. Ni, A. P. Gantapara, J. de Graaf, R. van Roij, M. Dijkstra, 'Phase diagram of colloidal hard superballs: from cubes *via* spheres to octahedra', *Soft Matter* **2012**, *8*, 8826–8834, DOI 0.1039/C2SM25813G.
25. L. Rossi, S. Sacanna, W. T. M. Irvine, P. M. Chaikin, D. J. Pine, A. P. Philipse, 'Cubic crystals from cubic colloids', *Soft Matter* **2011**, *7*, 4139–4142, DOI 10.1039/C0SM01246G.
26. J.-M. Meijer, F. Hagemans, L. Rossi, D. V. Byelov, S. I. R. Castillo, A. Snigirev, I. Snigireva, A. P. Philipse, A. V. Petukhov, 'Self-Assembly of Colloidal Cubes via Vertical Deposition', *Langmuir* **2012**, *28*, 7631–7638, DOI 10.1021/la3007052.
27. S. I. R. Castillo, D. M. E. Thies-Weesie, A. P. Philipse, 'Formation and liquid permeability of dense colloidal cube packings', *Physical Review E* **2015**, *91*, 022311, DOI 10.1103/PhysRevE.91.022311.
28. D. S. Lopes, M. T. Silva, J. A. Ambrósio, P. Flores, 'A mathematical framework for rigid contact detection between quadric and superquadric surfaces', *Multibody System Dynamics* **2010**, *24*, 255–280, DOI 10.1007/s11044-010-9220-0.
29. F. Solina, R. Bajcsy, 'Recovery of parametric models from range images: the case for superquadrics with global deformations', *IEEE Transactions on Pattern Analysis and Machine Intelligence* **1990**, *12*, 131–147, DOI 10.1109/34.44401.
30. A. J. Hanson, 'Hyperquadrics: Smoothly deformable shapes with convex polyhedral bounds', *Computer Vision Graphics and Image Processing* **1988**, *44*, 191–210, DOI 10.1016/S0734-189X(88)80005-7.

31. J. R. Williams, A. P. Pentland, 'Superquadrics and modal dynamics for discrete elements in interactive design', *Engineering Computations* **1992**, *9*, 115–127, DOI 10.1108/eb023852.
32. R. Portal, J. Dias, L. de Sousa, 'Contact Detection Between Convex Superquadric Surfaces', *Archive of Mechanical Engineering* **2010**, *57*, 165–186, DOI 10.2478/v10180-010-0009-8.
33. C. Wellmann, C. Lillie, P. Wriggers, 'A contact detection algorithm for superellipsoids based on the common-normal concept', *Engineering Computations* **2008**, *25*, 432–442, DOI 10.1108/02644400810881374.
34. E. W. Weisstein, "Newton's Method", From *MathWorld*—A Wolfram Web Resource, Last visited on 01/10/2015, http://mathworld.wolfram.com/NewtonsMethod.html.
35. E. W. Weisstein, "QR Decomposition", From *MathWorld*—A Wolfram Web Resource, Last visited on 01/10/2015, http://mathworld.wolfram.com/QRDecomposition.html.
36. A. S. Householder, 'Unitary Triangularization of a Nonsymmetric Matrix', *Journal of the ACM* **1958**, *5*, 339–342, DOI 10.1145/320941.320947.
37. M. Pilu, R. B. Fisher in Proceedings of the British Machine Vision Conference, BMVA Press, **1995**, pp. 257–266, DOI 10.5244/C.9.26.
38. J. L. Bentley, 'Multidimensional Binary Search Trees Used for Associative Searching', *Communications of the ACM* **1975**, *18*, 509–517, DOI 10.1145/361002.361007.
39. A. Wouterse, S. R. Williams, A. P. Philipse, 'Effect of particle shape on the density and microstructure of random packings', *Journal of Physics: Condensed Matter* **2007**, *19*, 406215, DOI 10.1088/0953-8984/19/40/406215.
40. S. F. Edwards, D. V. Grinev, 'Statistical Mechanics of Stress Transmission in Disordered Granular Arrays', *Physical Review Letters* **1999**, *82*, 5397, DOI 10.1103/PhysRevLett.82.5397.
43. A. Jaklič, A. Leonardis, F. Solina, 'Segmentation and Recovery of superquadrics' in, Computational Imaging and Vision, Springer Science & Business Media, Dordrecht, **2000**.

Appendix 4.A Properties of superquadrics

Superquadrics as defined in Equation 4.3 have not yet been studied in great detail. Therefore, we derive some properties of the SQ shape to aid future work.

Volume The volume of a SQ parameterized by coordinates (u, v) and three shape parameters ϵ_i (see Equation 4.3), can be found by integrating over infinitesimally thin slices in the xy-plane along the z-axis [43]. Each slice is a general superellipse with two shape parameters, a scaling dependent on the z-coordinate, and an area given by,

$$A(v) = a_1'(v) a_2'(v) \epsilon_1 \epsilon_2 \frac{\Gamma\left(\frac{\epsilon_1}{2}\right) \Gamma\left(\frac{\epsilon_2}{2}\right)}{\Gamma\left(1 + \frac{\epsilon_1}{2} + \frac{\epsilon_2}{2}\right)} \tag{4.18}$$

where $\Gamma(x)$ is the gamma-function. The scaling is modulated via,

$$a_1'(v) = a_1 \cos^{\epsilon_1} v \qquad a_2'(v) = a_2 \cos^{\epsilon_2} v \tag{4.19}$$

The volume of each slice of infinitesimal thickness $\mathrm{d}z$ is given by

$$\begin{aligned} \mathrm{d}V = A(z)\,\mathrm{d}z = A(v)\frac{\partial z}{\partial v}\,\mathrm{d}v\,, \qquad \text{with} \quad \frac{\partial z}{\partial v} = a_3 \epsilon_3 \cos v \sin^{\epsilon_3 - 1} v \\ = a_1 a_2 a_3 \epsilon_1 \epsilon_2 \epsilon_3 \cos^{1+\epsilon_1+\epsilon_2} v \sin^{\epsilon_3 - 1} v \frac{\Gamma\left(\frac{\epsilon_1}{2}\right) \Gamma\left(\frac{\epsilon_2}{2}\right)}{\Gamma\left(1 + \frac{\epsilon_1}{2} + \frac{\epsilon_2}{2}\right)} \mathrm{d}v \end{aligned} \tag{4.20}$$

Integration over v gives the volume,

$$\begin{aligned} V &= a_1 a_2 a_3 \epsilon_1 \epsilon_2 \epsilon_3 \frac{\Gamma\left(\frac{\epsilon_1}{2}\right) \Gamma\left(\frac{\epsilon_2}{2}\right)}{\Gamma\left(1 + \frac{\epsilon_1}{2} + \frac{\epsilon_2}{2}\right)} \int_{-\pi/2}^{\pi/2} \mathrm{d}v \;\cos^{1+\epsilon_1+\epsilon_2} v \sin^{\epsilon_3 - 1} v \\ &= a_1 a_2 a_3 \epsilon_1 \epsilon_2 \epsilon_3 \frac{\Gamma\left(\frac{\epsilon_1}{2}\right) \Gamma\left(\frac{\epsilon_2}{2}\right) \Gamma\left(\frac{\epsilon_3}{2}\right)}{\Gamma\left(1 + \frac{\epsilon_1}{2} + \frac{\epsilon_2}{2} + \frac{\epsilon_3}{2}\right)} \end{aligned} \tag{4.21}$$

where some terms canceled out, and the property $x\Gamma(x) = \Gamma(1 + x)$ is applied.

Moment of inertia The principal moments of inertia I_{xx}, I_{yy} and I_{zz} of a superquadric can be obtained in a similar way as for superellipsoids [43]. For I_{xx} we have by definition,

$$\begin{aligned} I_{xx} &= \iiint_V \mathrm{d}x\,\mathrm{d}y\,\mathrm{d}z\;(y^2 + z^2) \\ &= \int_{-a_3}^{a_3} \mathrm{d}z \left(\iint_S \mathrm{d}x\,\mathrm{d}y\; y^2 + \iint_S \mathrm{d}x\,\mathrm{d}y\; z^2 \right) \end{aligned} \tag{4.22}$$

Here, the first double integral is the moment of inertia of a superellipse around the x-axis, I^0_{xx}, and the second double integral is the area of a superellipse (see Equation 4.18). Changing the integration variable to v results in,

$$I_{xx} = \int_{-\pi/2}^{\pi/2} \mathrm{d}v \, \frac{\partial z}{\partial v} \left(I^0_{xx}(v) + z(v)^2 A(v) \right) \tag{4.23}$$

To find I^0_{xx}, we again follow [43]. A "superquadric" coordinate system is used,

$$\begin{aligned} x &= a_1 r \cos^{\epsilon_1} u \\ y &= a_2 r \sin^{\epsilon_2} u \end{aligned} \tag{4.24}$$

The determinant of the Jacobian for this transformation is given by,

$$|\mathbf{J}| = a_1 a_2 r \cos^{\epsilon_1 - 1} u \sin^{\epsilon_2 - 1} u \left(\epsilon_1 \sin^2 u + \epsilon_2 \cos^2 u \right) \tag{4.25}$$

so that the moment of inertia about the x-axis can now be found, as follows,

$$\begin{aligned} I^0_{xx} &= \iint_S \mathrm{d}x \, \mathrm{d}y \; y^2 \\ &= \int_{-\pi}^{\pi} \mathrm{d}u \int_0^1 \mathrm{d}r \; \left(a_2 r \sin^{\epsilon_2} u \right)^2 |\mathbf{J}| \\ &= a_1 a_2^3 \epsilon_1 \epsilon_2 \frac{\Gamma\left(\frac{\epsilon_1}{2}\right) \Gamma\left(\frac{3\epsilon_2}{2}\right)}{\Gamma\left(1 + \frac{\epsilon_1}{2} + \frac{3\epsilon_2}{2}\right)} \end{aligned} \tag{4.26}$$

The other moments can be found analogously,

$$\begin{aligned} I^0_{yy} &= a_1^3 a_2 \epsilon_1 \epsilon_2 \frac{\Gamma\left(\frac{3\epsilon_1}{2}\right) \Gamma\left(\frac{\epsilon_2}{2}\right)}{\Gamma\left(1 + \frac{3\epsilon_1}{2} + \frac{\epsilon_2}{2}\right)} \\ I^0_{zz} &= I^0_{xx} + I^0_{yy} \end{aligned} \tag{4.27}$$

For the next step and integration over v, the a_i for the superellipses are again dependent on v via Equation 4.19. Equation 4.18 and Equation 4.26 can be substituted into Equation 4.23 to give,

$$\begin{aligned} I_{xx} = \int_{-\pi/2}^{\pi/2} \mathrm{d}v \, \left(a_3 \epsilon_3 \cos v \sin^{\epsilon_3 - 1} v \right) \Bigg(& a_1' (a_2')^3 \epsilon_1 \epsilon_2 \frac{\Gamma\left(\frac{\epsilon_1}{2}\right) \Gamma\left(\frac{3\epsilon_2}{2}\right)}{\Gamma\left(1 + \frac{\epsilon_1}{2} + \frac{3\epsilon_2}{2}\right)} + \\ & (a_3 \sin^{\epsilon_3} v)^2 \, 4 a_1' a_2' \frac{\Gamma\left(1 + \frac{\epsilon_1}{2}\right) \Gamma\left(1 + \frac{\epsilon_2}{2}\right)}{\Gamma\left(1 + \frac{\epsilon_1}{2} + \frac{\epsilon_2}{2}\right)} \Bigg) \end{aligned} \tag{4.28}$$

This integral can be solved with help of Mathematica, yielding,

$$I_{xx} = a_1 a_2 a_3 \epsilon_1 \epsilon_2 \epsilon_3 \left(a_2^2 \frac{\Gamma\left(\frac{\epsilon_1}{2}\right)\Gamma\left(\frac{3\epsilon_2}{2}\right)\Gamma\left(\frac{\epsilon_3}{2}\right)}{\Gamma\left(1+\frac{\epsilon_1}{2}+\frac{3\epsilon_2}{2}+\frac{\epsilon_3}{2}\right)} + a_3^2 \frac{\Gamma\left(\frac{\epsilon_1}{2}\right)\Gamma\left(\frac{\epsilon_2}{2}\right)\Gamma\left(\frac{3\epsilon_3}{2}\right)}{\Gamma\left(1+\frac{\epsilon_1}{2}+\frac{\epsilon_2}{2}+\frac{3\epsilon_3}{2}\right)} \right) \tag{4.29}$$

Analogously we can find for the other inertia components,

$$I_{yy} = a_1 a_2 a_3 \epsilon_1 \epsilon_2 \epsilon_3 \left(a_1^2 \frac{\Gamma\left(\frac{3\epsilon_1}{2}\right)\Gamma\left(\frac{\epsilon_2}{2}\right)\Gamma\left(\frac{\epsilon_3}{2}\right)}{\Gamma\left(1+\frac{3\epsilon_1}{2}+\frac{\epsilon_2}{2}+\frac{\epsilon_3}{2}\right)} + a_3^2 \frac{\Gamma\left(\frac{\epsilon_1}{2}\right)\Gamma\left(\frac{\epsilon_2}{2}\right)\Gamma\left(\frac{3\epsilon_3}{2}\right)}{\Gamma\left(1+\frac{\epsilon_1}{2}+\frac{\epsilon_2}{2}+\frac{3\epsilon_3}{2}\right)} \right) \tag{4.30}$$

$$I_{zz} = a_1 a_2 a_3 \epsilon_1 \epsilon_2 \epsilon_3 \left(a_1^2 \frac{\Gamma\left(\frac{3\epsilon_1}{2}\right)\Gamma\left(\frac{\epsilon_2}{2}\right)\Gamma\left(\frac{\epsilon_3}{2}\right)}{\Gamma\left(1+\frac{3\epsilon_1}{2}+\frac{\epsilon_2}{2}+\frac{\epsilon_3}{2}\right)} + a_2^2 \frac{\Gamma\left(\frac{\epsilon_1}{2}\right)\Gamma\left(\frac{3\epsilon_2}{2}\right)\Gamma\left(\frac{\epsilon_3}{2}\right)}{\Gamma\left(1+\frac{\epsilon_1}{2}+\frac{3\epsilon_2}{2}+\frac{\epsilon_3}{2}\right)} \right) \tag{4.31}$$

Note that these formula's implicitly contain the particle volume at unit density.

Appendix 4.B Operational formulas

In this appendix we provide expressions for all relevant quantities to evaluate Equation 4.12 for superquadrics, so that a computer implementation will be straightforward.

The main vector quantities for the distance minimization procedure are,

$$
\begin{aligned}
\mathbf{k}_{ij} &= (\mathbf{x}_j + \mathbf{R}_j\mathbf{s}_j) - (\mathbf{x}_i + \mathbf{R}_i\mathbf{s}_i) \\
\mathbf{n}_i &= \mathbf{R}_i\mathbf{n}(\mathbf{r}_i) \\
\mathbf{n}_j &= \mathbf{R}_j\mathbf{n}(\mathbf{r}_j) \\
\mathbf{h}_j &= \left(n_{j,x} + \|\mathbf{n}_j\|, n_{j,y}, n_{j,z}\right) \\
\mathbf{t}_j &= \mathrm{R}_j \begin{bmatrix} -2\frac{(n_{j,x}+\|\mathbf{n}_j\|)n_{j,y}}{\|\mathbf{h}_j\|^2} \\ 1 - 2\frac{n_{j,y}^2}{\|\mathbf{h}_j\|^2} \\ -2\frac{n_{j,z}n_{j,y}}{\|\mathbf{h}_j\|^2} \end{bmatrix} = \mathrm{R}_j \begin{bmatrix} -\frac{n_{j,y}}{\|\mathbf{n}_j\|}\frac{h_{j,x}}{h_{j,x}} \\ 1 - \frac{n_{j,y}}{\|\mathbf{n}_j\|}\frac{h_{j,y}}{h_{j,x}} \\ -\frac{n_{j,y}}{\|\mathbf{n}_j\|}\frac{h_{j,z}}{h_{j,x}} \end{bmatrix} \\
\mathbf{b}_j &= \mathrm{R}_j \begin{bmatrix} -2\frac{(n_{j,x}+\|\mathbf{n}_j\|)n_{j,z}}{\|\mathbf{h}_j\|^2} \\ -2\frac{n_{j,y}n_{j,z}}{\|\mathbf{h}_j\|^2} \\ 1 - 2\frac{n_{j,z}^2}{\|\mathbf{h}_j\|^2} \end{bmatrix} = \mathrm{R}_j \begin{bmatrix} -\frac{n_{j,z}}{\|\mathbf{n}_j\|}\frac{h_{j,x}}{h_{j,x}} \\ -\frac{n_{j,z}}{\|\mathbf{n}_j\|}\frac{h_{j,y}}{h_{j,x}} \\ 1 - \frac{n_{j,z}}{\|\mathbf{n}_j\|}\frac{h_{j,z}}{h_{j,x}} \end{bmatrix}
\end{aligned}
\tag{4.32}
$$

For SQs, each component of the surface normal is only dependent on one coordinate, so that only the following partial derivatives exist,

$$
\begin{aligned}
\frac{\partial n_x}{\partial x} &= a_1^{-\gamma_1}\gamma_1\left(\gamma_1 - 1\right)\left(x^2\right)^{\gamma_1/2-1} \\
\frac{\partial n_y}{\partial y} &= a_2^{-\gamma_2}\gamma_2\left(\gamma_2 - 1\right)\left(y^2\right)^{\gamma_2/2-1} \\
\frac{\partial n_z}{\partial z} &= a_3^{-\gamma_3}\gamma_3\left(\gamma_3 - 1\right)\left(z^2\right)^{\gamma_3/2-1}
\end{aligned}
\tag{4.33}
$$

When SEs or other super-surfaces are considered, cross-derivatives may occur, complicating the computation significantly.

The partial derivatives of the above vectors can be obtained,

$$\frac{\partial}{\partial \mathbf{q}}\mathbf{k}_{ij} = \mathrm{R}_j \begin{bmatrix} 0 & 0 & 0 & 1 & 0 & 0 \\ 0 & 0 & 0 & 0 & 1 & 0 \\ 0 & 0 & 0 & 0 & 0 & 1 \end{bmatrix} - \mathrm{R}_i \begin{bmatrix} 1 & 0 & 0 & 0 & 0 & 0 \\ 0 & 1 & 0 & 0 & 0 & 0 \\ 0 & 0 & 1 & 0 & 0 & 0 \end{bmatrix}$$

$$\frac{\partial}{\partial \mathbf{q}}\mathbf{n}_i = \mathrm{R}_i \begin{bmatrix} \frac{\partial n_{i,x}}{\partial x} & 0 & 0 & 0 & 0 & 0 \\ 0 & \frac{\partial n_{i,y}}{\partial y} & 0 & 0 & 0 & 0 \\ 0 & 0 & \frac{\partial n_{i,z}}{\partial z} & 0 & 0 & 0 \end{bmatrix}$$

$$\frac{\partial}{\partial \mathbf{q}}\mathbf{n}_j = \mathrm{R}_j \begin{bmatrix} 0 & 0 & 0 & \frac{\partial n_{j,x}}{\partial x} & 0 & 0 \\ 0 & 0 & 0 & 0 & \frac{\partial n_{j,y}}{\partial y} & 0 \\ 0 & 0 & 0 & 0 & 0 & \frac{\partial n_{j,z}}{\partial z} \end{bmatrix} \tag{4.34}$$

$$\frac{\partial}{\partial \mathbf{q}}\mathbf{t}_j = 2\frac{n_y}{\|\mathbf{h}\|^2}\mathrm{R}_j \begin{bmatrix} 0 & 0 & 0 & \frac{\partial n_x}{\partial x}\left(\frac{n_x h_x}{\|\mathbf{n}\|^2}\right) & \frac{\partial n_y}{\partial y}\left(\frac{n_y h_x}{\|\mathbf{n}\|^2} - \frac{h_x}{n_y}\right) & \frac{\partial n_z}{\partial z}\left(\frac{n_z h_x}{\|\mathbf{n}\|^2}\right) \\ 0 & 0 & 0 & \frac{\partial n_x}{\partial x}\left(\frac{n_x h_y}{\|\mathbf{n}\|^2} + 2\frac{n_y h_x}{\|\mathbf{h}\|^2}\right) & \frac{\partial n_y}{\partial y}\left(\frac{n_y h_y}{\|\mathbf{n}\|^2} + 2\frac{n_y h_y}{\|\mathbf{h}\|^2} - 2\frac{h_y}{n_y}\right) & \frac{\partial n_z}{\partial z}\left(\frac{n_z h_y}{\|\mathbf{n}\|^2} + 2\frac{n_y h_z}{\|\mathbf{h}\|^2}\right) \\ 0 & 0 & 0 & \frac{\partial n_x}{\partial x}\left(\frac{n_x h_z}{\|\mathbf{n}\|^2} + 2\frac{n_z h_x}{\|\mathbf{h}\|^2}\right) & \frac{\partial n_y}{\partial y}\left(\frac{n_y h_z}{\|\mathbf{n}\|^2} + 2\frac{n_z h_y}{\|\mathbf{h}\|^2} - \frac{h_z}{n_y}\right) & \frac{\partial n_z}{\partial z}\left(\frac{n_z h_z}{\|\mathbf{n}\|^2} + 2\frac{n_z h_z}{\|\mathbf{h}\|^2} - 1\right) \end{bmatrix}$$

$$\frac{\partial}{\partial \mathbf{q}}\mathbf{b}_j = 2\frac{n_z}{\|\mathbf{h}\|^2}\mathrm{R}_j \begin{bmatrix} 0 & 0 & 0 & \frac{\partial n_x}{\partial x}\left(\frac{n_x h_x}{\|\mathbf{n}\|^2}\right) & \frac{\partial n_y}{\partial y}\left(\frac{n_y h_x}{\|\mathbf{n}\|^2}\right) & \frac{\partial n_z}{\partial z}\left(\frac{n_z h_x}{\|\mathbf{n}\|^2} - \frac{h_x}{n_z}\right) \\ 0 & 0 & 0 & \frac{\partial n_x}{\partial x}\left(\frac{n_x h_y}{\|\mathbf{n}\|^2} + 2\frac{n_y h_x}{\|\mathbf{h}\|^2}\right) & \frac{\partial n_y}{\partial y}\left(\frac{n_y h_y}{\|\mathbf{n}\|^2} + 2\frac{n_y h_y}{\|\mathbf{h}\|^2} - 1\right) & \frac{\partial n_z}{\partial z}\left(\frac{n_z h_y}{\|\mathbf{n}\|^2} + 2\frac{n_y h_z}{\|\mathbf{h}\|^2} - \frac{h_y}{n_z}\right) \\ 0 & 0 & 0 & \frac{\partial n_x}{\partial x}\left(\frac{n_x h_z}{\|\mathbf{n}\|^2} + 2\frac{n_z h_x}{\|\mathbf{h}\|^2}\right) & \frac{\partial n_y}{\partial y}\left(\frac{n_y h_z}{\|\mathbf{n}\|^2} + 2\frac{n_z h_y}{\|\mathbf{h}\|^2}\right) & \frac{\partial n_z}{\partial z}\left(\frac{n_z h_z}{\|\mathbf{n}\|^2} + 2\frac{n_z h_z}{\|\mathbf{h}\|^2} - 2\frac{h_z}{n_z}\right) \end{bmatrix}$$

Appendix 4.C Bounding sphere

To determine if two superquadrics are in contact, the SQs can be (crudely) approximated by spheres. If the bounding spheres do not overlap, then the superquadrics are also separated. The radius r of the smallest enveloping sphere is found by means of a constrained minimization,

$$\begin{aligned} &\text{minimize} \quad r^2 = x^2 + y^2 + z^2 \\ &\text{subjectto} \quad \left(\frac{x}{a_1}\right)^{\gamma_1} + \left(\frac{y}{a_2}\right)^{\gamma_2} + \left(\frac{z}{a_3}\right)^{\gamma_3} = 1 \end{aligned} \tag{4.35}$$

Note that the absolute signs in the superquadric equation have been dropped, since, because of its symmetry, it is enough to consider only one quadrant of the superquadric ($x, y, z > 0$) to find its extremum.

For a general superquadric ($\gamma_1 \neq \gamma_2 \neq \gamma_3, a_1 \neq a_2 \neq a_3$) no closed-form solution exists, and a numerical approach is necessary. For a supercuboid ($\gamma_1 = \gamma_2 = \gamma_3, a_1 \neq a_2 \neq a_3$) an analytical solution can be found by application of a Lagrange multiplier. We use Equation 4.4, and the substitution $\epsilon = 2/\gamma$, to write the function to be maximized as,

$$\Lambda = (x^2 + y^2 + z^2) - \lambda \left(\left(\frac{x^2}{a_1^2}\right)^{1/\epsilon} + \left(\frac{y^2}{a_2^2}\right)^{1/\epsilon} + \left(\frac{z^2}{a_3^2}\right)^{1/\epsilon} - 1 \right) \tag{4.36}$$

where λ is the Lagrange multiplier. Taking the partial derivatives of Λ with respect to x, y and z, setting them to zero and rewriting slightly results in,

$$x^2 = \epsilon^{-\epsilon/(\epsilon-1)} \lambda^{\epsilon/(\epsilon-1)} (a_1^2)^{1/(\epsilon-1)} \tag{4.37}$$

and analogous equations for y and z. Substituting these equations back into the original constraint, allows to derive an expression for λ. Subsequent substitution of λ back into Equation 4.37 allows to write for a final solution for r^2, after some manipulation,

$$r_{\text{min}}^2 = \left(\left(a_1^2\right)^{1/(1-\epsilon)} + \left(a_2^2\right)^{1/(1-\epsilon)} + \left(a_3^2\right)^{1/(1-\epsilon)} \right)^{1-\epsilon} \tag{4.38}$$

For superballs ($\gamma_1 = \gamma_2 = \gamma_3, a_1 = a_2 = a_3$) this is simplified further to

$$r_{\text{min}}^2 = 3^{1-\epsilon} a^2 \tag{4.39}$$

It is also possible to find an exact solution for an enveloping ellipsoid for a given supercuboids, which may result in a better ratio between the enveloping volume and the particle volume. However, this does not help in speeding up the contact detection, as ellipsoid-ellipsoid distances must also be numerically approximated.

Part II

Magnetic separation

Exact expression for the magnetic field of a finite cylinder with arbitrary uniform magnetization

Abstract

An exact analytical expression for the magnetic field of a cylinder of finite length with a uniform, transverse magnetization is derived. Linear superposition with known expressions for longitudinal magnetization, allows for the calculation of magnetic fields for cylinders with an arbitrary magnetization direction. The expression for transverse magnetization is validated successfully against the well-known limits of an infinitely long cylinder, the field on the axis of the cylinder and in the far field limit. Comparison with a commercially available finite-element method displays excellent agreement, making the advantage of an analytical method over grid-based methods evident. For externally magnetized cylinders, our approach also gives a reasonable prediction for the magnetic field generated by multiple cylinders, except close to the cylinder edges when mutual interactions are important.

5.1 Introduction

Analytic expressions for the magnetic fields produced by inherently magnetic materials or induced in magnetically susceptible materials, are only well-known for some classic textbook cases, such as the field of point multipoles and infinitely long wires carrying a current [1]. Complex geometries often can be solved only numerically via finite element methods (FEM) [2, 3]. The domain discretization inherent to these methods may ultimately lead to numerical inaccuracies, unless expensive higher-order calculations are performed, or the calculation mesh is repeatedly refined. The analytic modelling of the field has a clear advantage over finite-element methods as the necessary magnetic quantities can be probed at all required coordinates, with minimal computational effort. This is highly useful, for example, when dynamical systems are modelled, such as the movement of magnetic nanoparticles in magnetic field gradient [4, 5].

A geometry for which analytical expressions for magnetic quantities are readily available, is an axisymmetric solenoid of finite length [6–9]. Exact expressions for the vector potential $\mathbf{\Phi}$, magnetic flux density $\mathbf{B}$ (with axial and radial components), magnetic force $\mathbf{F} = (\mathbf{m} \cdot \boldsymbol{\nabla})\mathbf{B}$ and other quantities can be formulated using special functions such as elliptic integrals. The derivation of these expressions usually extends the treatment of a single circular current loop by integrating over a certain length along the symmetry axis of the loop [10, 11]. The solenoid field also describes the field of a cylindrical ideal permanent magnet with its magnetization vector $\mathbf{M}$ along the axis of symmetry (longitudinal magnetization). For different magnetization directions, such as $\mathbf{M}$ perpendicular to the axis of symmetry (transverse magnetization), other field equations are required. In the case of transverse magnetization, analytical results are available for an infinite cylinder [12, 13], and for the on-axis field of a finite cylinder [14]. To expand upon these known relations, we derive here an analytical expression for the magnetic field of a transversely magnetized finite cylinder in all spatial locations. By combining the expression for longitudinal and transverse magnetization we will also demonstrate the possibility of accurately calculating the resulting magnetic field for a cylinder with an arbitrarily chosen magnetization vector.

Analytically describing the field of a non-ideal magnet or magnetized material poses an additional challenge. For example, the magnetization is likely not to be uniform throughout such an object. We will test the applicability of our analytical model to also describe the field of a finite magnetizable cylinder induced by an external source, by comparing our analytical model with numerical methods.

A specific application of the expressions derived here is found in the modelling of a high-gradient magnetic separation process, using a separation filter comprising many small magnetizable fibres. By combining the local magnetic fields of a large collection of (non-overlapping) cylinders, we aim to calculate the movement of magnetic nanoparticles through such a separation filter. This will be further discussed in Chapter 6. In this chapter, in addition to the calculations for a single cylinder, we explore the possibility to calculate the magnetic field for a combination of multiple cylinders by means of our analytical expressions.

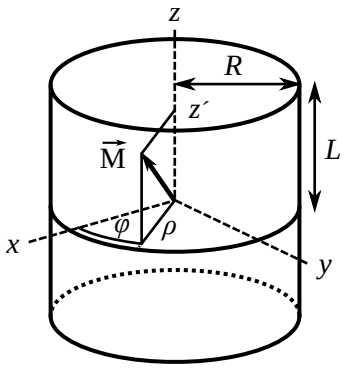

Figure 5.1. Schematic representation of a magnetized cylinder of semi-length L and radius R with an arbitrary magnetization vector $\mathbf{M}$. The cylindrical (ρ, φ, z), and Cartesian (x, y, z) coordinate systems are indicated.

5.2 Preliminary

Consider a circular cylindrical body of radius R and semi-length L, with its centroid at the origin of a cylindrical coordinate system (ρ, φ, z) and its axis aligned with the z-direction (see Figure 5.1). A uniform magnetization of the body along an arbitrarily chosen magnetization vector $\mathbf{M}$ can always be decomposed into a longitudinal and transverse component,

$$\mathbf{M} = M_{\mathrm{l}}\hat{\mathbf{z}} + M_{\mathrm{t}}\hat{\boldsymbol{\rho}} \tag{5.1}$$

In reality, for a magnetizable material, the acquired magnetization will not have the same direction as the applied field $\mathbf{H}_{\mathrm{ext}}$, as the magnetization vector will rotate to minimize its energy depending on the magnetic susceptibility of the material and the demagnetization factors of the body. The Stoner-Wohlfarth model describes this principle in detail [15, 16]. In general, the magnetization is related to the magnetic field $\mathbf{H}$, the magnetic flux density $\mathbf{B}$ and the permeability of vacuum μ_0 through,

$$\mathbf{B} = \mu_0(\mathbf{H} + \mathbf{M}) \tag{5.2}$$

We proceed by restating the known expression for $\mathbf{B}$ for longitudinal magnetization [7, 9] and continue by deriving an expression for the case of transverse magnetization. The validity of the equations are tested by determining several limiting cases. By combining Equation 5.1 and Equation 5.2, the field of a finite cylinder with an off-axis magnetization vector is calculated and these results are compared with numerical calculations. Finally, the applicability of our model to the description of magnetizable cylinders are tested.

5.3 Longitudinal magnetization

Equations for the field inside and outside a longitudinally magnetized, finite cylinder were first retrieved by Callaghan and Maslen [7]. They obtained their result by

considering a finite cylinder as a collection of current loops (i.e. an ideal solenoid). The total magnetization is $M \equiv nI$, with n the number of turns per unit of length and I the current per turn. By applying the Biot–Savart law, the magnetic field can be calculated directly in terms of elliptic integrals. Derby and Olbert [9] revisited the derivation and provided a computationally convenient form using a combination of generalized complete elliptic integrals [17]. They correctly retrieved the field of a current loop when $L \to 0$ and the field of a point dipole at large distances from the cylinder.

In [9] only an integral form of the field equations is given. Here we restate these results in closed form, in terms of elliptic integrals, obtaining equations very similar to those for the transverse case presented in the following section.

$$\begin{aligned} B_\rho &= \frac{\mu_0 M R}{\pi} \left[\alpha_+ P_1(k_+) - \alpha_- P_1(k_-)\right] \\ B_z &= \frac{\mu_0 M R}{\pi(\rho + R)} \left[\beta_+ P_2(k_+) - \beta_- P_2(k_-)\right] \end{aligned} \tag{5.3}$$

where B_ρ and B_z are the radial and axial components of the magnetic flux density, respectively. Two auxiliary functions are defined (see Section 5.A) as,

$$\begin{aligned} P_1(k) &= \mathcal{K} - \frac{2}{1-k^2}(\mathcal{K} - \mathcal{E}) \\ P_2(k) &= -\frac{\gamma}{1-\gamma^2}(\mathcal{P} - \mathcal{K}) - \frac{1}{1-\gamma^2}\left(\gamma^2 \mathcal{P} - \mathcal{K}\right) \end{aligned} \tag{5.4}$$

and the following shorthand is introduced,

$$\begin{aligned} \xi_\pm &= z \pm L \\ \alpha_\pm &= \frac{1}{\sqrt{\xi_\pm^2 + (\rho + R)^2}} \qquad & \beta_\pm &= \xi_\pm \alpha_\pm \\ \gamma &= \frac{\rho - R}{\rho + R} & k_\pm^2 &= \frac{\xi_\pm^2 + (\rho - R)^2}{\xi_\pm^2 + (\rho + R)^2} \end{aligned} \tag{5.5}$$

The symbols $\mathcal{K}$, $\mathcal{E}$ and $\mathcal{P}$ are used to indicate the evaluation of the complete elliptic integrals of the first, second and third kind, as follows,

$$\begin{aligned} \mathcal{K} &= \mathrm{K}\left(\sqrt{1-k^2}\right) &&= \int_0^{\frac{\pi}{2}} \frac{\mathrm{d}\theta}{\sqrt{1-(1-k^2)\sin^2\theta}} \\ \mathcal{E} &= \mathrm{E}\left(\sqrt{1-k^2}\right) &&= \int_0^{\frac{\pi}{2}} \mathrm{d}\theta \sqrt{1-(1-k^2)\sin^2\theta} \\ \mathcal{P} &= \Pi\left(1-\gamma^2, \sqrt{1-k^2}\right) &&= \int_0^{\frac{\pi}{2}} \frac{\mathrm{d}\theta}{(1-(1-\gamma^2)\sin^2\theta)\sqrt{1-(1-k^2)\sin^2\theta}} \end{aligned} \tag{5.6}$$

Note that B_φ is absent in Equation 5.3 due to the radial symmetry of the system. A visualization of the field lines produced by these equations is given in Figure 5.2a.

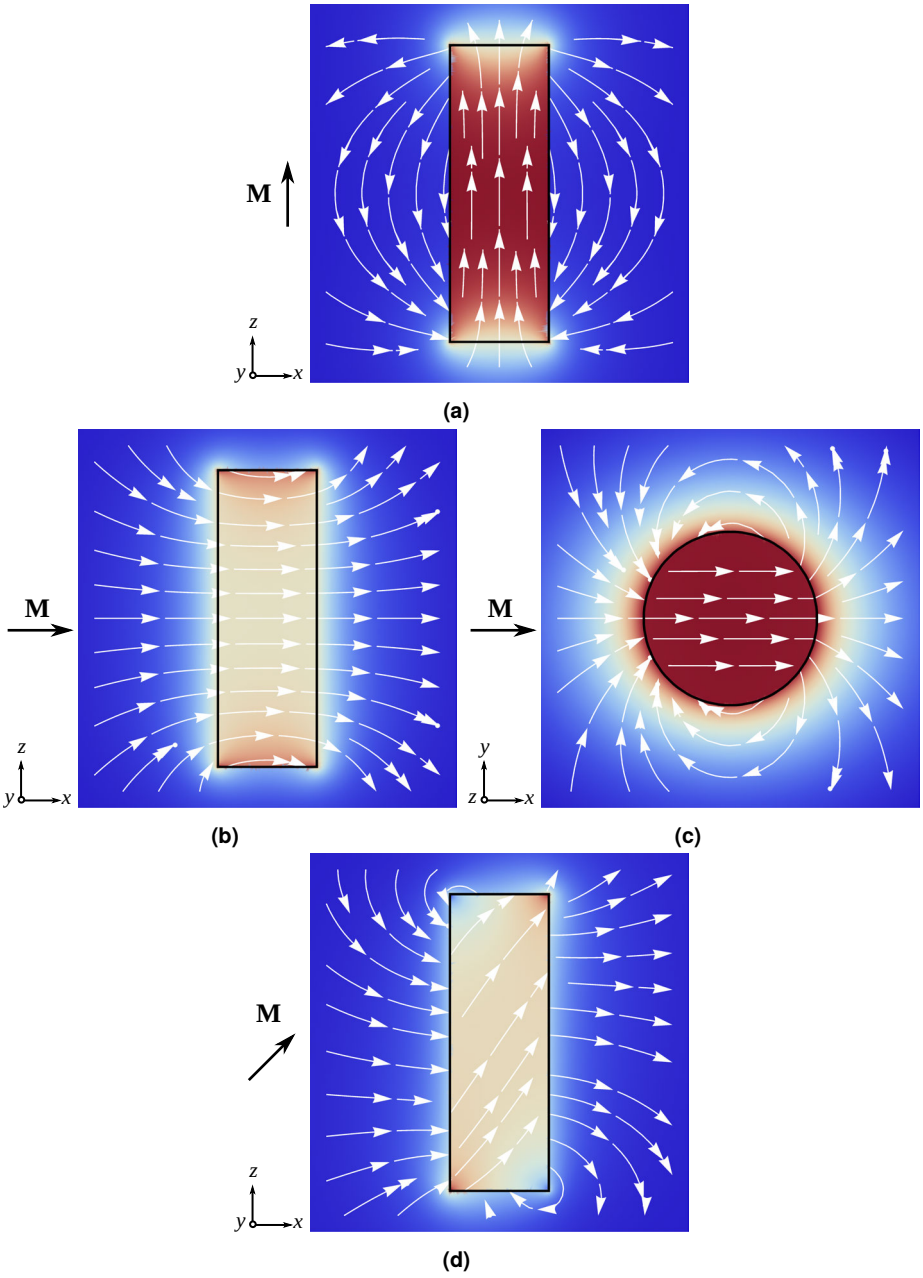

Figure 5.2. Magnetic flux lines and density plots for a cylinder ($R = 1, L = 3$) with longitudinal (a), transverse (b) and (c), and off-axis magnetization (d). The outline of the cylinder is marked with a black rectangle or circle. The colours indicate the magnitude of the B-field strength (blue = low, red = high).

5.4 Transverse magnetization

To derive the field equations for a transversely magnetized cylinder, we follow the approach of [7, 9]. We start by choosing a magnetization vector perpendicular to the long axis of the cylinder. A convenient choice is a magnetization along the Cartesian x-axis, $\mathbf{M} = M\hat{\mathbf{x}}$, although any direction in the xy-plane would be suitable for symmetry reasons. Assuming there are no free currents present, the magnetic field can be expressed as the gradient of a magnetostatic scalar potential

$$\mathbf{H} = -\boldsymbol{\nabla}\Phi_{\mathrm{m}} \tag{5.7}$$

In the following, we derive the exact expression for the potential Φ_{m}. The components of the $\mathbf{H}$-field can be derived following similar mathematical manipulations, but only the final results will be presented in Section 5.4.2.

5.4.1 Magnetostatic potential

In general, the magnetostatic potential at a point $\mathbf{r}$ can be written as [12],

$$\Phi(\mathbf{r}) = \int_V \mathrm{d}\mathbf{r}' \, \frac{\rho(\mathbf{r}')}{4\pi|\mathbf{r} - \mathbf{r}'|} \tag{5.8}$$

using the bound magnetic charge formulation, where $\rho(\mathbf{r}')$ is the volume charge density. One may recognize Green's function for the Laplacian, $G(\mathbf{r}) = (4\pi|\mathbf{r}|)^{-1}$. In the problem of interest, the volume charge density reduces to a surface charge distribution σ on the lateral surface of the cylinder. In cylindrical coordinates this is given by $\sigma(\varphi') = M\cos\varphi'$. The integral in Equation 5.8 is now reduced to an integral over the surface of the cylinder,

$$\Phi(\rho, \varphi, z) = \frac{M}{4\pi} \int_0^{2\pi} \mathrm{d}\varphi' \int_{-L}^{L} \mathrm{d}z' \, \frac{R\cos\varphi'}{\sqrt{\rho^2 + R^2 - 2\rho R\cos(\varphi - \varphi') + (z - z')^2}} \tag{5.9}$$

We proceed by evaluating above integral in several steps, to a functional form containing elliptic integrals. First, the integral over z' is evaluated, giving,

$$\frac{MR}{4\pi} \int_0^{2\pi} \mathrm{d}\varphi' \, \cos\varphi' \ln\left(\xi + \sqrt{\xi^2 + \rho^2 + R^2 - 2\rho R\cos(\varphi - \varphi')}\right)\Bigg|_{\xi_-}^{\xi_+} \tag{5.10}$$

where the substitution $\xi_\pm = z \pm L$ from Equation 5.5 is introduced.

Integration by parts can be applied, leading to the somewhat involved expression,

$$\frac{MR}{4\pi}\left\{\left[\sin\varphi'\,\ln\left(\xi+\sqrt{\xi^2+\rho^2+R^2-2\rho R\cos(\varphi-\varphi')}\right)\Bigg|_{\xi_-}^{\xi_+}\Bigg|_{\varphi'=0}^{\varphi'=2\pi}\right]+\int_0^{2\pi}\mathrm{d}\varphi'\,\sin\varphi'\left[\frac{\rho R\sin(\varphi-\varphi')}{\sqrt{\xi^2+\rho^2+R^2-2\rho R\cos(\varphi-\varphi')}}\times\frac{1}{\xi+\sqrt{\xi^2+\rho^2+R^2-2\rho R\cos(\varphi-\varphi')}}\Bigg|_{\xi_-}^{\xi_+}\right]\right\} \tag{5.11}$$

Evaluation of the first term between square brackets shows that it vanishes. The remainder can be rewritten to,

$$-\frac{M\rho R^2}{4\pi}\int_0^{2\pi}\mathrm{d}\varphi'\,\sin\varphi'\left[\frac{\sin(\varphi-\varphi')}{\rho^2+R^2-2\rho R\cos(\varphi-\varphi')}\times\frac{\xi}{\sqrt{\xi^2+\rho^2+R^2-2\rho R\cos(\varphi-\varphi')}}\Bigg|_{\xi_-}^{\xi_+}\right] \tag{5.12}$$

The integral over φ' is solved by two consecutive changes in integration variable. First, $2\psi=\pi-(\varphi-\varphi')$, resulting in,

$$-\frac{M\rho R^2}{\pi}\int_{\frac{\pi}{2}-\frac{\varphi}{2}}^{\frac{3}{2}\pi-\frac{\varphi}{2}}\mathrm{d}\psi\,\left(\sin\varphi(\sin^2\psi-\cos^2\psi)-2\cos\varphi\sin\psi\cos\psi\right)\times\frac{\cos\psi\sin\psi}{\rho^2+R^2-2\rho R(\sin^2\psi-\cos^2\psi)}\,\frac{\xi}{\sqrt{\xi^2+\rho^2+R^2-2\rho R(\sin^2\psi-\cos^2\psi)}}\Bigg|_{\xi_-}^{\xi_+} \tag{5.13}$$

where $\sin\varphi'$, $\sin(\varphi-\varphi')$ and $\cos(\varphi-\varphi')$ have been evaluated in terms of basic trigonometric functions. It can be shown that the first term between the larger parentheses does not contribute to the integral, leaving,

$$\frac{2M\rho R^2\cos\varphi}{\pi}\int_{\frac{\pi}{2}-\frac{\varphi}{2}}^{\frac{3}{2}\pi-\frac{\varphi}{2}}\mathrm{d}\psi\,\frac{\cos^2\psi\sin^2\psi}{\rho^2+R^2-2\rho R(\sin^2\psi-\cos^2\psi)}\times\frac{\xi}{\sqrt{\xi^2+\rho^2+R^2-2\rho R(\sin^2\psi-\cos^2\psi)}}\Bigg|_{\xi_-}^{\xi_+} \tag{5.14}$$

Making use of the shorthand from Equation 5.5 and applying a second change in variable, $\sin\psi=x$, allows us to write,

$$\begin{aligned}\rho^2+R^2-2\rho R(\sin^2\psi-\cos^2\psi)&=(\rho+R)^2\left(1-x^2(1-\gamma^2)\right)\\ \xi_\pm^2+\rho^2+R^2-2\rho R(\sin^2\psi-\cos^2\psi)&=\left(\xi_\pm^2+(\rho+R)^2\right)\left(1-x^2(1-k_\pm^2)\right)\end{aligned} \tag{5.15}$$

which upon substitution into Equation 5.14 leads to,

$$\frac{2M\rho R^2\cos\varphi}{\pi(\rho+R)^2}\int_{-\cos\frac{\varphi}{2}}^{\cos\frac{\varphi}{2}}\mathrm{d}x\,\frac{(1-x^2)x^2}{1-x^2(1-\gamma^2)}\,\frac{\beta_\pm}{\sqrt{(1-x^2)\left(1-x^2\left(1-k_\pm^2\right)\right)}}\Bigg|_{\xi_-}^{\xi_+} \tag{5.16}$$

Note the additional factor $1/\sqrt{1-x^2}$ entering the expression because of the change of variable. A more convenient form of this integral is found by applying the following substitution,

$$\frac{(1-x^2)x^2}{1-x^2(1-\gamma^2)} = \frac{1}{1-\gamma^2}\left(\frac{\gamma^2}{1-\gamma^2}+x^2-\frac{\gamma^2}{1-\gamma^2}\frac{1}{1-x^2\,(1-\gamma^2)}\right) \tag{5.17}$$

Splitting the integral in Equation 5.16 according to the terms in Equation 5.17, gives three separate integrals representing (combinations of) elliptic integrals of the first, second and third kind.

The full expression now becomes,

$$\begin{aligned}\frac{2M\rho R^2\cos\varphi}{\pi(\rho+R)^2(1-\gamma^2)}\Bigg(&\frac{\gamma^2}{1-\gamma^2}\int_{-\cos\frac{\varphi}{2}}^{\cos\frac{\varphi}{2}}\mathrm{d}x\,\frac{\beta_\pm}{\sqrt{(1-x^2)\left(1-x^2\left(1-k_\pm^2\right)\right)}}\Bigg|_{\xi_-}^{\xi_+}+\\ &\int_{-\cos\frac{\varphi}{2}}^{\cos\frac{\varphi}{2}}\mathrm{d}x\,x^2\,\frac{\beta_\pm}{\sqrt{(1-x^2)\left(1-x^2\left(1-k_\pm^2\right)\right)}}\Bigg|_{\xi_-}^{\xi_+}-\\ &\frac{\gamma^2}{1-\gamma^2}\int_{-\cos\frac{\varphi}{2}}^{\cos\frac{\varphi}{2}}\mathrm{d}x\,\frac{1}{1-x^2(1-\gamma^2)}\,\frac{\beta_\pm}{\sqrt{(1-x^2)\left(1-x^2\left(1-k_\pm^2\right)\right)}}\Bigg|_{\xi_-}^{\xi_+}\Bigg)\end{aligned} \tag{5.18}$$

Each term can be evaluated using tabulated integrals (cf. [18]). After some elementary rewriting, a concise final result is obtained,

$$\Phi = \frac{MR\cos\varphi}{\pi}\left[\beta_+P_3(k_+)-\beta_-P_3(k_-)\right] \tag{5.19}$$

where we define the auxiliary function $P_3(k)$ as,

$$P_3(k) = \frac{1}{1-k^2}\left(\mathcal{K}-\mathcal{E}\right)-\frac{\gamma^2}{1-\gamma^2}\left(\mathcal{P}-\mathcal{K}\right) \tag{5.20}$$

5.4.2 Magnetic field

To obtain expressions for the magnetic field components in Equation 5.7, the derivatives of the scalar potential Φ in Equation 5.19 can be taken directly. Alternatively, the derivatives can be taken in Equation 5.9, followed by a similar mathematical treatment

as was used for the scalar potential. For brevity, only the final expressions are presented here:

$$\begin{aligned} H_\rho &= -\frac{\partial \Phi}{\partial \rho} &&= \frac{MR\cos\varphi}{2\pi\rho}\left[\beta_+ P_4(k_+) - \beta_- P_4(k_-)\right] \\ H_\varphi &= -\frac{1}{\rho}\frac{\partial \Phi}{\partial \varphi} &&= \frac{MR\sin\varphi}{\pi\rho}\left[\beta_+ P_3(k_+) - \beta_- P_3(k_-)\right] \\ H_z &= -\frac{\partial \Phi}{\partial z} &&= \frac{MR\cos\varphi}{\pi}\left[\alpha_+ P_1(k_+) - \alpha_- P_1(k_-)\right] \end{aligned} \tag{5.21}$$

where a final, slightly more complicated, auxiliary function is defined as,

$$P_4(k) = \frac{\gamma}{1-\gamma^2}\left(\mathcal{P} - \mathcal{K}\right) + \frac{\gamma}{1-\gamma^2}\left(\gamma^2\mathcal{P} - \mathcal{K}\right) - P_1(k) \tag{5.22}$$

Computational effort in the evaluation of these equations is minimal, because of the availability of efficient algorithms to calculate elliptical integrals [19–21]. Figure 5.2b and Figure 5.2c show a graphical representation of the field lines for a cylinder with transverse magnetization.

Note that analytical expressions for the derivatives of Equation 5.21 can be derived easily. This enables the calculation of magnetic forces through $\mathbf{F} = (\mathbf{m}\cdot\boldsymbol{\nabla})\mathbf{B}$ for all points in space, except on the cylinder surface. The magnetic forces are an important element in the Brownian dynamics simulations described in Chapter 6.

5.4.3 Mixed magnetization

Knowing the magnetic field equations for a cylinder with fully longitudinal and transverse magnetization (Equation 5.3 and Equation 5.21), allows the calculation of the field also for intermediate magnetizations. By decomposing the total magnetization in its longitudinal and transverse contributions according to Equation 5.1, the magnetic field for an off-axis magnetization direction is calculated. For the magnetization direction $\mathbf{M} = (1/\sqrt{2}, 0, 1/\sqrt{2})$, the resulting field is shown in Figure 5.2d.

5.5 Limiting cases

In this section we evaluate some limiting cases for the transversely magnetized cylinder, Equation 5.21, and compare these with known expressions from literature. See for example [7] for a treatment of the limiting cases for a longitudinally magnetized cylinder.

5.5.1 Infinite cylinder

In the limit of an infinite cylinder, $L \to \infty$, we have $k = 1$ and $\beta_\pm = \pm 1$. This simplifies the auxiliary functions for the radial and angular components in Equation 5.21 to,

$$\begin{aligned} \left[\beta_+ P_4(\kappa_+) - \beta_- P_4(\kappa_-)\right] &= \pi\frac{1+\gamma^2-2\sqrt{\gamma^2}}{1-\gamma^2}\frac{\gamma}{\sqrt{\gamma^2}} \\ \left[\beta_+ P_3(\kappa_+) - \beta_- P_3(\kappa_-)\right] &= \frac{\pi}{2}\frac{1+\gamma^2-2\sqrt{\gamma^2}}{1-\gamma^2} \end{aligned} \tag{5.23}$$

The z-component correctly vanishes when evaluating the limits. These expressions contain a square root term accounting for points outside ($\gamma > 0$) and inside ($\gamma < 0$) the cylinder. Substitution of Equation 5.23 into Equation 5.21 gives for the radial and angular component, after some rewriting,

$$H_\rho = \begin{cases} \frac{M}{2}\frac{R^2}{\rho^2}\cos\varphi, & \gamma > 0 \\ -\frac{M}{2}\cos\varphi, & \gamma < 0 \end{cases} \qquad H_\varphi = \begin{cases} \frac{M}{2}\frac{R^2}{\rho^2}\sin\varphi, & \gamma > 0 \\ \frac{M}{2}\sin\varphi, & \gamma < 0 \end{cases} \tag{5.24}$$

which are identical to the known expressions from classical magnetostatics [12, 13].

5.5.2 Field on axis

The magnetic field along the axis of the cylinder is found by evaluating Equation 5.21 in the limit of $\rho \to 0$ and $\varphi = 0$. No angular or z-component will be present. In this case we have $\beta_\pm = \xi_\pm/\sqrt{(\xi_\pm^2 + R^2)}$, $\cos\varphi = 1$ and the elliptic integrals $\mathcal{K} = \mathcal{E} = \mathcal{P} = \pi/2$, so that $P_4(k) = -\frac{\pi}{2}(1+\gamma)/(1-\gamma)$. We can write,

$$H_\rho(0,0,z) = -\frac{MR}{4\rho}\frac{1+\gamma}{1-\gamma}\left(\frac{\xi_+}{\sqrt{\xi_+^2 + R^2}} - \frac{\xi_-}{\sqrt{\xi_-^2 + R^2}}\right) \tag{5.25}$$

The term $R/\rho(1+\gamma)/(1-\gamma)$ equals unity so that now the same expression is obtained as in [14],

$$H_\rho(0,0,z) = -\frac{M}{4}\left(\frac{\xi_+}{\sqrt{\xi_+^2 + R^2}} - \frac{\xi_-}{\sqrt{\xi_-^2 + R^2}}\right) \tag{5.26}$$

Evaluating the field in the origin $z = 0$ gives,

$$H_\rho(0,0,0) = -\frac{M}{2}\frac{L}{\sqrt{R^2 + L^2}} = \begin{cases} -\frac{M}{2} & \text{if} L \gg R \\ -\frac{ML}{2R} & \text{if} L \ll R \end{cases} \tag{5.27}$$

again in agreement with earlier findings [14].

5.5.3 Far field limit

For the field far away from the cylinder, $\rho, z \gg R, L$, the field of a point dipole should be retrieved. This is identical in evaluating the limit of $R, L \to 0$. We can arbitrarily set $\varphi = 0$ to eliminate the angular dependence through $\sin\varphi = 0$. To obtain the field equations, we make a first order series expansion around $L = 0$, followed by an additional expansion around $R = 0$. It is impractical to perform these expansions on the final results in Equation 5.21 directly. We therefore start by considering the partial derivatives $H_\rho = -\partial\Phi/\partial\rho$ and $H_z = -\partial\Phi/\partial z$ in integral form (see Equation 5.21,

coming from Equation 5.9). For the radial component we have,

$$\frac{MR}{4\pi}\int_0^{2\pi} \mathrm{d}\varphi' \cos\varphi' \frac{\rho - R\cos\varphi'}{\rho^2 + R^2 - 2R\rho\cos\varphi'} \left.\frac{\xi}{\sqrt{\xi^2 + \rho^2 + R^2 - 2\rho R\cos\varphi'}}\right|_{\xi_-}^{\xi_+} \tag{5.28}$$

The first order expansion of the argument of the integral around $L = 0$ gives,

$$\frac{MRL}{2\pi}\int_0^{2\pi} \mathrm{d}\varphi' \cos\varphi' \frac{\rho - R\cos\varphi'}{\left(z^2 + \rho^2 + R^2 - 2R\rho\cos\varphi'\right)^{3/2}} \tag{5.29}$$

Performing a consecutive expansion around $R = 0$ results in,

$$\frac{MRL}{2\pi}\int_0^{2\pi} \mathrm{d}\varphi' \left(\frac{\rho\cos\varphi'}{\left(z^2 + \rho^2\right)^{3/2}} - \frac{R(z^2 - 2\rho^2)\cos^2\varphi'}{\left(z^2 + \rho^2\right)^{5/2}}\right) \tag{5.30}$$

Evaluation of the integral eliminates the first term. Solving the remaining integral immediately leads to the final results for the radial component,

$$H_\rho = \frac{MR^2L}{2}\frac{2\rho^2 - z^2}{\left(z^2 + \rho^2\right)^{5/2}} \tag{5.31}$$

For the z-component, we follow similar steps, starting with,

$$-\frac{MR}{4\pi}\int_0^{2\pi} \mathrm{d}\varphi' \cos\varphi' \left.\frac{1}{\sqrt{\xi^2 + \rho^2 + R^2 - 2\rho R\cos\varphi'}}\right|_{\xi_-}^{\xi_+} \tag{5.32}$$

where the expansion around $L = 0$ leads to,

$$\frac{MRL}{2\pi}\int_0^{2\pi} \mathrm{d}\varphi' \cos\varphi' \frac{z}{\left(z^2 + \rho^2 + R^2 - 2\rho R\cos\varphi'\right)^{3/2}} \tag{5.33}$$

The second expansion around $R = 0$ gives,

$$-\frac{MRL}{2\pi}\int_0^{2\pi} \mathrm{d}\varphi' \left(\frac{z\cos\varphi'}{\left(z^2 + \rho^2\right)^{3/2}} + \frac{3z\rho R\cos^2\varphi'}{\left(z^2 + \rho^2\right)^{5/2}}\right) \tag{5.34}$$

As before, the first term in the integral cancels out, so that the final solution is given by,

$$H_z = \frac{MR^2L}{2}\frac{3\rho z}{\left(z^2 + \rho^2\right)^{5/2}} \tag{5.35}$$

Equation 5.31 and Equation 5.35 match the field for a point dipole [9], where only the radial and z variable are swapped because the alignment of the magnetization vector here is along the x-axis and not the z-axis.

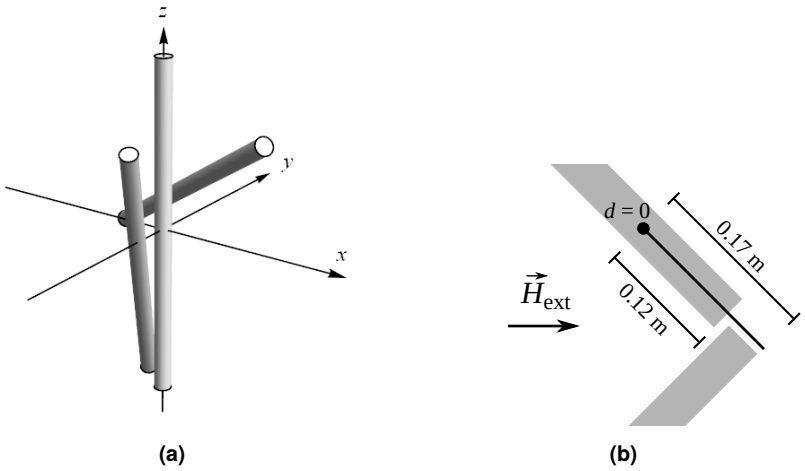

Figure 5.3. (a) Relative configuration of the three cylinder case. The permanent magnetization direction for the three unrotated cylinders is identical. (b) The relative configuration of two cylinders placed in an homogeneous external field. The resulting field is sampled along the thick line, starting from the point marked with a dot ($d = 0$).

5.6 Numerical validation

The validity of our analytical approach is tested by comparison with numerical calculations in a finite-element solver (MagNet 7.5, Infolytica Corp.). As a first case we consider a single, permanently magnetized cylinder, aligned along the z-axis of a Cartesian coordinate system. The cylinder has a radius of $R = 0.3$ m and semi-length $L = 6.0$ m. Note that due to the nature of the software, object dimensions have to have units, but this is not expected to influence the qualitative magnetic behaviour of the object. Its material properties are set to represent an ideal permanent magnet with a fixed magnetization direction and a magnitude of 800 000 A m^{-1}, in order to generate a B-field of approximately 1 T. For the single cylinder, three magnetization directions are considered: completely longitudinal, completely transversal, and a mixed case with magnetization vector $\mathbf{M} = (1/\sqrt{2}, 1/\sqrt{2}, 0)$. As a second case, a set of three cylinders with different orientations and positions is considered (see Figure 5.3a). The permanent magnetization direction in each cylinder is equal to the mixed magnetization case of the single cylinder.

The magnetic field is calculated using the built-in solver of MagNet, ensuring that the calculation mesh in the vicinity of the cylinder is sufficiently fine-grained. The field components B_x, B_y and B_z are sampled on the three perpendicular Cartesian planes through the origin, with 50 sample points per unit length along each axis. The field is also calculated for all sampled points using our analytical model. The correlation between the values from the analytical and numerical model is determined for each case by plotting the numerical values against the analytical values, and by calculating the coefficient of determination R^2, using the Pearson product-moment correlation.

As an example result, the comparison for the three cylinders case measured across

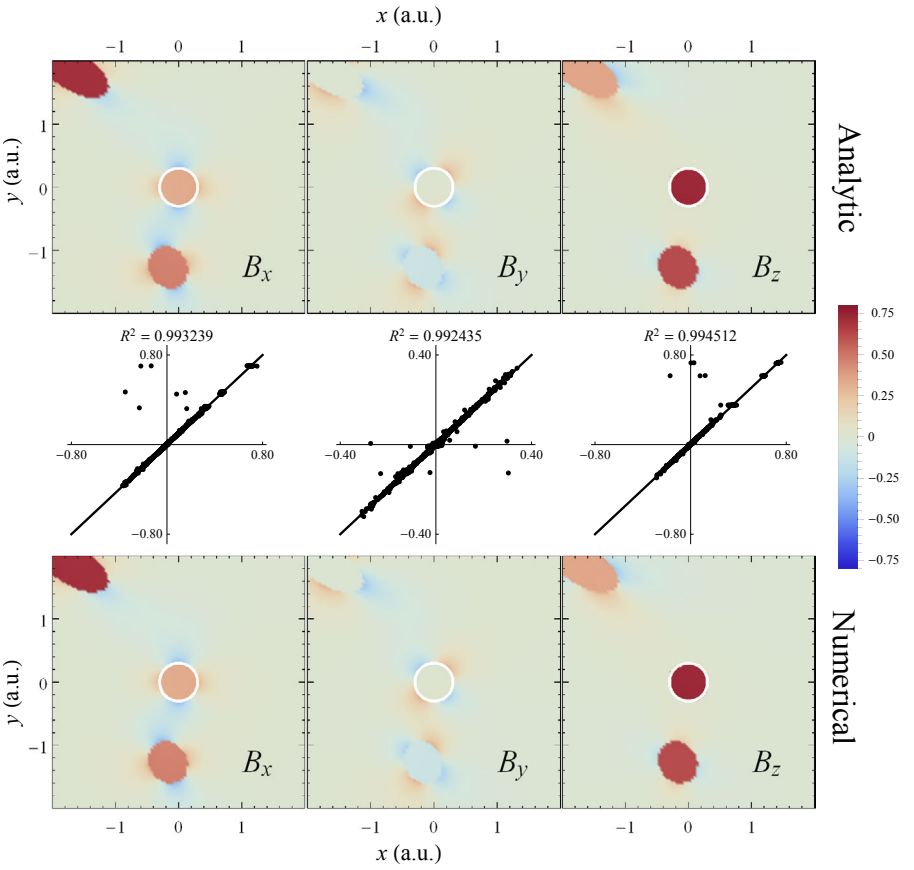

Figure 5.4. Comparison of the analytical model and numerical calculations of the magnetic field (in T) sampled at the xy-plane for a configuration of three cylinders (see Figure 5.3a). The top row shows our analytical calculations and the bottom row shows the results from the finite-element calculations in MagNet. The excellent agreement between the two is visible from the correlation plots in the middle row.

the xy-plane is shown in Figure 5.4. The agreement between the analytical model and the numerical results is excellent (in all cases $R^2 > 0.99$), confirming that the superposition of multiple individual fields through the combination of transverse and longitudinal magnetization components gives correct results. Any noise is due to the mesh-based approach of the finite-element solver, giving rise to artefacts near the edge of the cylinder, where there is a discontinuity in the field. In Section 5.B an overview is given of all comparisons for the single cylinder and three cylinders cases. Here agreement is also excellent ($R^2 > 0.98$).

We also investigate the validity of our analytic equations for the description of magnetizable materials and the mutual influence of two magnetized cylinders. Two perpendicular cylinders are placed in a homogeneous field (0.95 T), with a small gap in between them (see Figure 5.3b). As a reference state, the same cylinder configuration

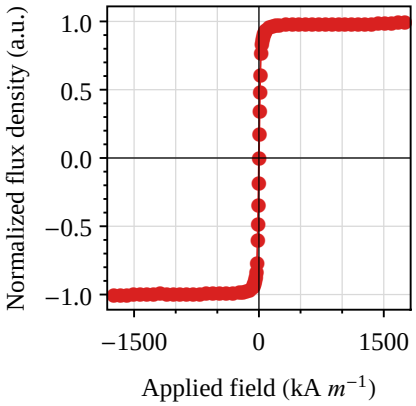

Figure 5.5. Normalized magnetic hysteresis curve for an iron alloy AluChrom cylinder.

is taken, but without the external field, and both cylinders are permanently magnetized in the direction of the external field (PP state). In two alternative states, the external field is applied, and one or both cylinders are constructed from a magnetizable material (MP and MM states). The material properties for the magnetizable material are set as magnetically non-linear and isotropic with a saturation magnetization of 985 000 A m^{-1}, corresponding to the properties of the commercial low-remanence iron alloy AluChrom® (ThyssenKrupp). The magnetic hysteresis curve of the alloy material is measured using a Microsense EZ9 vibrating sample magnetometer and is used as input for the AluChrom material properties (see Figure 5.5).

The x and z-components of the magnetic field are calculated along the line indicated in Figure 5.3b. The calculation is repeated for the different combinations of cylinders and the results are shown in Figure 5.6. The y-component displays very similar behaviour and is therefore not shown. The agreement between the permanently magnetized case (and by extension, our analytical model) and the magnetizable cylinder is quite good, except near the edges where numerical deviations up to 25 % are observed. This can be explained in part by the fact that the magnetization vector for the permanently magnetized cylinder is fixed, whereas the magnetization vector for the magnetizable cylinder will rotate as described by the Stoner-Wohlfarth model, thus altering the local magnetic fields. Updating the magnetization vector of the permanently magnetized cylinders to reflect the actual, average magnetization vector found for the magnetizable cylinders, will likely improve the description of the magnetic field. A second effect is the non-uniform magnetization of the magnetizable cylinders inherent to the magnetizability of the material. This gives rise to a different magnetization of the material near the end points of the cylinder and a subsequent effect on the local magnetic field. A final effect is the mutual influence of the cylinders on their respective magnetizations through perturbation of the local magnetic field, which is not accounted for in the case of permanently magnetized cylinders.

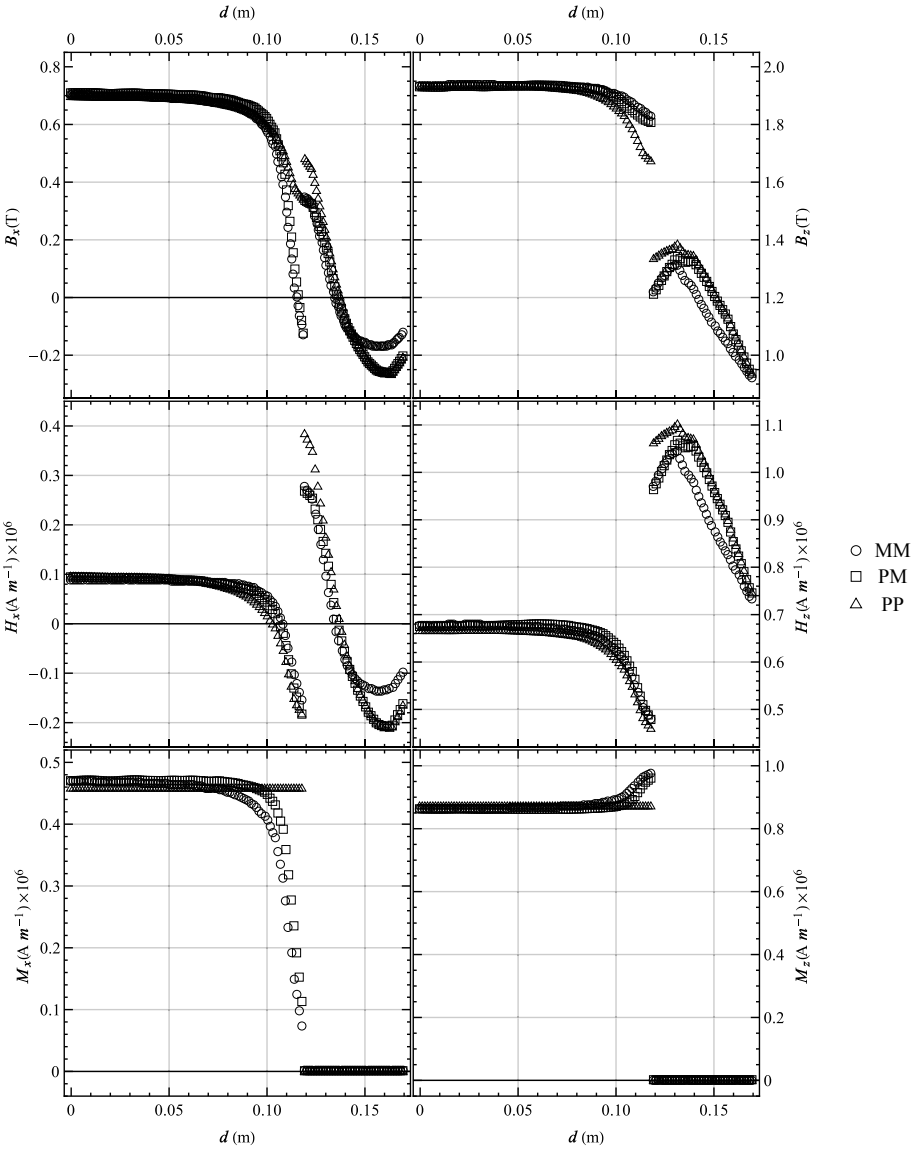

Figure 5.6. Plots of different magnetic quantities (left column, B_x, H_x and M_x; right column, B_z, H_z and M_z) calculated with a finite-element method along the measurement line as shown in Figure 5.3b. The three different combinations of cylinders are marked with circles (magnetized-magnetized, ○), squares (magnetized-permanent, □), and triangles (permanent-permanent △). The PP-case gives results identical to our analytic expressions. The discontinuity at $d = 0.12\,\mathrm{m}$ marks the end of the cylinder and the transition to air.

5.7 Conclusion and outlook

In this chapter we have derived an analytical expression for the magnetic field of a transversely magnetized cylinder of finite length, as an addition to the known expression for longitudinal magnetization. The formulation in terms of elliptic integrals allows for the evaluation of the field strength at any desired coordinate. Combining both expressions through linear superposition allows the calculation of the magnetic field of a cylinder with an arbitrary magnetization vector. Our results are in very good agreement with finite-element calculations, and even provide a mesh-less solution without artefacts.

A comparison has been made between the analytical expression and finite-element numerical calculations for a magnetizable cylinder. Along the length of the cylinder only a minor disagreement is found, but close to the edges the disagreement increases up to 25 %. These deviations may be attributed to a rotated magnetization vector in light of the Stoner-Wohlfarth model, inhomogeneous magnetization of the cylinder and ignoring mutual influences between the cylinders. In principle it is possible to account for inhomogeneously magnetized cylinders, provided a functional form of the magnetization is known. This requires a replacement of the constant magnetization in the integral formulation, by a position dependent magnetization density.

As an outlook for the application of the formulas derived in this chapter, it is also possible to calculate the gradient of the magnetic field analytically. This is especially convenient for applications where magnetic forces need to be calculated, for example in the simulation of the movement of magnetic (nano)particles in a field gradient. This topic will be further investigated in Chapter 6.

Acknowledgements

Alessio Caciagli is thanked for his major contributions to the mathematics and calculations presented in this chapter. Bonny Kuipers is thanked for useful discussions, and Remie Janssen is thanked for critically reading the manuscript.

References

1. J. D. Jackson, *Classical electrodynamics*, 3rd ed., Wiley, New York, NY, **1999**.
2. J. H. Coggon, 'Electromagnetic and electrical modeling by the finite element method', *Geophysics* **1971**, *36*, 132–155, DOI 10.1190/1.1440151.
3. J.-M. Jin, *The finite element method in electromagnetics*, 3rd ed., John Wiley & Sons, **2014**.
4. K. Warnke, 'Finite-element modeling of the separation of magnetic microparticles in fluid', *IEEE Transactions on Magnetics* **2003**, *39*, 1771–1777, DOI 10.1109/TMAG.2003.810609.
5. V. Schaller, U. Kräling, C. Rusu, K. Petersson, J. Wipenmyr, A. Krozer, G. Wahnström, A. Sanz-Velasco, P. Enoksson, C. Johansson, 'Motion of nanometer sized magnetic particles in a magnetic field gradient', *Journal of Applied Physics* **2008**, *104*, 093918, DOI 10.1063/1.3009686.
6. M. W. Garrett, 'Axially symmetric systems for generating and measuring magnetic fields. Part I', *Journal of Applied Physics* **1951**, *22*, 1091–1107, DOI 10.1063/1.1700115.
7. E. E. Callaghan, S. H. Maslen, The Magnetic Field of a Finite Solenoid, Technical Note D-465, National Aeronautics and Space Administration, Washington, **1960**.
8. J. T. Conway, 'Exact solutions for the magnetic fields of axisymmetric solenoids and current distributions', *IEEE Transactions on Magnetics* **2001**, *37*, 2977–2988, DOI 10.1109/20.947050.
9. N. Derby, S. Olbert, 'Cylindrical magnets and ideal solenoids', *American Journal of Physics* **2010**, *78*, 229–235, DOI 10.1119/1.3256157.

10. M. W. Garrett, 'Calculation of Fields, Forces, and Mutual Inductances of Current Systems by Elliptic Integrals', *Journal of Applied Physics* **1963**, *34*, 2567–2573, DOI 10.1063/1.1729771.
11. J. E. Lane, R. C. Youngquist, C. D. Immer, J. C. Simpson, Magnetic Field, Force, and Inductance Computations for an Axially Symmetric Solenoid, Technical Note TM—2013-217918, National Aeronautics and Space Administration, Washington, **2001**.
12. J. Stratton, *Electromagnetic theory*, McGraw-Hill Book Company, New York and London, **1941**.
13. J. A. Oberteuffer, 'Magnetic separation: A review of principles, devices, and applications', *IEEE Transactions on Magnetics* **1974**, *10*, 223–238, DOI 10.1109/TMAG.1974.1058315.
14. G. M. Wysin, Demagnetization Fields, Lecture notes (online at https://www.phys.ksu.edu/personal/wysin/), **2012**.
15. E. C. Stoner, E. P. Wohlfarth, 'A mechanism of magnetic hysteresis in heterogeneous alloys', *IEEE Transactions on Magnetics* **1991**, *27*, 3475–3518, DOI 10.1109/TMAG.1991.1183750.
16. Z. Nagy, B. J. Nelson, 'Lagrangian Modeling of the Magnetization and the Magnetic Torque on Assembled Soft-Magnetic MEMS Devices for Fast Computation and Analysis', *IEEE Transactions on Robotics* **2012**, *28*, 787–797, DOI 10.1109/TRO.2012.2193230.
17. R. Bulirsch, 'Numerical calculation of elliptic integrals and elliptic functions', *Numerische Mathematik* **1965**, *7*, 78–90, DOI 10.1007/BF01397975.
18. I. Ryzhik, I. Gradstein, *Tables of Series, Products and Integrals*, Veb. Deutscher Verlag der Wissenschaften, **1957**.
19. B. C. Carlson, 'Computing elliptic integrals by duplication', *Numerische Mathematik* **1979**, *33*, 1–16, DOI 10.1007/BF01396491.
20. T. Fukushima, 'Precise and fast computation of the general complete elliptic integral of the second kind', *Mathematics of Computation* **2011**, *80*, 1725–1743, DOI 10.1090/S0025-5718-2011-02455-5.
21. T. Fukushima, 'Precise and fast computation of a general incomplete elliptic integral of third kind by half and double argument transformations', *Journal of Computational and Applied Mathematics* **2012**, *236*, 1961–1975, DOI 10.1016/j.cam.2011.11.007.

Appendix 5.A Rewriting the generalized elliptic integral

Derby and Olbert [9] provide an expression for the magnetic field of a longitudinally magnetized cylinder (equivalently, an ideal solenoid of finite length) in terms of a generalized complete elliptic integral, $C(k_c, p, c, s)$. This integral is evaluated numerically by an efficient computational procedure [17]. We find it useful to express C in the more commonly used complete elliptic integrals of the first, second and third kind to obtain expressions similar to Equation 5.21.

The generalized complete elliptic integral is defined in [9] as

$$C(k_c, p, c, s) = \int_0^{\pi/2} \mathrm{d}\varphi \, \frac{c\cos^2\varphi + s\sin^2\varphi}{\sqrt{\cos^2\varphi + k_c^2\sin^2\varphi}\,(\cos^2\varphi + p\sin^2\varphi)} \tag{5.36}$$

For the evaluation of B_ρ, $C(k_\pm, 1, 1, -1)$, is required, simplifying Equation 5.36 to

$$\int_0^{\pi/2} \mathrm{d}\varphi \, \frac{\cos^2\varphi - \sin^2\varphi}{\sqrt{\cos^2\varphi + k_\pm^2\sin^2\varphi}\,(\cos^2\varphi + \sin^2\varphi)} \tag{5.37}$$

We now make a change in variable $\sin\varphi = x$, and rewrite to obtain,

$$\begin{aligned} &\int_0^1 \frac{\mathrm{d}x}{\sqrt{1-x^2}} \frac{\left(1-x^2\right) - x^2}{\sqrt{\left(1-x^2\right) + k_\pm^2 x^2}\,\left(\left(1-x^2\right) + x^2\right)} \\ &= \int_0^1 \mathrm{d}x \, \frac{1}{\sqrt{\left(1-x^2\right)\left(1-\left(1-k_\pm^2\right)x^2\right)}} - 2\int_0^1 \mathrm{d}x \, \frac{x^2}{\sqrt{\left(1-x^2\right)\left(1-\left(1-k_\pm^2\right)x^2\right)}} \end{aligned} \tag{5.38}$$

These integrals can be solved immediately using tabulated functions [18] (eq. 8.112). This gives finally,

$$C(k_\pm, 1, 1, -1) = \mathcal{K} - 2\left(1-k_\pm^2\right)^{-1}(\mathcal{K} - \mathcal{E}) \tag{5.39}$$

Where the usual substitutions have been made (see Equation 5.6). This result is used in Equation 5.4 as $P_1(k)$.

For the evaluation of B_z, $C(k_\pm, \gamma^2, 1, \gamma)$ is needed[1], resulting in

$$\int_0^{\pi/2} \mathrm{d}\varphi \, \frac{\cos^2\varphi + \gamma\sin^2\varphi}{\sqrt{\cos^2\varphi + k_\pm^2\sin^2\varphi}\,(\cos^2\varphi + \gamma^2\sin^2\varphi)} \tag{5.40}$$

[1]The fourth argument changes sign here with respect to [9], because of our change of sign of γ

Following as before gives,

$$\begin{aligned}
&\int_0^1 \frac{\mathrm{d}x}{\sqrt{1-x^2}} \frac{\left(1-x^2\right)-\gamma x^2}{\sqrt{\left(1-x^2\right)+k_{\pm}^2 x^2}\left(\left(1-x^2\right)+\gamma^2 x^2\right)} \\
&= \int_0^1 \mathrm{d}x \frac{1}{\sqrt{\left(1-x^2\right)\left(1-\left(1-k_{\pm}^2\right)x^2\right)}\left(1-\left(1-\gamma^2\right)x^2\right)} - \\
&\qquad (1+\gamma)\int_0^1 \mathrm{d}x \frac{x^2}{\sqrt{\left(1-x^2\right)\left(1-\left(1-k_{\pm}^2\right)x^2\right)}\left(1-\left(1-\gamma^2\right)x^2\right)}
\end{aligned} \tag{5.41}$$

Evaluating these integrals leads to the final result, which is used in Equation 5.4 as $P_2(k)$.

$$\begin{aligned}
C(k_{\pm},\gamma^2,1,\gamma) &= \mathcal{P} - (1+\gamma)\frac{1}{1-\gamma^2}(\mathcal{P}-\mathcal{K}) \\
&= \frac{1-\gamma^2}{1-\gamma^2}\mathcal{P} - \frac{1}{1-\gamma^2}(\mathcal{P}-\mathcal{K}) - \frac{\gamma}{1-\gamma^2}(\mathcal{P}-\mathcal{K}) \\
&= -\frac{1}{1-\gamma^2}\left(\gamma^2\mathcal{P}-\mathcal{K}\right) - \frac{\gamma}{1-\gamma^2}(\mathcal{P}-\mathcal{K})
\end{aligned} \tag{5.42}$$

Note that in all cases, the evaluation of the integral at $\gamma = \pm 1$ (i.e. evaluation at $\rho = R$) leads to division by zero, so that the field on the surface of the cylinder cannot be probed by these formulas.

Appendix 5.B Comparison plots of magnetic field

In this appendix, plots are presented for the comparison between the analytical model and numerical calculations using MagNet's finite-element solver, similar to Figure 5.4. See the main text for an explanation of the different situations.

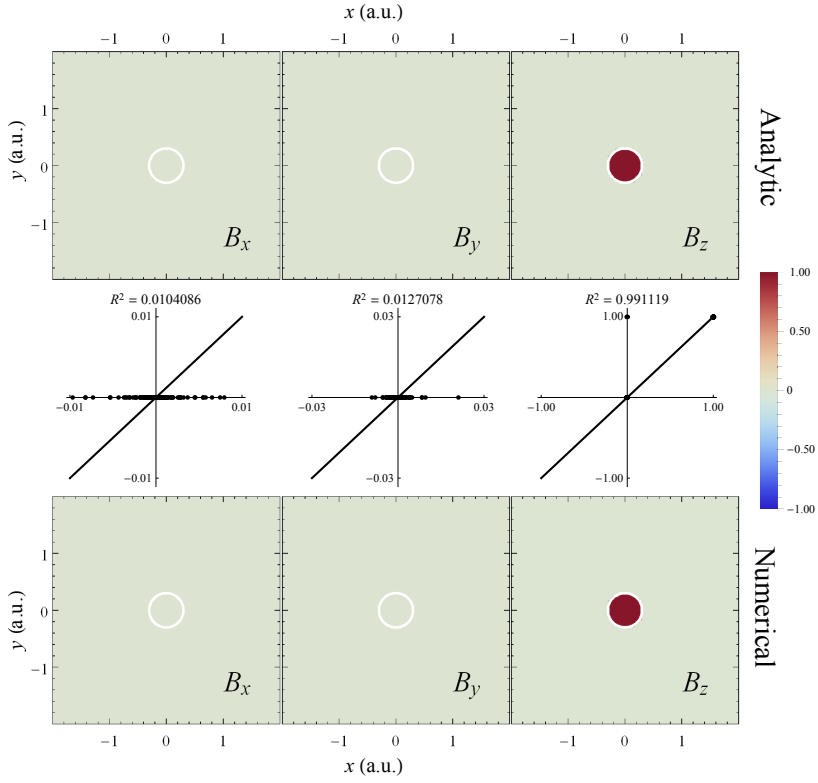

Figure 5.7. Longitudinally magnetized cylinder, xy-plane, $z = 0$.

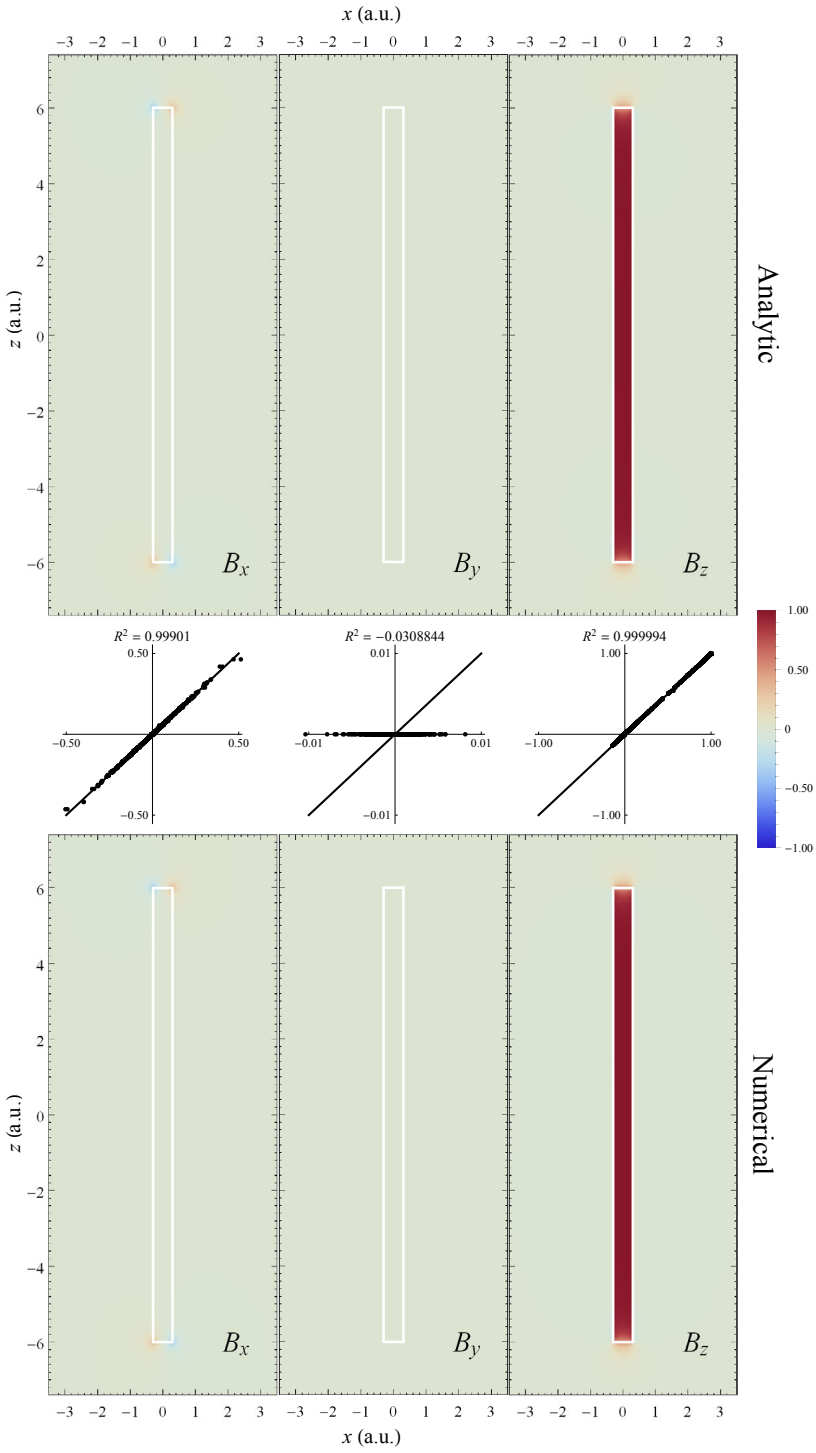

Figure 5.8. Longitudinally magnetized cylinder, xz-plane, $y = 0$.

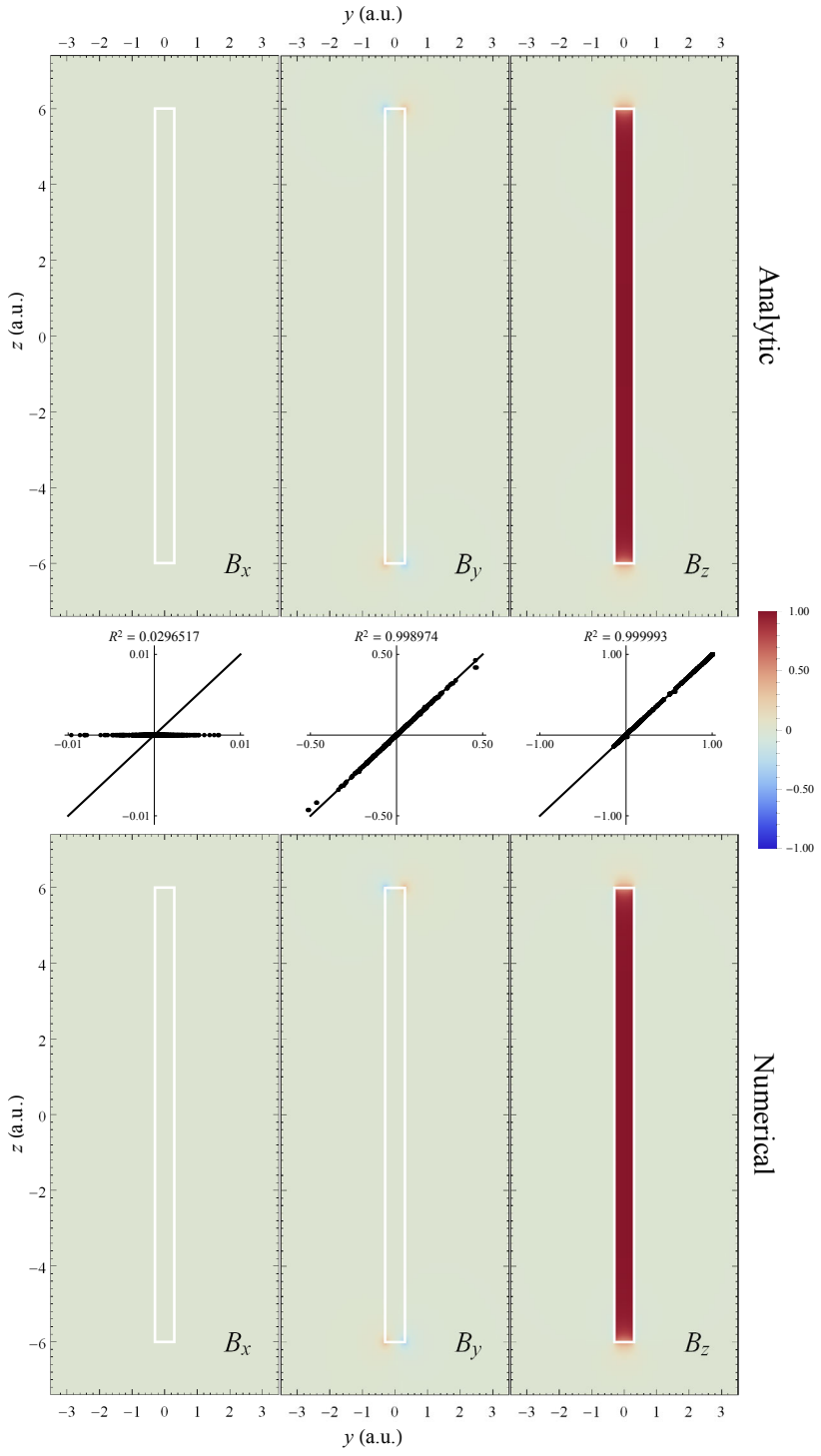

Figure 5.9. Longitudinally magnetized cylinder, yz-plane, $x = 0$.

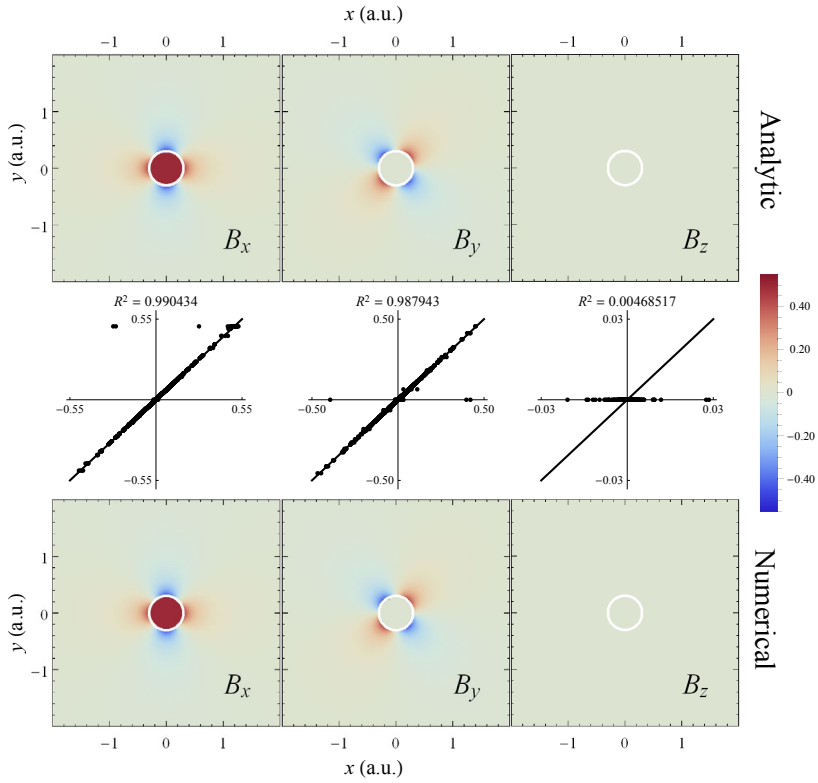

Figure 5.10. Transversally magnetized cylinder, xy-plane, $z = 0$.

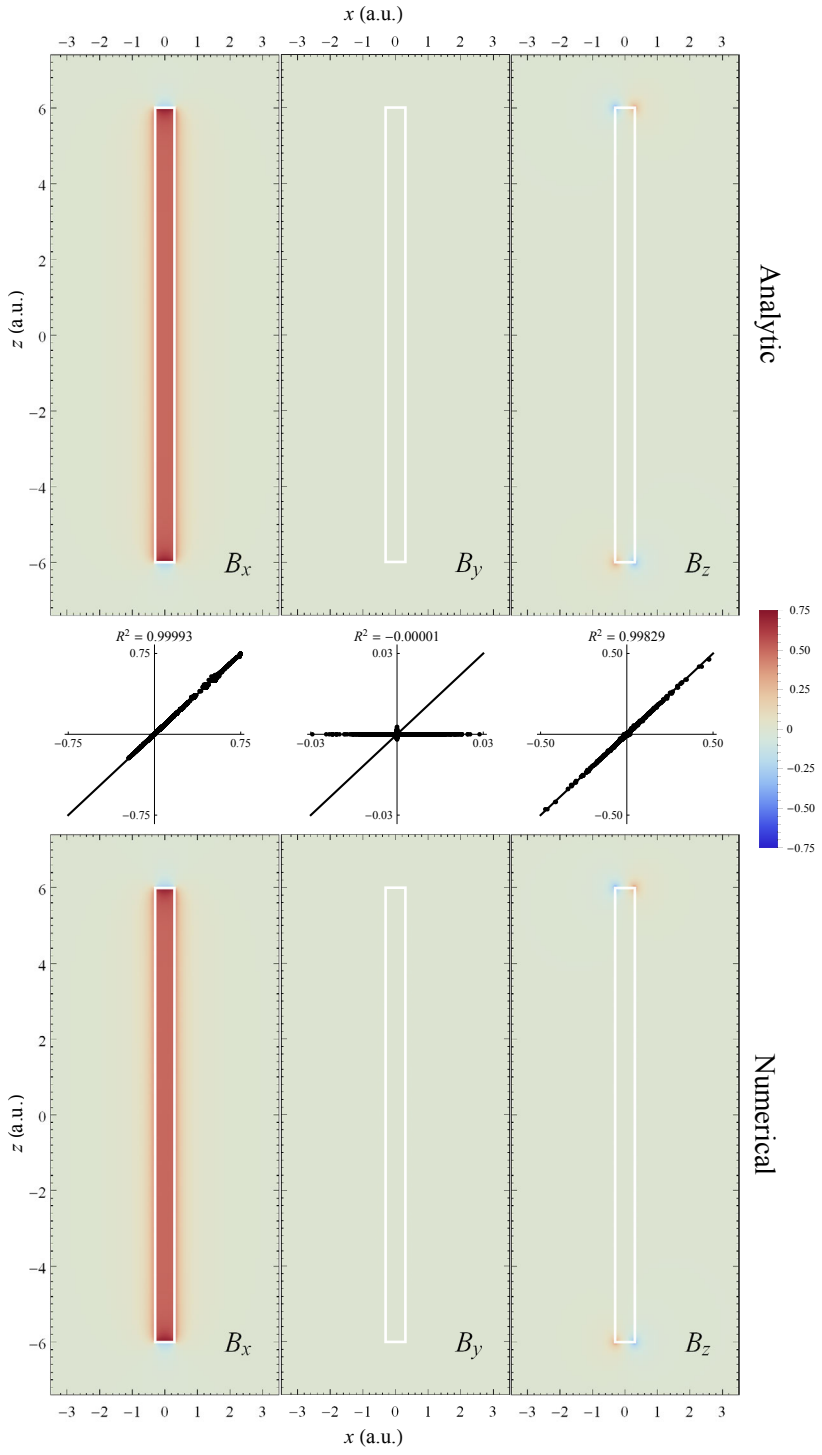

Figure 5.11. Transversally magnetized cylinder, xz-plane, $y = 0$.

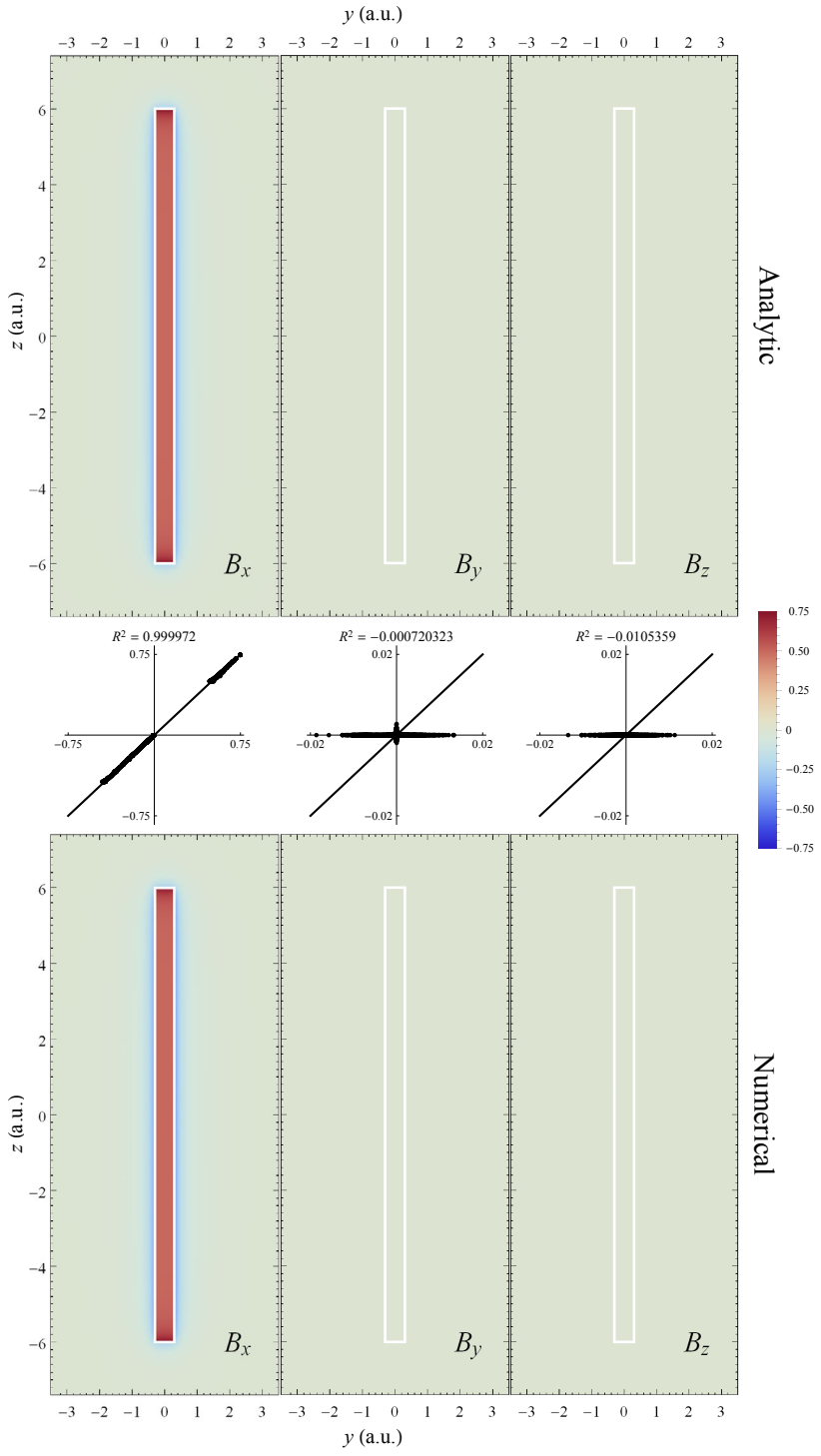

Figure 5.12. Transversally magnetized cylinder, yz-plane, $x = 0$.

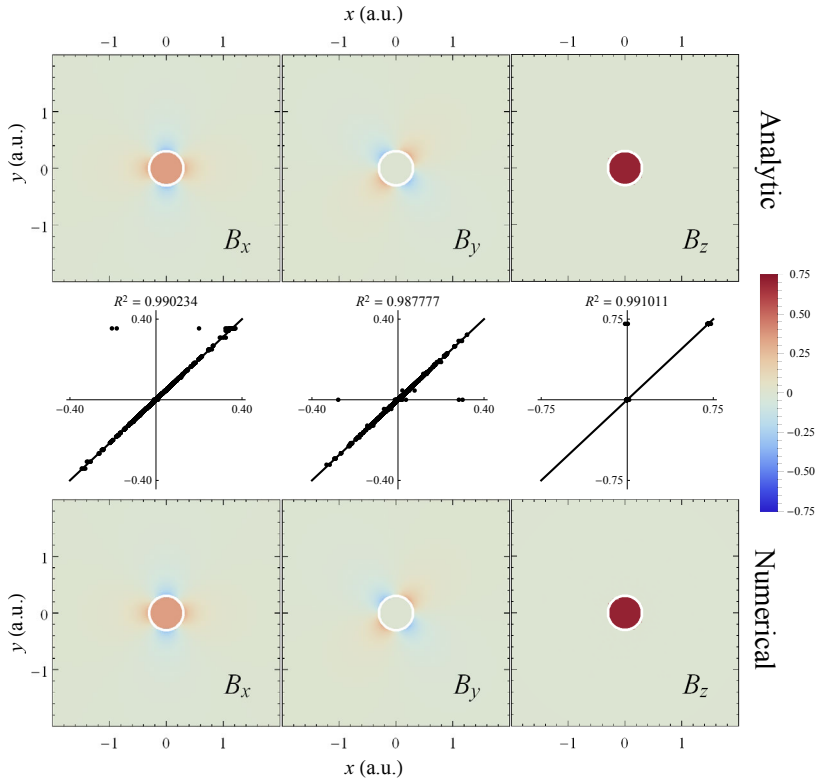

Figure 5.13. Mixed magnetized cylinder, xy-plane, $z = 0$.

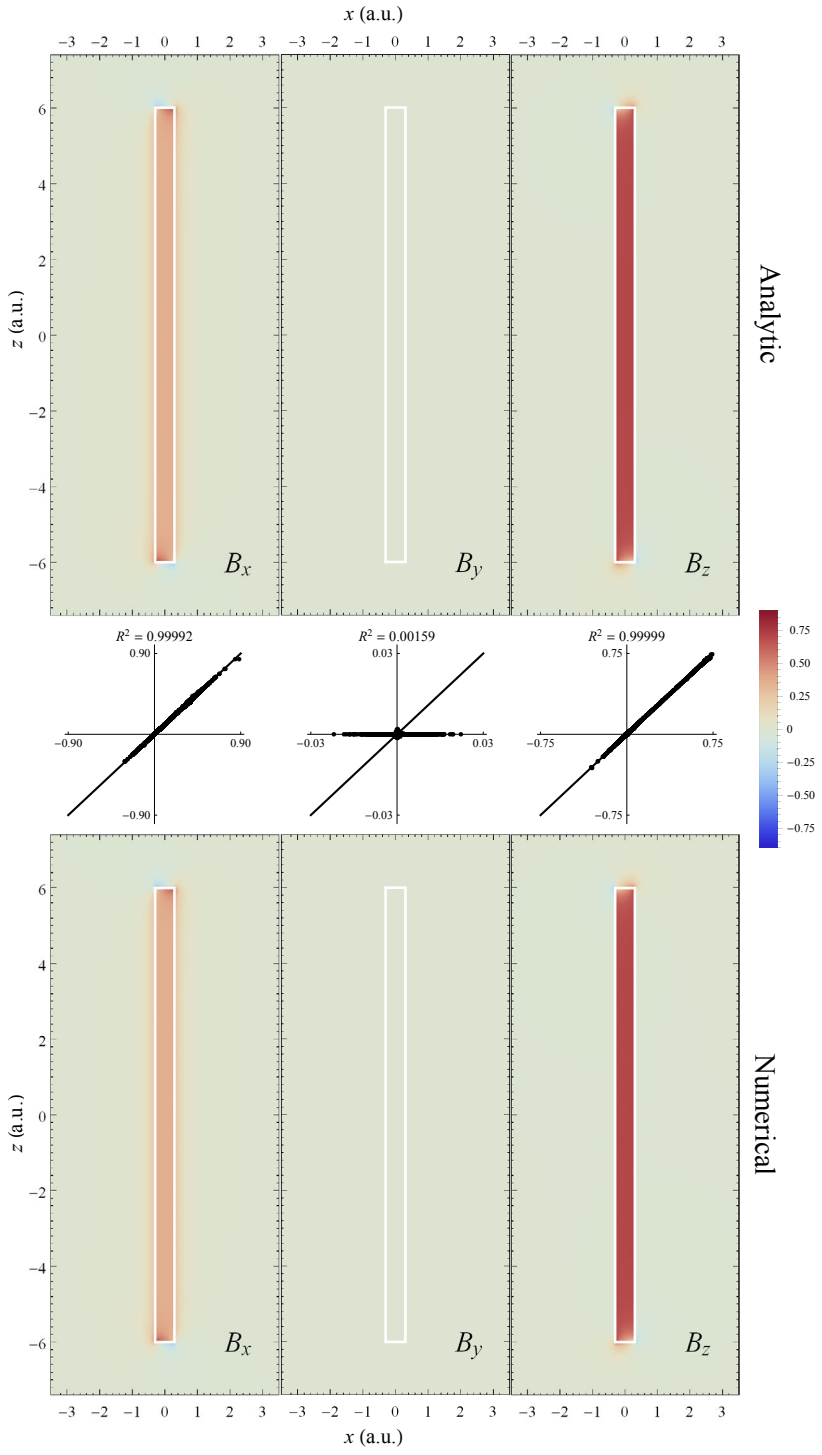

Figure 5.14. Mixed magnetized cylinder, xz-plane, $y = 0$.

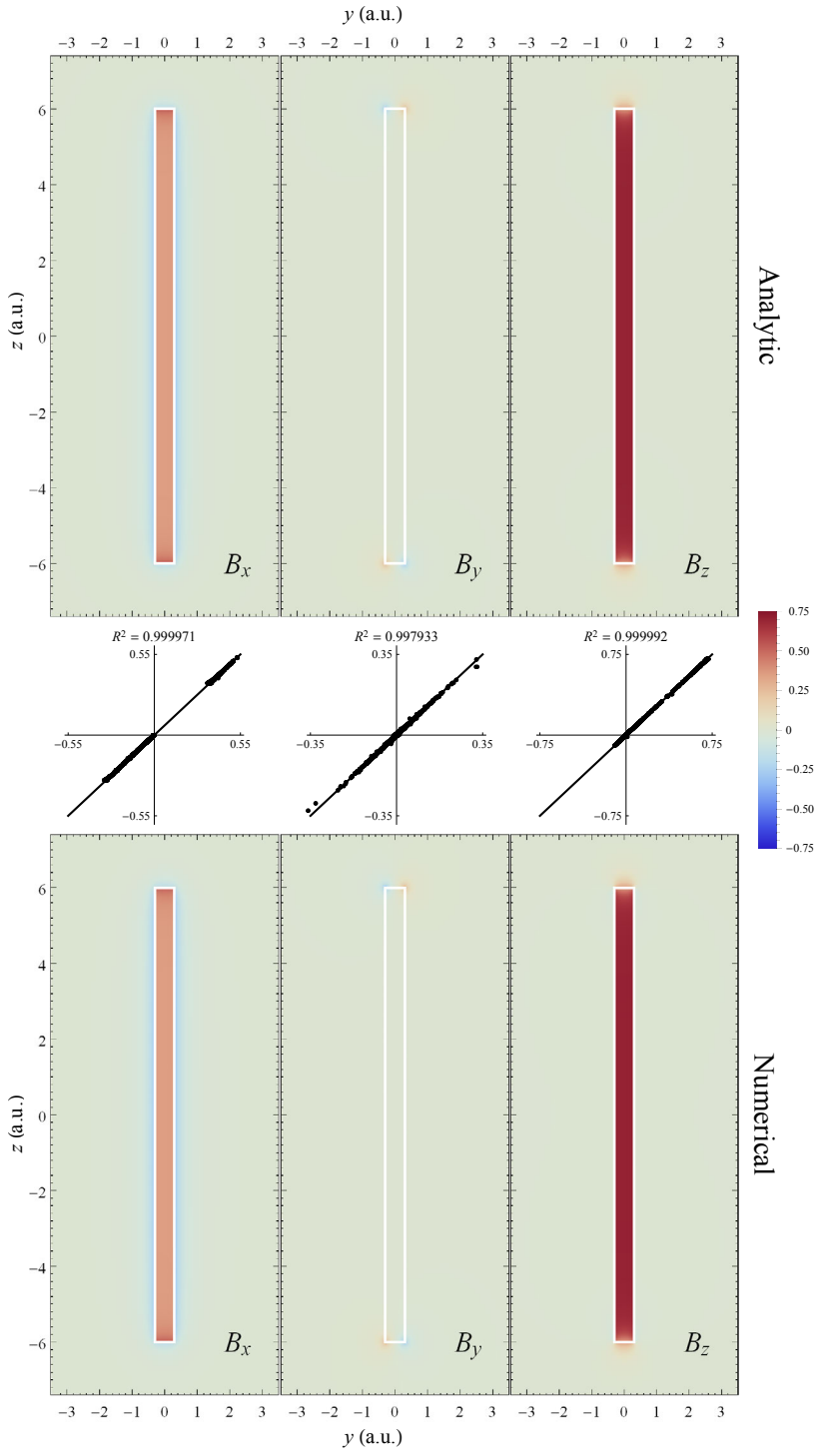

Figure 5.15. Mixed magnetized cylinder, yz-plane, $x = 0$.

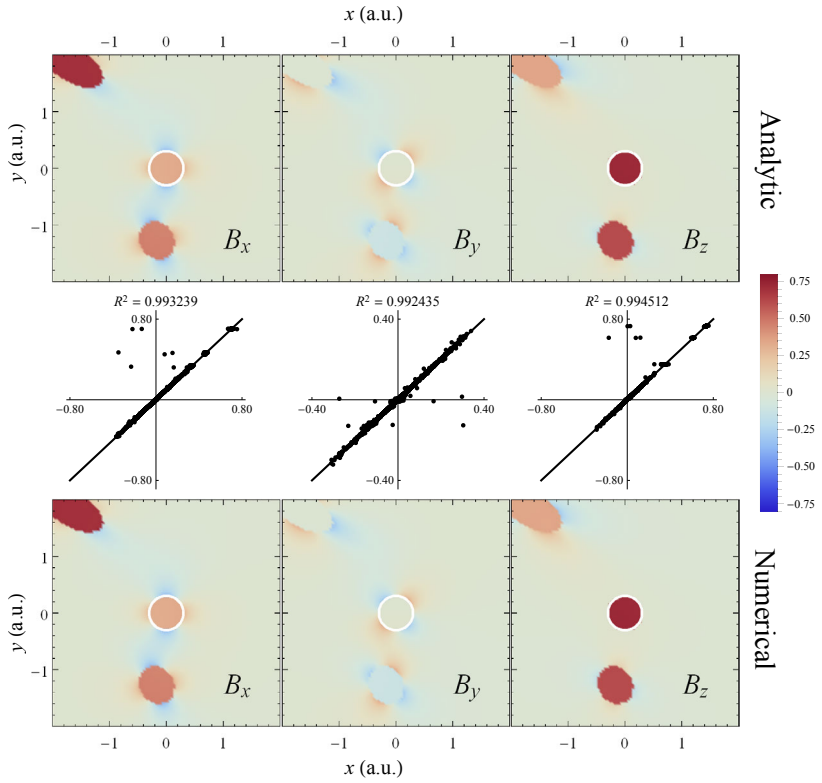

Figure 5.16. Three cylinder case, xy-plane, $z = 0$.

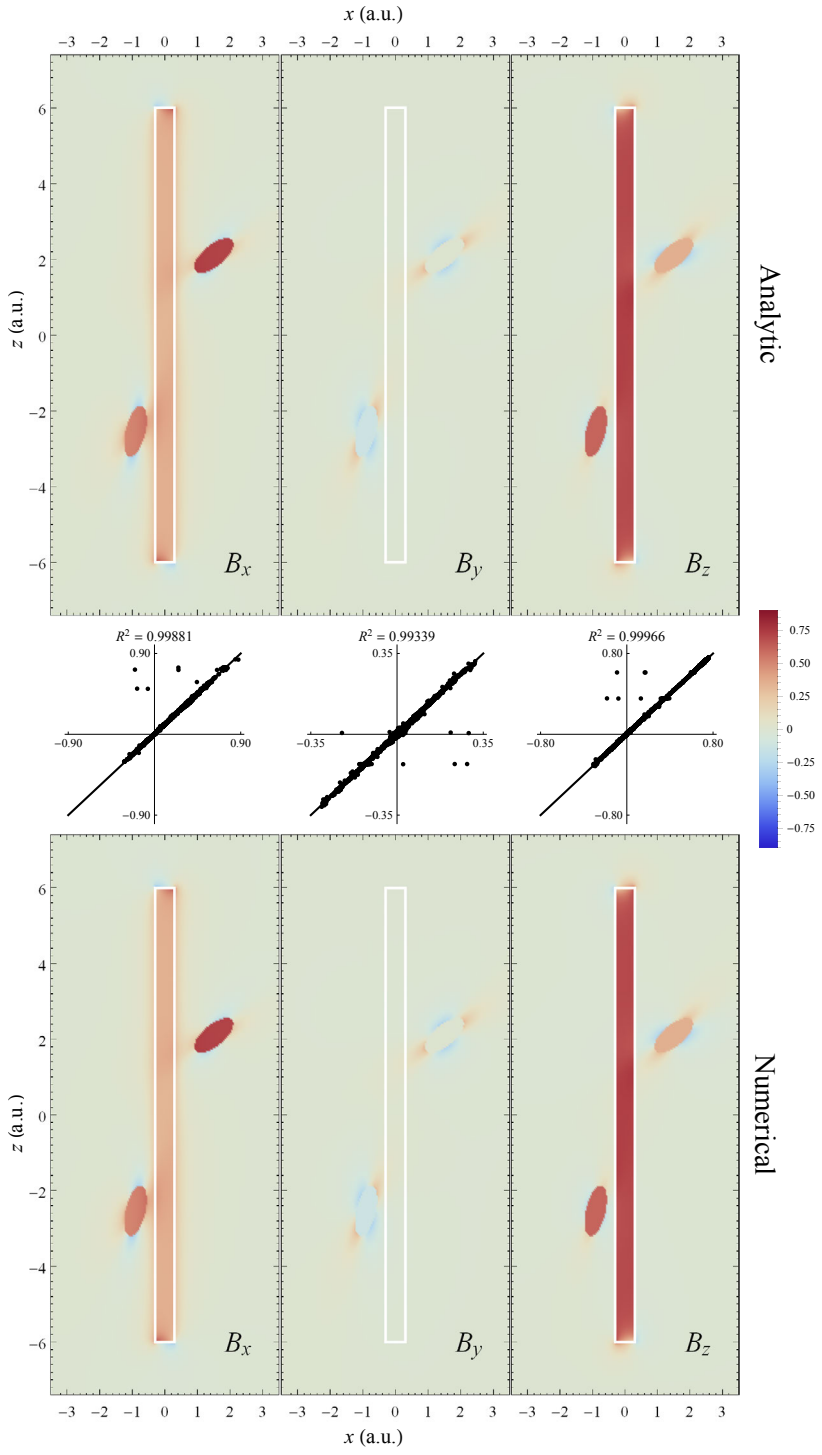

Figure 5.17. Three cylinder case, xz-plane, $y = 0$.

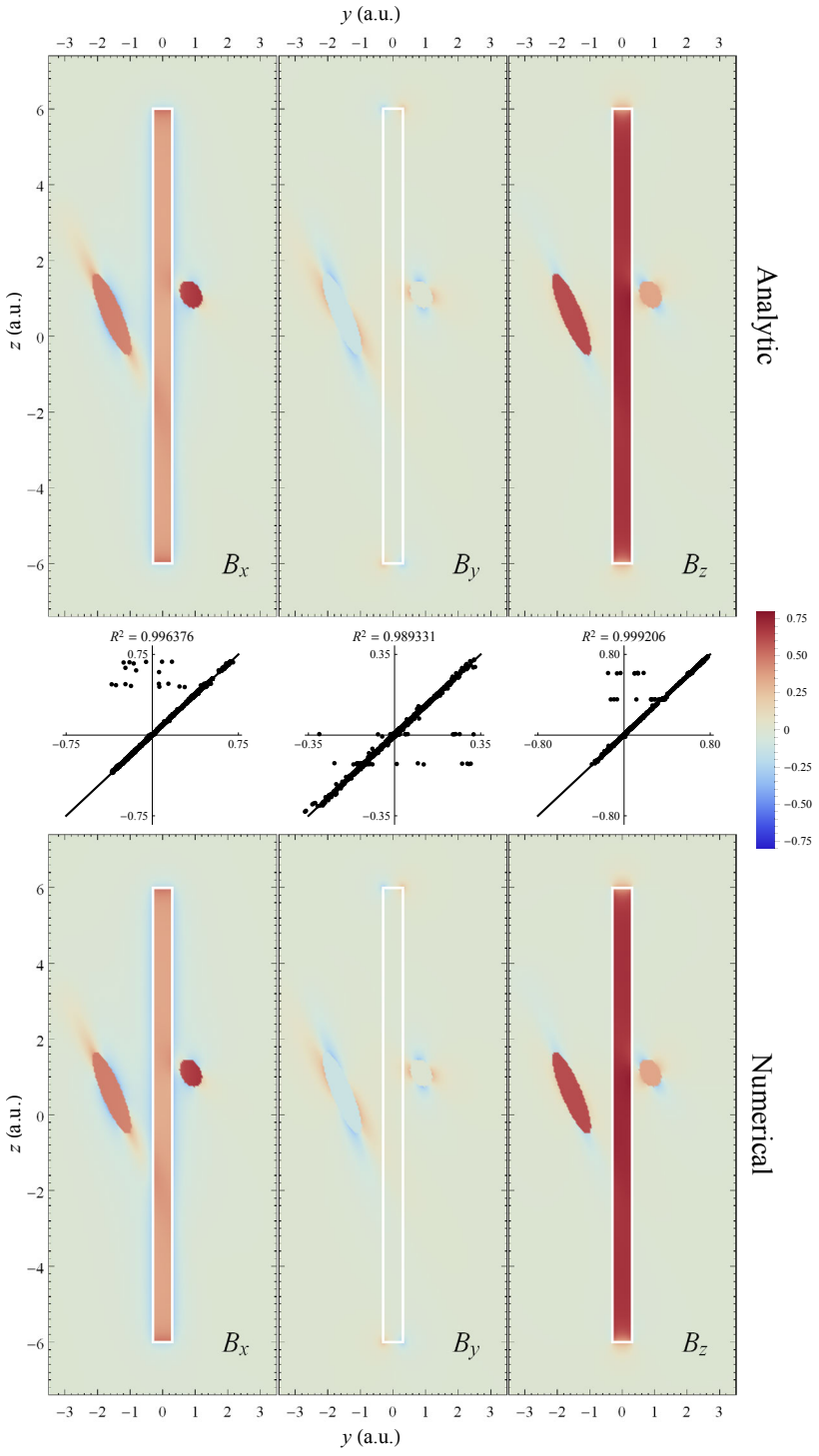

Figure 5.18. Three cylinder case, yz-plane, $x = 0$.

6

Separation of magnetic nanoparticles in magnetic random porous media I: Brownian dynamics simulation

Abstract

The separation of magnetic nanoparticles by a magnetizable cylinder is studied through Brownian dynamics simulations. A cylinder is chosen as a magnetic source to produce strong magnetic field gradients, allowing a fast capture of nanoparticles. Particles down to sizes of 50 nm are successfully and completely captured, typically within 50 s simulated time. For smaller particles, Brownian motion starts to dominate over magnetic forces, making rapid capture difficult. We find that cylinders that are oriented perpendicular to the external field and have an aspect ratio of $L/D \lessapprox 6$ are best suited for particle capture. Hydrodynamic interactions and magnetic dipole-dipole interactions are included in the simulation, leading to chain formation of nanoparticles and an enhanced capture speed.

6.1 Introduction

The magnetic separation problem [1] concerns itself with the separation of magnetic nanoparticles from a dispersion. This process has major applications in various areas, such as the extraction of organic and inorganic compounds from water [2, 3], extraction and assays of bio-molecules [4] and novel biomedicine delivery methods [5]. To extract the particles from a dispersion, usually some form of a high-gradient magnetic separation (HGMS) is applied, using a porous matrix of a magnetically susceptible material placed in an external electromagnetic field [6]. The external field induces strong field gradients in the matrix, translating into an attractive force on magnetically susceptible particles that are being transported through the matrix.

Magnetically separating nanoparticles is ostensibly a hard problem, mainly because of the Brownian motion that the particles exhibit which counteracts magnetic forces applied to the particle. This opposes the main advantage of the use of nanoparticles, which is their large surface-to-volume ratio. That separation of particles of sizes well below 50 nm is still possible was shown, for example, by Yavuz *et al.* [3], who managed to extract 12 nm iron oxide nanocrystals from an aqueous dispersion, by simply using a hand-held magnet. Their findings are explained by considering collective effects of the nanoparticles, for example due to the enhanced magnetic interactions between particles upon the application of an external field. Effects such as chain-formation of particles that enhance their separation behaviour were also shown by others [7].

The behaviour of magnetically susceptible particles in a homogeneous field is quite well understood theoretically and experimentally [8–11]. Computational fluid dynamics simulations allow for the investigation of a magnetic nanoparticle separation process in a complex environment [12, 13]. However, a more analytical approach to the behaviour of nanoparticles in a magnetic field gradient has not been investigated often [14].

We investigate the magnetic separation of nanoparticles in this chapter and in Chapter 7, by simulation and experiment, respectively. In Chapter 7 we describe the construction of a high-gradient magnetic separation device using a ferromagnetic matrix of metallic fibres packed randomly into a cylinder. Since the average structure of such a random packing of cylinder-shaped objects is reproducible and can be predicted based on the aspect ratio of the fibres (see Chapter 2), our aim is to model the separation efficiency of such a system in terms of e.g. the random packing density. We present an initial step towards this goal, by investigating the motion of nanoparticles influenced by a magnetized cylinder in an external magnetic field. To this end, we perform Brownian dynamics simulations with included hydrodynamic and magnetic dipole-dipole interactions. The force on the particles due to the complicated magnetic gradients that arise from the presence of the cylinder, can be calculated analytically using the equations derived in Chapter 5.

The structure of this chapter is as follows. We first discuss the theoretical basis of our Brownian dynamics simulations, followed by a description of some simulation details. Afterwards, we present results on a few related studies regarding the capture behaviour of magnetic nanoparticles. We conclude by discussing the optimal conditions for separation of nanoparticles using magnetizable cylinders.

6.2 Theory

6.2.1 Brownian dynamics

Two of the most popular stochastic methods for the simulation of colloidal particles, are Langevin dynamics (LD) and the closely related Brownian dynamics (BD). In both cases, the starting point for the equation of motion of a particle i is Newton's Second Law, $\mathbf{F}_i = m_i \mathbf{a}_i$. In our case, the force has three contributions: a hydrodynamic friction force $\mathbf{F}_i^{\mathrm{fr}}$ proportional to the particle velocity, a Gaussian fluctuating force $\mathbf{F}_i^{\mathrm{B}}$ (Brownian force) due to the random collisions of solvent molecules with the particle, and a term containing all other external forces present $\mathbf{F}_i^{\mathrm{ext}}$, such as magnetic (dipole) interactions and Van der Waals forces. Assuming a low Reynolds number and neglecting hydrodynamic interactions, the friction force is given by,

$$\mathbf{F}_i^{\mathrm{fr}} = -\xi_i \mathbf{v}_i \qquad \text{with} \qquad D_i = \xi_i^{-1} k_{\mathrm{B}} T = \frac{k_{\mathrm{B}} T}{6\pi\eta R_i} \tag{6.1}$$

where $\mathbf{v}_i$ is the particle velocity, and ξ_i is the friction coefficient related to the diffusion coefficient D_i through the Stokes-Einstein relation. Here $k_{\mathrm{B}}T$ is the thermal energy, η the solvent viscosity and R_i the particle radius. Assuming isotropic particles, rotational degrees of freedom can be ignored.

In Langevin dynamics, the change in position $\mathbf{r}_i$ of particle i is now described by the following differential equation, known as the *Langevin equation*,

$$m_i \frac{\mathrm{d}^2 \mathbf{r}_i(t)}{\mathrm{d}t^2} = \mathbf{F}_i^{\mathrm{ext}}\left(\{\mathbf{r}_j(t)\}\right) - \xi_i \frac{\mathrm{d}\,\mathbf{r}_i(t)}{\mathrm{d}t} + \mathbf{F}_i^{\mathrm{B}}(t) \tag{6.2}$$

where m_i is the mass of the particle and the external force may be dependent on the positions of all particles, $\{\mathbf{r}_j\}$. A net fluid flow is not taken into account here, but can be incorporated with an additional linear term. Under the assumption of a small particle mass, we can neglect inertia effects and reduce Equation 6.2 to,

$$\frac{\mathrm{d}\,\mathbf{r}_i(t)}{\mathrm{d}t} = \xi_i^{-1}\left(\mathbf{F}_i^{\mathrm{ext}}\left(\{\mathbf{r}_j(t)\}\right) + \mathbf{F}_i^{\mathrm{B}}(t)\right) \tag{6.3}$$

Equation 6.3 is sometimes called the overdamped Langevin equation, and it is the governing equation for *Brownian dynamics* simulations. The random forces are uncorrelated, following the fluctuation-dissipation theorem [15],

$$\begin{aligned} \langle \mathbf{F}_i^{\mathrm{B}}(t) \rangle &= 0 \\ \langle \mathbf{F}_i^{\mathrm{B}}(t) \mathbf{F}_j^{\mathrm{B}}(t') \rangle &= 2 k_{\mathrm{B}} T \xi_i \delta_{ij} \delta(t - t') \mathbf{I} \end{aligned} \tag{6.4}$$

where $k_{\mathrm{B}}T$ is the thermal energy as before, δ_{ij} is the Kronecker delta, δ is the Dirac delta function and $\mathbf{I}$ is the identity matrix.

In a BD simulation, Equation 6.3 is integrated forward in time and many runs are averaged to evaluate ensemble-averaged properties [16, 17].

6.2.2 Hydrodynamic interactions

The dynamics of a single spherical particle of radius R are represented by Equation 6.3. The presence of other particles results in long-ranged *hydrodynamic interactions* (HI), as each sphere causes a perturbation of the fluid flow field, indirectly affecting the motion of other particles. In order to correctly describe the motion of superparamagnetic nanoparticle in a magnetic field gradient, these HI are required, as was shown by Schaller *et al.* [14].

For a system of N identical particles, the HI can be described by [18],

$$\mathbf{V} = (k_\mathrm{B}T)^{-1}\mathbf{D}\cdot\mathbf{F} \tag{6.5}$$

where $\mathbf{V} = (\mathbf{v}_1, \mathbf{v}_2, \ldots, \mathbf{v}_N)$ are the particle velocities, $\mathbf{F} = (\mathbf{f}_1, \mathbf{f}_2, \ldots, \mathbf{f}_N)$ are the forces acting on the particles, and $\mathbf{D}$ is the diffusion tensor of which the components can be represented in matrix form as,

$$\mathbf{D} = \begin{pmatrix} \mathbf{D}_{11} & \mathbf{D}_{12} & \cdots & \mathbf{D}_{1N} \\ \mathbf{D}_{21} & \mathbf{D}_{22} & \cdots & \mathbf{D}_{2N} \\ \vdots & \vdots & & \vdots \\ \mathbf{D}_{N1} & \mathbf{D}_{N2} & \cdots & \mathbf{D}_{NN} \end{pmatrix} \tag{6.6}$$

where each component $\mathbf{D}_{ij}$ is again a 3×3 tensor. For a detailed description of how HI are incorporated into the overdamped Langevin equation (Equation 6.3) we refer to the seminal paper by Ermak and McCammon [19]. The final result for the time evolution of the position of a particle i is,

$$\mathbf{r}_i(t+\Delta t) = \mathbf{r}_i(t) + \frac{\Delta t}{k_\mathrm{B}T}\sum_j \mathbf{D}_{ij}\cdot\mathbf{F}_j + \Delta t\sum_j \boldsymbol{\nabla}_j\cdot\mathbf{D}_{ij} + \mathbf{R}_i(\Delta t) \tag{6.7}$$

where $\mathbf{R}_i(\Delta t)$ is a random displacement due to the Brownian forces. The calculation of the exact diffusion tensor is a complex problem, and the tensor is typically expanded up to a certain order [19, 20]. A zeroth order approximation neglects all hydrodynamic interactions, making the off-diagonal components of the diffusion tensor zero. The components for $i = j$ are given by,

$$\mathbf{D}_{ii} = \frac{k_\mathrm{B}T}{6\pi\eta R}\mathbf{I} \tag{6.8}$$

Oseen [21] and Burgers [22] used a first order expansion, adding terms to the off-diagonal components. This is commonly referred to as the Oseen tensor,

$$\mathbf{D}_{ij} = \frac{k_\mathrm{B}T}{8\pi\eta r_{ij}}\left(\mathbf{I} + \frac{\mathbf{r}_{ij}\otimes\mathbf{r}_{ij}}{r_{ij}^2}\right) \qquad i \neq j \tag{6.9}$$

where $\otimes$ is the tensor product and, $\mathbf{r}_{ij}$ is the vector connecting the centres of particles i and j, and r_{ij} is the norm of this vector. The Oseen tensor is not guaranteed to be

positive definite when particles are close to each other, $r_{ij} < 2R$, yielding unphysical behaviour for concentrated systems. A higher order expansion is due to Rotne and Prager [23], and Yamakawa [24] (named the RPY tensor). Here the finite size of particles is taken into account. The tensor elements for $i = j$ are again given by Equation 6.8, and otherwise,

$$\mathbf{D}_{ij} = \frac{k_\mathrm{B}T}{6\pi\eta R} \begin{cases} \left(\frac{3R}{4r_{ij}} + \frac{R^3}{2r_{ij}^3}\right)\mathbf{I} + \left(\frac{3R}{4r_{ij}} - \frac{3R^3}{2r_{ij}^3}\right)\frac{\mathbf{r}_{ij}\otimes\mathbf{r}_{ij}}{r_{ij}^2} & r_{ij} > 2R \\ \left(1 - \frac{9r_{ij}}{32R}\right)\mathbf{I} + \left(\frac{3r_{ij}}{32R}\right)\frac{\mathbf{r}_{ij}\otimes\mathbf{r}_{ij}}{r_{ij}^2} & r_{ij} < 2R \end{cases} \tag{6.10}$$

where for the second case the particles are allowed to overlap. Note that the RPY tensor is still an approximate tensor based on pair-wise interactions. It can not accurately describe the regime where the inter-particle distances tend to zero. In that case *lubrication effects* will need to be incorporated [18, 25].

A notable property of the Oseen and RPY tensors is that their gradients are zero ($\boldsymbol{\nabla}\cdot\mathbf{D} = 0$), eliminating a term from Equation 6.7 and simplifying calculations greatly.

This leaves,

$$\mathbf{r}_i(t+\Delta t) = \mathbf{r}_i(t) + \frac{\Delta t}{k_\mathrm{B}T}\sum_j \mathbf{D}_{ij}\cdot\mathbf{F}_j + \mathbf{R}_i(\Delta t) \tag{6.11}$$

In our simulations, the instantaneous force in Equation 6.11 consist of three components,

$$\mathbf{F}_j = \sum_{m=1}^{M}\mathbf{F}_{jm}^{\mathrm{mag}} + \sum_{i\neq j}\mathbf{F}_{ij}^{\mathrm{dip}} + \sum_{i\neq j}\mathbf{F}_{ij}^{\mathrm{HS}} \tag{6.12}$$

where $\mathbf{F}_{jm}^{\mathrm{mag}}$ is the force due to the magnetic field of a cylinder, summed over all M cylinders present, $\mathbf{F}_{ij}^{\mathrm{dip}}$ is the magnetic dipole interaction between particles (see Section 6.2.4), and $\mathbf{F}_{ij}^{\mathrm{HS}}$ is the pseudo hard-sphere repulsion (see Section 6.2.3).

Similar to Equation 6.4, the random vector $\mathbf{R}_i$ in Equation 6.11 satisfies the properties,

$$\langle\mathbf{R}_i\rangle = 0 \tag{6.13}$$

$$\langle\mathbf{R}_i(\Delta t)\mathbf{R}_j(\Delta t)\rangle = 2\mathbf{D}_{ij}\Delta t \tag{6.14}$$

A common method to calculate the random vectors is by evaluating,

$$\mathbf{R}_i = \sqrt{2\Delta t}\sum_{j=1}^{N}\mathbf{C}_{ij}\mathbf{g}_j \tag{6.15}$$

where $\mathbf{g}_j$ is vector of Gaussian distributed random numbers. $\mathbf{C}$ is a lower triangular

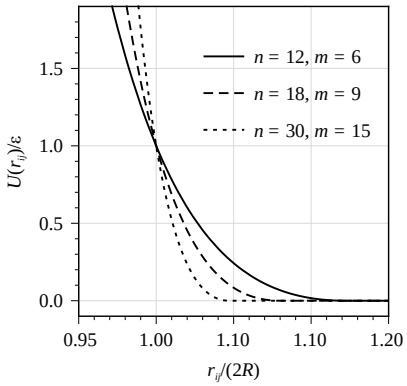

Figure 6.1. Shifted and truncated Mie(n, m) potentials for different combinations of n and m.

matrix that satisfies the relation,

$$\mathbf{D} = \mathbf{C}\mathbf{C}^{\mathsf{T}} \tag{6.16}$$

and can be obtained by the Cholesky decomposition of the diffusion tensor via standard linear algebra methods [26].

6.2.3 Hard sphere interaction

A hard-sphere (HS) interaction potential assures that particles cannot overlap. For two spherical nanoparticles of radius R, separated by a distance r_{ij}, this potential is given by,

$$U^{\mathrm{HS}}(r_{ij}) = \begin{cases} 0 & r_{ij} \geq 2R \\ \infty & r_{ij} < 2R \end{cases} \tag{6.17}$$

The discontinuity in the HS potential does not allow for a continuous gradient of the potential (i.e. a force), rendering it unusable in a BD simulation. A suitable differentiable alternative is the Mie(n, m) potential [27] (see Figure 6.1),

$$U^{\mathrm{Mie}}(r_{ij}) = \left(\frac{n}{n-m}\right)\left(\frac{n}{m}\right)^{\frac{m}{n-m}} \epsilon \left[\left(\frac{2R}{r_{ij}}\right)^{n} - \left(\frac{2R}{r_{ij}}\right)^{m}\right] \tag{6.18}$$

where $n, m \in \mathbb{N}$ and $n > m$. ϵ is the intermolecular energy parameter, for which $U^{\mathrm{Mie}}_{\mathrm{min}} = -\epsilon$ at position $r_{\mathrm{min}} = 2R\,(n/m)^{1/(n-m)}$. The Mie$(n, m)$ potential is a generalized form of the well known Lennard-Jones (LJ) potential which is equivalent to Mie$(12, 6)$. To mimic the HS potential better, the attractive part of the Mie potential is ignored by shifting it and truncating it to zero for larger intermolecular distances. This results in

the following piecewise potential,

$$U^{\mathrm{Mie}}(r_{ij}) = \begin{cases} \left(\frac{n}{n-m}\right)\left(\frac{n}{m}\right)^{\frac{m}{n-m}} \epsilon \left[\left(\frac{2R}{r_{ij}}\right)^n - \left(\frac{2R}{r_{ij}}\right)^m\right] + \epsilon & r_{ij} < 2R\left(\frac{n}{m}\right)^{\frac{1}{n-m}} \\ 0 & r_{ij} \geq 2R\left(\frac{n}{m}\right)^{\frac{1}{n-m}} \end{cases} \tag{6.19}$$

6.2.4 Magnetic interaction

The force on a particle with magnetic moment $\mathbf{m}$ due to the presence of a magnetic field $\mathbf{B}$, is in general given by,

$$\mathbf{F}_{\mathrm{m}} = (\mathbf{m} \cdot \nabla)\mathbf{B} \tag{6.20}$$

where ∇ is the gradient operator. In our simulation setup we consider $\mathbf{B}$ to be the sum of an external field and an induced field around the metallic fibres. The induced field and its gradient can be calculated exactly in terms of elliptic integrals, see Chapter 5.

In addition to the force exerted by an external field, particles with an (induced) magnetic moment, will exhibit a mutual interaction. The interaction energy between two particles is given by,

$$U^{\mathrm{dip}}\left(\mathbf{r}_{ij}, \boldsymbol{\mu}_i, \boldsymbol{\mu}_j\right) = -\frac{\mu_0}{4\pi}\left(\frac{3(\mathbf{r}_{ij} \cdot \boldsymbol{\mu}_i)(\mathbf{r}_{ij} \cdot \boldsymbol{\mu}_j)}{r_{ij}^5} - \frac{\boldsymbol{\mu}_i \cdot \boldsymbol{\mu}_j}{r_{ij}^3}\right) \tag{6.21}$$

where $\mathbf{r}_{ij}$ is the vector connecting the two particle centres, $\boldsymbol{\mu}$ is the magnetic moment and r_{ij} is the distance between the two particles. The magnetic moment is related to the magnetization of the nanoparticle, given by a Langevin function (see for example [28]),

$$M(H) = M_{\mathrm{sat}}\left(\coth x - \frac{1}{x}\right) \qquad \text{with} \quad x = \frac{\mu_0 \mu_{\mathrm{d}} H}{k_{\mathrm{B}} T} \tag{6.22}$$

where M_{sat} ($\mathrm{A\,m^{-1}}$) is the sample saturation magnetization, $\mu_0 = 4\pi \times 10^{-7}\,\mathrm{N\,A^{-2}}$, is the magnetic permeability of vacuum, μ_{d} ($\mathrm{A\,m^2}$) is the magnetic dipole moment of a single magnetic domain, and $k_{\mathrm{B}}T$ (J) is the thermal energy.

The particles under consideration are considered superparamagnetic, so that the direction of their magnetic moments will be parallel to the magnetic field. The force between the dipoles is then given by,

$$\mathbf{F}_{ij}^{\mathrm{dip}} = -\nabla_{\mathbf{r}_i} U^{\mathrm{dip}}(\mathbf{r}_{ij}, \boldsymbol{\mu}_i, \boldsymbol{\mu}_j) \tag{6.23}$$

Note that a magnetic dipole will perturb the local magnetic field slightly and therefore influence the magnetic moment of particles in its proximity. An iterative method may be used to calculate the effective magnetic moment [14]. However, this effect only contributes significantly for weak external fields ($\sim$ mT). In our simulations we apply an external field of ~ 1 T, so that we can safely ignore any mutual influence.

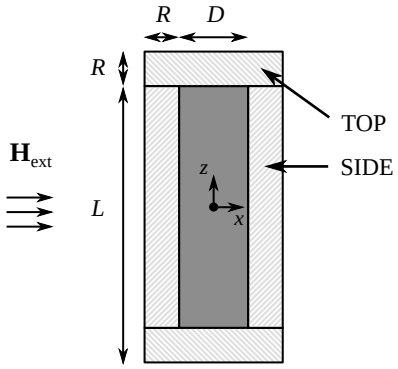

Figure 6.2. Two dimensional representation of the regions around the cylinder in which the nanoparticles are placed initially (TOP and SIDE). R is the radius of the cylinder, D its diameter and L its length.

6.3 Simulation details

Simulation runs using the Brownian dynamics method outlined in the previous section are performed according to the following general principle. A magnetizable cylinder of length L and diameter D, fixed throughout at $D = 600\,\mu\text{m}$, is centred at the origin of a Cartesian coordinate system (see Figure 6.2). A uniform external magnetic field is applied in the positive x-direction with a strength of 1 T. The orientation of the long axis of the cylinder is chosen between fully parallel or fully perpendicular to the direction of the external field, characterized by the angle α. A parallel cylinder ($\alpha = 0°$) will become longitudinally magnetized, and a perpendicular cylinder ($\alpha = 90°$) will become transversely magnetized. In order to reach saturation in the applied field, the cylinder is given a saturation magnetization of $985\,\text{kA m}^{-1}$. To simplify the calculations, we assume that the cylinder acquires a uniform magnetization throughout its volume. This allows us to calculate the magnetic field and gradients produced by the cylinder using the exact model from Chapter 5. The effective magnetization direction is determined using the Stoner-Wohlfarth energy minimization model [29, 30], except where otherwise noted.

As a starting configuration, N identical spherical particles of radius R are placed in the vicinity of the cylinder, distributed uniformly over two regions, TOP and SIDE (Figure 6.2). It is expected that particles in these regions behave very differently because of the influence of the local magnetic field and its gradient. The particle properties are matched to those of the particles used by Schaller *et al.* [14]. They performed experiments using polymer particles with embedded single domain iron oxide Fe_3O_4 nanoparticles. The hydrodynamic radius R_h of the polymer particles ranges from 25–212 nm and the embedded nanoparticles contribute to total magnetic moment of the particle (see Table 6.1 for details).

Starting from the initial configuration, the particles are moved according to Equation 6.11 using a sufficiently small time step. Unless otherwise stated, the number of particles is $N = 100$, the time step is $\Delta t = 5 \times 10^{-5}$ s, and simulations are run for a

Table 6.1. Magnetic properties for different Fe_3O_4 magnetic particles, with R_h the hydrodynamic particle radius and μ_s the particle magnetic moment. Data taken from [14].

R_h (nm)	μ_s (A m^2 10^{-16})
25	0.016
50	0.344
75	0.870
100	0.662
125	5.151
212	19.35

maximum of $t_{max} = 50$ s. In order to obtain good statistics, a minimum of 30 independent runs are averaged. Simulations are performed at room temperature, $T = 298$ K, and with water as solvent, having a viscosity of $\eta = 1.0$ mPa s. An interaction parameter of $\epsilon = 100 k_B T$ is used in a a pseudo hard-sphere Mie(30,15)-potential.

If during the simulation run, a particle comes into contact with the cylinder, it is considered to be 'captured' and will remain fixed for the remainder of the simulation by setting the particle forces to zero. This is a reasonable assumption when the viscous drag force on the particle is compared with the magnetic force on the particle, see for example the argument of Butter [31].

Two methods are employed to speed up calculations. First, since the magnetic interactions between particle pairs is relatively short-ranged, a cut-off can be made above which the interactions are neglected. For a particle of radius $R = 250$ nm and a magnetic moment of $\mu = 2.2 \times 10^{-3}$ A µm^2 (calculated from experimental data in [14] for two particles in head-tail configuration), the interaction energy will be lower than the thermal energy at $r_{cut} \gtrapprox 20R$. Therefore, we choose a cut-off radius of $r_{cut} = 30R$, also in accordance with other studies [32]. Second, we approximate the decomposition of the diffusion tensor (Equation 6.16), as this is computationally the most expensive step in the Brownian dynamics algorithm [33]. We implement the TEA-HI scheme by Geyer and Winter [34], and find identical diffusive behaviour of particles in a dilute situation, and only minor differences (up to 5 %) for very small inter-particle distances. This deviation may become relevant when very concentrated systems are studied, or when particles form chains under influence of a magnetic field (see Section 6.4.6). In these cases the TEA-HI scheme slightly underestimates the hydrodynamic coupling between particles.

6.4 Results and discussion

This section is divided into several separate 'experiments' performed in order to quantify different aspects of the capture of magnetic nanoparticles by one or more magnetized cylinders. The main parameters that are varied in the experiments are the magnetization direction of the cylinder (via their orientation in the external field), its aspect ratio and the nanoparticle size (according to Table 6.1). During the simulations, particle

trajectories are obtained and the fraction of particles that is captured by the cylinders is monitored. We first treat the particle behaviour around a single cylinder and afterwards make an approximation for multiple cylinders.

6.4.1 Single cylinder: capture volume

To estimate in which region around a cylinder the magnetic nanoparticles will accumulate, we define a capture volume V_{cap} as the region bounded by a certain cut-off value for the attractive magnetic force on a particle generated by the magnetic field gradient of the cylinder. The force is calculated using Equation 6.20, taking the direction of $\mathbf{m}$ parallel to $\mathbf{B}$ because the particle dipole moment will align in the direction of the external field. A large region around the full length of the cylinder will be the most advantageous situation for particle capture. The capture volume is calculated using the magnetic field equations from Chapter 5, for cylinders with an aspect ratio $L/D = 5/3$ and 20/3. In these calculations we do not use the Stoner-Wohlfarth method to calculate the effective magnetization direction for the cylinder, but fix the magnetization direction at an angle α from the long axis of the cylinder. We choose values of $\alpha = 0°$ (parallel), $45°$ (intermediate) and $90°$ (perpendicular). A cut-off value of 0.5×10^{-15} N is used for the force, but the shape of the volume is quite insensitive to the exact value. The results are shown in Figure 6.3.

The main characteristics of the capture volume are clear: for longitudinal magnetization, only the top and bottom of the cylinder provide a strong enough gradient to attract particles, while for transverse magnetization the capture volume encompasses the entire cylinder. This makes it highly advantageous to have cylinders mostly perpendicular to the magnetic field when separating nanoparticles. The benefit of shorter cylinder is also apparent, as the capture volume relative to the cylinder volume is larger in that case.

6.4.2 Single cylinder: angle dependence

To see the effect of the differences in predicted capture zones, a series of Brownian dynamic simulations is performed. The orientation of the cylinder with respect to the external field is varied from $\alpha = 0°$ (longitudinal magnetization) to $90°$ (transverse magnetization) in steps of $15°$. A cylinder aspect ratio of $L/D = 20$ is chosen to have a clear distinction between the transverse and longitudinal magnetization behaviour. In Figure 6.4 the average fraction of captured particles during the simulation is shown for two particle sizes ($R = 75$ nm and $R = 212$ nm) in the TOP and SIDE regions, respectively (see Figure 6.2). Note that the labels TOP and SIDE only refer to the *initial* position of the particles, and not the location where they are captured on the cylinder.

A comparison of the graphs for the two regions, shows a distinctly different behaviour. For the TOP region, the final capture fractions are generally higher for smaller angles. Conversely, for the SIDE region, the final capture fractions are higher for larger angles. This confirms the hypothesis that for longitudinal magnetization ($\alpha = 0°$) the top and bottom of the cylinder cause the highest magnetic gradients and best particle capture, while the lateral surface of the cylinder is only minimally active, and *vice versa* for transverse magnetization ($\alpha = 90°$).

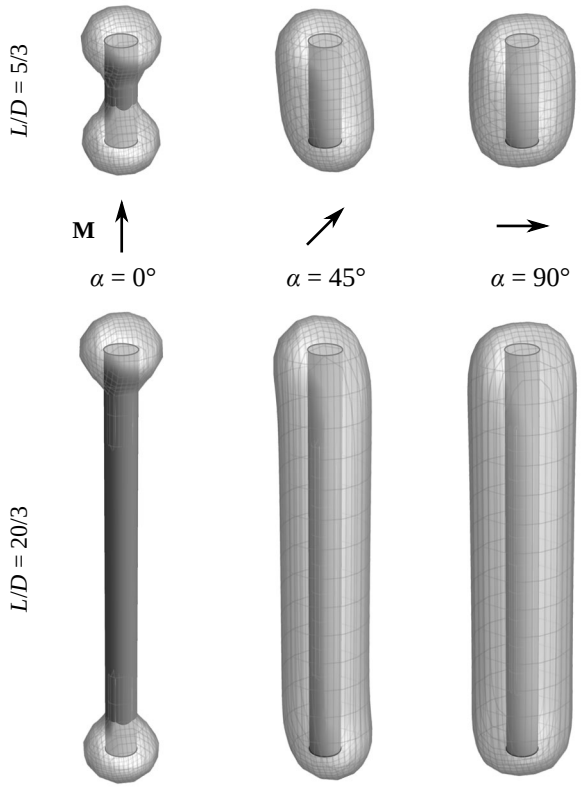

Figure 6.3. Representation of the regions around differently magnetized cylinders where magnetic particles will be captured. Three different magnetization directions α are shown and two different aspect ratios (shorter and longer cylinder).

The cause for the lower capture fractions can be found by closer inspection of the particle trajectories. For a cylinder of aspect ratio $L/D = 5/3$ the trajectories of $N = 200$ particles of size $R = 125$ nm are shown in Figure 6.5a and b. The trajectories are colour coded according to the time progression of the simulation, with blue points indicating the particle positions at the beginning of the simulation, and red points indicating the particle's final position. It can be seen that due to local field gradients, in combination with the orientation of the particle dipole moment, particles can move away from the cylinder. At a certain distance away from the cylinder the Brownian forces will start to dominate over the magnetic attraction by the cylinder, and the particle will no longer be captured, thereby leading to lower capture fractions. The fraction of these Brownian particles will be investigated further in Section 6.4.4.

Further comparison of the graphs in Figure 6.4 shows that larger particles are captured sooner than the smaller particles and that higher capture fractions are achieved within the same simulation duration. This is in accordance with the increase in particle

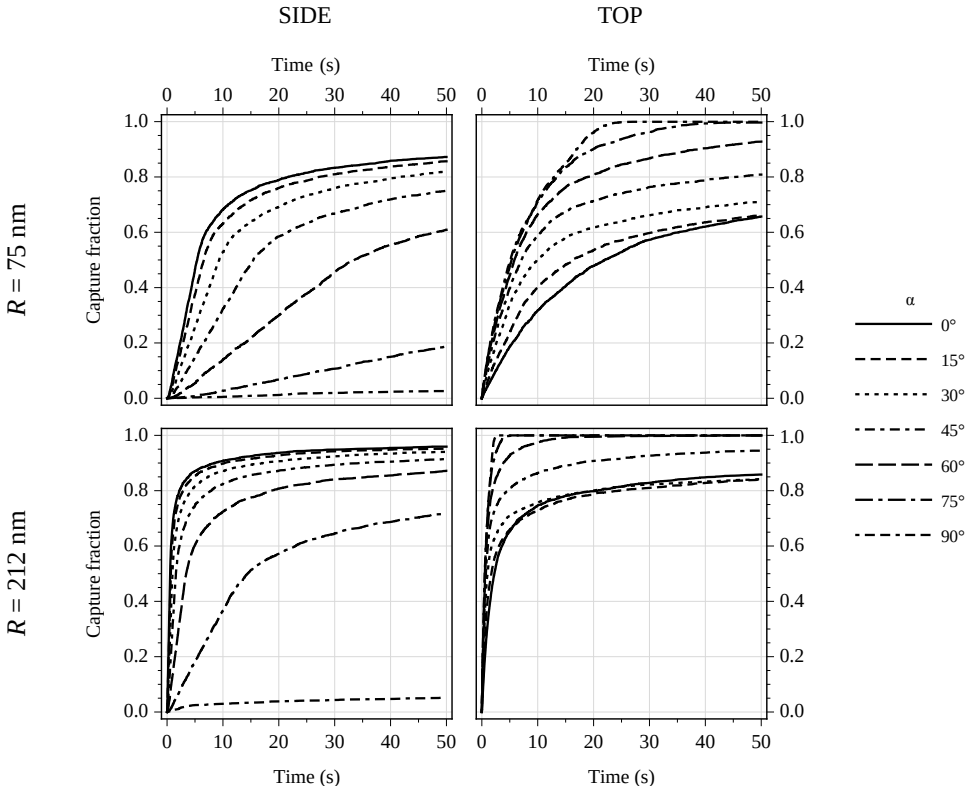

Figure 6.4. Time evolution of the capture fraction for particles of 75 nm (top row) and 212 nm (bottom row) in the presence of a magnetized cylinder of aspect ratio $L/D = 20$. The magnetization direction of the cylinder increases from $\alpha = 0°$ (longitudinal magnetization) to $\alpha = 90°$ (transverse magnetization). The labels TOP and SIDE refer to the initial positioning of the particles (see Figure 6.2).

magnetic moment when the particle size increases, leading to stronger attractive forces. In Figure 6.6a the capture fractions at the end of the simulations are presented as a function of the cylinder magnetization angle, for particles of different sizes. Here, the contributions from the TOP and SIDE regions are averaged with a weight proportional to the volume of the respective region. For particle sizes greater than $R = 25$ nm there is a gradual (non-linear) increase in capture fraction, with final capture fractions of approximately 80 % or more. The initial slower rise can be explained by the different behaviour of the TOP and SIDE regions (see Figure 6.4). The smallest particles are not captured as efficiently due to the combination of their much smaller magnetic moment and more prominently present Brownian motion. Also, in agreement with our expectations, the capture efficiency is lowest for longitudinally magnetized cylinders, where only the top and bottom part of the cylinder contribute to the effective capture area.

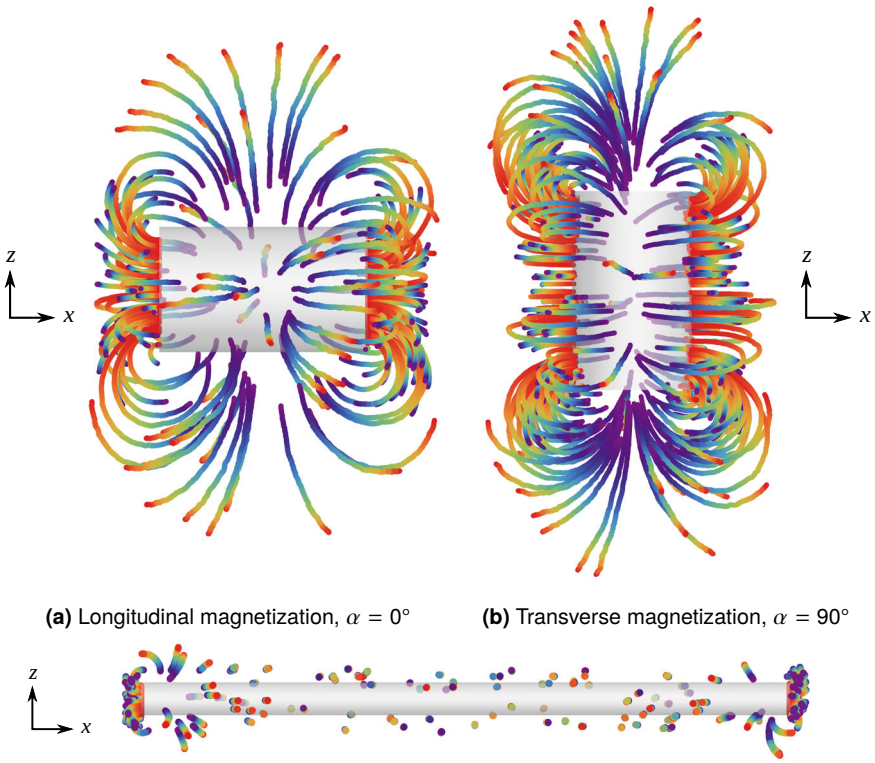

(a) Longitudinal magnetization, $\alpha = 0°$ **(b)** Transverse magnetization, $\alpha = 90°$

(c) Longitudinal magnetization, $\alpha = 0°$

Figure 6.5. Time trajectories of $R = 125\,\text{nm}$ particles near a cylinder of $L/D = 1.67$ (a and b), and $L/D = 20$ (c). The graphics are two dimensional projections in the xz-plane. The progression of the simulation is shown via a rainbow colour gradient of the data points, with the particle positions at the beginning of the simulation shown in purple and at the end of the simulation in red. The magnetic field is applied in the x-direction.

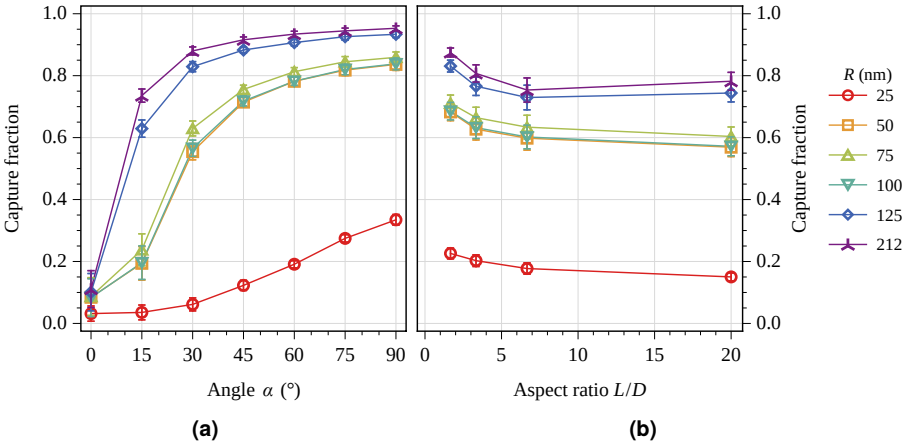

Figure 6.6. Plot of the overall final capture fraction versus (a) the magnetization angle and (b) the aspect ratio, both at varying particle size. Error margins are indicated. The contributions from the particles originating from the TOP and SIDE regions are averaged with a weight proportional to the volume of the regions. Additionally for the right plot, averages are also taken over all magnetization angles.

6.4.3 Single cylinder: aspect ratio dependence

As seen in the previous section, the capture fraction is strongly influenced by the orientation of the cylinder as it determines if the top and bottom, or the lateral surface of the cylinder is the primary effective capture area. The aspect ratio of the cylinder may have a similar influence as it determines the ratio between the different areas of the cylinder. Therefore, a series of simulations have been performed where the aspect ratio is varied from $L/D = 5/3$–20, and cylinder orientations and particle sizes have been varied as well.

Figure 6.7 shows the capture fraction for the TOP and SIDE regions during the simulation for cylinders of two different aspect ratios and at different magnetization angles, but for a fixed particle size of $R = 125$ nm. The difference between the capture fraction for the two aspect ratios is minimal for the TOP region, whereas for the SIDE region the smaller aspect ratio captures a significantly larger number of particles at smaller angles. This can be explained by the fact that in this case the 'inactive' lateral surface of the cylinder for longitudinal magnetization is relatively small and capture at the top and bottom will always dominate. This effect is shown visually by comparing Figure 6.5a and c. For the larger aspect ratio, the particles in the SIDE region will hardly move, as opposed to the particles in de TOP region that move quickly towards the cylinder. For the smaller aspect ratio, all particles experience some effect of the field gradient.

Similar to Figure 6.6a, the average final capture fraction for differently sized particles is plotted against the varying cylinder aspect ratio Figure 6.6b. As before, the results from the TOP and SIDE regions are averaged proportionally to the volume of the regions. Here the averages are also taken over the different angles of the cylinders, based

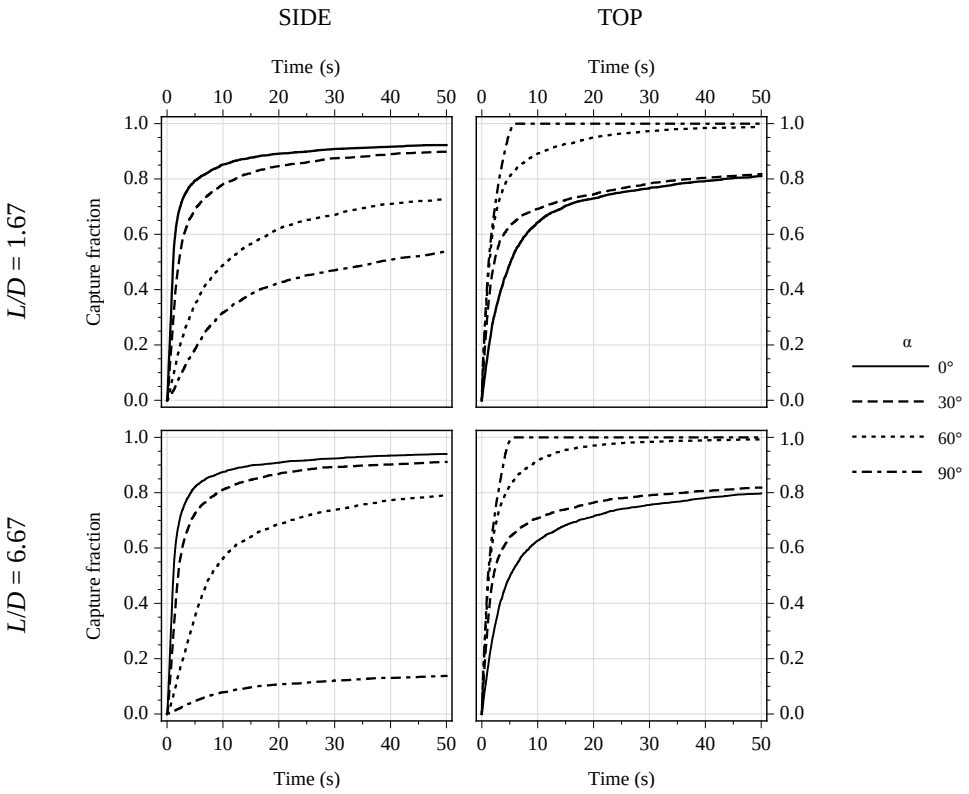

Figure 6.7. Time evolution of the capture fraction for a cylinder of aspect ratio $L/D = 1.67$ (top row), and aspect ratio $L/D = 6.67$ (bottom row). Different curves correspond to different magnetization angles of the cylinder, from $\alpha = 0°$ (longitudinal magnetization) to $\alpha = 90°$ (transverse magnetization). The labels TOP and SIDE refer to the initial positioning of the particles (see Figure 6.2).

on the notion that in a random packing of cylinders (this is the case in our experimental setup, cf. Chapter 7) all orientations are equally likely. It can be seen that the influence of the aspect ratio is rather minor on average. There is a small but significant increase in capture fraction for smaller aspect ratio that can be ascribed to the decreasing size of the 'inactive' lateral area of the cylinder. It should be noted however, that most of the captured particles are initially found in the TOP regions and therefore a certain bias may have been introduced here. Nevertheless, it is not unreasonable to conclude from these results that the cylinder aspect ratio is of lesser importance in determining the capture fraction than the orientation of the cylinder.

6.4.4 Single cylinder: Brownian motion

One main reason why not all particles are captured by a cylinder is the fact that at some point during the simulation their Brownian motion becomes dominant over the

magnetic forces acting on them. To assess the fraction of these 'Brownian particles', the mean square displacement at the end of the separation process (at $t = 50\,\mathrm{s}$) is calculated. We consider a particle to behave Brownian when,

$$\langle r^2 \rangle < 2\langle r^2 \rangle_{\mathrm{Brown}} \tag{6.24}$$

where $\langle r^2 \rangle_{\mathrm{Brown}} = 6Dt$ is the usual Einstein equation for the mean quadratic displacement of a Brownian particle [18].

The fraction of Brownian particles is determined in the TOP and SIDE regions for a cylinder of aspect ratio $L/D = 20$, different particle sizes and at different cylinder orientations. The results are shown in Figure 6.8a where the difference in behaviour between the TOP and SIDE regions is evident. As mentioned earlier, the SIDE region becomes much more active in particle capture when the cylinder acquires a transverse magnetization component ($\alpha \to 90°$). This leads to a strong decrease in the fraction of Brownian particles. Even for the smallest particle size nearly all particles are non-Brownian at $\alpha = 90°$, meaning that they are likely to be captured given enough time. For the TOP region all particles are captured at all magnetization angles, except for the smallest size where, independent of the magnetization, there is never sufficient magnetic force acting on the particles, or they are repelled away from the magnet (cf. Figure 6.5). It is likely that in the presence of multiple cylinders, the Brownian particles will feel an additional magnetic force towards another cylinder, and may be captured there. This idea will be explored in Section 6.4.5.

In Figure 6.9, the total fraction of Brownian particles is plotted against the particle size, averaged over the different magnetization angles. A small fraction ($< 10\,\%$) of Brownian particles is always present, primarily due to configurations with longitudinal magnetization.

Finally, the influence of the cylinder aspect ratio on the fraction of Brownian particles is shown in Figure 6.8b. It is clear that the smaller aspect ratio cylinder is more efficient in capturing magnetic particles of all except the smallest size, supporting the findings in Section 6.4.3. Also here, the trend that a longitudinally magnetized cylinder $\alpha = 0°$ captures fewer particles than a transversely magnetized cylinder can be observed.

Based on the results in this and previous sections, a qualitative criterion can be given for a high rate of success for magnetic particle capture. Assuming that a large collection of cylinders will be used in an experimental setup, we can state that particle capture will be most efficient by using cylinders with a relatively small aspect ratios ($L/D < 6$), oriented on average perpendicular to the applied field. Such a configuration is expected to capture nearly all magnetic particles of size ($R \geq 50\,\mathrm{nm}$) within a time period of 50 s. Under these conditions, already very few Brownian particles are found in the simulation of a *single cylinder*. The presence of *multiple cylinders* will likely decrease the number of Brownian particles even further, which will be explored in the next section. For particles smaller than 50 nm, where capture is difficult in any case, the choice of a smaller aspect ratio cylinder becomes more important.

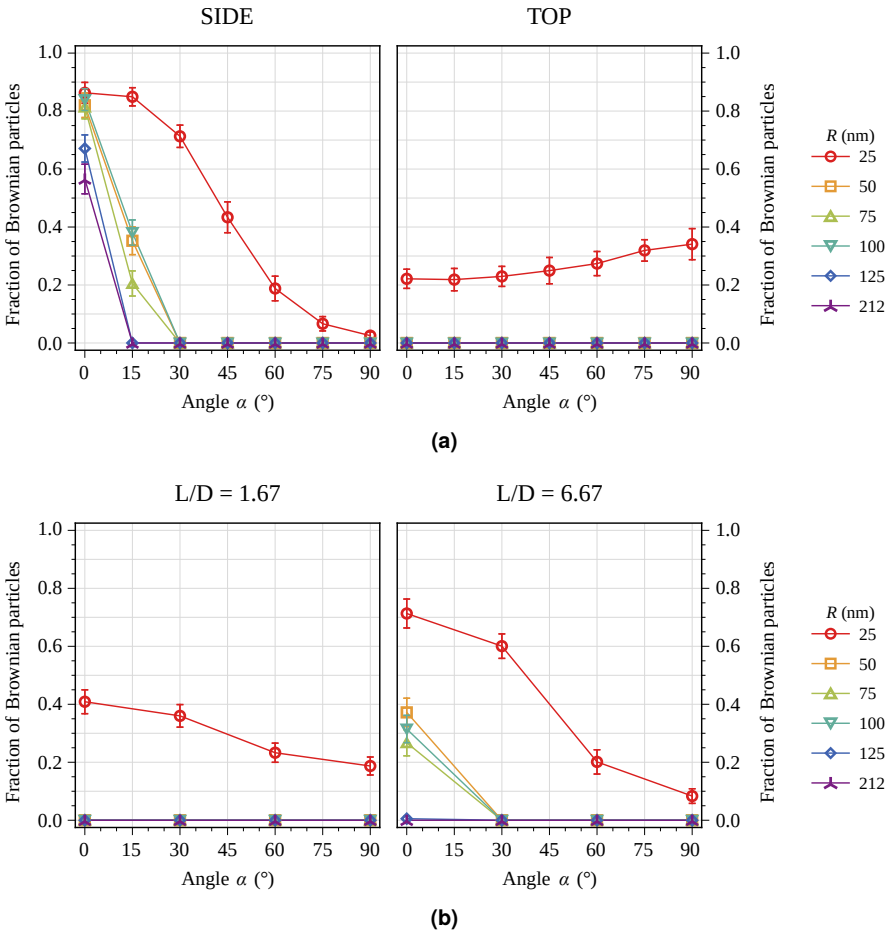

Figure 6.8. (a) The fraction of Brownian particles according to Equation 6.24 plotted against the magnetization angle of the cylinder ($L/D = 20$). Error bars are indicated and a distinction is made between the TOP and SIDE regions (see Figure 6.2). The different curves correspond to different particle sizes. For a particle size larger than $R = 25$ nm in the TOP region, the percentage of Brownian particles is always zero. (b) The percentage of Brownian particles plotted against the magnetization angle, for particles of different size and two different aspect ratios $L/D = 1.67$ (left) and $L/D = 6.67$ (right). Averages have been taken over de TOP and SIDE regions as before, and error bars are indicated.

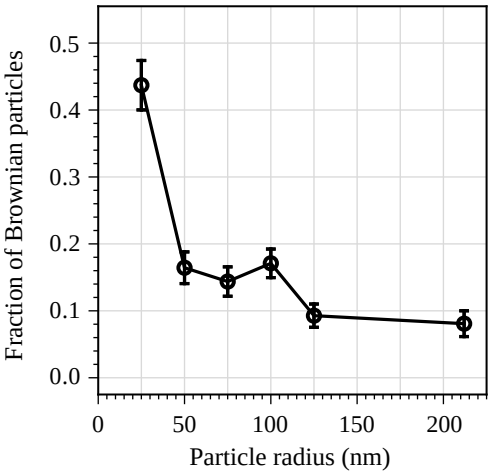

Figure 6.9. The relation between the final percentage of Brownian particles and particle size, including error margins, for a cylinder of aspect ratio $L/D = 20$. The contributions of the TOP and SIDE region are averaged as before, and an additional averaging is made over all orientations.

6.4.5 Multiple cylinders

In the previous sections the capture of magnetic particles by a single cylinder has been considered. While in principle it is possible to simulate multiple cylinders simultaneously with our Brownian dynamics algorithm, it significantly slows down the computation. To get an estimate for the efficiency of particle capture with multiple cylinders, we therefore employ a *cascade procedure*. In this procedure, the initial configuration of the system comprises N particles and a single cylinder of random orientation. The Brownian dynamics simulation is then run for a time interval of Δt_{run} (s), after which N_1 particles have been captured. Afterwards, the remaining $N - N_1$ free particles are randomly placed around a cylinder of a different random orientation and the simulation is repeated. After k repeats there are $N - \sum_{i=1}^{k} N_i$ free particles left. For large time intervals or many iterations, the fraction of captured particles will tend to unity. See Figure 6.10 for a graphical representation of the cascade process.

In the previous section it was shown that particle capture is maximal for cylinders with transverse magnetization. We therefore also simulate an 'optimal' cascade, by setting the orientation of each cylinder perpendicular to the field and parallel to each other. A comparison for a random cascade and the optimal cascade is given in Figure 6.11a for particles of 25 nm and 125 nm. Because the smaller particles are separated slowly, a time step of $\Delta t_{\text{run}} = 10\,\text{s}$ is chosen. For the larger particle size a time step of $\Delta t_{\text{run}} = 0.5\,\text{s}$ is sufficient. Both curves exhibit a similar shape, and the cascade with optimally oriented cylinders performs substantially better than for randomly oriented cylinders, as expected. Given enough time, however, both situations converge to the same value, close to (or exactly) unity.

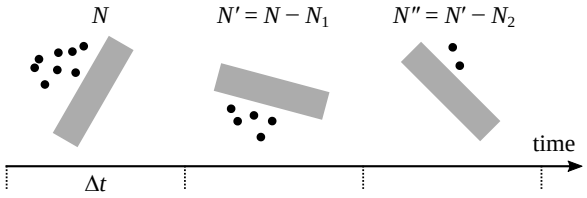

Figure 6.10. Schematic representation of the cascade procedure used to model a separation process in which more than one cylinder is involved. Δt_{run} is the maximum time allowed for each single separation process in the sequence. Values of N indicate the number of free particles at the beginning of each step.

We can quantify the separation efficiency by determining the time it takes to capture 90 % of the particles (see marked lines in Figure 6.11a). For the particles of 25 nm, the random cascade takes approximately 2.2× as long to reach 90 % capture than the optimal cascade (1100 s vs. 500 s). For the larger particle size, this factor is very similar, approximately 2.3× as long (12.5 s vs. 5.5 s). The effect of the choice of the time step is shown in Figure 6.11b for particles of 125 nm. Here it can be seen that a time step either too small, or too large reduces the capture speed (especially noticeable in the random cascade). This can be explained by drawing a qualitative analogy to the flow velocity in an experimental separation procedure, where a liquid containing magnetic nanoparticles is transported through a collection of magnetized fibres. For a low flow velocity the nanoparticles feel the presence of a single cylinder for a relatively long time, before being transported to the next. If the former cylinder happens to be mostly longitudinally magnetized, relatively few particles will be captured, which is a disadvantage. In contrast, if particles are transported too quickly most nanoparticles do not have enough time to be captured.

6.4.6 Effects of concentration

So far only dilute dispersions of nanoparticles have been considered, so that the magnetic dipole interactions between the particles do no play an important role. In reality however, the clustering of particles and chain formation can greatly aid the separation process, as many authors have shown [3, 14, 35–37]. We hereby show that also our Brownian dynamics simulations with included magnetic dipole-dipole interactions show chain-formation when the particle concentration is increased, and we present some initial results on the concentration dependent capture behaviour.

We generate starting configurations of $N = 500$ particles in a small volume at a distance of 100 µm from the top of a single cylinder, and placed close to the rim of the cylinder. As was shown previously, the magnetic gradients are strongest in this location, so that fast capture is expected. Data from 10 independent runs are averaged. Different particle concentrations are simulated by generating the initial configuration inside a box with vertex length $d = \sqrt[3]{\rho V_{\mathrm{p}}/c}$ where c is the desired concentration, ρ is the particle density set to $\rho = 5.0\,\mathrm{g\,cm^{-3}}$ and V_{p} is the volume of a single particle. Concentrations in the range 0.5–2.0 $\mathrm{g\,mL^{-1}}$ are considered, for particles in the size range 25–125 nm.

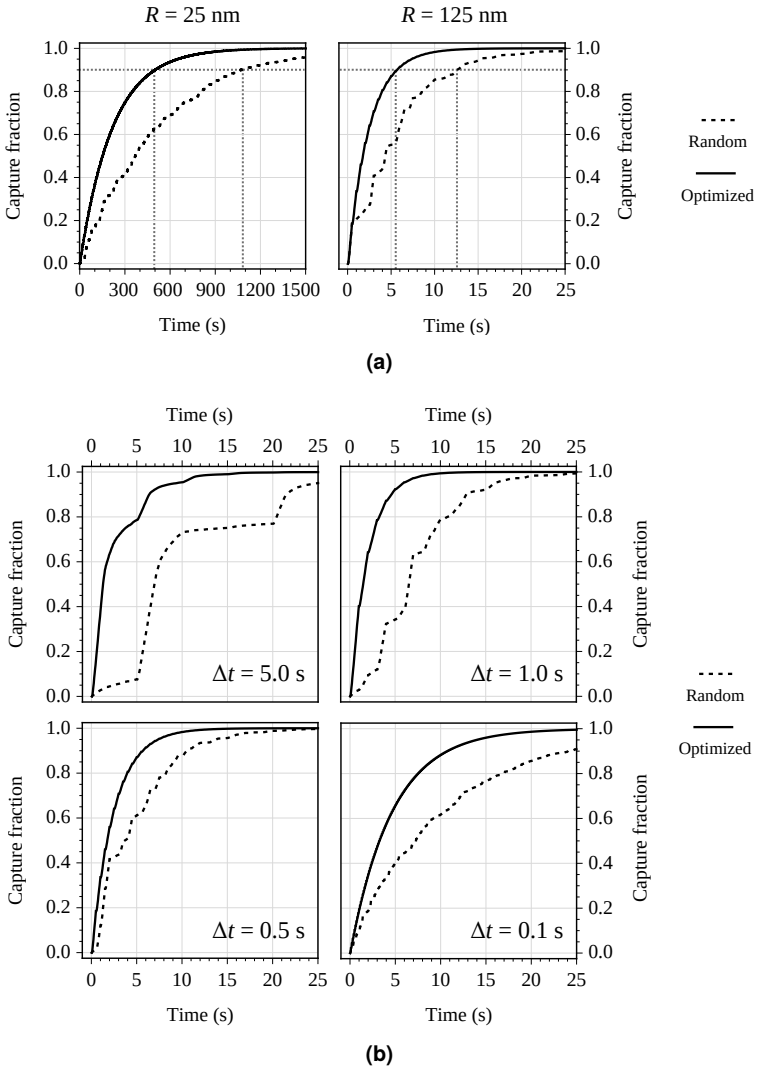

Figure 6.11. (a) Typical separation curves for a cascade procedure for two different particle sizes (solid line = optimal cascade, dotted line = random cascade). The gray dotted lines mark a capture fraction of 0.9. For $R = 25\,\mathrm{nm}$, a value of $\Delta t_{\mathrm{run}} = 10\,\mathrm{s}$ is used. For $R = 125\,\mathrm{nm}$, a value of $\Delta t_{\mathrm{run}} = 0.5\,\mathrm{s}$ is used. (b) Typical separation curves produced by the cascade procedure (solid line = optimal cascade, dotted line = random cascade), for different time steps Δt_{run}. A particle size of 125 nm is used.

A simulation time step of $\Delta t = 10^{-6}$ s is used to allow more accurate simulation of particle interactions. Each simulation is run for a maximum duration of $t_{\max} = 1$ s.

Chain formation Investigation of the particle positions in the initial phase of the simulation run, shows that particles sometimes aggregate into chains, depending on their size and the local concentration (see Figure 6.12). For the 25 nm particles chain formation is absent for the low concentration, and only very slightly present for the high concentration. This is primarily due to their relatively weak magnetic interaction. The 75 nm particles always show chain formation, but it is more pronounced at the higher concentration. These results are explained by considering a criterion for chain formation found in ferrofluid theory [38]. Consider the ratio between the dipole interaction energy and the thermal energy,

$$\Gamma = \frac{\mu_0 \mu^2}{2\pi d^3 k_B T} \tag{6.25}$$

where μ is the magnetic moment of the particles and d is the particle diameter. Then for $\Gamma \gg 1$, chains are formed. Andreu *et al.* [32] give an approximate expression for the average chain length $\bar{n}$,

$$\bar{n} \approx \sqrt{\phi_0 e^{\Gamma - 1}} \tag{6.26}$$

with ϕ_0 the volume fraction of magnetic particles. For our larger particle size $\Gamma \approx 825$ and $\bar{n} \gg 1$ over the concentration range under investigation, always predicting chain formation. For the 25 nm particles $\Gamma \approx 1$ and $\bar{n}$ is strongly concentration dependent, resulting in little or no chain formation. For the larger particles we actually obtain far less chain formation and shorter chains ($\bar{n}_{\text{exp}} \approx 4$) than expected. This can be ascribed to the fact that we have simulated still rather dilute systems, and in the presence of strong magnetic gradients. Therefore, particles will mostly move towards the cylinder individually and only form chains if they were close to another particle in their initial positions. This behaviour has also been observed by others [14].

Separation efficiency Analogous to the investigation of the capture efficiency by a single cylinder for a dilute system of particles, we investigate here the change in capture fraction during the simulation run in the case of a higher concentration. As before, we vary the orientation of the cylinder, the particle size, and additionally, the concentration of the nanoparticles in the initial volume.

In Figure 6.13 the fraction of captured particles is shown during the simulation for a cylinder of aspect ratio $L/D = 20$ with $\alpha = 0°$ and $\alpha = 90°$ respectively. The results are shown for a particle size of 75 nm, and behaviour for 125 nm was found to be very similar. For both magnetization directions an initial short period is seen (0.1 s–0.25 s) where no particles are captured by the cylinder. This is due to the fact that the particles are generated in a relatively small volume some distance away from the cylinder. All particles must travel this initial distance before they can be captured. After this initial period, there is a very steep increase in capture fraction, followed by a slower increase reaching a value of 1.0 well within 0.5 s. The particles that are part of a chain structure are captured during the steep increase (this can be seen by

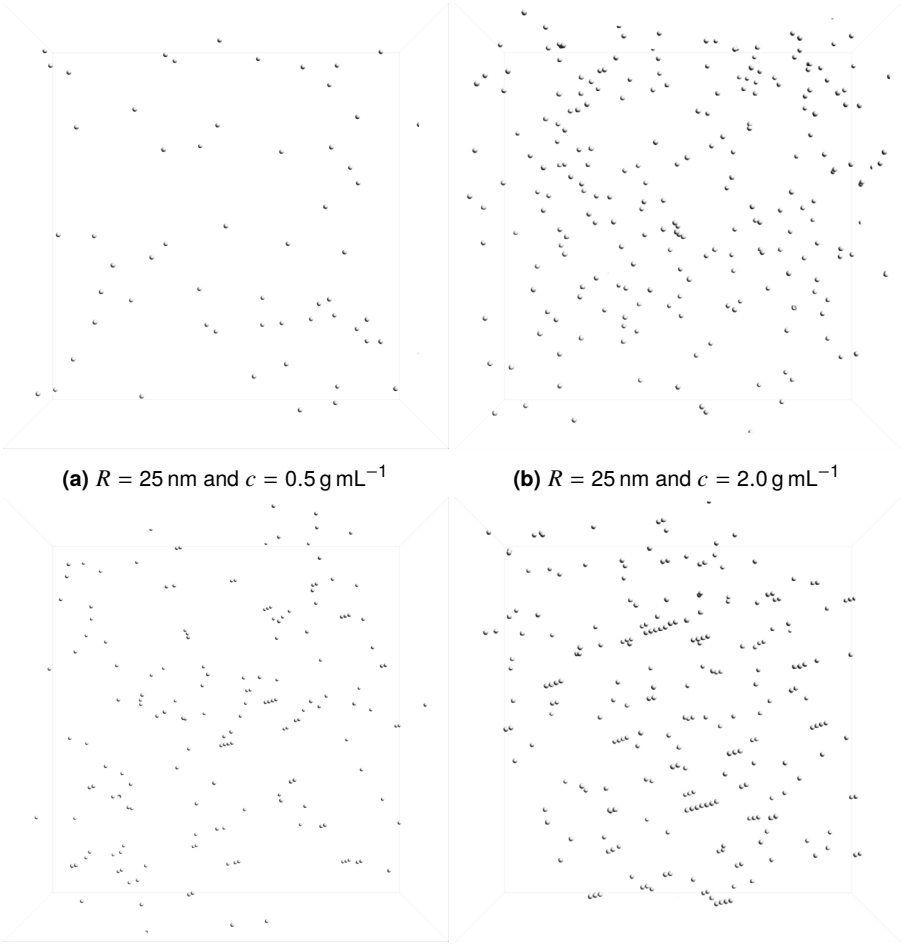

(a) $R = 25\,\text{nm}$ and $c = 0.5\,\text{g mL}^{-1}$

(b) $R = 25\,\text{nm}$ and $c = 2.0\,\text{g mL}^{-1}$

(c) $R = 75\,\text{nm}$ and $c = 0.5\,\text{g mL}^{-1}$

(d) $R = 75\,\text{nm}$ and $c = 2.0\,\text{g mL}^{-1}$

Figure 6.12. Snapshot of the nanoparticles during the separation process, for different sizes and concentrations of the samples.

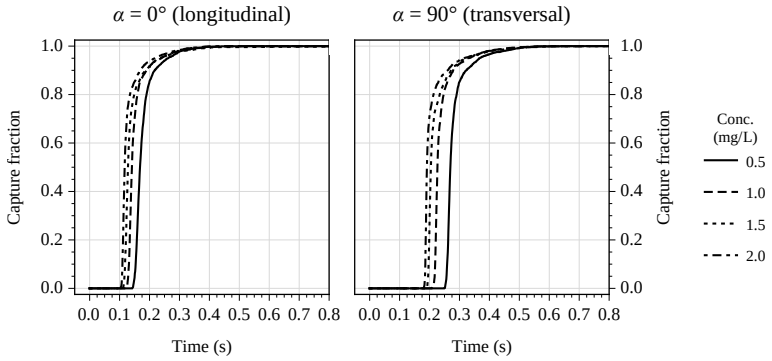

Figure 6.13. Particle capture fraction versus the simulation progression for different sample concentrations (in mg L^{-1}) and two magnetization directions. A cylinder of aspect ratio $L/D = 20$ is used, and particles have a radius of $R = 75$ nm.

visual inspection), establishing the enhanced capture efficiency of chains. During the final stages, the remaining single particles are captured. The capture time for the transverse magnetization is almost twice that of the longitudinal magnetization, due to the fact that the TOP region for transverse magnetization is less active than for longitudinal magnetization (cf. the dilute case). Finally, the shortest separation times are found for the highest particle concentrations. This agrees with a higher fraction of chain-structures, leading to faster separation.

Further investigation of the capture enhancement due to concentration effects can include a comparison with experimental and theoretical studies on magnetophoresis [7, 39].

6.5 Conclusion and outlook

In this chapter we have described a detailed Brownian dynamics approach to simulate the behaviour of magnetic nanoparticles in the presence of a magnetized cylinder. The motion of magnetic nanoparticle is calculated by considering a combination of Brownian forces, hydrodynamic interactions, magnetic dipole-dipole interactions and most importantly, a magnetic force due to the presence of a magnetic field gradient. We have made extensive use of the ability to analytically calculate the magnetic field and field gradients produced by a magnetized cylinder, which allowed us to directly calculate particle trajectories in the presence of a rather complex magnetic field.

Particle capture zones were predicted, showing that for longitudinally magnetized cylinders only the top and bottom areas of the cylinder actively contribute to particle capture. For a cylinder that acquires a transverse magnetization component, particles were also expected to be captured at the lateral surface of the cylinder. These predictions were confirmed by the Brownian dynamics simulations, where longitudinally magnetized cylinders were found to capture a significantly smaller fraction of particles than transversely magnetized cylinders. This effect was somewhat reduced by using cylinders of a smaller aspect ratio.

These findings suggest that a separation medium consisting of cylinders oriented perpendicular to the external field, will provide a more effective medium for particle separation than a random packing of fibres. However, the particular choice of packing structure will also influence macroscopic hydrodynamic properties of the separation medium, and aspects such as the available surface area for particle capture. The exact influence of these factors on the actual separation efficiency will yet have to be investigated.

Our simulations show that magnetic nanoparticles with sizes down to 50 nm can be captured within 50 s reaching capture fractions close to 100 %. For smaller particles, the relative strength of Brownian motion increases with respect to the magnetic attraction towards the cylinder, and particles are no longer guaranteed to be captured, or only very slowly. Similar to others [14], we have shown that by increasing the concentration of the magnetic nanoparticles, chain formation may occur, which enhances particle capture due to collective motion.

As an outlook, our simulations can be extended rather easily to include multiple cylinders and a uniform background flow field. This will allow us to make a next step towards a comprehensive model of magnetic separation in magnetic porous media.

Acknowledgements

Alessio Caciagli is thanked for his major contributions to the realization of this chapter. Johan Padding is acknowledged for initial discussion on the Brownian dynamics.

References

1. K. Mandel, F. Hutter, 'The magnetic nanoparticle separation problem', *Nano Today* **2012**, *7*, 485–487, DOI 10.1016/j.nantod.2012.05.001.
2. G. D. Moeser, K. A. Roach, W. H. Green, T. A. Hatton, P. E. Laibinis, 'High-gradient magnetic separation of coated magnetic nanoparticles', *AIChE Journal* **2004**, *50*, 2835–2848, DOI 10.1002/aic.10270.
3. C. T. Yavuz, J. T. Mayo, W. Y. William, A. Prakash, J. C. Falkner, S. Yean, L. Cong, H. J. Shipley, A. Kan, M. Tomson, D. Natelson, V. L. Colvin, 'Low-field Magnetic Separation of Monodisperse Fe_3O_4 Nanocrystals', *Science* **2006**, *314*, 964–967, DOI 10.1126/science.1131475.
4. S. Miltenyi, W. Müller, W. Weichel, A. Radbruch, 'High gradient magnetic cell separation with MACS', *Cytometry* **1990**, *11*, 231–238, DOI 10.1002/cyto.990110203.
5. Q. A. Pankhurst, N. T. K. Thanh, S. K. Jones, J. Dobson, 'Progress in applications of magnetic nanoparticles in biomedicine', *Journal of Physics D: Applied Physics* **2009**, *42*, 224001, DOI 10.1088/0022-3727/42/22/224001.
6. J. A. Oberteuffer, 'Magnetic separation: A review of principles, devices, and applications', *IEEE Transactions on Magnetics* **1974**, *10*, 223–238, DOI 10.1109/TMAG.1974.1058315.
7. G. De Las Cuevas, J. Faraudo, J. Camacho, 'Low-gradient magnetophoresis through field-induced reversible aggregation', *Journal of Physical Chemistry C* **2008**, *112*, 945–950, DOI 10.1021/jp0755286.
8. P. G. De Gennes, P. A. Pincus, 'Pair correlations in a ferromagnetic colloid', *Physik der kondensierten Materie* **1970**, *11*, 189–198, DOI 10.1007/BF02422637.
9. J. J. Weis, D. Levesque, 'Chain formation in low density dipolar hard spheres: a Monte Carlo study', *Physical Review Letters* **1993**, *71*, 2729, DOI 10.1103/PhysRevLett.71.2729.
10. K. Butter, P. H. H. Bomans, P. M. Frederik, G. J. Vroege, A. P. Philipse, 'Direct observation of dipolar chains in iron ferrofluids by cryogenic electron microscopy', *Nature Materials* **2003**, *2*, 88–91, DOI 10.1038/nmat811.

11. M. Klokkenburg, C. Vonk, E. M. Claesson, J. D. Meeldijk, B. H. Erné, A. P. Philipse, 'Direct Imaging of Zero-Field Dipolar Structures in Colloidal Dispersions of Synthetic Magnetite', *Journal of the American Chemical Society* **2004**, *126*, 16706–16707, DOI 10.1021/ja0456252.
12. J. A. Ritter, A. D. Ebner, K. D. Daniel, K. L. Stewart, 'Application of high gradient magnetic separation principles to magnetic drug targeting', *Journal of Magnetism and Magnetic Materials* **2004**, *280*, 184–201, DOI 10.1016/j.jmmm.2004.03.012.
13. H. Okada, K. Mitsuhashi, T. Ohara, E. R. Whitby, H. Wada, 'Computational Fluid Dynamics Simulation of High Gradient Magnetic Separation', *Separation Science and Technology* **2005**, *40*, 1567–1584, DOI 10.1081/SS-200056063.
14. V. Schaller, U. Kräling, C. Rusu, K. Petersson, J. Wipenmyr, A. Krozer, G. Wahnström, A. Sanz-Velasco, P. Enoksson, C. Johansson, 'Motion of nanometer sized magnetic particles in a magnetic field gradient', *Journal of Applied Physics* **2008**, *104*, 093918, DOI 10.1063/1.3009686.
15. R. Kubo, 'The fluctuation-dissipation theorem', *Reports on Progress in Physics* **1966**, *29*, 255–284, DOI 10.1088/0034-4885/29/1/306.
16. M. P. Allen, D. J. Tildesley, *Computer simulation of liquids*, 2nd ed., Clarendon Press - Oxford, **1989**.
17. D. Frenkel, B. Smit, *Understanding Molecular Simulation: From Algorithm to Applications*, 1st ed., Academic Press, **1996**.
18. J. K. G. Dhont, *An introduction to dynamics of colloids*, (Eds.: R. Miller, D. Mobius), Elsevier B.V., **1996**.
19. D. L. Ermak, J. A. McCammon, 'Brownian dynamics with hydrodynamic interactions', *The Journal of Chemical Physics* **1978**, *69*, 1352, DOI 10.1063/1.436761.
20. J. G. de la Torre, V. A. Bloomfield, 'Hydrodynamic properties of complex, rigid, biological macromolecules: theory and applications', *Quarterly Reviews of Biophysics* **1981**, *14*, 81–139, DOI 10.1017/S0033583500002080.
21. C. W. Oseen, *Hydrodynamik*, Leipzig: Teubner, **1927**, as noted in G. K. Batchelor, *Introduction to Fluid Dynamics*, Cambridge University Press, Cambridge, UK, **2000**.
22. J. Burgers, *Second Report on Viscosity and Plasticity*, *Vol. Eerste sectie, Deel XVI (4)*, Verhandelingen der Koninklijke Nederlandsche Akademie van Wetenschappen, Afdeeling Natuurkunde, **1939**.
23. J. Rotne, S. Prager, 'Variational Treatment of Hydrodynamic Interaction in Polymers', *The Journal of Chemical Physics* **1969**, *50*, 4831–4837, DOI 10.1063/1.1670977.
24. H. Yamakawa, 'Transport Properties of Polymer Chains in Dilute Solution: Hydrodynamic Interaction', *The Journal of Chemical Physics* **1970**, *53*, 436–443, DOI 10.1063/1.1673799.
25. L. Durlofsky, J. F. Brady, G. Bossis, 'Dynamic simulation of hydrodynamically interacting particles', *Journal of Fluid Mechanics* **1987**, *180*, 21–49, DOI 10.1017/S002211208700171X.
26. N.J. Higham (originator), Encyclopaedia of Mathematics, Last visited on 03/10/2015, http://www.encyclopediaofmath.org/index.php?title=Cholesky_factorization&oldid=11469.
27. G. Mie, 'Zur kinetischen Theorie der einatomigen Körper', *Annalen der Physik* **1903**, *316*, 657–697, DOI 10.1002/andp.19033160802.
28. M. Knobel, W. C. Nunes, L. M. Socolovsky, E. De Biasi, J. M. Vargas, J. C. Denardin, 'Superparamagnetism and Other Magnetic Features in Granular Materials: A Review on Ideal and Real Systems', *Journal of Nanoscience and Nanotechnology* **2008**, *8*, 2836–2857, DOI 10.1166/jnn.2008.017.
29. E. C. Stoner, E. P. Wohlfarth, 'A mechanism of magnetic hysteresis in heterogeneous alloys', *IEEE Transactions on Magnetics* **1991**, *27*, 3475–3518, DOI 10.1109/TMAG.1991.1183750.
30. Z. Nagy, B. J. Nelson, 'Lagrangian Modeling of the Magnetization and the Magnetic Torque on Assembled Soft-Magnetic MEMS Devices for Fast Computation and Analysis', *IEEE Transactions on Robotics* **2012**, *28*, 787–797, DOI 10.1109/TRO.2012.2193230.
31. K. Butter, PhD thesis, Universiteit Utrecht, The Netherlands, **2003**.
32. J. S. Andreu, J. Camacho, J. Faraudo, 'Aggregation of superparamagnetic colloids in magnetic fields: the quest for the equilibrium state', *Soft Matter* **2011**, *7*, 2336–2339, DOI 10.1039/C0SM01424A.
33. S. Jiang, Z. Liang, J. Huang, 'A fast algorithm for Brownian dynamics simulation with hydrodynamic interactions', *Mathematics of Computation* **2013**, *82*, 1631–1645, DOI 10.1090/S0025-5718-2013-02672-5.
34. T. Geyer, U. Winter, 'An $O(N^2)$ approximation for hydrodynamic interactions in Brownian dynamics simulations.', *The Journal of Chemical Physics* **2009**, *130*, 114905, DOI 10.1063/1.3089668.

35. F. Martínez-Pedrero, M. Tirado-Miranda, A. Schmitt, J. Callejas-Fernández, 'Formation of magnetic filaments: A kinetic study', *Physical Review E* **2007**, *76*, 011405, DOI 10.1103/PhysRevE.76.011405.
36. D. Heinrich, A. R. Goñi, C. Thomsen, 'Dynamics of magnetic-field-induced clustering in ionic ferrofluids from Raman scattering', *Journal of Chemical Physics* **2007**, *126*, 124701, DOI 10.1063/1.2713112.
37. G. P. Gajula, M. T. Neves-Petersen, S. B. Petersen, 'Visualization and quantification of four steps in magnetic field induced two-dimensional ordering of superparamagnetic submicron particles', *Applied Physics Letters* **2010**, *97*, 1–3, DOI 10.1063/1.3475770.
38. R. E. Rosensweig, *Ferrohydrodynamics*, Cambridge University Press, **1985**.
39. J. Andreu, J. Camacho, J. Faraudo, M. Benelmekki, C. Rebollo, Ll. M. Martínez, 'Simple analytical model for the magnetophoretic separation of superparamagnetic dispersions in a uniform magnetic gradient', *Physical Review E* **2011**, *84*, 021402, DOI 10.1103/PhysRevE.84.021402.

7

Separation of magnetic nanoparticles in magnetic random porous media II: experimental setup

Abstract

We experimentally explore the separation of magnetic nanoparticles in a porous medium composed of magnetizable metallic fibres. The construction of a high-gradient magnetic separation setup is discussed, and preliminary, proof-of-principle results are obtained for the magnetic separation of iron oxide (magnetite) nanoparticles. As a first step towards the modelling of experimental magnetic separation in fibrous media, we determined the liquid permeability of our separation matrices.

7.1 Introduction

Magnetic separation is a technique to extract magnetic, or magnetically susceptible materials from a non-magnetic, containing medium, by means of magnetic forces. This principle is widely used, and on varying length scales, from ore refinery, to removal of heavy metals in water purification and biological cell-specific assays. For an overview see e.g., [1–4]. High-gradient magnetic separation (HGMS) is specifically designed to separate micrometer to millimetre sized materials dispersed in a liquid [1]. An HGMS system usually consists of a column with a matrix (wires, packed bed, etc.) of a magnetically susceptible material. An applied external magnetic field will induce strong magnetic gradients around the matrix material that will exert a proportionally large force on any passing particles. This force can be expressed as [5, 6],

$$\mathbf{F}_\mathrm{m} = \mu_0 V_\mathrm{p} (\mathbf{M}_\mathrm{p} \cdot \nabla)\mathbf{H} \tag{7.1}$$

where μ_0 is the permeability of vacuum, V_p is the volume of the magnetically susceptible particle, $\mathbf{M}_\mathrm{p}$ its magnetization vector, and $\mathbf{H}$ the magnetic field at the position of the particle. Particles will accumulate in the matrix only if the magnetic force is larger than competing forces, such as drag forces or thermal forces. Accumulation becomes problematic for sub-micron sized particles, as thermal forces will start to dominate. Theoretical estimates predict that the limiting size for the capture of a single, isolated particle is $\sim 50\,\mathrm{nm}$ [7]. However, particle-particle interactions may induce the formation of (reversible) aggregates which act as one, larger magnetic particle, leading again to successful capture. Yavuz *et al.* [8] show that by using this effect and a careful choice of the particle chemistry, reversible separation of particles smaller than $\sim 20\,\mathrm{nm}$ is experimentally possible. Experiments by Beveridge *et al.* also show the successful separation and purification of particles smaller than 20 nm by a technique called differential magnetic catch and release [9–11]. Additionally, narrowed size distributions can be obtained [10].

In this work, we explore a method to perform high-gradient magnetic separation within a well-defined separation matrix. For this purpose we opt for a matrix consisting of randomly packed cylindrical fibres. Such packings are easy to create, and have well-known structural properties [12] (see also Chapter 2). The immediate advantage of such a magnetizable porous medium on the separation efficiency can be easily demonstrated, as can be seen in Figure 7.1. By choosing a low-remanent metal alloy as the fibre material, any captured particles are unlikely to remain attached to the fibre by magnetic forces after the external field has been removed. They may, however, stay attached due to Van der Waals forces. Magnetic separation experiments in a fibrous medium have been explored previously by Butter [13].

The fact that the structural properties of a random packing of rods are determined only by the aspect ratio of the rods, potentially allows for the creation of simple models for other properties of the packing as well, such as the liquid permeability [14–16]. Currently available models usually are derived from the empirical Kozeny-Carman relation [17, 18] which relates the permeability to the porosity of the packing.

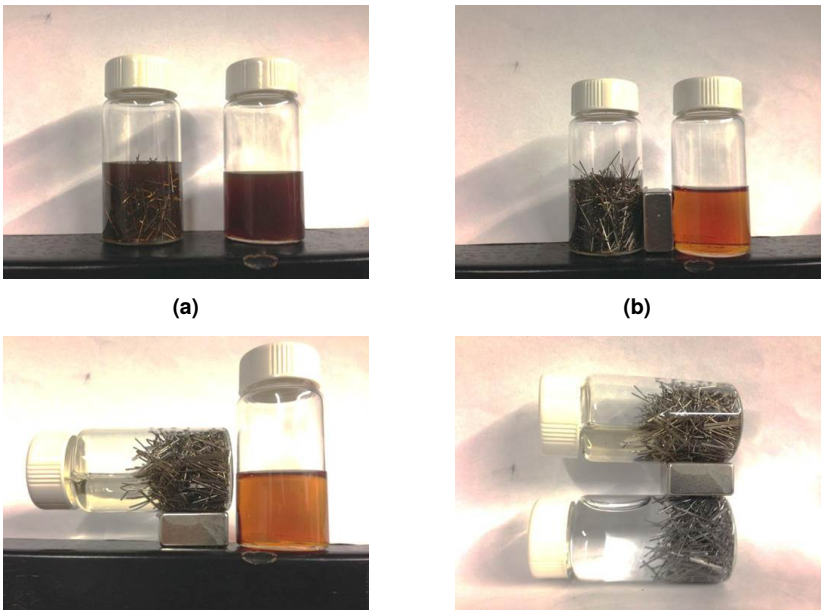

Figure 7.1. Proof-of-principle experiment for the separation enhancement due to the presence of magnetizable fibres. (a) Two flasks are filled with the same amount of diluted dispersion of magnetite nanoparticles (Fe_3O_4, mean diameter $\approx$ 15 nm). In the left flask, a small amount of magnetizable fibres is added and a hand magnet is placed in between the flasks for a period of 6 hours. This results in a clear difference in the colour of the liquid ((b) and (c)). Already after a few minutes a clear colour change is visible in the flask with fibres. (d) A comparison of the liquid after separation (top) and the original solvent (bottom). Only a minor difference is visible, indicating that most of the nanoparticles have been captured by the fibres.

We build upon this idea by constructing a magnetic separation method that for a given type of magnetically separable (nano)material, ultimately would depend only on a few parameters: 1) the rod aspect ratio, controlling the packing permeability and available surface area, 2) the applied field strength, controlling the magnetic separation forces, and 3) the applied external pressure, controlling the separation speed. How these variables are specifically related to the separation efficiency (i.e. the fraction of nanoparticles that can be extracted from a dispersion within a certain amount of time) is yet unknown. The experimental work described in this chapter, together with the simulations in Chapter 6, aim to provide a starting point for further investigation.

This chapter is organized as follows. First, the theoretical background of the structure and fluid flow properties of the fibrous porous medium, and magnetization measurements are discussed. Second, the experimental setup is described, together with the type of nanoparticles used and the different characterization methods. Finally, the results for permeability measurements and initial separation measurements are shown and discussed, followed by a conclusion and outlook for future experiments.

7.2 Theory

7.2.1 Random fibrous porous media

It is well established through experiments and simulations that when identical rod-like objects are poured or put in a large container, they form random packings with reproducible structures and densities depending only on their aspect ratio (see Chapter 2 for more details). Philipse [12] used spherocylinders as a model particle and discussed this phenomenon in light of a random contact model, that for rigid long rods gives the relation,

$$\phi \frac{L}{D} \sim \frac{\langle C \rangle}{2} \qquad \text{for} \qquad \frac{L}{D} \gg 1 \tag{7.2}$$

where ϕ is the volume fraction of the packing, L and D are the length and diameter of the rod respectively, and $\langle C \rangle$ is the average number of contacting particles per particle. For sufficiently long rods, packings of high mechanical stability are found with $\langle C \rangle \approx 9.8$, corresponding to experiments and simulations [12, 19–21]. At these increased aspect ratios, the two hemispheres at either end of a spherocylinder will have a decreased influence on the packing structure. This allows us to apply the results for spherocylinder packings to our cylinder-based separation matrix packings as well.

The use of a random rod packing as porous medium for magnetic separation opens possibilities for modelling the separation process. We have derived the magnetic properties of a single magnetized cylinder in Chapter 5, where we have also shown that within reasonable approximation (e.g. by leaving out mutual interactions), the resulting magnetic field of an assembly of multiple cylinders can be calculated. This allows a full description of the magnetic field and magnetic field gradients of fibrous porous media. The capture efficiency of magnetized cylinders is studied by simulation in Chapter 6. In general, a cylinder perpendicular to the applied magnetic field will have the highest probability to capture the most particles, and a cylinder parallel to the field the lowest. Because our medium is composed of randomly oriented cylindrical fibres, this effect is averaged out.

7.2.2 Permeability

For a viscous fluid flow through a porous medium, a relation exists between the mass flow velocity and the packing permeability. This relation is known as Darcy's Law [22, 23], and can be stated as,

$$U = k \frac{\rho_0}{\eta_0} \frac{A \Delta P}{L} \tag{7.3}$$

where U is the mass flow velocity, ρ_0 the solvent density, η_0 the solvent viscosity, and A the cross sectional area of the medium. ΔP is the applied pressure difference over a distance L. Darcy's Law is derived under the assumption of laminar flow, which requires the pore volume and flow speeds in the porous medium to be sufficiently small. Under these circumstances, the packing permeability k (units of m^2) can be estimated by the Kozeny-Carman (KC) equation [17, 18], a scaling relation between k and the

packing fraction ϕ, or porosity $(1-\phi)$,

$$k = \frac{(1-\phi)^3}{C_{\mathrm{KC}}\phi^2}\nu^2 \qquad \text{with} \qquad \nu = \frac{V}{S} \tag{7.4}$$

Here C_{KC} is a constant dependent on the details of the specific packing structure, V and S are the volume and surface area per particle, respectively, and ν is a characteristic length scale associated with the packing (typically related to the average pore size). As with Darcy's Law, the KC scaling is strictly speaking only valid for laminar flows. The scaling law has been successfully applied for many different materials, including sandstone [24], soils [25], and random packings of colloidal spheres and ellipsoids [26–28].

Note that the characteristic length scale ν and packing fraction ϕ are treated frequently as uncorrelated parameters. For a random packing of sufficienctly long rods however, they are closely related via Equation 7.2. In the limit of long rods we have $\nu = D/4$, which can be substituted directly into Equation 7.4.

7.2.3 Magnetization

A superparamagnetic particle will orient itself in the direction of the applied field **H**. Assuming the particle exhibits no magnetic hysteresis, its magnetization M is given as a simple function of the magnitude of the field, H. It is described by the Langevin function,

$$M(H) = M_{\mathrm{sat}}\left(\coth x - \frac{1}{x}\right) \qquad \text{with} \qquad x = \frac{\mu_0\mu H}{k_{\mathrm{B}}T} \tag{7.5}$$

where M_{sat} is the saturation magnetization, μ_0 is the magnetic permeability of vacuum, μ is the particle magnetic dipole moment, and $k_{\mathrm{B}}T$ is the thermal energy. The dipole moment of a particle is proportional to the volume of its magnetic core, given by,

$$\mu = \tfrac{4}{3}\pi r_{\mathrm{mag}}^3 m_{\mathrm{sat}} \tag{7.6}$$

with r_{mag} the particle's magnetic radius and m_{sat} the bulk material saturation magnetization (for magnetite, $4.46 \times 10^5\ \mathrm{A\,m^{-1}}$ [7]. For low fields ($\mu_0\mu H \ll kT$), Equation 7.5 can be approximated by,

$$M(H) \approx \chi_{\mathrm{i}} H = M_{\mathrm{sat}}\left(\frac{\mu_0\mu H}{3kT}\right) \tag{7.7}$$

where χ_{i} is the initial susceptibility that can be determined from the (linear) slope of an experimental magnetization curve around $H = 0$. When assuming monodisperse particles, the magnetic radius is given by,

$$r_{\mathrm{M}}^3 = \frac{\chi_{\mathrm{i}}}{M_{\mathrm{sat}}}\left(\frac{9kT}{4\pi\mu_0 m_{\mathrm{sat}}}\right) \tag{7.8}$$

For a polydisperse size distribution, the magnetization becomes an integral over all particle dipole moments,

$$M(H) = \int_0^\infty \mathrm{d}\mu\, \mu L(H, \mu) P(\mu) \tag{7.9}$$

The magnetic dipole moment distribution $P(\mu)$ can be obtained by a numerical inversion procedure with the experimental magnetization curve as input. We apply the MINORIM method [29] to obtain $P(\mu)$. MINORIM has been successfully applied to the analysis of ferrofluids before [30]. A major advantage of MINORIM over other inversion methods is that there is no *a priori* assumption of an underlying distribution. Prior to analysis, any linear contribution, such as a diamagnetic contribution, are subtracted from the magnetization curve. The obtained dipole moment distribution can be converted to a particle size distribution via Equation 7.6.

7.3 Experimental

7.3.1 Nanoparticle dispersions

Dispersions of charge stabilized superparamagnetic magnetite (Fe_3O_4) were synthesized following Massart [31]. Typically, 0.02 mol $FeCl_2 \cdot 4\,H_2O$ is dissolved in 10 mL 2 M hydrochloric acid and 0.04 mol $FeCl_3 \cdot 6\,H_2O$ is dissolved in 40 mL demineralized water. The solutions are mixed and after brief ultrasonication, the mixture is added to 500 mL 0.7 M ammonia while stirring vigorously. A black precipitate is formed immediately and the mixture is stirred for another 10 minutes. Afterwards, the magnetite is collected by a hand magnet and the supernatant is discarded. The particles are redispersed in 50 mL 1 M tetramethylammonium hydroxide (TMAH) solution and stirred overnight. To remove excess TMAH, the particles are collected again and redispersed in demineralized water, yielding a stock solution with a typical weight concentration of 2.7 g L^{-1}.

Another aqueous, charge stabilized, ferrofluid of was obtained from Ioniqa Technologies [32] for testing purposes.

7.3.2 Separation setup

The magnetic separation setup used in this work, was constructed based on the filtration and permeation setup described by Thies-Weesie [27], adapted for flow in a magnetic field (see Figure 7.2). The setup was originally used to prepare and measure the permeability of dense sediments of colloidal particles [27, 28, 33].

A glass solvent reservoir (I) is pressurized by a controllable nitrogen gas source (II), allowing for excess pressures of up to 2 bar. A series of valves and tubing connects the reservoir to the separation cell (III) placed in between the tapered poles of an electromagnet (Bruker BE 25V). Homogeneous fields between 0–2 T, perpendicular to the cell, can be generated along the entire length of the cell. Glass separation cells of length 28 cm with two different diameters were used (⌀= 20 mm and ⌀= 40 mm). A

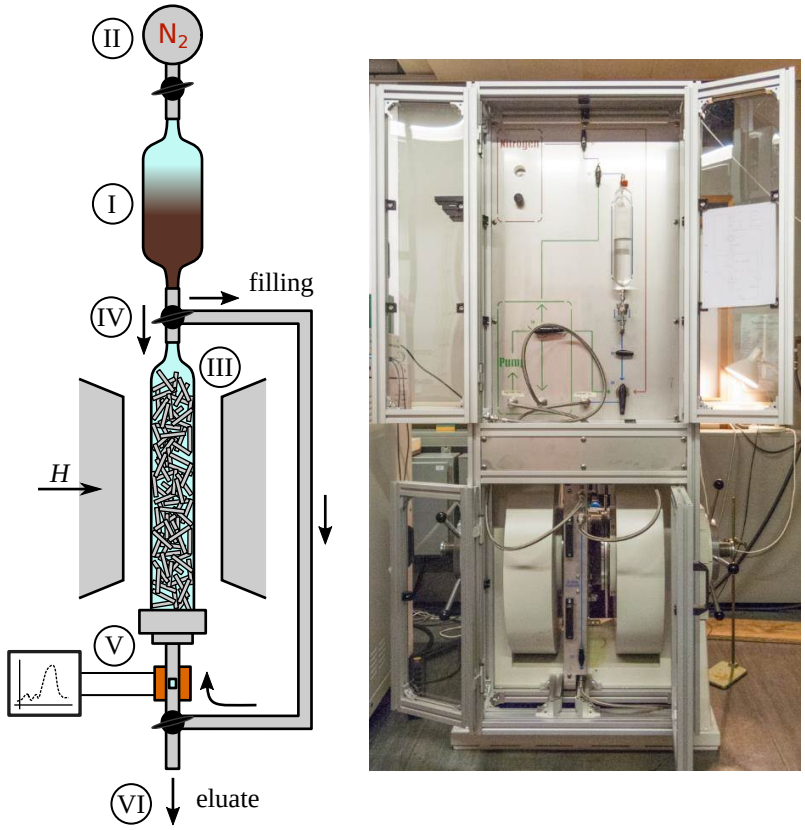

Figure 7.2. A schematic of the constructed separation setup (*left*), not drawn to scale, and a photograph of the setup as constructed (*right*). See text for the description of the components marked with Roman numerals.

separation cell of acrylic glass, poly(methyl methacrylate), was also used as a more mechanically rigid alternative. A valve (IV) allows to switch between top-to-bottom or bottom-to-top flow. The latter setting is used to fill the separation cell containing the porous fibrous medium, reducing the number of trapped air bubbles. An in-line flow cell (V) connected to a Sensline Avaspec 2048 XL (Avantes) spectrophotometer with an Avalight DHc light source, is used to measure the absorbance of the sample directly after the separation cell. The absorbance is used as a qualitative measure for the nanoparticle concentration. Finally, the eluted liquid is collected in a beaker and is automatically weighed on a calibrated balance (VI) at regular intervals.

7.3.3 Separation experiments

Two types of exploratory separation experiments have been performed, to test the newly constructed setup. In all experiments, the entire setup was flushed with water before each separation run. The absorbance was measured continuously to obtain a concentration profile for the separation and release. For the magnetite dispersions under consideration, there is no distinctive absorption peak and the light absorbance is obtained at an arbitrarily chosen wavelength of 530 nm.

Dynamic separation experiments In this experiment, the separation cell containing the fibre matrix is filled with solvent initially and a diluted ferrofluid is placed in the reservoir. The electromagnet is activated and the setup is pressurized, allowing the ferrofluid to slowly replace the solvent in the separation cell. A fraction of the magnetic particles will be captured by the matrix, while the remaining particles (including non-magnetic particles) exit the column. When the reservoir is empty, the flow is stopped and the setup is temporarily depressurized to fill the reservoir with solvent. When the measured absorbance has returned to nearly its baseline value, the electromagnet is deactivated and the release of magnetic particles can be observed by the spectrophotometer. Note that only qualitative experiments have been performed.

Static separation experiments For the static experiments, the separation cell with fibre matrix is initially filled with diluted ferrofluid. The electromagnet is activated and after a certain waiting period, the liquid is eluted from the column at ambient pressure. Captured nanoparticles remain attached to the fibre matrix. Magnetization curves are measured for the eluted ferrofluid and they are analysed to determine particle size distributions.

7.3.4 Separation medium and permeation experiments

A large number of fibres were cut from metal wire ($\varnothing$= 400 µm) of a low-remanence iron-aluminum-chromium alloy AluChrom © (Thyssen Krupp), using a GLW LC100 automated cross cutting machine. Fibres of length 4 mm, 7 mm and 11 mm were cut. To prepare a packing, fibres were poured into the separation cell and then densified slightly by tapping of the cylinder (see Figure 7.3 for examples of a filled column).

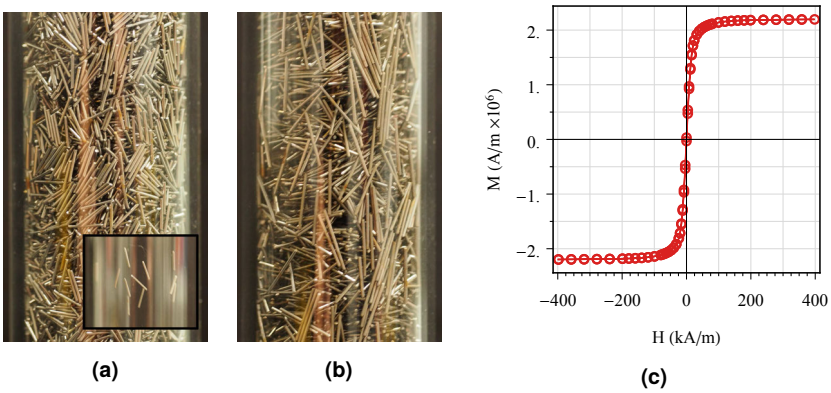

Figure 7.3. (a and b) Two example packings of the ferromagnetic Aluchrom© rods of length 4 mm and 7 mm, respectively, inside the separation cell ($\varnothing$ = 2 cm). The inset shows that even after emptying, some fibres tend to stick to the glass wall due to strong adhesion. (c) Magnetic hysteresis curve for a single rod (D = 0.4 mm, L = 4.5 mm), oriented parallel to the applied field.

Some alignment of the fibres with the wall was unavoidable, partly due to relatively strong adhesive forces (inset of Figure 7.3a).

The magnetic hysteresis curve of a single rod was determined using a EZ9 VSM (MicroSense) vibrating sample magnetometer (Figure 7.3c). A saturation magnetization of 2.2×10^6 A m^{-1} was found, and no magnetic remanence was observed. Note that the saturation magnetization value is slightly higher than reported values for bulk iron [34].

The permeability of the separation medium with fibres of length 4 mm is determined by flowing water through the packing at a series of increasing excess pressures (0.0–1.0 bar in steps of 0.2 bar). The mass of the eluate is recorded at 1 s intervals and linear fits are made through the acquired data points.

7.3.5 Characterization

Transmission electron microscopy images were obtained using a Philips Tecnai10, operating at 100 kV. Dispersion of nanoparticles were diluted and dried in air on copper grids coated with formvar. Particle size distributions were obtained using AnalySIS software by manual measurement of at least 100 particles. Scanning electron microscopy images of the metallic fibres were obtained with a FEI XL30 FEG, operating at 5 kV, without additional conductive coating. Particle concentrations were determined by weighing and drying of a known volume of a dispersion. Magnetization curves were measured with a vibrating sample magnetometer (VSM) EZ9 VSM (MicroSense) at room temperature. Small sample cups were filled with a weighed amount of ferrofluid and symmetric hysteresis loops were recorded with a maximum applied field strength of 1.194×10^6 A m^{-1} (15×10^3 Oe). Each measured curve contains at least 1000 data points. This high accuracy is required for the distribution analysis with MINORIM. A cut-off value of 35×10^3 A m^{-1} was used for the diamagnetic correction.

7.4 Results and discussion

7.4.1 Dispersion characterization

Synthesized magnetite dispersions were analysed by electron microscopy. A typical result is given in Figure 7.4a. By manual measurement, an average particle diameter of 11.2 nm was found with a size polydispersity of 31 %. Such a high polydispersity is expected for aqueous co-precipitation methods. Magnetization curves were also obtained by VSM measurement. From these curves, size distributions were extracted by analysis with MINORIM, giving an average (magnetic) diameter of 5.9 nm and a polydispersity of 47.5 %. The particle size distribution of the ferrofluid supplied by Ioniqa was determined in the same way, and an average magnetic radius of 5.1 nm and polydispersity of 40.0 % was found. The particle's magnetic size distributions are shown in Figure 7.4b.

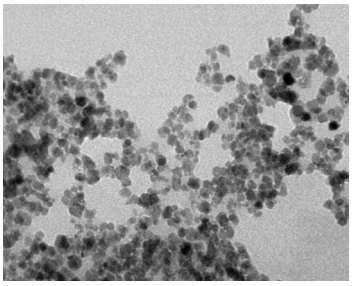

(a)

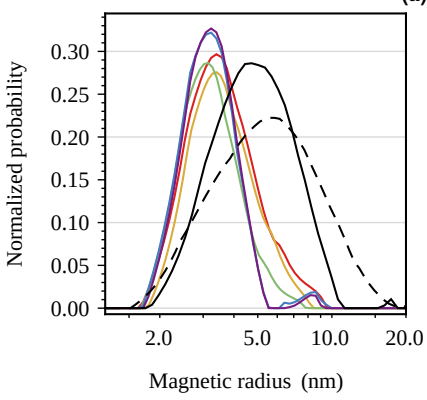

Sample	μ_{mag} (nm)	σ_d (%)
10s	3.43	31.8
20s	3.46	29.9
40s	3.11	26.9
60s	3.13	24.9
180s	3.17	24.2
Ioniqa	4.77	39.0
TMAH	5.39	51.2

(b)

Figure 7.4. (a) A typical electron micrograph of the synthesized magnetite nanoparticles with an average particle diameter of 11.2 nm. (b) The magnetic size distributions as obtained from analysis with the VSM: stock solution of the synthesized particles (labelled TMAH), stock solution of the particles obtained from Ioniqa, and a series of the PSDs of the uncaptured particles for increasing waiting time in the static separation experiments (10–180 s, see Section 7.4.3). In the accompanying table the average magnetic radius μ_{mag} and distribution width σ_{d} is given.

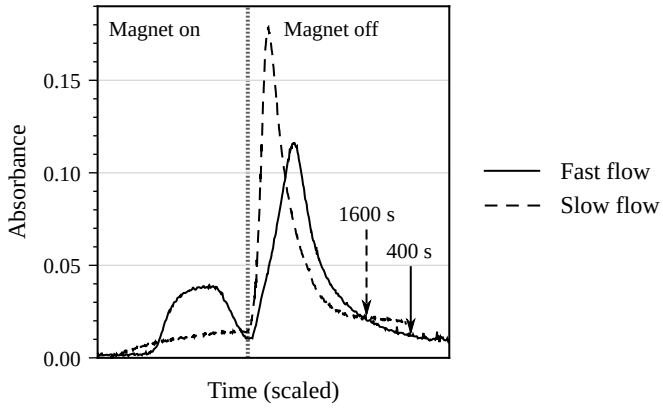

Figure 7.5. A overview of two qualitative separation experiments at different flow speeds. The duration of the experiments is scaled so that the points where the magnet is deactivated coincide (marked by the dashed line). After this point, the large increase in aborbance indicates that a large fraction of magnetic particles had been retained. For the fast flow, some signal is measured before the magnet is switched off, meaning that not all particles were able to be retained by the separation matrix.

7.4.2 Dynamic separation

The performed dynamic separation experiments have been done in a qualitative fashion, primarily to assess the feasibility of the separation setup. A working solution of TMAH-stabilized magnetite was prepared by dilution with a 0.1 % TMAH-solution to an approximate concentration of 0.01 wt%. Fibres of 11 mm were packed into the separation cell and the system was filled bottom-to-top with 0.1 % TMAH-solution, until the level of the reservoir. Approximately 100 mL diluted ferrofluid was added to the reservoir and the magnetic field strength was set to approximately 1.5 T. During two separate runs with different flow speeds (exact values undetermined) the absorbance was recorded. The faster flow is obtained by emptying the column by gravitational forces only, whereas for the slower flow the outlet valve is only partially opened.

The results from the experiments can be seen in Figure 7.5, where the moment the magnet is switched off is marked by a dashed line. The x-axis is rescaled so that the moment where the magnet is switched off, coincides for both graphs. In absolute terms, the fast flow experiment has approximately a 4× higher flow velocity than the slow flow experiment (cf. the points marked 400 s and 1600 s). For the faster flow there is a significant signal measured *before* the magnet is switched off, indicating that a fraction of the magnetic particles is not yet captured by the matrix. Reducing the flow speed allows the dispersion to reside in the column longer, leading to the capture of (nearly) all particles. An alternative explanation for the initial signal could be that some non-magnetic material is detected. This is unlikely though, as the same stock solution is used for the slower flow experiment and a signal is not present there.

Note that if the concentration dependent response of the spectrophotometer and the stock concentration are known, the exact amount of captured and released material could

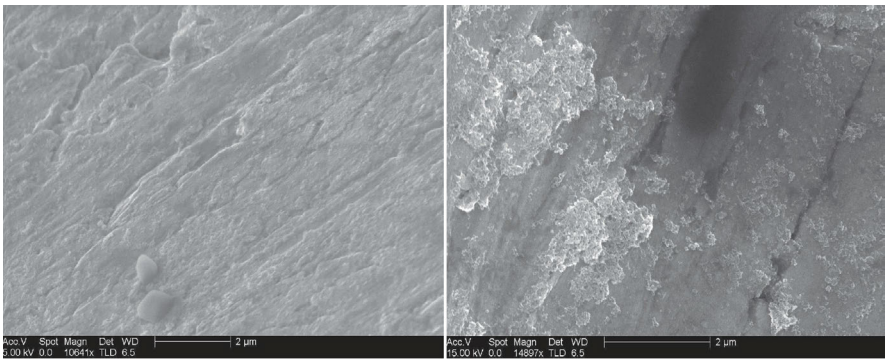

Figure 7.6. Scanning electron microscopy images of the surface of an unused rod (*left*) and a rod after a separation experiment and subsequent thorough rinsing (*right*).

be calculated by integrating the area under the curves in Figure 7.5. For the (qualitative) experiments presented here, this is not yet possible. However, by visual inspection of the column after one cycle of capture and release, it is clear that irreversible adsorption of nanoparticles has occurred. Even after thorough rinsing and shaking of a portion of the fibres with water or a TMAH-solution, a brownish colour remained visible on the fibres. Scanning electron micrographs were obtained for an unused rod and several rods after a separation experiment (see Figure 7.6) confirming the presence of clusters of nanoparticles on the fibre surface. This is likely due to strong Van der Waals forces.

7.4.3 Static separation

For the static separation experiments, a working solution of the ferrofluid supplied by Ioniqa was made by dilution with demineralized water to a concentration of 0.005 wt%. The separation cell was packed with fibres of 7 mm, and was filled bottom-to-top with the diluted ferrofluid. The magnet was turned on at a field strength of ~ 1 T, and after waiting for a duration ranging from 10–180 s, the liquid was eluted from the separation cell while measuring the absorbance. We stress here that elution takes place while the magnetic field is still present, so that most particles are not expected to leave the separation cell.

The resulting graphs for the absorbance are shown in Figure 7.7. At time $t = 0$ the valve is opened to evacuate the liquid from the column. Since the separation cell has been filled from the bottom, the in-line spectrophotometer measurement cell contains the original nanoparticle dispersion. As particles are captured by the fibre matrix, fewer arrive in the measurement cell and the absorbance decreases. The graphs are normalized by the initial absorbance. It can be seen that the relative absorbance goes down when the waiting time increases, meaning that increasingly fewer particles are eluted. This is a clear indication that a longer residence time in the separation cell allows the capture of more particles. Values for the absorbance decrease to approximately 40–50 % of their original, suggesting that 50–60 % of the particles have been successfully captured by the fibre matrix.

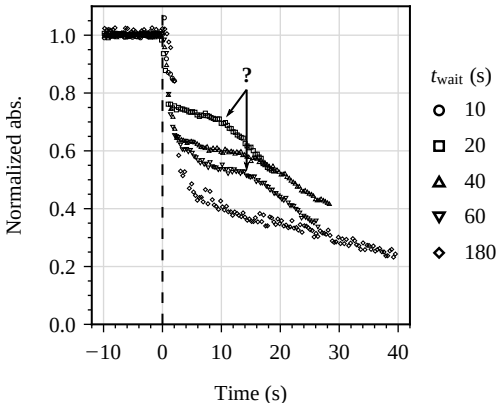

Figure 7.7. Normalized absorbance for the elution of a diluted ferrofluid in a static separation experiment at different waiting times. The valve starting the elution process is opened at $t = 0$. The question mark indicates the unexplained shoulder that is visible for all waiting times, except for 180 s.

It must be noted however that the overall behaviour of the absorbance graphs is highly irregular, with an initial sudden drop and a distinct shoulder (though not for all waiting times). Both effects cannot be explained yet, but may have to do with trapped air bubbles in the tubing. This casts some doubt on the validity of these measurements, and closer inspection and repeated measurements should be performed.

Small portions of the eluted liquid for the different waiting times have been analysed by VSM and MINORIM to obtain particle size distributions (see Figure 7.4b). Two observations can be made here by comparison of the PSDs. First, the change in PSD coming from the stock solutions is significant, with the mean particle's magnetic radius shifting from ~ 5 nm to ~ 3 nm and having a reduced distribution width (see Figure 7.4b). This suggests some size limit in the separation process, where the smaller particles are likely not to have a sufficiently large magnetic moment to be attracted by the magnetized fibres; their thermal motion will dominate over any net motion towards the fibres due to a magnetic force. This size-selection may have merit if small particles with a relatively narrow size distribution are required.

Second, the PSDs of the different waiting times do not differ much, except for a diminishing tail of the distribution for increasing waiting time. Apparently the change in PSD from the stock dispersion to the much narrower and shifted distribution already takes place in the first 10 s of the experiment, implying a rapid separation process. The subsequent change of the PSD is minor, but distinct, further narrowing the distribution. The PSDs for 60 s and 180 s are nearly identical, suggesting no more change in particle capture after this time.

7.4.4 Permeability

The permeability of a packing using fibres of length 4 mm is determined at different applied pressures. Figure 7.8a shows the increase in eluted liquid mass over time, and

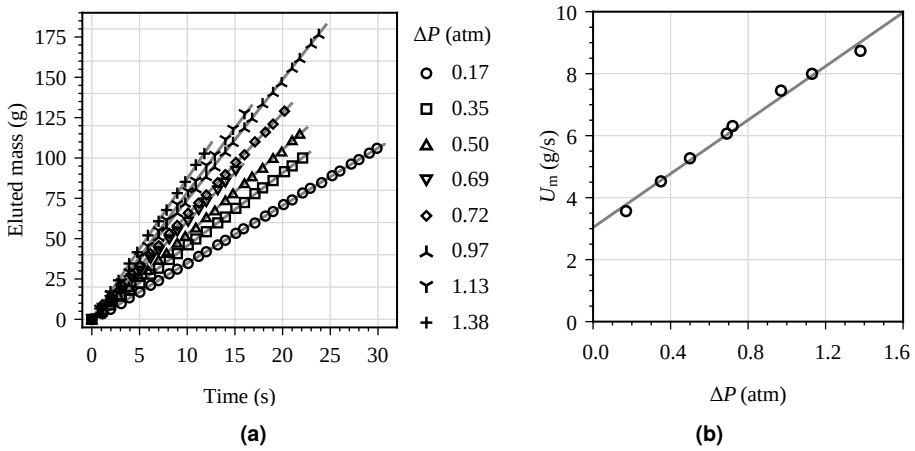

Figure 7.8. (a) The measured mass of the eluted liquid versus the elution time for the different applied excess pressures, including linear fits. (b) The mass flow velocities plotted against the different excess pressures. A linear fit gives a slope, corresponding to U_m (Equation 7.10).

the slope of the linear fits give the corresponding mass flow velocities, U. We correct these velocities by subtracting the mass flow velocity in the case of an empty column, so to account only for the mass flow velocity due to the packing. Another linear fit is made for the relation between the corrected mass flow velocity and the excess pressure, Figure 7.8b, defining the slope as U_m. Now using Equation 7.3, we can determine the effective permeability as follows,

$$k = U_m \frac{\eta_0}{\rho_0} \frac{L}{\frac{1}{4}\pi D^2} \tag{7.10}$$

where $\eta_0 = 0.89\,\text{mPa s}$ and $\rho_0 = 0.997\,\text{g cm}^{-3}$ for water, and D is the diameter of the separation cell. The viscosity and density are not expected to change significantly by the presence of the magnetic nanoparticles. The value of L is determined by measuring the height of the packing from the bottom of the cylinder to slightly below the highest placed fibre.

It can be seen in Figure 7.8b, that even without an applied pressure, there will be a substantial flow rate. This is due to gravitational forces acting on the water column. Note that this does not influence the slope and therefore the determination of the permeability. Using Equation 7.10 a value of $k = 2.2 \times 10^{-4}\,\text{cm}^2$ can be obtained, comparable to the permeability of a well sorted sand and gravel bed [35], classifying it as a 'pervious' material. This value corresponds to a mean pore diameter of ~ 0.1 mm, estimated via the Brinkman screening length [36], $\sqrt{k}$, which may be on the low size, based on visual inspection of the separation column.

7.4.5 Mechanical robustness

During our experimentation we found that the connector at the top of the glass separation cell, linking it to the metal tubing, was a major mechanical weak point in our setup. Due to the large magnetic forces acting on the magnetized separation matrix, this connection broke often, rendering the separation cell useless. The alternative plastic separation cell alleviated this problem somewhat, but a much more robust construction, or an entirely different approach to the separation setup is needed to continue experimentation.

7.5 Conclusion and outlook

In this chapter we have conducted preliminary experiments on the separation of magnetic nanoparticles in a porous magnetizable medium. The capture enhancement due to the presence of magnetized rods was shown in a simple proof-of-principle experiment, turning a dilute dispersion of magnetite particles colourless within a few minutes. In extension of this experiment, we have constructed a larger experimental setup using a porous matrix of randomly packed magnetizable fibres as the separation medium. Several qualitative separation experiments show that given enough time in the separation matrix (i.e. slow or no fluid velocity), 90–100 % of the particles in a diluted ferrofluid can be captured. At most approximately 60 % of the particles is released upon flushing. Particles remain attached to the fibres likely due to high Van der Waals forces. Due to unfortunate problems with the mechanical stability of the separation column, further extensive experimentation was prohibited. Modifying the setup to become more robust is a necessary next step for continuation.

As a first step towards further modelling of the separation process, we have determined the permeability of our separation medium for a particular choice of fibre aspect ratio. The value found conforms reasonably well to values for such open packings. The determination of the permeabilities of packings of different composition may allow us to determine an empirical relation between the packing properties of random rod packings and their hydrodynamic properties.

Acknowledgements

We are grateful for the technical support by Bonny Kuipers, Sander Deelen, Matthijs Krijnen and Hans Heesen in the construction of the setup and Stephan Zevenhuizen for the software interface. Robbert van Dinther is thanked for his exploratory experimental work. A sample of ferrofluid was kindly supplied by Ioniqa Technologies. Sonja Castillo is thanked for the experimental collaboration and the scanning electron micrographs.

References

1. J. A. Oberteuffer, ‘Magnetic separation: A review of principles, devices, and applications’, *IEEE Transactions on Magnetics* **1974**, *10*, 223–238, DOI 10.1109/TMAG.1974.1058315.
2. Ø. Olsvik, T. Popovic, E. Skjerve, K. S. Cudjoe, E. Hornes, J. Ugelstad, M. Uhlén, ‘Magnetic separation techniques in diagnostic microbiology’, *Clinical Microbiology Reviews* **1994**, *7*, 43–54, DOI 10.1128/CMR.7.1.43.
3. Q. A. Pankhurst, J. Connolly, S. K. Jones, J. Dobson, ‘Applications of magnetic nanoparticles in biomedicine’, *Journal of Physics D: Applied Physics* **2003**, *36*, R167, DOI 10.1088/0022-3727/36/13/201.

4. Q. A. Pankhurst, N. T. K. Thanh, S. K. Jones, J. Dobson, 'Progress in applications of magnetic nanoparticles in biomedicine', *Journal of Physics D: Applied Physics* **2009**, *42*, 224001, DOI 10.1088/0022-3727/42/22/224001.
5. R. Gerber, R. R. Birss, *High gradient magnetic separation*, John Wiley & Sons, Ltd., **1983**, p. 209.
6. S. S. Shevkoplyas, A. C. Siegel, R. M. Westervelt, M. G. Prentiss, G. M. Whitesides, 'The force acting on a superparamagnetic bead due to an applied magnetic field', *Lab on a Chip* **2007**, *7*, 1294–1302, DOI 10.1039/B705045C.
7. R. E. Rosensweig, *Ferrohydrodynamics*, Cambridge University Press, **1985**.
8. C. T. Yavuz, J. T. Mayo, W. Y. William, A. Prakash, J. C. Falkner, S. Yean, L. Cong, H. J. Shipley, A. Kan, M. Tomson, D. Natelson, V. L. Colvin, 'Low-field Magnetic Separation of Monodisperse Fe_3O_4 Nanocrystals', *Science* **2006**, *314*, 964–967, DOI 10.1126/science.1131475.
9. J. S. Beveridge, J. R. Stephens, A. H. Latham, M. E. Williams, 'Differential Magnetic Catch and Release: Analysis and Separation of Magnetic Nanoparticles', *Analytical Chemistry* **2009**, *81*, 9618–9624, DOI 10.1021/ac9016456.
10. J. S. Beveridge, J. R. Stephens, M. E. Williams, 'Differential magnetic catch and release: experimental parameters for controlled separation of magnetic nanoparticles', *Analyst* **2011**, *136*, 2564–2571, DOI 10.1039/C1AN15168A.
11. J. R. Stephens, J. S. Beveridge, M. E. Williams, 'Analytical methods for separating and isolating magnetic nanoparticles', *Physical Chemistry Chemical Physics* **2012**, *14*, 3280–3289, DOI 10.1039/C2CP22982J.
12. A. P. Philipse, 'The Random Contact Equation and Its Implications for (Colloidal) Rods in Packings, Suspensions, and Anisotropic Powders', *Langmuir* **1996**, *12*, 1127–1133, DOI 10.1021/la950671o, (correction) **1996**, *12*, 5971–5971.
13. K. Butter, PhD thesis, Universiteit Utrecht, The Netherlands, **2003**.
14. A. Koponen, D. Kandhai, E. Hellen, M. Alava, A. Hoekstra, M. Kataja, K. Niskanen, P. Sloot, J. Timonen, 'Permeability of Three-Dimensional Random Fiber Webs', *Physical Review Letters* **1998**, *80*, 716, DOI 10.1103/PhysRevLett.80.716.
15. A. Nabovati, E. W. Llewellin, A. C. M. Sousa, 'A general model for the permeability of fibrous porous media based on fluid flow simulations using the lattice Boltzmann method', *Composites Part A: Applied Science and Manufacturing* **2009**, *40*, 860–869, DOI 10.1016/j.compositesa.2009.04.009.
16. K. Yazdchi, S. Srivastava, S. Luding, 'Microstructural effects on the permeability of periodic fibrous porous media', *International Journal of Multiphase Flow* **2011**, *37*, 956–966, DOI 10.1016/j.ijmultiphaseflow.2011.05.003.
17. J. Kozeny, 'Über kapillare Leitung des Wassers im Boden (Aufstieg, Versickerung und Anwendung auf die Bewässerung)', *Sitzungsber Akad. Wiss. Wien* **1927**, *136*, 271–306.
18. P. Carman, 'Fluid flow through granular beds', *Chemical Engineering Research and Design* **1937**, *75*, S32–S48, DOI 10.1016/S0263-8762(97)80003-2.
19. S. R. Williams, A. P. Philipse, 'Random packings of spheres and spherocylinders simulated by mechanical contraction', *Physical Review E* **2003**, *67*, 051301, DOI 10.1103/PhysRevE.67.051301.
20. J. Blouwolff, S. Fraden, 'The coordination number of granular cylinders', *EPL (Europhysics Letters)* **2006**, *76*, 1095, DOI 10.1209/epl/i2006-10376-1.
21. A. Wouterse, S. Luding, A. P. Philipse, 'On contact numbers in random rod packings', *Granular Matter* **2009**, *11*, 169–177, DOI 10.1007/s10035-009-0126-6.
22. H. Darcy, *Les fontaines publiques de la ville de Dijon, Chapitre III: puits artésiens*, Victor Dalmont, Paris, **1856**.
23. S. Whitaker, 'Flow in porous media I: A theoretical derivation of Darcy's law', *Transport in Porous Media* **1986**, *1*, 3–25, DOI 10.1007/BF01036523.
24. P. M. Doyen, 'Permeability, conductivity, and pore geometry of sandstone', *Journal of Geophysical Research: Solid Earth* **1988**, *93*, 7729–7740, DOI 10.1029/JB093iB07p07729.
25. R. P. Chapuis, M. Aubertin, 'On the use of the Kozeny Carman equation to predict the hydraulic conductivity of soils', *Canadian Geotechnical Journal* **2003**, *40*, 616–628, DOI 10.1139/t03-013.
26. A. P. Philipse, C. Pathmamanoharan, 'Liquid permeation (and sedimentation) of dense colloidal hard-sphere packings', *Journal of Colloid and Interface Science* **1993**, *159*, 96–107, DOI 10.1006/jcis.1993.1301.

27. D. M. Thies-Weesie, A. P. Philipse, 'Liquid Permeation of Bidisperse Colloidal Hard-Sphere Packings and the Kozeny-Carman Scaling Relation', *Journal of Colloid and Interface Science* **1994**, *162*, 470–480, DOI 10.1006/jcis.1994.1062.
28. D. Thies-Weesie, A. Philipse, S. Kluijtmans, 'Preparation of Sterically Stabilized Silica-Hematite Ellipsoids: Sedimentation, Permeation, and Packing Properties of Prolate Colloids', *Journal of Colloid and Interface Science* **1995**, *174*, 211–223, DOI 10.1016/S0021-9797(85)90000-1.
29. J. van Rijssel, B. Kuipers, MINORIM Inversion method, v.15, Last visited on 07/10/2015, http://hdl.handle.net/10411/10164.
30. J. van Rijssel, B. Kuipers, B. Erné, 'Non-regularized inversion method from light scattering applied to ferrofluid magnetization curves for magnetic size distribution analysis', *Journal of Magnetism and Magnetic Materials* **2014**, *353*, 110–115, DOI 10.1016/j.jmmm.2013.10.025.
31. R. Massart, 'Preparation of aqueous magnetic liquids in alkaline and acidic media', *IEEE Transactions on Magnetics* **1981**, *17*, 1247–1248, DOI 10.1109/TMAG.1981.1061188.
32. Ioniqa Technologies BV, *Patent*, WO2014142661, **Mar. 2014**.
33. S. I. R. Castillo, D. M. E. Thies-Weesie, A. P. Philipse, 'Formation and liquid permeability of dense colloidal cube packings', *Physical Review E* **2015**, *91*, 022311, DOI 10.1103/PhysRevE.91.022311.
34. Kaye & Laby Online, Tables of Physical & Chemical Constants. 2.6.6 Magnetic properties of materials. Last visited on 07/10/2015, **2008**, http://www.kayelaby.npl.co.uk.
35. J. Bear, *Dynamics of fluids in porous media*, American Elsevier, **1972**.
36. L. Durlofsky, J. F. Brady, 'Analysis of the Brinkman equation as a model for flow in porous media', *Physics of Fluids* **1987**, *30*, 3329–3341, DOI 10.1063/1.866465.

Part III

Magnetic colloids

Morphology-controlled functional colloids by heterocoagulation of zein and nanoparticles

The contents of this chapter have appeared in modified form in:
R. J. Baars, Y. M. van Leeuwen, Y. Hendrix, K. P. Velikov, W. K. Kegel, A. P. Philipse, *Surfaces and Colloids A: Physicochemical and Engineering Aspects* **2015** *483*, 209–215

Abstract

A general and reproducible heterocoagulation method is presented to prepare sub-micron sized zein protein particles, loaded with negatively charged nanoparticles. These composite carrier particles can be obtained in three different morphologies, and each morphology can be prepared using nanoparticles of various size, shape and composition. An important feature of the zein composites is their long-term stability in water even in conditions where free nanoparticles often aggregate within days. Additionally, we modify the composite particles by coating them with a thin layer of silica via condensation of sodium silicate, opening possibilities for highly specific, functionalized carrier particles. Finally, the formation of hollow silica shells containing negatively charged nanoparticles is demonstrated, using the zein composites as a template.

8.1 Introduction

Nanoparticles provide many interesting new properties over their bulk material counterparts, because of their small size and high surface-to-volume ratio. The preparation of composite nanoparticles out of multiple materials can present further, important modifications of the nanoparticle properties, such as decreased reactivity [1], increased stability [2], combined properties within one system (such as optic and magnetic) [3] or highly specific and targeted interactions, useful in medical imaging [4] or drug delivery [5]. However, synthesis methods for such particles are usually laborious and require expensive starting materials or equipment. In addition, synthesis methods often lack general applicability, as they are designed for one specific material or morphology [6–8].

To alleviate some of these problems, we report in this paper a general and reproducible method to prepare sub-micron sized, core-shell particles that can contain a broad variety of nanoparticles, using the protein zein as a template material. Our method involves the heterocoagulation of positively charged zein together with, in principle, any negatively charged nanoparticle, into one composite colloid, without the use of any other additives.

Zein is a major storage protein from corn (*Zea mays*). It is used in a variety of foodstuffs, pharmaceuticals and other applications such as binders, adhesives and fabrics [9, 10]. Because of its hydrophobic nature and biocompatibility, its use as a potential drug or nutrient delivery mechanism has received increased attention recently [11]. Our method of incorporating nanoparticles expands the number of possible applications of zein-based particles. For instance, incorporation of magnetic or optically active materials may result in particles relevant for medical imaging or (targeted) drug delivery.

The application of zein particles is hindered in several ways, related to its poor colloidal stability in aqueous media [12], with an iso-electric point around pH 6. Patel *et al.* show that the particle stability could be increased by coating the zein particles with sodium caseinate. We provide an alternative method to increase the stability of zein composite particles by coating them with a thin layer of silica via the condensation of sodium silicate. This layer additionally expands the versatility of zein composites, as it provides a starting point for a variety of surface functionalization through the use of silane coupling agents [13]. In addition, we also show that the protein can be removed after the growth of a silica layer, leaving hollow silica shells containing nanoparticles.

In this work we investigate the incorporation of six different types of nanoparticles into the zein protein matrix: iron (III) pyrophosphate (FePPi), magnetite (mag), cobalt ferrite (CoFe), gold (Au), silver (Ag) and hematite spindles (hem). Three different composite morphologies are prepared, schematically shown in Figure 8.1: zein with embedded nanoparticles (NP-Z), zein with nanoparticles on its surface (Z-NP) and Z-NP particles with an added layer of zein (Z-NP-Z). Silica coating is applied to bare zein particles and composite systems of NP-Z containing magnetite and silver.

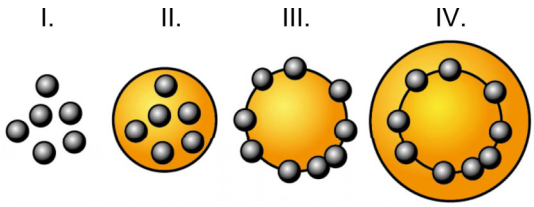

Figure 8.1. Schematic representation of the four particle morphologies: I. bare nanoparticles (NP), II. Zein with embedded nanoparticles (NP-Z), III. Zein with surface coverage of nanoparticles (Z-NP), IV. Zein with an internal shell of nanoparticles (Z-NP-Z).

8.2 Methods

8.2.1 Materials

The following chemicals were obtained from their respective suppliers: zein protein, ammonia solution (28–30 % in water), $FeCl_2 \cdot 4\,H_2O$ (98 %), $FeCl_3 \cdot 6\,H_2O$ (ACS Reagent Grade, 97 %), $NaBH_4$ (reagent grade, ≥ 98.5 %), $Fe(ClO_4)_3 \cdot 6\,H_2O$ (crystalline), $HAuCl_4$ (puriss. p.a.) and sodium silicate solution (reagent grade) from Sigma-Aldrich Chemie B.V., ethanol (100 %) from Interchema, tetramethyl ammonium hydroxide solution (TMAH, 25 % in water), NaH_2PO_4 (purum p.a., ≥ 99.0 % (T)), $CoCl_2 \cdot 6\,H_2O$ (purum, ≥ 98.0 (KT)) and Dowex 50Wx8-200 ion exchange resin from Fluka Analytical (Sigma-Aldrich Chemie B.V.), $Na_4P_2O_7 \cdot 10\,H_2O$ (ACS reagent grade), trisodium citrate dehydrate (crystalline), NaOH (pellets, pure), HCl (fuming, 37 %) and HNO_3 (GR p.a., 65 %) from Merck, urea (ACS, 99 %) and $AgNO_3$ (ACS, 99.9 %) from Brunschwig Chemie B.V and $Fe(NO_3)_3 \cdot 9\,H_2O$ (99+ % p.a.) from Acros Organics.

Chemicals were used as received. In all experiments, deionized water was used from a Millipore Synergy purification system.

8.2.2 Nanoparticle preparation

Iron pyrophosphate (FePPi) — Iron pyrophosphate nanoparticles were prepared by coprecipitation following the method described by Rossi *et al.* [14]. In a typical preparation, 50 mL of an aqueous solution of 0.86 mol $FeCl_3$ is added drop-wise to 100 mL of an aqueous solution of $Na_4P_2O_7$, over a period of 15 minutes. A turbid white suspension forms in the final minutes of the addition (at pH 4). Nanoparticles were prepared shortly before further processing with zein, as colloidal iron pyrophosphate aggregates over time in water [15].

Magnetite (Mag) — Superparamagnetic magnetite (Fe_3O_4) nanoparticles stabilized by tetramethylammonium hydroxide (TMAH) were prepared by the Massart coprecipitation method [16]. A typical preparation involves mixing 0.02 mol $FeCl_2 \cdot 4\,H_2O$ dissolved in 10 mL 2 M hydrochloric acid with 0.04 mol $FeCl_3 \cdot 6\,H_2O$ dissolved in 40 mL water. After brief ultrasonication, the mixture is added to 500 mL 0.7 M ammonia while stirring vigorously, where a black precipitate forms immediately. The mixture is stirred for another 10 minutes, after which the magnetite is collected by a hand magnet and the

supernatant is discarded. The particles are redispersed in 50 mL 1 M TMAH solution and stirred overnight. To remove excess TMAH, the particles are collected again and redispersed in water, yielding a typical stock solution of 2.7 g L^{-1}.

Cobalt ferrite (CoFe) — Nanoparticles of cobalt ferrite ($CoFe_2O_4$) were prepared following the coprecipitation method described by Claesson [17], following earlier work by Tourinho [18]. In a typical preparation 0.01 mol $CoCl_2$ is dissolved in 5 mL 2.4 M hydrochloric acid and 0.02 mol $FeCl_3$ is dissolved in 40 mL water. The solutions are heated to 50 °C, mixed and then immediately added to 200 mL of boiling 1 M NaOH solution while stirring vigorously. After 30 minutes of stirring at 100 °C, the black mixture is cooled to room temperature. The particles are washed four times with 100 mL water and then redispersed in 30 mL 2 M HNO_3. To this dispersion 30 mL 0.35 M $Fe(NO_3)_3$ is added and it is heated to 100 °C, at which it remains for 45 minutes. After cooling to room temperature, the particles were sedimented on a magnet, redispersed in 50 mL 1 M TMAH and stirred overnight. To remove excess TMAH, the particles are collected again and redispersed in 50 mL water.

Hematite (Hem) — Spindles of hematite (α-Fe_2O_3) were prepared by the method described by Ocaña [19, 20]. The preparation consists of dissolving 0.1 mol $Fe(ClO_4)_3$, 0.1 mol urea and 0.004 mol NaH_2PO_4 in 200 mL water and ageing the mixture for 24 hours at 100 °C. The mixture is purified by centrifugation and the particles are redispersed first in water, then in 1 M TMAH and finally again in water.

Gold (Au) — Citrate coated gold nanoparticles are synthesized as described by Pérez-Juste [21]. Typically, 0.3 mL freshly prepared, ice cold 0.01 M $NaBH_4$ solution is added to 20 mL of an aqueous mixture of 1.25×10^{-4} M $HAuCl_4$ and 2.5×10^{-4} M trisodium citrate, while stirring vigorously. The reaction is completed by storing the dispersion at 40 °C for 15 minutes.

Silver (Ag) — Silver nanoparticles were prepared through an aqueous reduction process with citrate at reflux temperature [22]. In a typical synthesis, 52 mL 0.769 M $AgNO_3$ solution in water is heated to reflux temperature, after which 4 mL 1.0 weight percent trisodium citrate solution is added. The reaction is completed by refluxing for 1 hour, during which a grey/yellow dispersion is formed.

8.2.3 Preparation of zein-based composites

Zein particles were prepared by an anti-solvent method, making use of the insolubility of zein in water [12, 23]. A stock solution of zein is typically made by dissolving 1.0 g zein in 40 mL 80 % ethanol. The solution is then poured slowly into 120 mL of pure water while stirring, resulting in a yellow turbid dispersion of colloidal zein particles. The size of the particles can be controlled by the concentration of ethanol [24]. Composite zein particles incorporating negatively charged nanoparticles were prepared with different morphologies.

For the general formation of NP-Z particles (Figure 8.1 II), the nanoparticle dispersions were diluted to a final volume of 120 mL, containing the following weight percentages of nanoparticles: magnetite and cobalt ferrite 0.3 wt% (at pH 8 and pH 7 respectively), hematite 0.03 wt% (at pH 7). To these dispersions, 40 mL zein solution

(1.0 g zein in 80 % ethanol) was added, while stirring. The dispersions were stirred for another 5 minutes after complete addition.

Z-NP composites (Figure 8.1 III) were prepared by pouring 40 mL zein solution (0.5 g zein in 80 % ethanol) into 80 mL water while stirring. After complete addition, 40 mL of nanoparticle dispersion was added to the dispersion, resulting in the same final weight percentage of nanoparticles as in the NP-Z system. To prepare Z-NP-Z composites (Figure 8.1 IV), another 40 mL zein solution is added immediately after the preparation of Z-NP particles. The dispersion is then stirred for another 10 minutes.

The formation of iron pyrophosphate composites requires special care due to the instability of colloidal iron pyrophosphate [15, 23]. For FePPi-Z composites 40 mL zein solution (1.0 g zein in 80 % ethanol) is poured slowly into a volume of 130 mL FePPi dispersion (as prepared above). The dispersion turns more turbid and slightly yellow. Some formed aggregates are removed by filtration before further analysis. Z-FePPi composites are prepared by slowly pouring 40 mL zein solution (0.5 g zein in 80 % ethanol) into 120 mL water. To the resulting turbid yellow dispersion, 0.21 mmol $Na_4P_2O_7$ in 5 mL water is added, immediately followed by 0.29 mmol $FeCl_3$ in 5 mL water. The dispersion slowly turns more turbid. Finally, Z-FePPi-Z composites are prepared as was done for other nanoparticles.

Composite particles with silver and gold were prepared using the same methods as for other nanoparticles, but in 10 times smaller volumes and with concentrations of 0.003 wt% (at pH 5) and 0.008 wt% (at pH 5) gold and silver respectively. Due to the large size of the nanoparticles in comparison with the zein particles, silver and hematite composites were only prepared as NP and NP-Z morphologies. All resulting dispersions have a pH of 4, regardless of the pH of the initial nanoparticle dispersion.

The composites filled with magnetic material were purified by sedimenting the dispersions next to a magnet, decanting the supernatant and redispersing the dark brown sediment in water.

8.2.4 Modification of zein particles with silica

Silica-zein core-shell colloids were prepared from bare zein particles and NP-Z particles, containing magnetite and silver nanoparticles. A silica layer is grown through condensation of sodium silicate, based on the method described by Philipse *et al.* [25], following earlier work by Iler [26]. First, the ethanol present in the zein samples was removed by rotary evaporation under reduced pressure until approximately half of the original volume was left, as ethanol may induce gelation of the sodium silicate solution. Shortly before use, a stock solution of aqueous sodium silicate is diluted with water to 1.28 % Si content. The diluted silicate solution is passed through a column with acidic ion exchange resin (Dowex 50Wx8) to reduce the sodium content and to lower the pH to a value of 11 [25]. An aliquot of 10 mL of NP-Z dispersion, prepared as above, is diluted to 50 mL with water and 10 mL of treated sodium silicate solution is quickly added while stirring. The pH of the dispersion is lowered by addition of 0.1 M hydrochloric acid, until a value of pH 8. The mixture is stirred for 1 hour and afterwards the excess sodium silicate is removed by dialysis against water over a period of 2 days, refreshing

the water daily. Afterwards, particles are collected by magnetic sedimentation or centrifugation, the supernatant is discarded and the particles are redispersed in water.

Hollow silica shells can be formed by transferring silica coated particles into 80 % ethanol. After stirring for 1 hour, the dissolved zein is washed away by centrifugation at 1500 rpm for 3 hours. Afterwards the hollow silica colloids are redispersed in water.

8.2.5 Characterization

Transmission electron microscopy (TEM) images were obtained using either a Philips Tecnai 10 or Tecnai 12, operating at 100 kV or 120 kV, respectively. Samples were diluted and dried in air on polymer coated copper grids. Dynamic light scattering (DLS) and electrophoretic mobility measurements for the determination of the zeta-potential were performed with a Malvern Instruments Zetasizer Nano in backscatter mode at 25 °C with five minutes of equilibration time. Samples were filtered and diluted appropriately before analysis. The DLS measurements were performed in ten runs of 15 measurements per run, electrophoretic measurements used ten runs of 50 measurements.

8.3 Results and discussion

We successfully prepared each of the composite morphologies as depicted in Figure 8.1 with each type of nanoparticle, as can be seen in the TEM images of Figure 8.2. Silver and hematite composites were only prepared as NP and NP-Z systems due to the large size of the nanoparticles. No nanoparticles were found outside the zein, except when gold nanoparticles were used (Z-Au and Z-Au-Z), as can be seen from electron microscopy images and from the pink colour of the supernatant after centrifugation of Z-Au (Figure 8.3). The morphology of the particles in Figure 8.2 sometimes seems distorted (c.f. Figure 8.2g), which may be attributed to drying effects.

Unfilled zein particles were found in nearly all samples (not shown), but their occurrence was somewhat less in the Z-NP-Z systems. Furthermore, some differences were found between NP-Z and Z-NP morphologies regarding the filling of the zein: for unknown reasons the NP-Z systems usually seemed more concentrated (compare for example Figure 8.2j and k).

Unfilled zein material was easily removed from the magnetically loaded zein particles by magnetic sedimentation and redispersal in water. The hematite composites proved insufficiently magnetic to be collected in this fashion. Separation by slow centrifugation was necessary for these particles and the non-magnetic particles; fast centrifugation usually led to the formation of aggregates that were no longer redispersable.

Zeta-potential analysis by electrophoretic mobility measurements show that for all composites, the nanoparticles were negatively charged and the composites were positively charged, see Table 8.1. As expected, the NP-Z and Z-NP-Z morphologies with an outer surface of zein show the highest zeta potential. DLS analysis showed average diameters comparable with values found for TEM, always with a broad size distribution. The Z-NP-Z systems always have a larger diameter because of the added layer of zein, although the thickness of this layer is not constant.

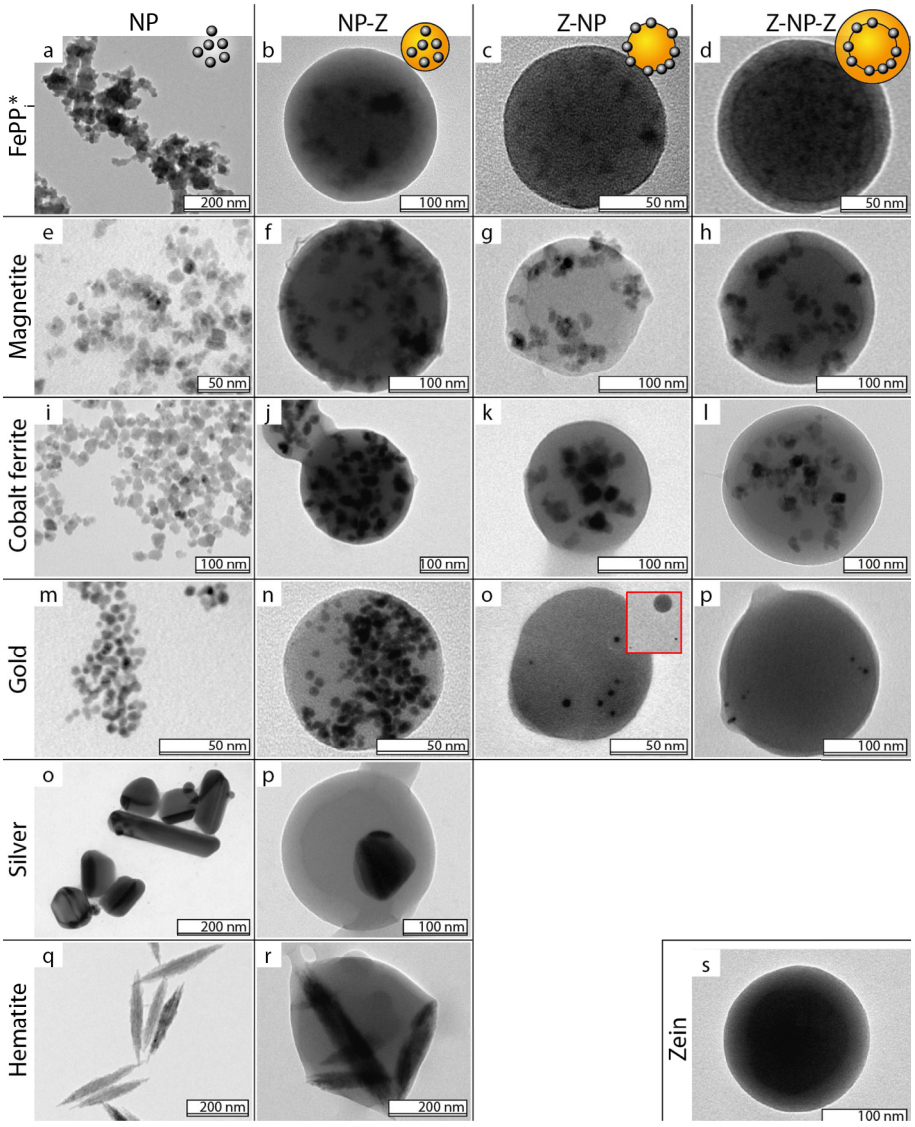

Figure 8.2. An image matrix of transmission electron micrographs of all prepared morphologies and compositions. Columns represent the different morphologies, from left to right: bare nanoparticles, NP-Z, Z-NP and Z-NP-Z. The different nanoparticle systems are represented in the rows, from top to bottom: iron pyrophosphate, magnetite, cobalt ferrite, gold, silver and hematite. A bare zein particle is shown in the bottom right corner, where the dark inner ring is due to the contact with the polymer film of the sample grid.

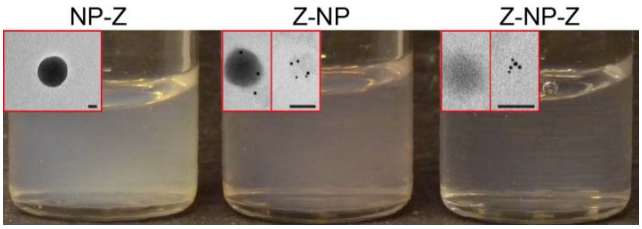

Figure 8.3. Supernatants after preparation of the gold composite systems. The lower turbidity of the Z-NP-Z supernatant shows the presence of less unfilled zein. Electron micrographs (insets) show empty zein particles (NP-Z) and separate nanoparticles (Z-NP, Z-NP-Z). Scale-bars are 50 nm.

All dispersions remain stable for several weeks, and can be redispersed by simple shaking, except the zein particles with exposed nanoparticles (Z-NP). These form aggregates on similar time-scales as dispersions of these nanoparticles [15].

The successful coating of zein with a thin layer of silica is illustrated in Figure 8.4 for unfilled zein particles, and NP-Z composites containing magnetite or silver nanoparticles. In all cases additional silica particles are present due to secondary nucleation. These particles are usually much smaller and can be removed by repeated centrifugation, or magnetic sedimentation. Sometimes larger, network structures are present which we attribute to drying effects, since no macroscopic aggregation is present and DLS measurements show size distributions that confirm that only single, non-aggregated particles are present in dispersion, see also Table 8.1. While the visibility of the silica layer is sometimes low due to surface irregularities, a clear indication that the coating is successful is provided by the much improved stability of the particles on the TEM grids. Uncoated particles consistently show many 'molten' or fused particles, because of the drying on the TEM grids (see Figure 8.4e).

The presence of silica is confirmed by determination of the iso-electric point of the particles (Figure 8.5). The silica layer clearly shifts the iso-electric point of the zein particles towards the values for pure silica colloids. Slightly higher values for the

Table 8.1. Results from electrophoretic mobility measurements and dynamic light scattering, providing the particle zeta-potential ζ and average particle diameter d.

	NP		NP-Z		Z-NP		Z-NP-Z	
	ζ (mV)	d (nm)	ζ (mV)	d (nm)	ζ (mV)	d (nm)	ζ (mV)	d (nm)
Zein	50	112	-	-	-	-	-	-
FePPi	42	135	42	166	15	188	53	228
FeO (mag)	−52	57	33	248	34	163	49	239
CoFe	−54	38	39	189	34	149	46	261
Au	−17	15	53	133	45	150	50	187
Ag	−43	84	54	145	-	-	-	-
FeO (hem)	−49	158	55	152	-	-	-	-
SiO_2@mag-Z	-	-	−36	158	-	-	-	-

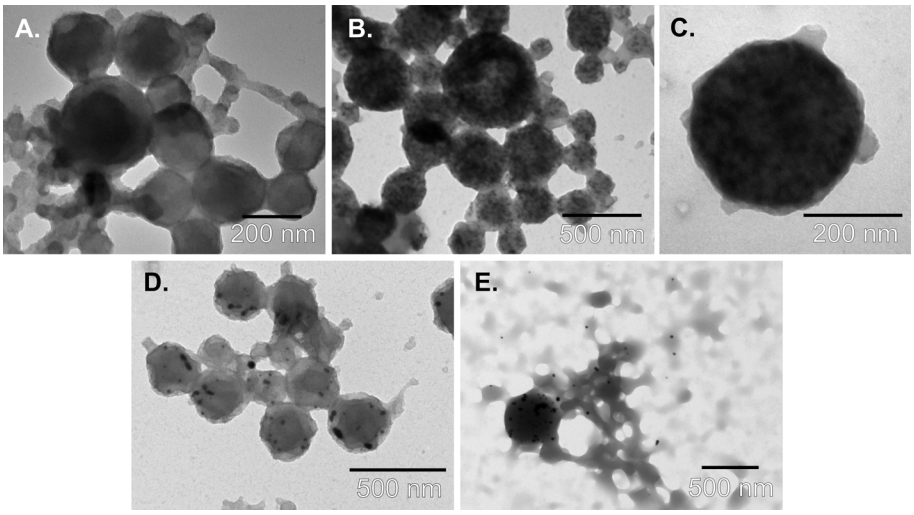

Figure 8.4. Silica coating of (A) zein particles and (B) zein with embedded magnetite nanoparticles, (C) single coated particle with embedded magnetite, and (D) zein with embedded silver nanoparticles. In all cases some residual silica is present from secondary nucleation. A typical uncoated NP-Z system is shown (E) as a reference image for the usual melting of zein particles during electron microscopy measurements.

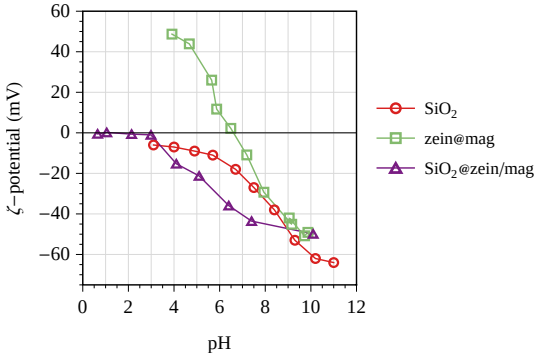

Figure 8.5. A comparison of the zeta-potential of bare silica particles (red circles, taken from [27]), bare zein particles (green squares) and our silica coated composite particles (purple triangles) at different pH. A clear shift in behaviour is visible for the coated zein in comparison with the bare zein, suggesting successful coating of the particles.

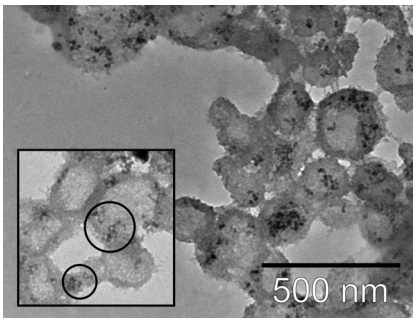

Figure 8.6. Electron micrograph showing irregularly shaped and collapsed shells of silica coated zein particles where the zein has been dissolved. Magnetite particles that were coagulated together with the zein (highlighted inside the open circles) remain inside the hollow shell. Inset: close-up of several hollow silica shells.

zeta potential are likely due to the presence of uncoated zein, or partially covered zein surfaces.

Figure 8.6 shows the hollow silica shells formed by dissolving the zein after the growth of a silica shell. The porosity of the silica layer allows for zein to diffuse through, but the nanoparticles are too large and remain inside the hollow silica shell. The mechanical stability of the shells is insufficient to keep them spherical, as many shells are deformed and collapsed.

8.4 Conclusion

We have demonstrated the use of zein protein in a general heterocoagulation process to prepare composite colloidal particles in aqueous environment. We used negatively charged nanoparticles of iron(III)pyrophosphate, cobalt ferrite, silver, gold and two types of iron oxides to prepare colloidal dispersions of different morphology (NP-Z, Z-NP and Z-NP-Z), establishing the versatility and broad applicability of the method. The composites are stabilized by a positive surface charge and are prepared without any further additives. We further improved the potential of zein composites by coating them with a thin layer of silica through condensation of sodium silicate, enabling further surface modification, such as the grafting of thiol-groups to bind gold colloids [28]. The silica layer acts as a stabilizing agent, preventing irreversible aggregation of the zein particles, in a similar fashion to stabilization with sodium caseinate [12]. An additional interesting morphology created are hollow silica shells containing nanoparticles, by dissolving the zein from a core-shell particle after its formation. Further investigation may open up possibilities for zein-based ‘micro reactors’ when catalytic nanoparticles are embedded [29].

Acknowledgements

Mikal van Leeuwen and Yuri Hendrix are thanked for their respective contributions to this work. Laura Rossi, Bob Luigjes and Julius de Folter are thanked for supplying

some of the nanoparticles used in this work. We thank Ping Liu for helpful suggestions in the closing stages of this research, and Bert Massop for additional proofreading. Part of this work was financed by Senter Novem and the Food Nutrition Delta program grant FND07002.

References

1. A. Prakash, A. McCormick, M. Zachariah, 'Tuning the Reactivity of Energetic Nanoparticles by Creation of a Core-Shell Nanostructure', *Nano Letters* **2005**, *5*, 1357–1360, DOI 10.1021/nl0506251.
2. Y. Ning, H. Zhang, J. Han, C. Yang, Y. Liu, D. Zhou, B. Yang, 'Versatile fabrication of water-dispersible nanoparticle-amphiphilic copolymer composite microspheres with specific functionalities', *Journal of Materials Chemistry* **2011**, *21*, 6837–6843, DOI 10.1039/C1JM00021G.
3. G. Wang, X. Su, 'The synthesis and bio-applications of magnetic and fluorescent bifunctional composite nanoparticles', *Analyst* **2011**, *136*, 1783–1798, DOI 10.1039/c1an15036g.
4. R. Koole, M. van Schooneveld, J. Hilhorst, K. Castermans, D. Cormode, G. Strijkers, C. de Mello Donegá, D. Vanmaekelbergh, A. Griffioen, K. Nicolay, Z. Fayad, A. Meijerink, W. Mulder, 'Paramagnetic Lipid-Coated Silica Nanoparticles with a Fluorescent Quantum Dot Core: A New Contrast Agent Platform for Multimodality Imaging', *Bioconjugate Chemistry* **2008**, *19*, 2471–2479, DOI 10.1021/bc800368x.
5. S. Caruthers, S. Wickline, G. Lanza, 'Nanotechnological applications in medicine', *Current Opinion in Biotechnology* **2007**, *18*, 26–30, DOI 10.1016/j.copbio.2007.01.006.
6. P. Hurtado-López, S. Murdan, 'Zein microspheres as drug/antigen carriers: A study of their degradation and erosion, in the presence and absence of enzymes', *Journal of Microencapsulation* **2006**, *23*, 303–314, DOI 10.1080/02652040500444149.
7. X. Liu, Q. Sun, H. Wang, L. Zhang, J.-Y. Wang, 'Microspheres of corn protein, zein, for an ivermectin drug delivery system', *Biomaterials* **2005**, *26*, 109–115, DOI 10.1016/j.biomaterials.2004.02.013.
8. K. Velikov, E. Pelan, 'Colloidal delivery systems for micronutrients and nutraceuticals', *Soft Matter* **2008**, *4*, 1964–1980, DOI 10.1039/b804863k.
9. R. Shukla, M. Cheryan, 'Zein: The industrial protein from corn', *Industrial Crops and Products* **2001**, *13*, 171–192, DOI 10.1016/S0926-6690(00)00064-9.
10. J. Lawton, 'Zein: A History of Processing and Use', *Cereal Chemistry* **2002**, *79*, 1–18, DOI 10.1094/CCHEM.2002.79.1.1.
11. Y. Luo, Q. Wang, 'Zein-based micro-and nano-particles for drug and nutrient delivery: A review', *Journal of Applied Polymer Science* **2014**, *131*, 40696, DOI 10.1002/app.40696.
12. A. Patel, E. Bouwens, K. Velikov, 'Sodium Caseinate Stabilized Zein Colloidal Particles', *Journal of Agricultural and Food Chemistry* **2010**, *58*, 12497–12503, DOI 10.1021/jf102959b.
13. E. P. Plueddemann, *Silane coupling agents*, Plenum Press, New York, **1982**.
14. L. Rossi, K. Velikov, A. Philipse, 'Colloidal iron(III) pyrophosphate particles', *Food Chemistry* **2014**, *151*, 243–247, DOI 10.1016/j.foodchem.2013.11.050.
15. Y. Van Leeuwen, K. Velikov, W. Kegel, 'Stabilization through precipitation in a system of colloidal iron(III) pyrophosphate salts', *Journal of Colloid and Interface Science* **2012**, *381*, 43–47, DOI 10.1016/j.jcis.2012.05.018.
16. R. Massart, 'Preparation of aqueous magnetic liquids in alkaline and acidic media', *IEEE Transactions on Magnetics* **1981**, *17*, 1247–1248, DOI 10.1109/TMAG.1981.1061188.
17. E. Claesson, A. Philipse, 'Monodisperse Magnetizable Composite Silica Spheres with Tunable Dipolar Interactions', *Langmuir* **2005**, *21*, 9412–9419, DOI 10.1021/la051127a.
18. F. Tourinho, R. Franck, R. Massart, 'Aqueous ferrofluids based on manganese and cobalt ferrites', *Journal of Materials Science* **1990**, *25*, 3249–3254, DOI 10.1007/BF00587682.
19. M. Ocaña, M. Morales, C. Serna, 'Homogeneous Precipitation of Uniform α-Fe_2O_3 Particles from Iron Salts Solutions in the Presence of Urea', *Journal of Colloid and Interface Science* **1999**, *212*, 317–323, DOI 10.1006/jcis.1998.6042.
20. S. Sacanna, L. Rossi, B. Kuipers, A. Philipse, 'Fluorescent Monodisperse Silica Ellipsoids for Optical Rotational Diffusion Studies', *Langmuir* **2006**, *22*, 1822–1827, DOI 10.1021/la052484o.

21. J. Pérez-Juste, L. Liz-Marzán, S. Carnie, D. Chan, P. Mulvaney, 'Electric-field-directed growth of gold nanorods in aqueous surfactant solutions', *Advanced Functional Materials* **2004**, *14*, 571–579, DOI 10.1002/adfm.200305068.
22. Y. Tan, Y. Li, D. Zhu, 'Preparation of silver nanocrystals in the presence of aniline', *Journal of Colloid and Interface Science* **2003**, *258*, 244–251, DOI 10.1016/S0021-9797(02)00151-0.
23. Y. Van Leeuwen, K. Velikov, W. Kegel, 'Colloidal stability and chemical reactivity of complex colloids containing Fe^{3+}', *Food Chemistry* **2014**, *155*, 161–166, DOI 10.1016/j.foodchem.2014.01.045.
24. Q. Zhong, M. Jin, 'Zein nanoparticles produced by liquid-liquid dispersion', *Food Hydrocolloids* **2009**, *23*, 2380–2387, DOI 10.1016/j.foodhyd.2009.06.015.
25. A. Philipse, A.-M. Nechifor, C. Patmamanoharan, 'Isotropic and Birefringent Dispersions of Surface Modified Silica Rods with a Boehmite-Needle Core', *Langmuir* **1994**, *10*, 4451–4458, DOI 10.1021/la00024a013.
26. R. K. Iler, *The Chemistry of Silica*, Wiley Press, New York, **1979**.
27. P. Wilhelm, D. Stephan, 'On-line tracking of the coating of nanoscaled silica with titania nanoparticles via zeta-potential measurements', *Journal of Colloid and Interface Science* **2006**, *293*, 88–92, DOI 10.1016/j.jcis.2005.06.047.
28. E. M. Claesson, A. P. Philipse, 'Thiol-functionalized silica colloids, grains, and membranes for irreversible adsorption of metal (oxide) nanoparticles', *Colloids and Surfaces A: Physicochemical and Engineering Aspects* **2007**, *297*, 46–54, DOI 10.1016/j.colsurfa.2006.10.019.
29. J. Liu, S. Qiao, J. Chen, X. Lou, X. Xing, G. Lu, 'Yolk/shell nanoparticles: New platforms for nanoreactors, drug delivery and lithium-ion batteries', *Chemical Communications* **2011**, *47*, 12578–12591, DOI 10.1039/c1cc13658e.

Summary

Magnetically susceptible (nano)particles are used in many technological applications, such as waste water treatment, catalytic processes, medical diagnostics and novel targeted drug delivery methods. Nanoparticles in particular are useful because of their large specific surface area. Typically at some point in the application, the particles need to be removed again from a liquid, for example, by using a magnet. In a magnetic field gradient, a dispersed particle experiences an attractive force in the direction of the gradient. This causes a net movement of the particle towards the magnet, allowing its collection and separation from the liquid.

The separation of magnetic nanoparticles is a challenging task, primarily because of their small size and therefore small magnetic moment, and their significant thermal motion opposing the capture. These properties demand strong attractive forces on the particle in order to capture it. This can be achieved experimentally in a so-called high-gradient magnetic separator. The size of a particle that needs to be captured is limited by the largest achievable magnetic gradient.

In this work we have investigated different facets of a high-gradient magnetic separation method aiming to capture small particles efficiently using a porous separation matrix built from magnetizable metallic fibres, and make first steps towards a model for this separation process.

In Chapter 2 we investigate the structure of the porous separation matrix by means of computer simulations, using the mechanical contraction method. This method is capable to generate random dense packings of spherocylinder particles in a periodic simulation box, by step-wise contraction of a dilute starting configuration. The existing method is modified by introducing a virtual particle method to emulate a hard cylindrical boundary. The effect of the boundary on the packing density and overall packing structure is investigated. Local ordering close to the boundary is always present as expected, but it is found that a significant amount of global ordering only occurs when the cylinder diameter is of approximately the same size as the particle length, or smaller. The generated packings can be further analysed to determine which one provides the largest available relative surface area for nanoparticle capture. In addition to a bounding cylinder, we show that also a wedge-shaped boundary induces various ordered structures, demonstrating the general usage of the virtual particle method.

A further modification and generalization of the mechanical contraction method is made in Chapter 3, where the governing equations are rederived in a mathematically more precise sense, and simultaneously allowing the simulation of (polydisperse) packings of particles of arbitrary (convex) shape. Results obtained for spherocylinder packings with the revised method are nearly identical to previous results. Central to the

modifications presented in Chapter 3 and Chapter 2, is that the mechanical contraction method it is now greatly enhanced and capable of simulating more types of particle packings.

The versatility of the revised mechanical contraction method is demonstrated by implementing a flexible new particle shape, the (convex) superquadric, in Chapter 4. With a superquadric object it is possible to represent a continuous transformation from a sphere to a cube, or ellipsoid to cuboid. By tweaking the shape parameters, also asymmetric and other oddly-shaped particle can be formed. We demonstrate the use of the superquadric by simulating random packings of superball particles, which continuously deform a sphere to a (rounded) cube.

In the second part of this work, the focus shifts to the magnetic properties of the separation process. In Chapter 5 an exact expression for the magnetic field of a transversally magnetised cylinder of finite length is derived. By superimposing the field of a longitudinally magnetised cylinder, the field of a homogeneously magnetised cylinder with an arbitrary magnetisation vector is calculated. The equations are successfully validated by comparison with numerical finite-element calculations, and by evaluating some limiting cases. The equations provide a way to calculate the field of a single magnetic fibre in the separation matrix quickly, accurately and for all points in space. For mutually influencing magnetised cylinders, our equations approximate the resulting magnetic field reasonably well, except at the edges of the cylinder.

From the expression for the magnetic field of a single cylinder, an exact expression for the magnetic field gradient and magnetic force can be calculated as well. This is used as input in the Brownian dynamics simulations described in Chapter 6. The simulations calculate the motion of magnetic nanoparticles in the vicinity of a single magnetised cylinder. We varied the particle diameter (and consequently their magnetic moment) from 50–250 nm, the cylinder aspect ratio and its magnetization direction. It is found that particles larger than 50 nm are fully captured, but that smaller particles primarily exhibit Brownian motion. When higher particle concentrations are simulated and hydrodynamic interactions between particles are included, chain-formation takes place. This is shown to facilitate capture, also allowing the smallest nanoparticles to become separated. Furthermore it is demonstrated that transversally magnetised cylinders are most effective in capturing nanoparticles.

In Chapter 7 the construction of an experimental magnetic separation setup is described. Preliminary experiments show that magnetite (iron oxide) nanoparticles of approximately 10 nm in size in a dilute dispersion, are almost completely captured after a single elution step of a few minutes. However, approximately 40 % of the particles are irreversibly captured, which is clearly disadvantageous if they need to be reused. More quantitative experimentation is required to characterize the different parameters influencing the separation efficiency, such as the flow velocity, packing density and nanoparticle concentration.

Finally, in Chapter 8 we have described a general heterocoagulation method to prepare composite colloidal particles incorporating different kinds of nanoparticles inside a polymer matrix. The positively charged protein zein is combined with different negatively charged nanoparticles, e.g. superparamagnetic magnetite particles,

to synthesize composite particles of different morphologies. Additionally, a thin layer of silica is deposited on the zein composites, enabling specific modification and functionalization of the particles through the use of silica surface chemistry. This provides a facile method to synthesize various colloidal composite carrier particles.

In conclusion, the results presented in this work provide independent but related contributions to further systematic understanding of a high-gradient magnetic separation process using a fibrous porous separation medium. The combination of a theoretical understanding of random dense particle packings, accurate Brownian dynamics simulations and supporting experimental investigation of separation parameters, builds a foundation for future investigation and modelling of an efficient separation process for magnetic nanoparticles.

Samenvatting

Magnetisch beïnvloedbare (nano)deeltjes worden gebruikt in vele toepassingen, zoals bij waterzuivering, katalytische processen, in de medische diagnostiek en als nieuwe methodes voor gerichte medicijnlevering in het lichaam. Nanodeeltjes zijn in het bijzonder nuttig vanwege hun grote specifieke oppervlakte. Geregeld moeten op een zeker moment tijdens hun toepassing, de nanodeeltjes weer uit een vloeistof worden gehaald, bijvoorbeeld met behulp van een magneet. In een magnetische veldgradiënt ondervindt een gedispergeerd deeltje een attractieve kracht in de richting van de gradiënt. Dit veroorzaakt een netto beweging van het deeltje richting de magneet, waardoor deze verzameld kan worden en kan worden gescheiden van de vloeistof.

Het scheiden van magnetische nanodeeltjes is een lastige taak, hoofdzakelijk vanwege hun kleine afmeting en het daarmee gepaarde kleine magneetmoment, en vanwege een significante thermische beweging die het afvangen tegenwerkt. Deze eigenschappen vereisen een sterke aantrekkingskracht op het deeltje zodat het gevangen kan worden. Dit kan experimenteel bereikt worden in een hoge-gradiënt magnetische separator ('high gradient magnetic separator'). De sterkst haalbare veldgradiënt bepaalt de kleinste deeltjesgrootte die afgevangen kan worden.

In dit werk hebben we verschillende facetten onderzocht van een hoge-gradiënt magnetische scheidingsmethode. Ons doel is het efficiënt vangen van kleine deeltjes in een poreuze scheidingsmatrix opgebouwd uit magnetiseerbare metaalfibers en om eerste stappen te zetten naar een modelmatige weergave van dit scheidingsproces.

In Hoofdstuk 2 hebben we de structuur van de poreuze scheidingsmatrix onderzocht met behulp van computersimulaties en de mechanischecontractiemethode. Met behulp van deze methode kunnen ongeordende dichtste pakkingen van sferocilinderdeeltjes gegenereerd worden in een periodieke simulatieruimte door een verdunde starttoestand stapsgewijs samen te trekken. De oorspronkelijke methode is uitgebreid met een nieuw-ontwikkelde virtueledeeltjesmethode om zo een harde cilinderwand na te bootsen. Het effect van de wand op de pakkingsdichtheid en algehele pakkingsstructuur is onderzocht. Nabij de wand is lokale ordening altijd aanwezig, zoals verwacht. Een significante hoeveelheid ordening in de gehele pakking vindt echter pas plaats als de cilinderdiameter van vergelijkbare grootte is als de sferocilinderlengte, of kleiner. De gegenereerde pakkingen kunnen verder geanalyseerd worden om te bepalen welk type pakking het grootste specifieke oppervlak oplevert voor het afvangen van nanodeeltjes. We hebben verder aangetoond dat de virtueledeeltjesmethode algemeen toepasbaar is door naast een cilinderwand ook een wigvormige wand te simuleren. Ook hier worden diverse geordende structuren gevonden.

Een verdere aanpassing en veralgemenisering van de mechanischecontractiemethode is gemaakt in Hoofdstuk 3. De achterliggende vergelijkingen zijn opnieuw afgeleid op

een wiskundig preciezere manier en tegelijkertijd is de methode toepasbaar gemaakt voor het genereren van (polydisperse) pakkingen van willekeurige (convexe) vormen. Resultaten die met de vernieuwde methode zijn verkregen voor sferocilinderpakkingen vertonen uitstekende overeenkomsten met eerdere resultaten. Centraal staat dat de aanpassingen aan de mechanischecontractiemethode in Hoofdstuk 3 en Hoofdstuk 2 de methode bijzonder verrijken en veel nieuwe pakkingssimulaties mogelijk maken.

De brede inzetbaarheid van de aangepaste mechanischecontractiemethode is gedemonstreerd in Hoofdstuk 4 door het implementeren van een flexibele nieuwe deeltjesvorm, het (convexe) superkwadratisch oppervlak ('superquadric'). Dergelijke oppervlakken zijn geleidelijk te vervormen van bollen tot kubussen, of van ellipsoïden tot balken. Door de juiste keuze van enkele parameters zijn ook asymmetrische en andere vreemdgevormde vormen mogelijk. We hebben het gebruik van superkwadratische deeltjes gedemonstreerd door ongeordende dichte superbalpakkingen te genereren, waarbij de deeltjes vervormen van een bol tot een (afgeronde) kubus.

In het tweede deel van dit werk, verschuift de aandacht naar de magnetische eigenschappen van het scheidingsproces. In Hoofdstuk 5 is een exacte uitdrukking afgeleid voor het magneetveld van een transversaal gemagnetiseerde cilinder van eindige lengte. Door het veld van een longitudinaal gemagnetiseerde cilinder hierop te superponeren, kan het veld van een homogeen gemagnetiseerde cilinder met een willekeurige magnetisatierichting berekend worden. De vergelijkingen zijn succesvol gevalideerd tegen numerieke eindige-elementenberekeningen en enkele limietgevallen. De vergelijkingen maken het mogelijk om het veld van een enkele gemagnetiseerde fiber in de separatiematrix snel, nauwkeurig en voor alle posities in de ruimte uit te rekenen. Voor wederzijds beïnvloedende gemagnetiseerde cilinders kunnen onze vergelijkingen het resulterende magneetveld redelijkerwijs benaderen, behalve aan de uiteinden van de cilinder.

Uit de uitdrukking voor het magneetveld van een enkele cilinder kan ook exacte de magnetische veldgradiënt en de magnetische kracht worden berekend. Dit heeft als input gediend voor de Brownse-dynamicasimulaties beschreven in Hoofdstuk 6. Deze simulaties berekenen de beweging van magnetische nanodeeltjes in de nabijheid van een enkele gemagnetiseerde cilinder. We hebben de deeltjesdiameter (en daarmee hun magneetmoment) gevarieerd van 50–250 nm, en daarnaast ook de cilinder lengte-breedteverhouding en magnetisatierichting gevarieerd. Er is gevonden dat deeltjes groter dan 50 nm volledig gevangen worden, maar dat kleinere deeltjes zich voornamelijk Browns gedragen. Bij het simuleren van een hogere deeltjesconcentratie en met gebruik van hydrodynamische interacties tussen de deeltjes, vindt ketting vorming plaats. Hiervan is aangetoond dat het de scheiding van losse nanodeeltjes helpt, zodat ook de kleinste deeltjes afgevangen worden. Verder is gedemonstreerd dat transversaal gemagnetiseerde cilinders het meest effectief zijn in het afvangen van nanodeeltjes.

In Hoofdstuk 7 is de bouw van een experimentele magnetische scheidingsopstelling beschreven. Voorlopige experimenten laten zien dat magnetiet (ijzeroxide) nanodeeltjes van ongeveer 10 nm in een verdunde dispersie vrijwel geheel afgevangen worden in een enkele scheidingsstap van enkele minuten. Echter, ongeveer 40 % van de deeltjes blijft onomkeerbaar vastzitten aan de staafjes, wat een duidelijk nadeel is als zij

hergebruikt moeten worden. Verdere kwantitatieve experimenten zijn nodig om de verschillende parameters in kaart te brengen die de scheidingsefficiëntie bepalen, zoals de doorstroomsnelheid, pakkingsdichtheid en nanodeeltjesconcentratie.

Tot slot hebben we in Hoofdstuk 8 een algemene heterocoagulatiemethode geschreven om composietcolloïden te synthetiseren die bestaan uit een polymeermatrix gevuld met verschillende soorten nanodeeltjes. Het positief geladen eiwit zeïne is gecombineerd met verschillende negatief geladen nanodeeltjes, zoals superparamagnetische magnetietdeeltjes, tot composietdeeltjes met verschillende morfologieën. Daarnaast is een laagje silica afgezet op de zeïne composietdeeltjes, wat verdere specifieke modificatie van het oppervlak mogelijk maakt via silica-oppervlaktechemie. Deze methode biedt een eenvoudige methode voor de synthese van diverse colloïdale dragerdeeltjes.

Concluderend bieden de resultaten in deze thesis onafhankelijke maar gerelateerde bijdragen aan het betere, systematische begrip van een hoge-gradiënt scheidingsmethode gebruikmakend van een poreus fibernetwerk als scheidingsmedium. De combinatie van theoretische kennis over ongeordende dichte deeltjespakkingen, nauwkeurige Brownse-dynamicasimulaties en ondersteunende experimenten bouwen een basis voor verder onderzoek en modellering van een efficiënt scheidingsproces voor magnetische nanodeeltjes.

List of publications

This thesis is partly based on the following publications:

- R. J. Baars, A. González-García, A. P. Philipse, "The random rod packing: disordered rods in suspensions, powders and glasses", *in preparation* (Chapter 2)
- R. J. Baars, A. González-García, A. P. Philipse, "The mechanical contraction method for arbitrary convex particles: random packing of superquadrics", *in preparation* (Chapters 3 and 4)
- A. Caciagli, B. W. M. Kuipers, A. P. Philipse, R. J. Baars, "Exact expression for the magnetic field of a finite cylinder with arbitrary uniform magnetization", *submitted* (Chapter 5)
- A. Caciagli, B. W. M. Kuipers, A. P. Philipse, R. J. Baars, "Brownian dynamics simulation of magnetic nanoparticle separation in magnetic random porous media", *in preparation* (Chapter 6)
- R. J. Baars, Y. M. van Leeuwen, Y. Hendrix, K. P. Velikov, W. K. Kegel, A. P. Philipse, "Morphology-controlled functional colloids by heterocoagulation of zein and nanoparticles", *Colloids and Surfaces A: Physicochemical and Engineering Aspects*, 483, 209–215 (**2015**) (Chapter 8)

Other publications by the author:

- B. W. M. Kuipers, M. C. A. van der Ven, R. J. Baars and A. P. Philipse, "Simultaneous measurement of rotational and translational diffusion of anisotropic colloids with a new integrated setup for fluorescence recovery after photobleaching", *Journal of Physics: Condensed Matter*, 24, 245101 (**2012**)

Curriculum Vitae

Roel Johannes Baars was born in Tiel, The Netherlands, on 17 January 1988. He graduated from secondary school at the "CSG De Lage Waard", Papendrecht, in 2005 and ranked 18th in the final round of the Dutch Biology Olympiad in the same year. Roel studied chemistry at Utrecht University, where he obtained his bachelor's degree *cum laude* in 2009. He continued his studies by enrolling in the Science Communication and Education master program at Utrecht University. During a scientific internship at the Van 't Hoff Laboratory for Physical and Colloid Chemistry at Utrecht University under the supervision of drs. B. W. M. Kuipers and prof. dr. A. P. Philipse, he investigated a setup to measure translational and rotational diffusion coefficients by fluorescence recovery after photobleaching. Afterwards, he undertook two half-year teaching internships, obtaining his secondary school teaching license and a Master of Science diploma in 2011. In September of that same year, he returned to the Van 't Hoff Laboratory to start his PhD research, again under supervision of drs. B. W. M. Kuipers and prof. dr. A. P. Philipse. This thesis comprises the results of his research. He presented his work at several national and international conferences and won a second prize with a poster on the Jam-Packed Conference in Erlangen, Germany in 2014.

Outside his studies and work, Roel has been involved with the Dutch Biology Olympiad since 2006. He has been a regular jury member for The Netherlands in the International Biology Olympiad since 2012 and is president of the Dutch Biology Olympiad foundation since 2014. He co-founded the olympiad alumni organisation "Rubisco" in 2012. In the same year, he became co-owner of Higgs Productions, a small company creating demonstration videos for use in secondary school (chemistry) class rooms.